REFERENCE ONLY

UNIVERSITY OF LONDON THESIS

Degree PhD Year 2006 Name of Author TOMLINSON E.L.

The role of fluid in the growth of fibrous diamond: a study of African and Canadian coated diamonds

Emma L. Tomlinson

Department of Earth Sciences

University College London

A thesis submitted for the degree of

Doctor of Philosophy

September 2005

ProQuest LLC
789 East Eisenhower Parkway
P.O. Box 1346
Ann Arbor, MI 48106-1346

Acknowledgements

This thesis is the result of three and half years of work and the support of many people. The first person I would like to thank is Dr Adrian Jones who provided an interesting PhD topic and supervised and encouraged my work. Dr Judith Milledge, is warmly thanked for her interest, enthusiasm and support. Judith was a mine of information on all aspects of diamond research and most of the samples in this study came from Judith's collection. I was fortunate to work along side Dr David Dobson in the Haskel Lab, David is thanked for support with the technical aspects of high pressure experimental work. I also benefited from the help of Dr Andy Beard in the probe room, the XRD knowledge of Dr Ian Wood and from Sarah Houghton in the aqueous geochemistry lab.

Dr's Chris Welbourn, Simon Lawson and Rob Caveney (DTC Maidenhead) are warmly thanked for their interest and support, and Dr Andy Taylor and Jacques Jones (also of the DTC) are thanked for cutting and polishing diamond samples. Special thanks are also due to Dr Jeff Harris and Dr Fanus Viljoen for their time and attention during by visit to DeBeers in South Africa. Jeff Harris is also thanked for providing the Panda coated diamonds described in this study.

I wish to thank my Collaborators, in particular Dr Katrien De Corte (Hoge Raad voor Diamant, Belgium), who provided access to the LA-ICP-MS, hospitality during my visits and valuable comments on the manuscript. Also Isabel De Schrijver (University of Ghent, Belgium) who carried out the LA-ICP-MS analyses. I am also indebted to Dr

Simon Redfern from the University of Cambridge, who provided access to their infrared spectrometer and to Dr Ming Zhang for support during the variable temperature infrared experiments. Paul McMillan (UCL Department of Chemistry) is thanked for his interest and enthusiasm, our discussions greatly improved my understanding of infrared spectroscopy. My published work received valuable comments from Dr Jeff Harris and Dr Ray Burgess (Panda study), Prof. Hillary Downes and Prof. Bill Griffin (LA-ICP-MS) and from Dr David Dobson and Dr George Harlow (HP-HT experiments).

I gratefully acknowledge funding support from an EPSRC (award no. 01302499) industrial CASE studentship with DeBeers, and additional support for the 8th International Kimberlite Conference from the Diamond Trading Company (DTC), Maidenhead.

I wish to acknowledge with great appreciation all the encouragement from my parents. I also wish to thank my fellow postgraduates for tea breaks, and my friends (in particular Vikki, Cathy, Liz, Jonny and Alice) and Iceni teammates for providing moral support and a life outside my thesis. Lastly and most importantly, I am grateful to Finn for the inspiration and moral support he has always provided.

Abstract

This multi-disciplinary study determines the composition and structure of mantle fluid inclusions in natural fibrous diamonds, and their role in diamond growth. Coated diamonds from Mbuji Mayi (Democratic Republic of Congo) and Panda (Canada) were analysed by electron microprobe, laser ablation inductively coupled mass spectrometry and infrared spectroscopy. Carbonate and KCl are important components of the complex fluid. Therefore, KCl-K_2CO_3 was used as a solvent catalyst for graphite in high-pressure high-temperature diamond growth experiments. Grown diamonds have skeletal morphologies; growth was rapid and occurred at temperatures as low as 1050°C.

Fluid-inclusions in Panda and Mbuji Mayi diamond coats are dominated by liquid water and carbonate. The absence of silicate melt indicates fibrous diamond growth occurred below or close to the host rock solidus. Three end-member fluid compositions are recognised: Fe-Mg-Ca carbonate, KCl and alumnosilicate. The trace element composition of the Mbuji Mayi coat fluids is consistent with K-rich carbonatite. The carbonate fluid component was derived externally before infiltration into peridotitic and eclogitic growth environments. The silicate fluid is restricted to eclogitic samples and is thought to have been derived locally by reactions between the oxidising fluid and more reduced mantle minerals. Carbonate reduction and crystallisation concentrated KCl.

Panda diamond coats contain silicate inclusions whose chemistries indicate formation in eclogitic and peridotitic (lherzolitic) hosts. Therefore, diamond coats grow in the same paragenetic environments as

octahedral diamonds. Inclusion geothermobarometry indicates that peridotitic inclusions equilibrated at 930-1010°C and 4.2-4.6 GPa. These conditions are below the lherzolite solidus and are ≈200°C lower than inclusions in Panda octahedral diamonds.

A model is presented in which fibrous diamonds grow in a solid host rock containing older octahedral diamonds, following the influx of H_2O-rich carbonate melt. This melt metasomatised and fertilised the host rock. Diamond was precipitated by the reduction of carbonate and nucleated on diamond cores.

Contents

List of Figures

List of Tables

Nomenclature

Abbreviations

carb. Carbonate

CCO Carbon-Carbonate/CO_2 buffer

CI Carbonaceous chondrite meteorite from type locality Ivuna, Canada

CL Cathodoluminescense

cpx. Clinopyroxene

DRC Democratic Republic of Congo

ecl. Eclogite

EDS Energy Dispersive Spectrometer

EMPA Electron Microprobe Analysis

FMQ fayalite-magnetite-quartz buffer

fO_2 Oxygen Fugacity

$Ft - ir$ Fourier Transform Infrared

grt. Garnet

HFSE High Field Strength Elements

$HP - HP$ High Pressure-High Temperature

$LA - ICP - MS$ Laser Ablation Inductively Coupled Mass Spectrometry

lherz. Lherzolite

LILE Large Ion Lithophile Elements

MARID Mica-Amphibole-Rutile-Ilmenite-Diopside

MIR Mid-Infrared, 4000-350 cm^{-1}

NIR Near-Infrared, 10000-4000 cm^{-1}

MORB Mid Ocean Ridge Basalt

na Not analysed

nd Not detected

ol. Olivine

opx. Orthopyroxene

PT Pressure-Temperature

pyx. Pyroxene

SEM Scanning Electron Microscope

Units

cm^{-1} Wavenumbers, = 1/frequency

Ct. Carats, 1 ct = 0.2 g

mol% Molecular proportion

ppm parts per million

wt% Oxide weight percent

Other

Ca# Ca-number, molar 100Ca/(Ca+Mg+Fe)

$H_2O\#$ H_2O-number, $100H_2O/(H_2O + CO_2)$

IaA Lattice nitrogen forming A-defect

IaB Lattice nitrogen forming B-defect

KD Distribution Coefficient

$Mg\#$ Mg-number, molar 100Mg/(Mg+Fe)

Chapter 1

Introduction

1.1 Objectives

This study is an investigation into the composition of mantle fluids [1] trapped as inclusions in natural fibrous diamonds and the role of those fluids in the growth of the diamond host. Evidence for the growth of diamond in fluid is provided by the low density of crystallographic dislocations in the diamond lattice (Sunagawa, 1984) and the polyhedral shape of diamond (Bulanova, 1995). In addition, the symmetrical and fibrous morphology and the presence of fluid inclusions in the diamond coat strengthen the argument for fluid involvement in the growth of fibrous diamond.

The approach taken was to compare and contrast the major element compositions of individual fluid inclusions in fibrous diamonds from two different locations: the Mbuji Mayi kimberlite (Democratic Republic of Congo (DRC), Congo-Kasai craton, Central Africa) and the Panda kimberlite (Slave craton, Canada). The compositions of silicate macro-inclusions in the Panda fibrous diamonds are compared to equivalents in Panda octahedral diamonds, and the trace element compositions of micro-inclusions in both the Mbuji Mayi diamond

[1]The term "fluid" is not adequately defined in the literature; some authors restrict its use to describe volatiles in the system C-O-H-(S-N); while others include all non-solid phases (carbonate, dissolved oxides). One reason for this is that at high pressure water-rich fluids and hydrous-silicate melts show increasing convergence toward the second critical end point, where the univarient melting curve ends in a divariant field (Stalder et al., 2000). In this thesis, fluid is defined as being a liquid phase consisting chiefly of volatiles, with some dissolved solutes (oxides, halides, sulfates, nitrates, and carbonates).

coats and cores was analysed in order to investigate differences between fibrous and octahedral diamond growth. High Pressure-High Temperature (HP-HT) experiments were then conducted using analogues of these natural mantle fluids. Chapter 1 provides an introduction to diamond research, the following chapters then detail each of the analytical and experimental approaches. The results are summarised in the conclusion (chapter 7) and are then used as the basis of a model for the genesis of coated diamonds.

1.2 Coated Diamonds

Coated diamonds comprise a symmetrical overgrowth (coat) of fibrous diamond on a single octahedral diamond (core). Several lines of evidence indicate that the diamond core and its coat had different carbon sources and grew during different events: 1) diamond cores show the full range of carbon and nitrogen isotope compositions seen in 'normal' diamonds and are therefore thought to have been sourced from the normal diamond population. In contrast, diamond coats globally show a narrow range of isotope compositions (δ^{13}C -7.5 to -4.1 ‰and δ^{15}N -8.7 to -1.7 ‰, Boyd et al. 1994); 2) nitrogen in the cores is generally aggregated IaA to IaB with platelet development, while coats are ubiquitously IaA, even though they have medium-to-high nitrogen concentrations (800-1500 ppm, Boyd et al. 1994). This indicates that the coat does not simply represent a late stage phase of core growth. The difference in aggregation state has been used to argue that the coat is significantly younger than the core, and suggests that the coat grew and was stored at cooler temperatures (<1100°C) than the core. The fact that the coats are not found with further diamond overgrowth suggests that the coat was the last growth event seen by the diamond. The lack of macro-sized mantle silicate inclusions in the diamond coat means that there are no isotopic age determinations. However, the similarity between the Sr isotope composition of fibrous diamonds from Mbuji Mayi and that of the kimberlite host, led Akagi & Masuda (1988) to suggest that the growth of the coat is related to the generation of the kimberlite melt and therefore occurs shortly before kimberlite eruption.

Fibrous growth on the octahedral {111} face of the core occurs almost perpendicular to the face (Machado, 1985) and the boundary between core and coat

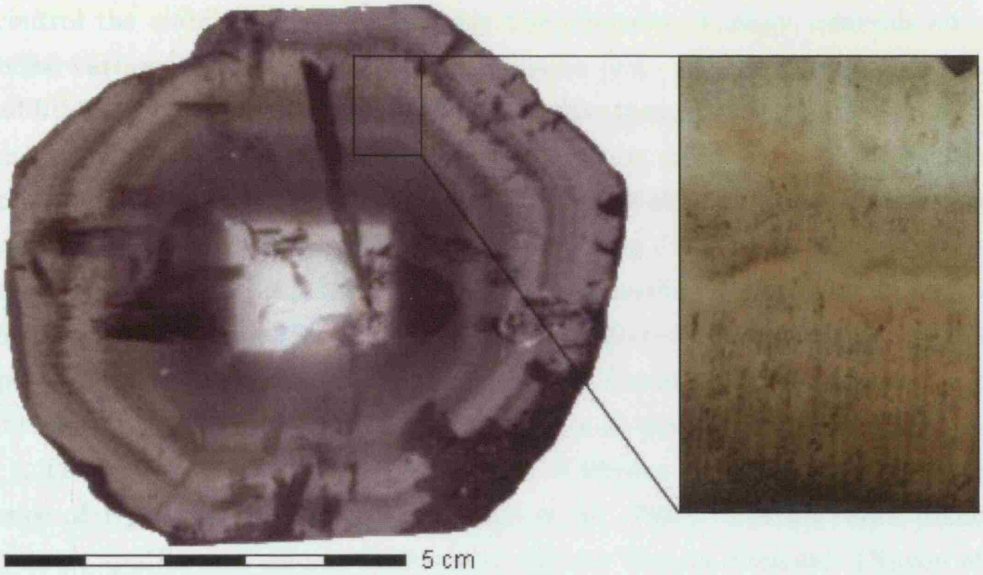

Figure 1.1: Photograph of a coated diamond sample, zoning is parallel to the core-coat boundary. Zoomed inset shows lateral alignment of fluid inclusions.

is sharp. The external surface has features such as trigons whose orientations correspond to the underlying core (Kamiya & Lang, 1965). The diamond fibres are ≈10 μm in diameter at the core-coat boundary, coarsening to ≈40 μm at the rim (Boyd et al., 1994; Kamiya & Lang, 1965). The coat captures a lot of impurities, both as small fluid inclusions, 10 nm to 1 μm (generally ≤0.5 μm) in diameter (Guthrie et al., 1991) trapped along the lateral surfaces of the fibres (Fig. 1.1) and at point defects (structural). When the core is small or absent, the resulting diamond is an opaque cube. The fibrous morphology and entrapment of inclusions indicates that diamond growth was rapid and occurred under conditions of carbon supersaturation.

1.2.1 Previous Work

H_2O- and CO_2-rich fluids and melts play an important role in many mantle processes. They are responsible for the transport of volatiles between mantle reservoirs; this strongly influences the trace element and isotopic signatures of those reservoirs and also causes metasomatism (e.g. Dawson (1980)). Fluids

control the stability fields and solidus temperatures of major minerals and stabilise carbonate and hydrous mineral phases (e.g. Grgoire et al. (2000)). In addition, C-O-H fluids are an important carbon source and may be a catalyst for diamond growth (e.g. Deines (2002)). Therefore, direct samples of the volatile phases present in the mantle are important sources of information about the physical and chemical conditions in the mantle during diamond growth. Diamond is mechanically strong and has a low reactivity in a silicate environment, so mantle fluids trapped as inclusions are preserved unaltered during subsequent mantle metasomatic events and kimberlite eruption. Therefore, there has been a lot of interest in the compositions of fluid inclusions in diamond.

The first infrared spectroscopic study of fibrous diamond revealed the presence of H_2O and carbonates (Chrenko et al., 1967). Further work identified quartz, apatite and silicate minerals in African fibrous diamond (Navon et al., 1988). The presence of apatite (Lang & Walmsley, 1983), biotite (Walmsley & Lang, 1992b) and ankerite (Walmsley & Lang, 1992a) in African samples was confirmed by transmission electron microscopy (TEM). This is a different mineral assemblage to that found in octahedral diamond (section 2.2.3.1). Guthrie et al. (1991) used TEM and AEM (Analytical Electron Microscopy) to show that the inclusions contain one or more euhedral crystals surrounded by low atomic number material interpreted to be fluid; opened inclusions contained crystals and a void due to fluid loss. Kamiya & Lang (1965) suggested that these mineral impurities divided the diamond surface into domains that develop into fibres, however not all fibrous diamonds contain mineral impurities. These solid phases are currently thought of as secondary (precipitated from the traped fluid after entrapment) minerals on the basis that 1) the uniform bulk composition of fluid in samples from a single location suggests that the components were dissolved in a fluid at the time of entrapment (Wyllie & Ryabchikov, 2000). However, mantle minerals have also been detected in micro-inclusions in fibrous diamonds from Canada (olivine, Cr-chromite, Cr-diopside; Klein-BenDavid et al. 2004) and Siberia (olivine; Zedgenizov et al. 2003a and Cr-chromite; Talnikova 1995). It is unlikely that included mantle minerals are secondary phases because garnet formation requires pressures higher than $\approx$ 1.5 GPa.

Kagi et al. (2000) used Near Infrared (NIR) spectroscopy to demonstrate that cubic diamond may contain solid H_2O ice VI in addition to liquid H_2O. Water may be present in two forms 1) samples in which HOH and OH are proportional contain liquid water, 2) samples with stronger OH absorption relative to HOH absorption contain hydrous minerals/melt in addition to fluid (Zedgenizov et al., 2003a). Fluid inclusions in fibrous diamond retain residual internal pressures of 1.4 to 2.0 GPa, this corresponds to a formation pressure of 4-7 GPa at $\approx$ 1100°C (Navon, 1991). The high internal pressure of inclusions suggests that these fibrous diamonds grow at depth.

The ground-breaking study of Navon et al. (1988) used Electron Micro-probe Analysis (EMPA) and infrared spectroscopy to sample a $\approx$40 μm area of fibrous diamond. This study showed that inclusions in fibrous diamonds from Botswana and the DRC are rich in H_2O, CO_3^{2-}, Si, K, Ca and Fe and contain measurable quantities of P, Al, Ti, Mg and Na. These elements are thought to be present as oxide compounds on the basis of the presence of quartz and apatite in the infrared spectra. These authors compare the inclusion compositions to potassic magmas (kimberlite and lamproite). By studying individual inclusions, Schrauder & Navon (1994) show that inclusion compositions vary between carbonatitic (rich in Ca, P, Mg and Fe) and silicate (rich in Si and Al) end-members; all inclusions are enriched in K. Schrauder & Navon (1994) suggested that the silicate-carbonatitic array was due to either 1) mixing of end-member fluids, 2) partial melting of a carbonated source rock, or 3) fractional crystallisation of a carbonatite melt. In contrast to the African samples, fluid in a fibrous diamond from Canada (Diavik) varies between Na-K-Cl brine and Na-rich carbonate and do not contain a hydrous-silicate component (Klein-BenDavid et al., 2004). Klein-BenDavid et al. (2004) suggest that the hydrous-silicate and brine fluids are products of carbonate crystallisation from a primary carbonatite melt and so are genetically related, while Navon et al. (2004) suggests that the brine may separate from the carbonatite melt forming a separate immiscible fluid. The brine end-member is similar to KCl brine described in internally cloudy diamonds from Koffiefontein, South Africa (Izraeli et al., 2001). Klein-BenDavid et al. (2003) describes Fe-Si-Ni sulfide melts coexisting with carbonate in K-, Ba-, Rb-, Sr-,

HFSE- and Cl-rich inclusions cuboid diamonds from Yubileinaya, (Siberia). All known fibrous diamond fluids contain a carbonate component.

The trace element compositions of African fibrous diamond have been analysed by instrumental neutron activation analysis (INAA) (Akagi & Masuda, 1988; Damarupurshad et al., 1997; Schrauder et al., 1996). Wang et al. (2003b) used Laser Ablation Inductively Coupled Plasma Mass Spectrometry (LA-ICP-MS) to analyse the trace element composition of inclusions in a fibrous coat. Compatible element abundances are similar to those in primitive mantle (Schrauder et al., 1996). Incompatible element concentrations in the fluids are higher than those in mantle-derived minerals and melt inclusions and have a similar enrichment pattern to carbonatite (Griffin et al., 2004; Schrauder et al., 1996). The concentration of incompatible elements decreases by a factor of 2 to 5 from carbonate-rich to silicate-rich fluids (Schrauder et al., 1996).

Burgess et al. (1998); Johnson et al. (2000) and Burgess et al. (2005) measured noble gas and halogen concentrations in fibrous diamonds. Ar and halogen compositions in coated diamonds from the DRC and Botswana (Africa) are similar to the composition of present day Mid Ocean Ridge Basalt (MORB) source (Johnson et al., 2000). Small scale halogen fractionation in the African samples may be due to crystallisation of a halogen-bearing phase e.g. apatite, or due to partitioning between hydrous-silicate and carbonatite melts (Burgess et al., 2005). In contrast, noble gas and halogen concentrations in diamond coats from Panda (Canada) are enriched by several orders of magnitude over normal upper mantle and Ar contents are an order of magnitude higher than than any previously reported mantle sample (Burgess et al., 2005). Br/I/K/Cl ratios are highly variable, this is attributed to unmixing of immiscible hydrous-silicate and brine fluids (Burgess et al., 2005) rather than fractionation of a Cl-bearing phase as suggested by Johnson et al. (2000). Both African and Canadian fibrous diamonds have high He and mantle $^{3}He/^{4}He$ ratios Johnson et al. (2000) showed that ^{40}Ar and Cl concentrations in fibrous diamonds are enriched by almost four orders of magnitude relative to bulk upper-mantle values and $^{40}Ar/Cl$ ratios are remarkably uniform over large distances, therefore African and Canadian coated diamonds contain a widespread chlorine-rich fluid component (Turner et al., 1990).

1.3 Geological Setting

The coated diamonds used in this study come from two locations: 23 samples from Africa, probably Mbuji Mayi (Democratic Republic of Congo) provided by Dr Judith Milledge and 8 samples from the Panda kimberlite (Canada), supplied by Dr Jeff Harris.

1.3.1 Mbuji Mayi

The Mbuji Mayi kimberlite field is located in the eastern part of the Kasai-Oriental Province in south central Democratic Republic of Congo (DRC), formerly Zaire (Fig. 1.2). The 62,000 km^2 Mbuji Mayi property is run by the Bakwanga Mining Company (Société Miniére de Bakwanga) and mine production is marketed by a subsidiary of DeBeers. The Mbuji Mayi kimberlite field consists of 14 diatremes and eluvial deposits. The ten kimberlites of the northern group are elliptical basins with or without small roots or pipes and are aligned along the EW fracture of the Archean Kasai Craton. The southern group consists of four irregularly distributed pipes (Javoy et al., 1984). The kimberlites intrude the high-grade Archaen basement of the Kasai-Congo Craton (2.8-2.4 Ga). The kimberlites in the Mbuji Mayi region are Cretaceous in age, based on stratigraphic relations. Scharer et al. (1997) reported an age of 69.8 $\pm$ 0.5 Ma for zircon and baddeleyite megacrysts from Mbuji Mayi.

The Mbuji Mayi kimberlite is a xeno-tuff, brecciated group I (basaltic) kimberlite containing numerous country rock xenoliths (granite gneiss, sandstone, limestone) and a xenocryst suite of low-Cr diopside, garnet, Mg-ilmenite and rutile. Eclogites comprise $\approx$90 % of the mantle xenolith population, the rest being lherzolite and garnet clinopyroxenites (El Fadili & Demaiffe, 1999). The presence of primary kimberlite nodules indicates at least two phases of kimberlite emplacement at Mbuji Mayi, the nodules probably represent early dykes and sills (Javoy et al., 1984). The primary kimberlite is porphyritic and contains Cr-chlorite and two generations of olivine; calcite, saponite and phlogopite are present as alteration phases (Fieremans et al., 1984). The matrix consists of Cr-chlorite, mica, calcite, saponite and accessory apatite, magnesite, ilmenite, sphene, clinopyroxene, rutile (Fieremans et al., 1984), zircon and baddleyite (Scharer et al., 1997).

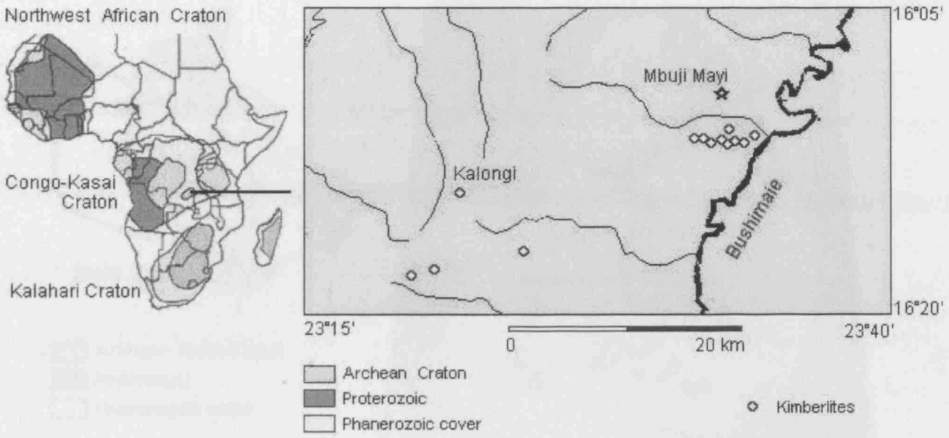

Figure 1.2: Location of the Mbuji Mayi kimberlite field in relation to African cratons. Modified after (Javoy et al., 1984).

The high carbonate and mica content of the matrix implies that the kimberlite magma had a high volatile content.

A distinctive feature of the Mbuji Mayi kimberlite is the high proportion of industrial quality diamond (≈90 % of production Kamiya & Lang 1965). This population includes transparent or opaque coloured fibrous cubes and coated diamonds, as well as irregular and aggregated crystals; the gem-quality diamond population is transparent, colourless and dominated by octahedra with rare rhombododecahedra (Javoy et al., 1984). Diamonds from Mbuji Mayi have a range of nitrogen concentrations from ≤100 to 2100 ppm (Javoy et al., 1984). U-Pb dating of a zircon inclusion in a single octahedral diamond from Mbuji Mayi revealed an age of 628 ± 12 Ma (Kinny & Meyer, 1994), this age is young for a a diamond originating in the Earth's upper mantle, athough it is still much older than the Cretaceous eruption age of the Mbuji Mayi kimberlite host.

1.3.2 Panda

The Panda diatreme is located in the central portion of the economically important BHP Billiton Ekati^{TM} diamond mine, 300 km from Yellowknife (Northwest Territories, Canada) and 200 km south of the Arctic Circle (Fig. 1.3). The 1,800 km^2 Ekati property lies in the Lac de Gras region and is part of the Central

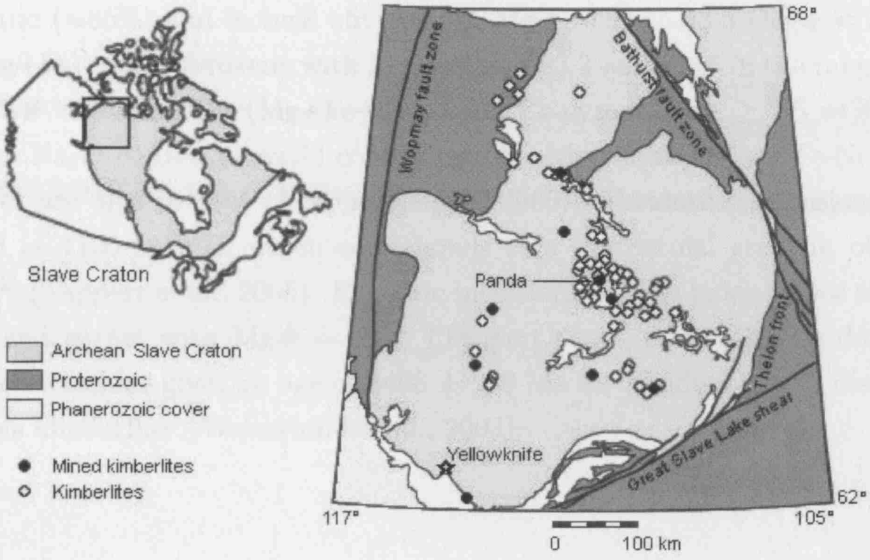

Figure 1.3: Location of the Panda kimberlite on the Slave craton. Map modified after Bleeker & Davis (1999) and Nowicki et al. (2004).

Slave Province kimberlite field, which comprises more than 200 individual pipes. Panda was the first pit to be developed at the Ekati Diamond Mine^{TM} and was the first diamond producing pit developed in Canada.

The kimberlites in the Lac de Gras region are Upper Cretaceous to Eocene in age (Creaser et al., 2004; Heaman et al., 2003). Creaser et al. (2004) reported a Rb-Sr isochron age of 52.3 $\pm$ 3.8 Ma for phlogopite macrocrysts from the Panda diatreme itself. Panda is a group I (basaltic) kimberlite, dominated by numerous discontinuous volcaniclastic units with lesser reworked volcaniclastics (Nowicki et al., 2004). The volcaniclastics are olivine-rich (up to 60%) with a fine-grained serpentine matrix. The Panda kimberlite carries country rock xenoliths (mudstone and granodiorite) and uncarbonised wood. The xenocryst population consists of mantle-derived olivine, garnet, pyroxene (Cr-diopside and enstatite), chromite and ilmenite (Nowicki et al., 2004). A distinctive feature of the Panda diamond production is the high proportion of coated diamonds (Stachel et al., 2003), this probably reflects low degrees of diamond resorption during kimberlite ascent.

Silicate mineral inclusions in octahedral diamonds from Panda are dominantly

peridotitic (≈85%) and include olivine with Mg# = 92 to 93.5 (Mg# = atomic Mg/(Mg+Fe)); clinopyroxene with Mg# = 90.8-93.3 and Ca# in the range 42.4-44.8 (Ca# = atomic Ca/(Mg+Fe+Ca)); and Cr-pyrope with $\geq$ 2.5 wt%Cr_2O_3 and high Na_2O (0.10-0.31 wt%) concentrations. Mg-chromites and Fe-Ni monosulphides are also present (Tappert et al., 2005). Peridotitic inclusions equilibrated at 1100-1250°C, which corresponds to a geothermal gradient of 40-42 mW/m^2 (Tappert et al., 2005). Eclogitic inclusions include jadeite-poor clinopyroxene and garnet with Mg# = 62.4 (Tappert et al., 2005). Re-Os dating of sulphide inclusions gives an age of 3408 ± 280 Ma for peridotitic gem diamonds from this kimberlite (Westerlund et al., 2003).

Chapter 2

Properties of Diamond

The purpose of this chapter is to outline the origin and the physical and chemical properties of diamond. This information is used to gain insights into the chemical and pressure-temperature conditions of diamond growth and its post-genetic history.

2.1 Origin of Diamond

2.1.1 Cratonic Diamonds

The vast majority of known diamonds originate in the cratonic lithosphere, which has roots that extend into the diamond stability field below ≈140 km. Multiple lines of evidence indicate that most mantle diamonds were formed and stored in the relatively cool Archean lithospheric mantle (Boyd & Gurney, 1986; Haggerty, 1986): 1) Diamond-bearing kimberlites of economic significance are found in Archons (Archean craton >2500 Ma) (Fig. 2.1); protons (Proterozoic craton, 1600 - 2500 Ma) are less likely to be diamond-bearing (Clifford, 1966). 2) Lithospheric mantle geotherms derived from mantle xenoliths intersect the diamond stability field (Boyd & Gurney, 1986; Boyd et al., 1985); 3) Harzburgitic inclusions in diamonds are ≈ 3000 Ma in age (Richardson et al., 1984). In contrast, eclogitic inclusions generally range from 3000 to <1000 Ma.

The generally accepted model is that the cratonic keel was created in the at around 3200 - 3300 Ma, by high degree melting of mantle lherzolite, forming harzburgite (Shirey et al., 2004). This coincided with diamond growth from

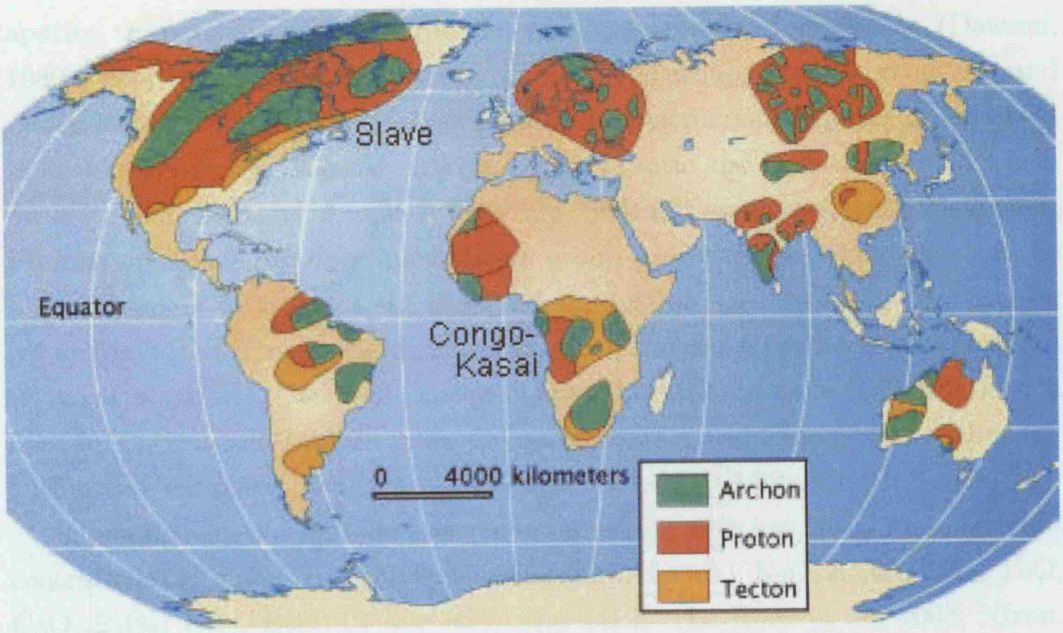

Figure 2.1: World map showing Archean and Proterozoic cratons, from Harlow (1998). Slave and the Congo-Kasai cratons are labeled

mantle carbon. Subsequent subduction of basaltic oceanic crust resulted in some portions adhering to the base of the continental keel and recrystallising as eclogite (Shirey et al., 2004). The subducting slab was the source of some organic carbon that also crystallised as diamond. More recently (between 50 and 1600 Ma), heating and/or fluid infiltration of the keel caused kimberlite (and related lamproite) melts to form and ascend to the surface carrying mantle xenoliths and xenocrysts, including diamond (Harlow, 1998). These melts must be generated deep enough to pick up diamond (> 140 km). It is not certain where fibrous diamond coats fit into this model.

2.1.1.1 Kimberlite

Kimberlite is the most important diamond-bearing mantle melt. Kimberlite is a volatile-rich potassic silica-undersaturated ultramafic igneous rock; it is a hybrid of magma, xenocrysts and xenoliths. Kimberlite contains macro- and megacrysts of forsteritic olivine, phlogopite, Cr-diopside, Ti-enstatite, chromite and pyrope in a fine-grained groundmass of olivine, monticellite, spinel, perovskite,

apatite, titanates, monazite, rutile, ilmenite, carbonate and serpentine (Dawson, 1980). Smith (1983) recognised two compositional groups based on chemistry and mineralogy: Group I (basaltic) contain ilmenite macrocrysts and lack groundmass phlogopite; they are CO_2-rich, have a low K/Ti ratio and lie within the OIB field on a Sr and Nd isotope plot. They are typically associated with melilitites. Fibrous diamonds are only known from group I kimberlites, where they can be a significant proportion of the diamond production e.g. Jwaneng (Botswana), Mbuji Mayi (DR Congo), Koidu (Sierra Leone), Yakutia (Russia), Ekati (Canada) (Boyd et al., 1994). Group II (micaceous) kimberlites are more H_2O-rich, have a high K/Ti ratio and contain groundmass phlogopite and clinopyroxene, they fall within the 'enriched' quadrant on a Sr and Nd isotope plot (Smith, 1983).

Kimberlite has an extreme magma composition with low Na_2O and high concentrations of Cr and Ni (both from xenocrystic olivine), K_2O, Al_2O_3, TiO_2, FeO, CaO, P_2O_5, CO_2, H_2O, Cl and REE and LILE (Le Roex et al., 2003; Nixon, 1995). Kimberlite has low Mg#, high K/Na, and a high LREE/HREE ratio (Le Roex et al., 2003). The normalised trace element pattern of kimberlite is similar to Ocean Island Basalt (OIB) but is more enriched in incompatible elements by an order of magnitude (Le Roex et al., 2003). The high LREE/HREE ratio suggests the presence of garnet in the kimberlite source region, the high Cr and Ni contents of xenocrysts indicate that the kimberlite source region experienced an early depletion event (Nixon, 1995). The source region must be enriched in K, Ti, Ba carbonate and water e.g. a phlogopite-bearing carbonated garnet lherzolite. The small volume of kimberlite melts indicates that they are either at the end of a long fractionation process or the 2) the products of low degree ($\approx 1\%$) partial melting. It is generally accepted that kimberlites form by a 2-stage process of low degree partial melting of garnet lherzolite lithology that has been pre-enriched by metasomatic interaction with an upwelling fluid/melt enriched in incompatible elements in the upper mantle (Brey et al., 1991; Dalton & Presnall, 1998; Girnis et al., 1995; Le Roex et al., 2003; Ringwood et al., 1992).

Kimberlites occur in cratons and stable platforms; diamondiferous kimberlites are confined to Archean and Proterozoic cratons. Kimberlite is usually found in diatremes and often forms dykes and sills. The exact locations are often controlled by faults and kimberlite pipes often occur in clusters.

2.1.1.2 Lamproite

Mantle diamonds are also mined from lamproite. Lamproite is an ultrapotassic), typically peralkaline (molar $K_2O+Na_2O/Al_2O_3 \geq 1$) mafic rock. Lamproites are characterized by the presence of forsterite, phlogopite, leucite, richterite, diopside and sanidine (Pell, 1998). They differ from kimberlites because they are richer in SiO_2 and contain groundmass glass, alkali feldspar and K-richterite. Lamproites commonly occur in dykes and flows but also in diatremes or pipes on cratonic margins. Diamonds are found in pyroclastic rocks within shallow "maar-type" craters, while magmatic lamproites are generally barren (Pell, 1998). Most olivine lamproites are post-tectonic and occur close to the margins of Archean cratons, either within the craton or in adjacent accreted Proterozoic mobile belts (Pell, 1998) e.g. at Argyle (Western Australia).

2.1.1.3 Carbonatite

Carbonatites comprise $\geq$50% modal carbonate and varied amounts of clinopyroxene, alkali-amphibloe, biotite, magnetite and apatite. The only known diamond-bearing carbonatite is found at the Chagatai Massif (Uzbekistan), which contains silicate minerals that are normally found in kimberlite and lamproite (garnet, diopside-hedenbergite clinopyroxene) in addition to calcite. The deposit consists of explosive dykes and diatremes, consistent with the rapid transport of a volatile-rich deep mantle melt (Moore & Wall, 2003).

2.1.2 Crustal Diamonds

Subduction metamorphism during collisional orogens leads to the development of diamond-bearing ultra-high-pressure (UHP) rocks at some localities, generally where continent-continent collision occurred. UHP diamonds were first reported as inclusions in garnets from the Kokchetav Massif, Kazakstan (Sobolev & Shatsky, 1990), further occurrences have been reported in China, Norway, Germany, Indonesia and Greece (see review by Osagawara 2005). The preservation of these UHP indicator minerals requires rapid exhumation. In the generally accepted model, the subducting slab brakes off and is extruded by normal and thrust faulting (Ernst & Liou, 1995).

2.1.3 Meteoritic Diamonds

Shock metamorphism during meteorite impacts causes a transient increase in pressure and temperature that may be sufficient to induce solid-state transformation from graphite to diamond (Koeberl et al., 1997) in the impacted rocks. Polycrystalline diamond aggregates (Yakutite) up to 1 cm diameter have been found at the 60 km Popagari crater (Siberia) (Nixon, 1995). Another type of meteoritic diamond is found in pre-solar meteorites. These nano-diamonds (approx 10 A diameter) and are thought to form by Carbon Vapor Deposition (CVD) fueled by CH_4 and other C-gases from dying stars (Anders & Zinner, 1993).

2.2 Chemical Properties

Diamond is an exceptionally pure form of carbon. The carbon atom has four electrons in its outer shell, which can hold eight. In diamond, each of the four available electrons in a carbon atom is paired with adjacent carbons, forming a tetrahedral unit. This covalent bonding is responsible for many of diamond's exceptional properties: hardness (10 on Mohs' scale), incompressibility (bulk modulus $\approx$500 GPa, Young's modulus $\approx$1050 GPa), high thermal conductivity (5-25 $Wcm^{-1o}C^{-1}$), electrically insulating (0-100 ohm cm^{-1}) and chemically inert below 450°C (Harlow & Davies, 2005). The diamond unit cell consists of 8 atoms which are arranged into two interpenetrating face centered cubic lattices. The high density of diamond (3.51 gcm^{-3}) relative to graphite (2.20 gcm^{-3}) indicates the high pressure origin of diamond. The strength and refractory nature of diamond make it the ideal vessel for protecting inclusions during metasomatism and transport to the surface in kimberlite eruptions.

Being pure carbon, diamond itself provides little information about conditions during crystallisation. However, the purity of diamond means that contaminants are easily identified. Substitutional impurities are those which substitute for carbon, or occupy interstitial sites in the diamond lattice. Included impurities are crystalline, melt and fluid inclusions encapsulated during diamond growth. Both substitutional and included impurities carry information about the prevailing conditions during diamond growth.

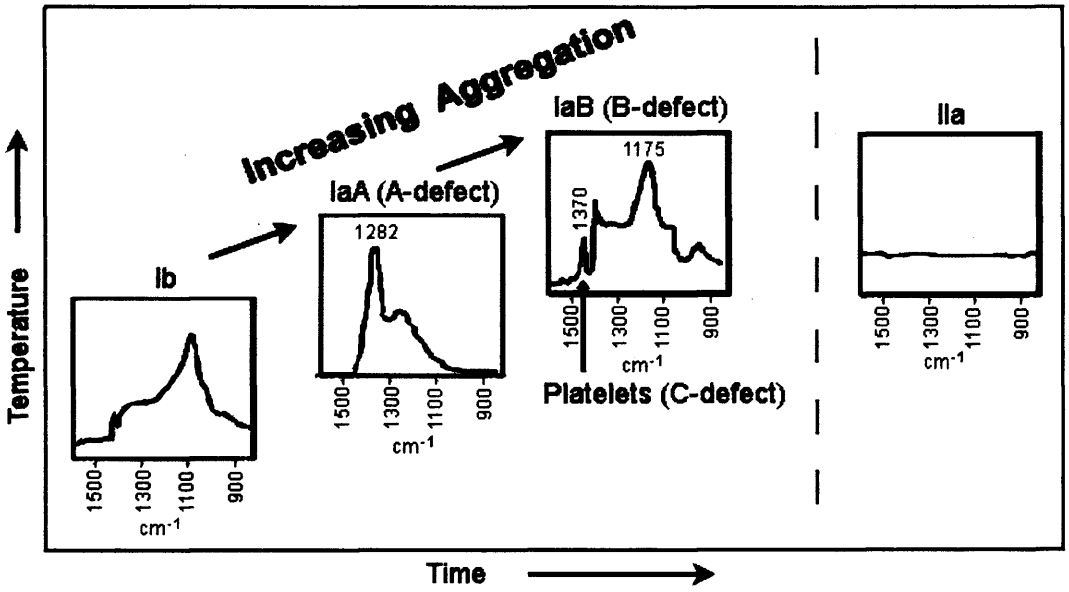

Figure 2.2: The infrared 1-phonon absorption spectra of the Ib, IaA and IaB nitrogen aggregation states of diamond, after (Mendelssohn & Milledge, 1995a,b). Ib is not necessarily at the end of the aggregation line.

2.2.1 Substitutional Impurities

Because of the small interatomic spacing and strong bonding in diamond, few foreign elements can be incorporated atomically into its crystal lattice. Nitrogen, boron, hydrogen, nickel and cobalt may all be incorporated.

2.2.1.1 Nitrogen

Nitrogen is the most common substitutional impurity and can reach 0.28% (Rocco et al., 1966); lattice nitrogen causes infrared absorption in the region 1400 - 900 cm^{-1}. Most diamonds contain $\leq$500 ppm nitrogen, but concentrations as high as 5800 ppm have been recorded (Bibby, 1982). Ultramafic parageneses are characterised by low nitrogen concentrations, while eclogitic diamonds have higher-than-average nitrogen contents (Meyer et al., 1997; Taylor et al., 1995).

Diamonds are classified according to the physical state of their substitutional nitrogen. Nominally nitrogen-free diamonds are classified as type-II; diamonds that contain detectable nitrogen[1] are classified as Type I (Robertson et al., 1934).

[1]Where the nitrogen absorption peaks are $\leq$10% of the diamond absorption peak at 1992

Type I diamonds typically accommodate between 10 and 5000 ppm nitrogen and are further subdivided according the the extent of nitrogen aggregation from type-Ib, with isolated substitutional nitrogen (C-centre, Chrenko et al. 1977; Evans & Qi 1982); though type-IaA, with nitrogen as substitutional pairs (A-defects, Davies 1976); to type-IaB, with four nitrogen atoms in tetrahedral arrangement with a carbon site vacancy (B-defects, Jones et al. 1992) as shown in figure 2.2. Aggregation is a diffusion process and is often accompanied by the development of nitrogen 'platelets', proposed to form when nitrogen is exsolved from diamond along the {111} plane (Woods, 1986) but may also be due to displaced carbon since platelets develop during IaB development. The aggregation process has a thermal activation energy barrier of 6.0 ± 0.2 eV in cube sectors and 4.4 ± 0.3 eV in octahedral sectors (Taylor et al., 1996b)), therefore the degree of aggregation is a function of the initial nitrogen content, the prevailing temperature and the time spent at this temperature. High aggregation states are thought to be indicative of long mantle residence times, high nitrogen content and/or storage at high temperature, while mildly aggregation states imply young crystallization ages and/or unusually cool conditions of mantle storage. Qualitative estimates of mantle residence time (at an assumed temperature) or mantle temperature (for an assumed residence time) can be gained from the degree of nitrogen aggregation (Mendelssohn & Milledge, 1995a; Taylor et al., 1996b, 1990).

Nitrogen concentrations of fibrous cuboid diamonds and diamond coats are typically high (800-1500 ppm; Boyd et al. 1994). Fibrous diamond coats from numerous locations are ubiquitously type-IaA (Boyd et al., 1987) having no absorbance due to platelets or the IaB aggregate. This is interpreted as evidence that they formed shortly before kimberlite eruption (Boyd et al., 1987, 1992, 1994). However, the nitrogen diffusion may be inhibited by the presence of large numbers of inclusions and by the fibrous diamond morphology.

2.2.1.2 Other Impurities

Hydrogen causes narrow peaks at 3107 and 1405 cm^{-1} and is attributed to CH stretching and bending modes (Woods & Collins, 1983), however these structures

cm^{-1}, less than approximately 20 ppm.

have not been identified unambiguously. Boron is the major impurity in a few natural diamonds, these type IIb diamonds are p-type semiconductors (Collins, 2000). Nickel forms Ni-N vacancy complexes, with an Ni ion at the centre of a carbon divacancy occupying a slightly distorted octahedral site (Lang et al., 2004). Ni and Co concentrations of $\leq$30ppm and $\leq$1 ppm have been recorded as lattice impurities in synthetic diamond grown from metal catalysts (Hayakawa et al., 2000). Ni concentrations in natural diamonds are 12 orders of magnitude less than in synthetic diamonds (Nadolinny et al., 1999). Yelisseyev et al. (2004) studied coated diamonds from Snap Lake (Canada) using confocal photoluminescence and local absorption spectroscopy. These authors show that high concentrations of nickel may be incorporated into the coat lattice, as well as being present in inclusions. Nickel-nitrogen complexes are responsible for the yellow-green luminescence of the diamond coat.

2.2.2 Stable Isotope Composition of Diamond

The isotopic composition of diamond is important in determining the source of carbon and nitrogen for diamond growth.

2.2.2.1 Carbon Isotopes

Carbon has two stable isotopes, δ^{12}C and δ^{13}C, whose abundances are approximately 98.89 % and 1.11 % respectively. The isotopic composition is expressed the as the difference between the sample and the Pee Dee Belemnite carbon standard, in parts per mil (‰).

Worldwide, diamond δ^{13}C values range from +5.0 to -38.5 ‰, with 72 % falling between -2 and -8 ‰ (Cartigny, 2005). Peridotitic diamonds have a relatively restricted range of carbon isotope compostions (+0.2 to -26.4 ‰; Cartigny 2005), with approximately 90% peridotitic diamonds being within the mantle range (δ^{13}C = -1 to -10 ‰; Taylor & Anand 2004 and references therein). This is taken as evidence for the mantle origin of carbon in peridotitic diamonds. However, Deines (2002) reports a number of more depleted isotopic compositions (down to -21 ‰) in diamonds from Southern Africa.

Eclogitic diamonds span the entire range of compositions ($\delta^{13}C$ = +27 to -38.5 ‰; Cartigny 2005) and only one third of eclogitic diamonds have $\delta^{13}C$ values in the mantle range. A much greater proportion of eclogitic diamonds have very negative $\delta^{13}C$ values (<< -10 ‰) relative to peridotitic diamonds (Cartigny, 2005). Three main models have been proposed to explain the range of carbon isotopic compositions in eclogitic diamonds: 1) fractionation during fluid transport and/or diamond growth e.g. during carbonate formation or the separation of immiscible fluids (Cartigny et al., 1998; Deines, 1980; Galimov, 1991; Javoy et al., 1984); 2) subducted carbonaceous material reflecting organic fractionation (Kirkley et al., 1991); 3) pre-existing mantle heterogeneities acquired during the Earth's accretion and not homogenised by convection (Deines et al., 1987, 1993).

Fibrous diamonds, such as diamond coats, from global locations have uniform carbon isotope compositions ($\delta^{13}C$ = -7.5 to -4.1 ‰; Boyd et al. 1994). Small scale (<1 ‰) isotopic variation has been recorded within single diamond coats (Boyd et al., 1994).

2.2.2.2 Nitrogen Isotopes

Nitrogen isotopic compositions are also of interest, nitrogen has two stable isotopes, $\delta^{14}N$ and $\delta^{15}N$, whose abundances are 99.65 % and 0.37 % respectively. The isotopic composition is expressed the as the difference between the sample and air in parts per mil.

Most diamonds have $\delta^{15}N$ compositions that fall in the range -12 to +4 ‰and there is no clear difference between peridotitic and eclogitic diamonds (Cartigny et al., 1998). This range is similar to MORB, which represents present day depleted mantle. However, the full diamond range is -25 to +6 ‰ (Cartigny et al., 1998). Depleted $\delta^{15}N$ contents have been attributed to mantle heterogeneities on the basis of the wide range in meteoritic isotope compositions (Cartigny et al., 1997). Fibrous diamonds, such as diamond coats, contain $\delta^{15}N$ = -8.7 to -1.7 ‰ (Boyd et al., 1987, 1992).

2.2.3 Included Impurities

Inclusions in diamonds are an invaluable tool for investigating the composition of the host mantle and mantle fluids and the pressure-temperature conditions and timing of growth.

2.2.3.1 Crystalline Inclusions

Two generations of crystalline inclusions were initially recognised: epigenetic and syngenetic. Epigenetic inclusions form by open system alteration of included minerals after diamond formation and do not represent mantle chemistry. Syngenetic inclusions form synchronously with the diamond host. Diamond inclusions are classified as syngenetic on the basis of 1) the negative morphology of included phases (e.g. Sobolev et al. 1972); 2) the epitaxial relationship between inclusion and diamond (Harris, 1968); and 3) inclusions may have a cubo-octahedral morphology regardless of their own crystal structure, this superposition of the diamond morphology is known as xenohedry. Meyer (1987) later suggested that many silicate inclusions are in fact protogenetic, i.e. formed prior to encapsulation in the diamond.

The criteria for syngenesis may be questioned, firstly because most inclusions are often poorly shaped and those with imposed morphologies are typically cubo-octahedral, which is incompatible with the octahedral host diamond (Milledge, 2004). Secondly, included minerals may develop an imposed morphology and an epitaxial relationship with their host, as demonstrated by 2.37-2.92 Ga sulphide inclusions in 350-600 Ma zircon (Spetsius et al., 2002). Thirdly, the trace element chemistries of silicate inclusions are often suggestive of complex histories prior to entrapment e.g. many harzburgitic and lherzolitic garnets have a humped or sinusoidal REE patterns suggesting melt extraction followed by metasomatic re-enrichment (Taylor et al., 2003). Finally, the lack of a correlation between the compositions of sulphide and silicate inclusions are independent of the $\delta^{13}C$ and $\delta^{15}N$ compositions of the host diamonds. This suggests that the diamonds grew by fluid processes rather than in conjunction with mantle minerals (Deines & Harris, 1995).

Agent	Mineralogical	Major element	Trace element	Reference
Carbonatite	apatite carbonate moissanite	High CaO, Na_2O Low SiO_2, K_2O	LREE and Sr rich Low HFSE and HREE High Nb/Ta, Zr/Hf	Rivalenti et al. 2004 Coltorti et al. 2000
K-rich hydrous Silicate melt	k-richerite phlogopite K-feldspar rutile zircon titanates	High SiO_2, K_2O TiO_2 Low CaO	high MREE-HREE high HFSE	Coltorti et al. 2000 Misra et al. 2004 Nixon 1995 Stachel & Harris 1997a
C-O-H fluid	amphibole phlogopite	Low Ti	Low HFSE REE enriched over LILE	Eggler 1987 Stalder et al. 1998

Table 2.1: Signatures of metasomatism ascribed to different agents: accessory minerals observed in host rock (modal changes; Dawson 1984) and major and trace element characteristics (cryptic changes; Dawson 1984).

Diamond inclusions originate from two major compositional suites of mantle rocks: eclogites and peridotites (Harris, 1979; Meyer & Boyd, 1972; Sobolev, 1977), this provides evidence for the mantle origin of diamonds. Growth of diamond in peridotite and eclogite host rocks is supported by the finding of diamondiferous eclogite and peridotite xenoliths in kimberlites.

Peridotitic (P-type) diamonds account for 75-80% of all inclusion-bearing diamonds (Taylor & Anand, 2004). Peridotite suite diamonds (also known as P-type) are defined by the presence of olivine, Cr-rich pyropic garnet, enstatite, diopsidic clinopyroxene and/or chromite. Sobolev (1977) subdivided peridotite inclusions into lherzolitic (clinopyroxene-bearing host rock) and harzburgitic (clinopyroxene-absent host rock) on the basis of CaO and Cr_2O_3 in garnet (lhertzolitic garnets are Ca-saturated). The Mg# (atomic Mg/(Mg+Fe)) of olivine may also be used to delineate the lherzolitic (Mg#$\approx$92) and harzburgitic (Mg#$\approx$94) parageneses (Harris, 1992).

Eclogitic (E-type) diamonds are characterised by pyrope-almandine garnet and omphacitic clinopyroxene; coesite, kyanite, rutile and sanidine also occur. A group of silicate inclusions intermediate between eclogitic and peridotitic form the minor websteritic suite. Sobolev (1977) classified websteritic and peridotitic diamonds into a single ultramafic (U-type) paragenesis.

Recent trace element studies indicate that silicate inclusions commonly show

evidence of complex histories. Depletion by removal of a silicate melt results in high Mg# values increased concentrations of compatible trace elements e.g. Ni in olivine (NiO up to 0.47 wt%) and orthopyroxene (NiO up to 0.19 wt%) and Cr in chromite (61.1 to 68.5 wt%) (Stachel & Harris, 1997b). Melt removal also causes decreased Ca, Ti, Zn, Ga, Zr in garnet (e.g. Griffin et al. 1992). Many inclusions also show evidence of metasomatism by a range of fluids. Table 2.1 lists the mineralogical and major and trace element characteristics used to classify different metasomatic fluids/agents. Some workers believe that these different fluid signatures reflect multi-stage metasomatism by different agents (e.g. Nielson & Wilshire 1993). Navon & Stoppler (1987) suggested that reactions between percolating metasomatic fluids/melts and their host rocks may be modelled by chromatographic processes. During infiltration, the melt/fluid tends towards equilibrium with the matrix: compatible and moderately compatible elements are buffered by the wall rock, whereas incompatible elements do not equilibrate so readily and travel further into the wall rock. This causes fractionation and progressive geochemical evolution of the infiltrating fluid/melt to produce silicate, hydrous and carbonate derivatives. Therefore, with reactive chromatographic fractionation, there is no need for genetically distinct melts. As this melt continues to infiltrate the porous mantle, it leaves an imprint of this fractionation in the form of wall rock zonation. Bodinier et al. (2004) applied the quantitative chromatographic model of Vasseur et al. (1991) to the trace element and Nd isotopic composition of a veined pyroxenite dyke from Lherz, France, and conclude that water-rich and carbonate rich melts were both derived by crystal segregation in the magma conduit and wall rock reactions of the same parental fluid. Initial crystallisation of pyroxene and garnet in the dyke drove the fluid to more H_2O-rich compositions, this fluid then infiltrated the wall rock in anastamosing veins and intergranular percolation; amphibole and clinopyroxene crystallisation in the wall rock resulted in the evolution of a P, LREE and Th-U enriched carbonate melt, which migrates further into the wall rock and deposited apatite (Bodinier et al., 2004).

It is often difficult to identify a specific depletion and/or metasomatic event(s) as the combined effects are superimposed. As a result of this complex history, mantle silicate populations commonly show compositional heterogeneity over a

range of scales (Sobolev & Efimova, 1998): Firstly, inclusions in diamonds often do not correspond to their equivalent minerals in the host xenolith (e.g. Ireland et al. 1994; Taylor et al. 2000), typically inclusions are more fertile[1] than their host (Taylor et al., 2000). Secondly, inclusion compositions vary may between diamonds from a within a single xenolith (e.g. Taylor et al. 1996a). Finally, inclusion compositions may vary within a single zoned diamond (e.g. Griffin et al. 1988; Sobolev et al. 1997). The most compelling example of intra-diamond compositional variability is the occurrence of diamonds containing inclusions of mixed paragenesis (e.g. Prinz et al. 1975; Wang 1998).

Sulphide inclusions also occur in diamond. Sulphide inclusions are more common in diamond than in peridotite and eclogite xenoliths (Gurney, 1989). The Ni concentration of sulphide may be related to the paragenesis of the host mantle; sulphides with higher Ni contents are thought to be peridotitic, while lower Ni-concentrations are associated with the eclogite paragenesis. African peridotitic sulphides are defined as having $\geq$8 % Ni (Deines & Harris, 1995), while Bulanova et al. (1996) defined Siberian peridotitic sulphides as having $\geq$12 % Ni, while acknowledging that the boundary is probably transitional.

Most diamond inclusions originate from the diamond window between the graphite-diamond phase boundary and the base of the lithosphere (140 to 200 km), however inclusions in some diamonds suggest that they were formed at pressures equivalent to the transition zone and lower mantle ($\geq$ 600 km) (Stachel, 2001). To date, most of these 'superdeep' diamonds are of the eclogitic paragenesis (Stachel, 2001). Majoritic garnet is the only reliable indicator of derivation from the transition zone and asthenosphere. E-type majoritic garnet differs from lithospheric E-type garnet in terms of its elevated Si content and a bias to higher Na and Ti and lower Fe contents. Rare peridotitic majorite inclusions have very high Cr relative to peridotitic garnet inclusions (Stachel et al., 2005). Additional inclusions that may indicate a sub-lithospheric origin for diamond, include ferropericlase, stishovite and CaSi and MgSi perovskite (Stachel, 2001), while tetragonal-almandine-pyrope phase (TAPP) is Ca-free garnet which may be a retrograde high-pressure phase (Stachel et al., 2005).

[1]Pyroxene-rich, capable of producing basalt melt e.g. partial melting of lherzolite to form a basalt melt and a harzburgite residue.

2.2.3.2 Diamond Age Determination

The purity of diamond makes it difficult to obtain age data directly. Traditionally, age information has been derived from isochrons based on the nitrogen concentration and aggregation states (Taylor et al., 1996a; Taylor, 1990), but there are large errors associated with this method because aggregation is also effected by temperature. Recently, Koga et al. (2003) used the spatial distribution of carbon and nitrogen isotopes in diamonds to provide information on mantle residence time. This thermochronometer is based on the large difference in diffusive relaxation times between carbon and nitrogen isotopes and is also temperature dependent.

Diamond ages may be determined indirectly by geochronology of silicate inclusions, using the U-Pb, Rb-Sr and Sm-Nd isotope systems for silicates. This method assumes that the inclusions are syngenetic (see section 2.2.3.1). If the inclusions are, protogenetic, then the determined ages date the formation of the inclusions and place an upper limit on the age of the host diamond. Furthermore, if the inclusions are syngenetic then the isotopic signatures may have been modified by metasomatism prior to encapsulation in diamond. This summary will focus on data from the Kaapvaal craton. Nd model ages of 3300 Ma were determined for batches of harzburgitic garnets in diamonds from Finsch and Kimberly, and of 1930 Ma for batches of lherzolitic garnet and clinopyroxene inclusions in diamonds from Premier (Richardson et al., 1993). Ages determined from bulk sampling of inclusions from multiple samples may be giving an average age with an unknown range. Two sulphide inclusions in a peridotitic diamond from Koffiefontein define an Re-Os isochron giving an age of 69 $\pm$30 Ma (Pearson et al., 1998).

Eclogitic garnet and clinopyroxene inclusions from multiple diamonds give Sm-Nd isochron ages that range from 1580 Ma (Finsch; Richardson et al. 1990), through 1150 Ma (Premier; Richardson 1986) to 990 Ma (Orapa; Richardson et al. 1990). Five individual garnet inclusions in a single large eclogitic diamond from Finsch also indicate that diamond growth occurred over a protracted period from 2408 to 1443 Ma (Smith et al., 1991). Sulphides in Koffiefontein eclogitic diamonds give an Re-Os isochron age of 1050 Ma (Pearson et al., 1998). Therefore,

eclogitic diamond growth appears to have been episodic during the Proterozoic, possibly reflecting tectonic and/or thermal events in the craton. This is supported by the complex internal stratigraphy of many diamonds, which represents multiple growth event separated by growth hiatuses and periods of dissolution. However, there is a question as to how representative these ages are of the overall diamond population.

Diamonds may also be dated indirectly by geochronology of sulphide inclusions, using the Re-Os system. In this case the central assumption is not that the inclusions are syngenetic, but that the isotope system was reset during the diamond growth event. Encapsulation then isolates the inclusion and the radioactive clock is started. Fortunately, the blocking temperatures of most isotope systems are well below the diamond growth temperatures. Furthermore, the abundance of fluid during diamond growth should enhance diffusion and allow isotope systems to be reset. In the case of sulphides, the compositions of sulphide inclusions suggest that few were ever in equilibrium with mantle olivine, and more likely formed from a fluid phase associated with diamond growth (Deines & Harris, 1995). However, some peridotitic inclusions may not be completely reset. Low Sr and Nd contents in peridotitic garnets make them susceptible to isotopic disturbance during metasomatic enrichment, leading to extreme isotopic compositions that are not necessarily overwritten during the diamond growth event. This is reflected in a discrepancy between ages determined from Rb-Sr and Sm-Nd systems in Mir and Udachnaya xenocysts (Pearson et al., 1995). The discrepancy between the silicate and sulphide ages for diamonds from the Kaapvaal craton may reflect the genuine range of peridotitic diamond ages; alternatively Archean ages may be artifacts of low Nd signatures of peridotitic garnets or inherited ancient isotopic signatures that were not reset during diamond growth (Pearson et al., 1998).

2.2.3.3 Fluid Inclusions

Fluid inclusions are tiny pockets of liquid and/or vapor trapped in minerals. Fluid inclusions are necessarily syngenetic, as they are isolated from the bulk fluid by the process of entrapment. Fluid inclusions in diamond are the deepest samples of upper mantle available. Fluid inclusions in diamonds indicate that a variety

of fluids may be present during gem diamond growth. Melton et al. (1972) used mass spectroscopy to detect CO_2, H_2O, CH_4, Ar, N_2 and possibly H_2 and CO in gases released from diamond by crushing. Subsequent spectroscopic work confirmed the presence of CO_2 (Chinn et al., 1995; Schrauder & Navon, 1993), N_2 and CH_4 (Tomilenko et al., 2001). In addition, nitrogen and hydrocarbons have been recorded from annealed cracks in diamonds form Yakutia (Tomilenko et al., 1997). Finally, Fesq et al. (1975) and Bibby (1982) used instrumental neutron activation analysis (INAA) to measure the trace element composition of octahedral diamond, concluding that diamond contained trapped melt inclusions. The compositions of fluids in fibrous diamond coats are reviewed in section 1.2.1.

2.3 Physical Properties

2.3.1 Diamond Morphology

Diamonds from different regions show distinctive morphological characteristics. The external morphology of a diamond is the combined effect of the primary morphology acquired during crystallization and the effect of secondary processes. This observation has led to a number of classification schemes (e.g. Orlov 1977 defined five morphological classes and ten varieties of Russian diamonds, variety IV is coated diamonds).

2.3.1.1 Primary Morphology

Three basic growth modes are recognized for diamond, from cube {100} through cubo-octahedra to octahedra {111}. Natural diamonds recovered from peridotite and eclogite xenoliths are octahedral (either single crystals, macles and aggregates) indicating that this is primary growth habit in the mantle. Cube faces are rare, although cuboid diamonds (rounded polycrystalline diamond masses with an external cubic shape but without distinct cubic 100 growth zones) are common in some deposits. In contrast, the most common morphology for synthetic diamonds is the cubo-octahedron, and cube faces are ubiquitous in synthetics. Diamond growth morphology is controlled by the slowest growth face, which is

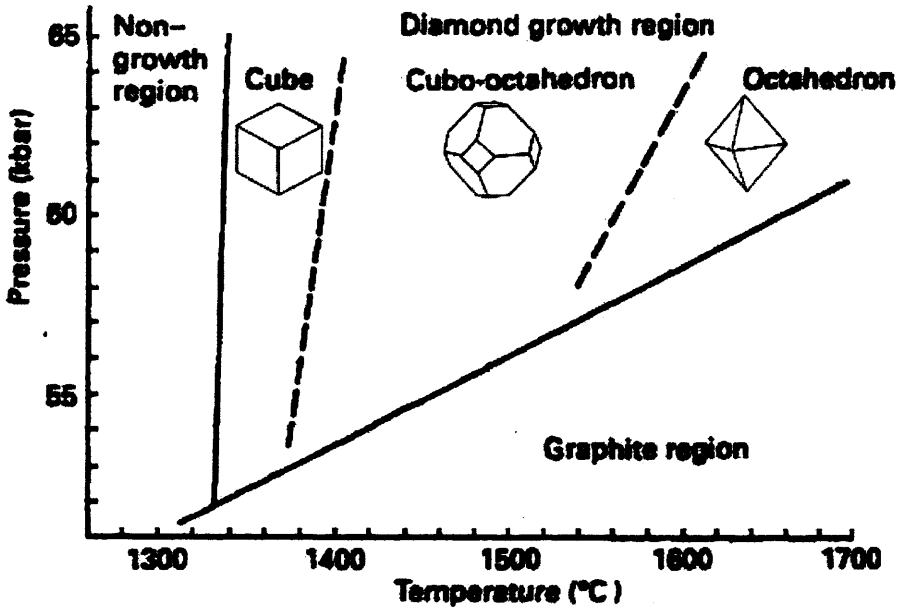

Figure 2.3: Pressure-temperature diagram for diamond growth using metal solvent-catalysts showing regions of characteristic morphology. High order faces are grown near the diamond-graphite equilibrium boundary. Modified after Clausing (1997).

dependent on the pressure-temperature conditions during growth (Fig 2.3) (Giardini & Tydings, 1962). At high temperature, the crystal is bound by eight {111} planes, leading to an octahedral morphology, at lower temperatures cube faces are dominant (Giardini & Tydings, 1962).

Sunagawa (1990) devised a morphological classification system to describe the importance of carbon saturation during diamond growth (Fig. 2.4). Under conditions of low-carbon saturation, single diamond crystals form by spiral growth, which adds layers parallel to a smooth crystal-fluid interface. This is known as layer-by-layer growth and produces crystals with flat faces and a regular atomic structure with few dislocations. Under conditions of fluid and carbon supersaturation, an adhesive-type growth occurs and there is an increase in the rate of diamond nucleation and precipitation. This leads to irregular atomic arrangement of carbons in the diamond lattice, a rough crystal-fluid interface and the formation of micro- and poly-crystalline diamond aggregates such as diamond coat, cuboid, ballas, bort and hailstone bort. The preferential orientation of

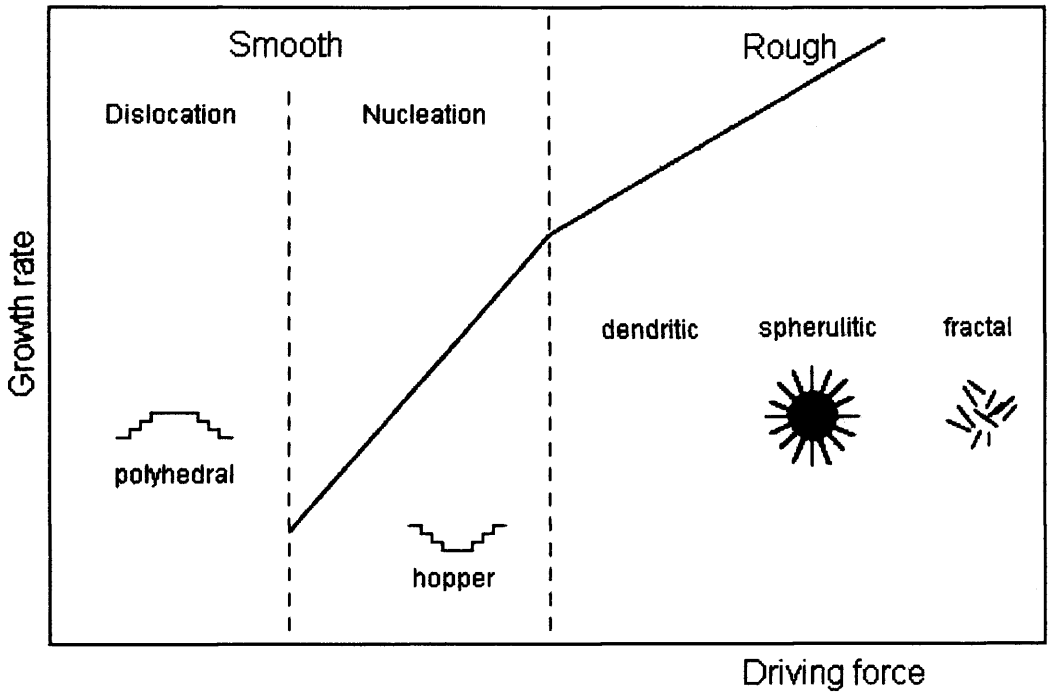

Figure 2.4: The morphological variation of single and polycrystalline diamonds related to the driving force conditions (fluid and carbon supersaturation), under higher driving force conditions polycrystalline like fibrous diamond appear, whereas under lower driving force conditions, single crystalline octahedral diamonds are formed (Sunagawa, 1990).

nuclei leads to inter-penetrating or contact twinning in diamond.

2.3.1.2 Secondary Morphologies

Deformation, resorption and etching/dissolution modify the primary growth morphology. Deformation leads to slip along glide planes parallel to the octahedral cleavage, leading to the development of parallel lamination lines (Taylor & Anand, 2004). High-nitrogen diamonds are more resistant to deformation and so are more likely to experience brittle fracture (Mendelssohn & Milledge, 1995b). Such features imply that the diamond once resided in a solid medium.

Resorption and etching occur when diamond is taken outside its thermodynamic or chemical stability field. Diamonds with fractures and cracks an those which contain defects (e.g. platelets) are particularly susceptible to chemical at-

tack (Mendelssohn & Milledge, 1995b). Resorption textures are related to the primary morphology; facets are often domed and edges are rounded leading to the formation of dodecahedral and tetrahexahedral external morphologies (Robinson et al., 1989). Resorption is recognised by the truncation of growth layers in the cathodoluminescence (CL) image. Etching, probably during transport in the kimberlite melt or during metasomatism involving CO_2 and H_2O fluids in the mantle, leads to the development of positive (pits edge parallel to face) or negative (pits reoriented by 180^o to face) triangular (trigons) and square etch pits (Clausing, 1997; Robinson et al., 1989). Experimental replication of etching in KNO_3 generated positive etch pits at temperatures below $\approx$1000°C and negative etch pits at higher temperatures (Evans & Sauter, 1961). As etching proceeds, the edges of the pits become curved. Once etching has proceeded far enough to produce an appreciable change in the overall shape of the diamond, the process is termed dissolution. Dissolution creates rounded dococahedal morphologies, the proportion of dodecahedral crystals increases as the diamond size decreases because of the higher surface:volume ration of smaller crystals (e.g. Harris 1979). Dissolution, graphitisation and oxidation, lead to truncated growth features and may eventually destroy the diamond (Orlov, 1977; Robinson et al., 1989).

2.3.2 Fibrous Diamond

The focus of this research is the fibrous coat of coated diamond, a form of diamond aggregate. Fibres run in octahedral directions from a mutual centre (Lang, 1974; Moore & Lang, 1972), choosing between them in a random walk of branched growth (Machado, 1985). Fibres are approximately parallel, only deviating by $\approx 0.43^o$ about the fibre axis (Kamiya & Lang, 1965). Fibres have curved {100} faces terminated either by zig-zag rows parallel to ⟨110⟩, leading to the formation of dodecahedral and cubic facets (Kamiya & Lang, 1965) or by flat {111} faces similar to mixed habit diamonds (cuboid+octahedral) (Shimobayashi & Kitamura, 2001). Sectors between these principal directions are filled by branched fibrous growth in four directions. In the {110} and {100} corner sectors, fibres are not perpendicular to the face, they appear to have grown in the ⟨111⟩ direction (Shimobayashi & Kitamura, 2001). The end result is a cube with rough

cubic surfaces; fibrous diamonds are cuboid, with each face being an average orientation in the cube direction. In rare samples, fibres propagate radially forming a sphere (Kamiya & Lang, 1965). Fibrous morphologies reflect high nucleation rates and rapid crystallization according to the model of Sunagawa (1990), section 2.3.1.1. The fibrous structure of the diamond coat is highly dislocation-rich (Kamiya & Lang, 1965).

2.4 Diamond Stability

Diamonds often have complex layering and internal morphologies (often known as internal stratigraphy) as a result of changing thermodynamic and chemical conditions. Growth may be episodic and growth rates variable as a result of changing pressure-temperature conditions and because of changes in the level of fluid and carbon saturation. Periods of diamond growth may be interspersed with periods of resorption and possibly plastic deformation.

2.4.1 Thermodynamic Stability

Carbon has two basic structures: diamond (cubic) and graphite (planar layers of hexagonally arranged carbon atoms). The graphite-diamond equilibrium boundary was calculated in 1938 by Rossini & Jessup (1938) and has been revised several times since. The phase diagram in Fig. 2.5 shows the temperature and pressure conditions under which diamond is stable in addition to several mantle geotherms, together these define the diamond window. The phase change between graphite and diamond requires more than just compression of the graphite lattice; it involves translation of atomic planes. The strong bonding energy between carbon atoms means that the energetic activation barrier for transformation is high and the conversion is therefore kinetically unfavorable. Hence, diamond will remain in a meta-stable state at room temperature and pressure without converting to graphite.

Related structures of carbon include hexagonal diamond, lonsdaleite (e.g. Meteor and Canyon Diabalo craters, U.S.A) and chaoite (e.g. Rise Crater, Germany). These high-pressure allotropes are formed by shock metamorphism of meteoric graphite, rapid transformation means that the high-pressure forms retain

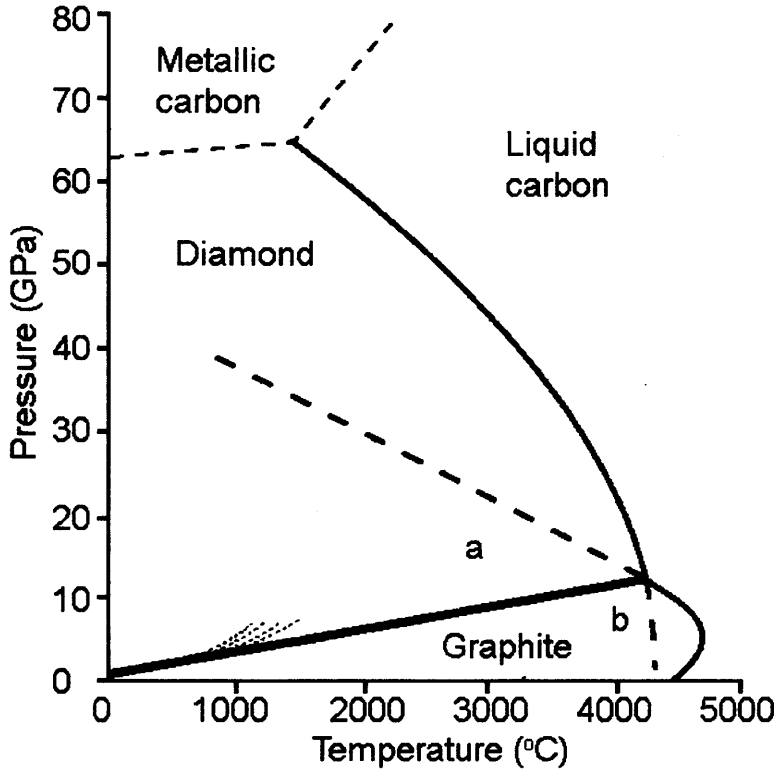

Figure 2.5: Phase diagram for elemental carbon showing fields of diamond, graphite and metallic carbon (to date, metallic carbon has not been found in nature); a) stable diamond and metastable graphite; b) stable graphite and metastable diamond (Bundy, 1989). The red dashed lines show shield geothermal gradients of 36 to 42 mW/m^2 between 4 and 8 GPa (calculated after Pollack & Chapman 1977).

the hexagonal crystal lattice of graphite. Low-pressure carbon allotropes include fullerene (rings of carbon atoms introduced into a layer of graphite hexagons) and amorphous carbon.

2.4.2 Chemical Stability

Carbon may exist in the mantle as elemental carbon (diamond or graphite), fluid (CO_2, CO, CH_4) or as carbonate, depending on the local oxidation state. The upper limit of f_{O_2} stability of diamond or graphite with respect to a free fluid is controlled by the DCO/GCO (or CCO) buffer:

$$C + O_2 \rightleftharpoons CO_2 \tag{2.1}$$

Diamond/graphite + oxygen $\rightleftharpoons$ carbon-dioxide (DCO/GCO)

Adding H to the system lowers the maximum f_{O_2} of diamond stability as CO_2-H_2O fluids are produced. Below DCO/GCO, H_2O becomes progressively more dominant with decreasing f_{O_2}, until at $\approx$ 4 log units below DCO/GCO, reduced species (CH_4 and H_2) become dominant (Jakobsson & Oskarsson, 1990; Sokol et al., 2000; Wood et al., 1990).

At $\geq$1.5 GPa and f_{O_2} above the DCO/GCO buffer, CO_2-rich fluids may react with mantle silicates to produce carbonate (Eggler, 1983). Lots of CO_2 is needed to saturate peridotite, therefore free-CO_2 should only be present in localised areas of the mantle e.g. armoured veins where there is a kinetic barrier to further reaction. At f_{O_2} below the DCO/GCO buffer, mantle silicates plus diamond (rather than CO_2) lie on the other side of the reaction line to carbonate. The carbonation reactions in eclogite (DCDD), lherzolite (EMOD) and harzburgite(EMFDD) (Eggler, 1983) are are the upper limit f_{O_2} of diamond stability in the presence of C-O-H fluid:

$$CaMg(CO_3)_2 + 2SiO_2 \rightleftharpoons CaMgSi_2O_6 + 2C + 2O_2 \tag{2.2}$$

dol + coe $\rightleftharpoons$ cpx + dia + volatiles (DCDD)

$$3Mg_2Si_2O_6 + 2CaCO_3 \rightleftharpoons 2Mg_2SiO_4 + CaMgSi_2O_6 + 2C + 2O_2 \tag{2.3}$$

opx + calcite $\rightleftharpoons$ olivine + cpx + diamond + volatiles (EMFDD)

$$Mg_2Si_2O_6 + 2MgCO_3 \rightleftharpoons 2Mg_2SiO_4 + 2C + 2O_2 \tag{2.4}$$

opx + magnesite $\rightleftharpoons$ olivine + diamond + volatiles (EMOD)

Diamond is present under reducing conditions, while more oxidising conditions stabilise carbonate or CO_2. C-bearing fluids may be reduced when they infiltrate peridotite or eclogite mantle, causing the precipitation of diamond or graphite, depending on the PT conditions. The relevance of these reactions is shown by reports of diamonds containing CO_2 (Chinn et al., 1995; Schrauder & Navon, 1993; Wang et al., 2005) and carbonate (Izraeli et al., 2001; Navon et al., 1988; Schrauder & Navon, 1994; Wang et al., 1996, 2005; Zedgenizov et al., 2004) inclusions. Conversely, diamond may be dissolved when the prevailing oxidation state is increased, leading to the development of surface dissolution pits and structures e.g. during diamond transport in kimberlite melt.

Chapter 3

Vibrational Spectroscopy

3.1 Introduction

Vibrational spectroscopy is one of three methods used to characterise the chemical compositions of inclusions in the Panda and Mbuji Mayi diamond coats. The aims of the spectroscopy study are: 1) to characterise and compare included impurity characteristics of fibrous diamonds from Panda (Slave Craton, Canada) and Mbuji Mayi (Kasai-Congo Craton, Democratic Republic of Congo); and 2) to investigate the structure of the trapped fluid at the PT conditions of diamond growth.

3.1.1 Principles of Vibrational Spectroscopy

Vibrational bands are produced by bonding properties of functional groups (e.g. CO_3^2, OH, SiO_2, SiO_4, SiO_6) and can therefore be used to determine their presence. Intrinsic diamond lattice absorption in infrared occurs in the region 2700 - 1500 cm^{-1} and is due to two and three phonon transitions (Collins & Fan, 1954), any additional absorption peaks are due to impurities. IaA lattice nitrogen gives peaks at 1282, 1220 and 480 cm^{-1}. Vibrational spectroscopy has several advantages over atomic and isotopic identification methods such as EMPA and LA-ICP-MS:

1. Minerals and volatiles can be identified.

2. The position and shape of functional group absorption bands allows structures to be resolved e.g. polymorph identification and recognition of amor-

phous phases. Using infrared spectroscopy, Zedgenizov et al. (2003b) showed that OH in cuboid diamonds may be present as H_2O or OH in minerals or melt. Kagi et al. (2000) investigated the combination OH stretch plus H_2O bend of molecular water at 5180 cm^{-1} and found evidence for both liquid water and ice VI.

3. Volatile concentrations may be quantified. Navon et al. (1988) and Schrauder & Navon (1994) have published values of 20 to 500 ppm H_2O and 15 to 900 ppm CO_2 in carbonate in fibrous diamonds from Botswana; Fibrous cuboid diamonds from Siberia contain 100-1000 ppm H_2O and up to 14000 ppm CO_2 (Zedgenizov et al., 2004). CO_2 ice has been observed in the infrared spectra of natural octahedral diamonds (Chinn et al., 1995; Schrauder & Navon, 1993; Wang et al., 2005), but not in fibrous diamonds;

4. Residual internal pressures of inclusions may be determined from the shift in the position of infrared peaks, due to structural deformation of functional groups. Diamonds are capable of maintaining high residual internal pressures on their inclusions: Navon (1991) used the pressure induced shift of quartz to calculate residual pressures of 1.5-2.1 GPa in inclusions in a fibrous cuboid diamond. This corresponds to a formation pressure of 4-7 GPa at 1000-1300°C. Izraeli et al. (1999) used the pressure induced shift of the 856 cm^{-1} line in the raman spectra of olivine to calculate the internal pressures of 0.13 to 0.65 GPa for olivine inclusions in non-fibrous Siberian diamond. Micro-Raman measurements of the vibrational band shifts of coesite inclusions in non-fibrous Venezuelan diamonds give a confining pressure of 3.62 GPa (Sobolev et al., 2000);

5. Infrared spectroscopy can be used to determine the nature and concentration of substitutional impurities in the diamond lattice e.g. N (section 2.2.1.1).

Vibrational spectroscopy a light-mediated spectroscopy technique based on the interaction between 1) the oscillating electric field associated with electromagnetic radiation in the infra-red region (1-1000 μm) and 2) the electric dipole

moment of molecules in the subject matter [1]. During analysis, the frequency (v) of the source radiation is varied. Photons are absorbed, emitted or scattered when the frequency of the radiation matches the vibrational frequency of a molecule in the sample i.e. when the energy held by the photon is the same as the energy gap between two states in the molecule.

The frequency and strength of the vibrational modes are a function of the force constant (k) of the molecular vibration and the atomic mass (m) of the participating atoms. The fundamental vibrational frequencies of volatile and mineral functional groups observed in fibrous diamonds are shown in figure 3.1. Each vibration also can occur at multiples of the fundamental frequencies. Overtones involve multiples of a single fundamental mode, while combinations involve different modes of vibrations e.g. if a molecule has vibration fundamentals v_1, v_2, v_3, then it may have overtones at $\approx 2v_2$ and combinations at $\approx v_1+v_2$. Each higher overtone or combination is typically 30 to 100 times weaker than the fundamental vibrational mode. Infrared spectroscopy measures the frequencies at which radiation is absorbed to excite the sample molecules. Sample absorbance is defined as $A=-\log(I/I_o)$ (where I is the intensity of transmitted light, I_o is the intensity through a the background).

[1] A dipole occurs when there is a charge difference across a bond, as the bond vibrates (bends or stretches) the atoms get closer or further apart causing a change in the moment; symmetrical molecules e.g. N_2 are not infrared active, unless they are distorted.

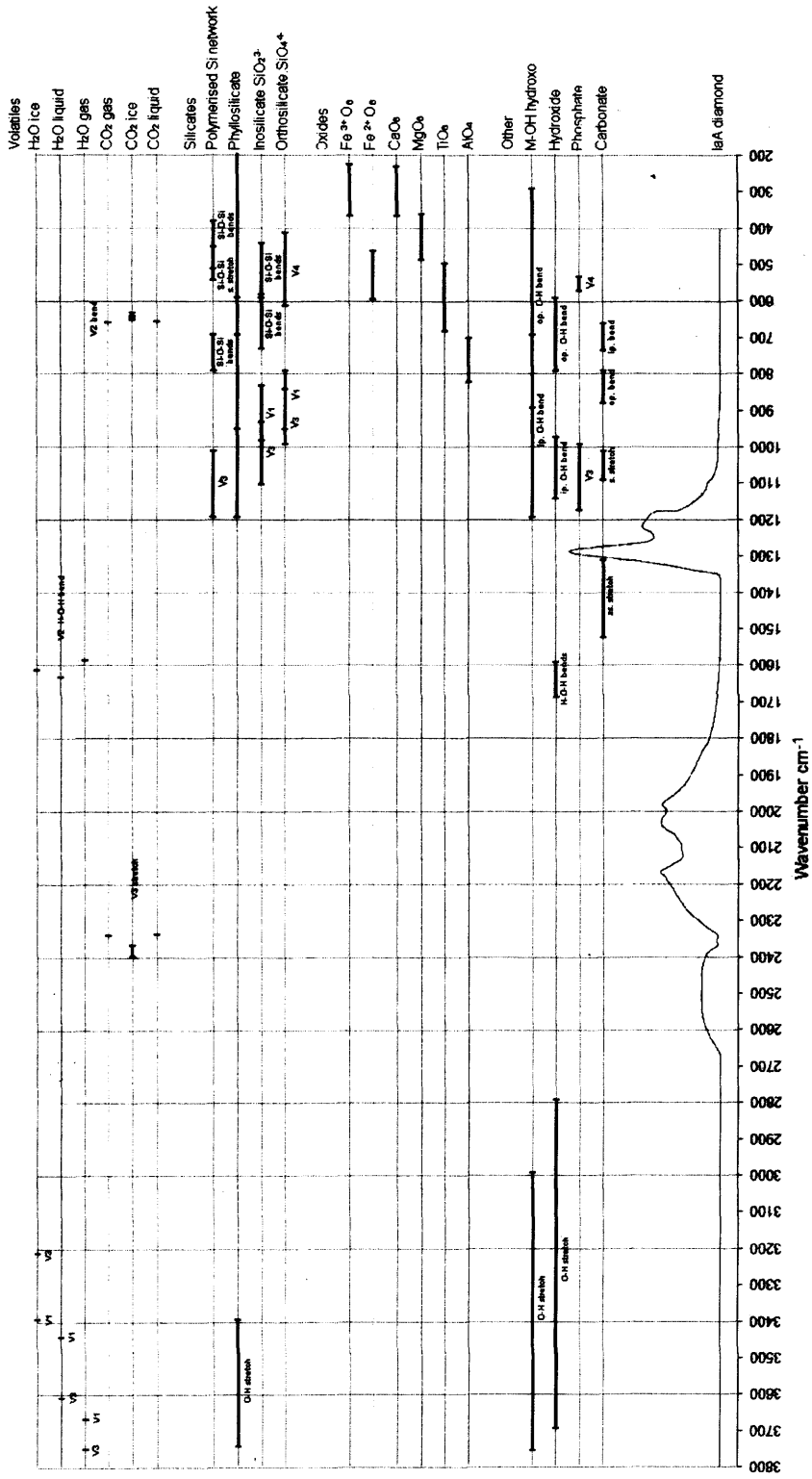

Figure 3.1: Vibrational ranges of volatile and common mineral (silicates, carbonates and phosphates) functional groups seen in fibrous diamond. The spectra for type-IaA diamond is also shown. Spectral ranges are derived from Williams (1995) (silicates, oxides), Nakamoto (1997) (volatiles), Socrates (2001) (hydroxide, M-OH hydroxo, phosphate, carbonate) and Farmer (1974a) (phyllosilicate).

3.2 Part 1: Impurities

3.2.1 Analytical Method

Infrared absorption spectra were collected using a Vector22 Fourier Transform infrared (ft-ir) spectrometer at University College London. The spectrometer is equipped with a HeNe laser (633 nm) and a KBr beam splitter. For bulk analyses, a deuterated triglycine sulfate (DTGS) detector was used and the beam diameter was $\approx$ 0.6 mm using a 3 mm aperture. Spectra were recorded in transmission with a resolution of 2 cm^{-1} in the range 4000 to 380 cm^{-1} with one spectrum being the average obtained from 512 scans. Polished diamond plates 0.5 to 1.3 mm thick with [100] orientation were mounted onto aluminium discs, which in turn were mounted on a A524 accessory plate with 5x beam condenser. An Al foil mask was used to ensure that only the fibrous coat was analysed. For sample traverses, the spectrometer was equipped with a Bruker IRScope-1 microscope. In samples with high volatile concentrations and thick coats, infrared spectra were collected along a traverse from the core-coat boundary to the coat rim. Traverse spectra were recorded in transmission with a resolution of 2 cm^{-1} in the range 4000 to 670 cm^{-1} with one spectrum being the average obtained from 128 scans. The spot size was 16 μm and spectra were collected at 20 μm increments across the sample.

Sample sets MM, CDR and PAN were laser cut and CTPs and CTPb were sawn to give parallel plates which were polished on both sides. Therefore most of the spectra have a linear baseline. However, in samples with a high inclusion content and opaque colour the baseline may not be horizontal and linear. The effect of IR radiation scattering was corrected manually, by baseline corrected at 4000, 2650, 1550 and 650 cm^{-1} (Fig 3.2).

The infrared spectra are the result of absorption along the path length of the IR beam through the sample, which depends on the sample thickness. The baseline-corrected spectra are normalised to a constant path length of 1 mm by setting the absorbance at 1992 cm^{-1} to 1.23. Absorption information was extracted from the sample spectra using the Opus macros UCPKMAIN.Mac and UCTRACE2.Mac (Mendelssohn & Milledge, 1995b) and then the IaA (and IaB in the diamond cores) spectral components and nitrogen concentration (in ppm)

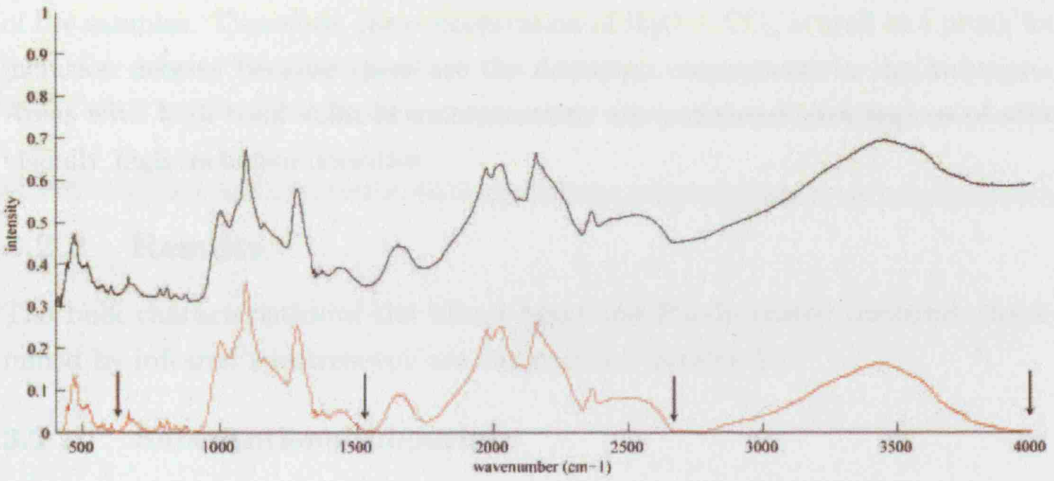

Figure 3.2: Baseline correction process in sample MM10, from raw spectra (black) to corrected spectra (red). Baseline points are: 4000, 2650, 1550 and 676 cm^{-1}.

were calculated using the Quattro Pro deconvolution program of Mendelssohn & Milledge (1995b), converted for Microsoft Excel. Lattice-bound nitrogen concentrations and aggregation states of the diamond cores and coats are given in table 3.1.

The abundance of lattice bound hydrogen is expressed as the ratio of hydrogen peak intensity to diamond peak intensity ($I_{3107}/_{1992}$). The reference spectrum of nitrogen-free (type II) diamond and an appropriate amount of IaA diamond are then subtracted to reveal the net absorption contribution of inclusions.

The concentrations of H_2O and carbonate as CO_2 were calculated from the intensities of the O-H stretching band of water (using ϵ_{3420}=80 L per mol cm^{-1}; Thompson 1965) and of the v_3 stretching band of calcium carbonate (using ϵ_{1430}=235 L per mol cm^{-1}; Fine & Stolper 1985). Taking into account the difference in absorption coefficients of different carbonates and the effect of pressure on water and carbonate absorption, the calculated H_2O and CO_2 concentrations have errors of $\pm$25 and $\pm$40 ppm respectively (Navon et al., 1988). Since the absolute concentration of volatiles is dependent on inclusion density, we use the molar ratio $H_2O\# = H_2O/(CO_2+H_2O)$ to describe the volatile composition.

Inclusion density is difficult to measure because of the extremely small size and high abundance of inclusions and because of the variable opacity and colour

of the samples. Therefore, the concentration of $H_2O + CO_2$ is used as a proxy for inclusion density because these are the dominant components in the inclusions. Areas with high total volatile concentrations are correlated with regions of with visually high inclusion densities.

3.2.2 Results

The bulk characteristics of the Mbuji Mayi and Panda coated diamonds determined by infrared spectroscopy are summarised in table 3.1.

3.2.2.1 Substitutional Impurities

Nitrogen is mildly aggregated IaA in all of the diamond coats, this is consistent with global fibrous diamond populations (Boyd et al., 1987, 1992, 1994). Nitrogen

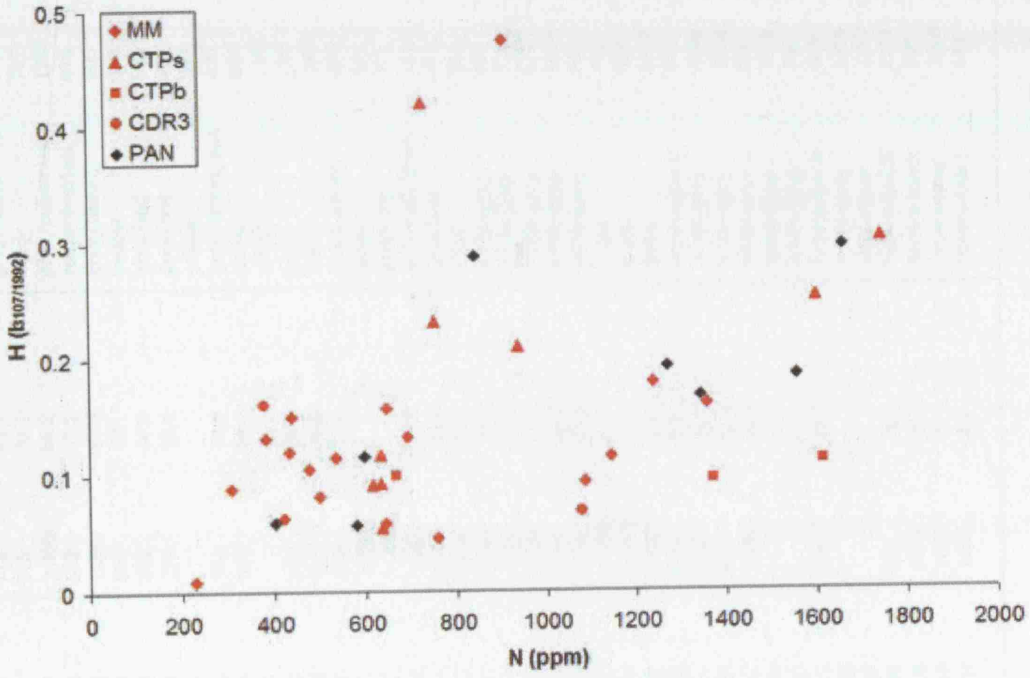

Figure 3.3: Substitutional impurities in the Mbuji Mayi (red) and Panda (black) diamond coats. Relationship between nitrogen (in ppm) and hydrogen absorption (given by the ratio of the H-band at 3107 cm^{-1} to the diamond absorption peak at 1992 cm^{-1}).

sample	ct.	Core N (ppm)	Core % N as IaB	colour	Coat N (ppm)	Coat H_2O	Coat CO_2	Coat H_2O#	minerals present
MM1	0.13	715	73.1	grey-brown/red	433	421	55	88	carb, qz
MM2	0.17	715	30.1	black	757	nd	nd	-	carb
MM3	0.07	>3000	66.2	grey/colourless	1236	187	15	93	carb, qz, apatite
MM4	0.15	522	81.2	red/colourless	910	nd	nd	-	kaolinite
MM6	0.26	1259	80.2	grey/brown	500	37	nd	-	carb
MM7	0.15	829	70	yellow	693	75	nd	-	carb, qz
MM8	0.26	538	48.3	grey/red	645	nd	nd	-	kaolinite
MM9	0.20	779	78.6	grey/red	535	110	20	84	carb, kaolinite, quartz
MM10	0.08	-	-	yellow	228	197	22	90	carb, qz, apatite
MM11	0.23	940	79.8	grey-brown/red	439	264	nd	-	carb, kaolinite, quartz
MM12	0.19	557	69	white	647	146	22	87	carb, qz
MM13	0.11	-	-	white	1356	154	14	92	carb, qz, apatite
MM15	0.22	559	59.9	grey	420	51	nd	-	carb
MM16	0.22	910	28.6	white	1085	58	12	83	carb, qz
MM17	0.27	608	68.9	black-brown	306	nd	nd	-	carb, qz
MM20	0.17	>3000	-	white	476	149	nd	-	carb
MM21	0.27	>3000	-	grey/red	377	45	13	78	carb, kaolinite, quartz
MM22	0.23	1063	11.6	yellowish white	1144	62	10	86	carb, qz, apatite
MM23	0.41	476	34.8	grey/red	383	73	18	80	carb, qz
CTPs1	0.05	1512	77.3	white	633	61	nd	-	carb, qz, apatite
CTPs2	0.06	1653	79.9	white-grey	634	64	14	82	carb, apatite
CTPs5	0.05	1262	11.6	white-grey	1743	62	11	85	carb
CTPs6	0.04	1310	77.1	white-grey	617	46	nd	-	carb, qz, apatite
CTPs7	0.05	2044	50.7	white-grey	1599	59	11	84	carb
CTPs8	0.04	1269	49.3	white-grey	636	43	nd	-	carb, apatite
CTPs12	0.05	>3000	20.7	green	752	35	nd	-	-
CTPs13	0.07	>3000	-	green	938	58	nd	-	carb, qz, apatite
CTPs14	0.02	1715	6.3	green	1049	452	192	70	carb, qz, apatite
CTPs15	0.05	1200	3.2	brown-green	730	72	nd	-	carb, qz
CTPb4	0.01	865	36.7	white-grey	1368	102	18	85	carb, qz, apatite
CTPb7	0.01	821	81.1	white-grey	1612	125	18	88	carb, qz
CTPb8	0.22	1035	26.6	white-grey	666	70	nd	-	carb, qz
CDR3	0.06	-	-	green-grey	1078	118	nd	-	qz
PAN1	0.05	-	-	white/grey	580	nd	nd	-	ol, pyx, carb
PAN2	0.07	501	32.7	brown-black	403	nd	nd	-	carb
PAN3	0.05	-	-	white-grey	1344	420	192	69	pyx, carb
PAN4	0.06	-	-	white-grey	1557	397	269	60	cpx,qz, carb
PAN5	0.05	585	30.3	brown-black	1271	911	663	58	grt, carb
PAN6	0.04	1539	10.1	brown-black	598	nd	nd	-	carb
PAN7	0.10	1048	8	brown-grey	1660	277	215	56	carb
PAN8	0.04	1201	3.2	brown-black	844	441	327	57	carb

Table 3.1: Ft-ir characteristic of Mbuji Mayi (DRC) and Panda (Canada) diamond coats. MM, CDR and PAN samples were prepared by laser cutting and polishing, while the CTPs and CTPb samples were sawn before polishing. Sample weight in carats (ct.), nitrogen and volatile concentrations are given in ppm. $H_2O=100H_2O/(H_2O+CO_2)$.

concentrations range between 228 and 1743 ppm in the Mbuji Mayi coats and between 403 and 1660 ppm in the Panda coats. Along traverses, there is a tenancy for nitrogen concentrations to decrease towards the rim in the Mbuji Mayi diamond coats (Fig 3.6); in contrast, nitrogen concentrations the Panda coats increase towards the rim (with the exception of PAN7). There is no relationship between the colour of the diamond coat and the concentration of substitutional nitrogen.

All coat samples have a sharp absorption peak at 3107 cm^{-1}, which is commonly attributed to lattice bound hydrogen. Diamonds with elevated H-absorption ($\geq$0.2 $I_{3107/1992}$) have moderate to high nitrogen concentrations $\geq$800 ppm, however there is no correlation between the hydrogen absorption intensity and nitrogen concentration (Fig 3.3).

The Panda diamond cores are more highly aggregated than their coats, having up to 33% IaB centres with some platelet development and nitrogen concentrations of 501 to 1539 ppm. The Mbuji Mayi diamond cores are highly aggregated Type IaA-IaB (up to 81% IaB centres) with strong platelet development and nitrogen concentrations are highly variable, from 538 to >3000 ppm. This is consistent with the cores being significantly older than their coats and may indicate mantle storage at higher temperatures, particularly in the case of the Mbuji Mayi diamond cores.

3.2.2.2 Included Impurities

There are significant differences between the minerals present in the Mbuji Mayi and Panda diamond coat inclusions.

Mbuji Mayi

The infrared spectra of the Mbuji Mayi samples reveal the presence of quartz ($\approx$778, $\approx$810 cm^{-1}, $\approx$1090 cm^{-1} and $\approx$1160 cm^{-1}), apatite (606 and 575 cm^{-1}), carbonate (880-874, 720-620 and 1490-1410 cm^{-1}) and H_2O ($\approx$1640 and $\approx$3440 cm^{-1}); example spectra are shown in figure 3.8. An intense sharp peak at 1000 cm^{-1} may be attributed to mica, probably phlogopite; other peaks at 840 cm^{-1}

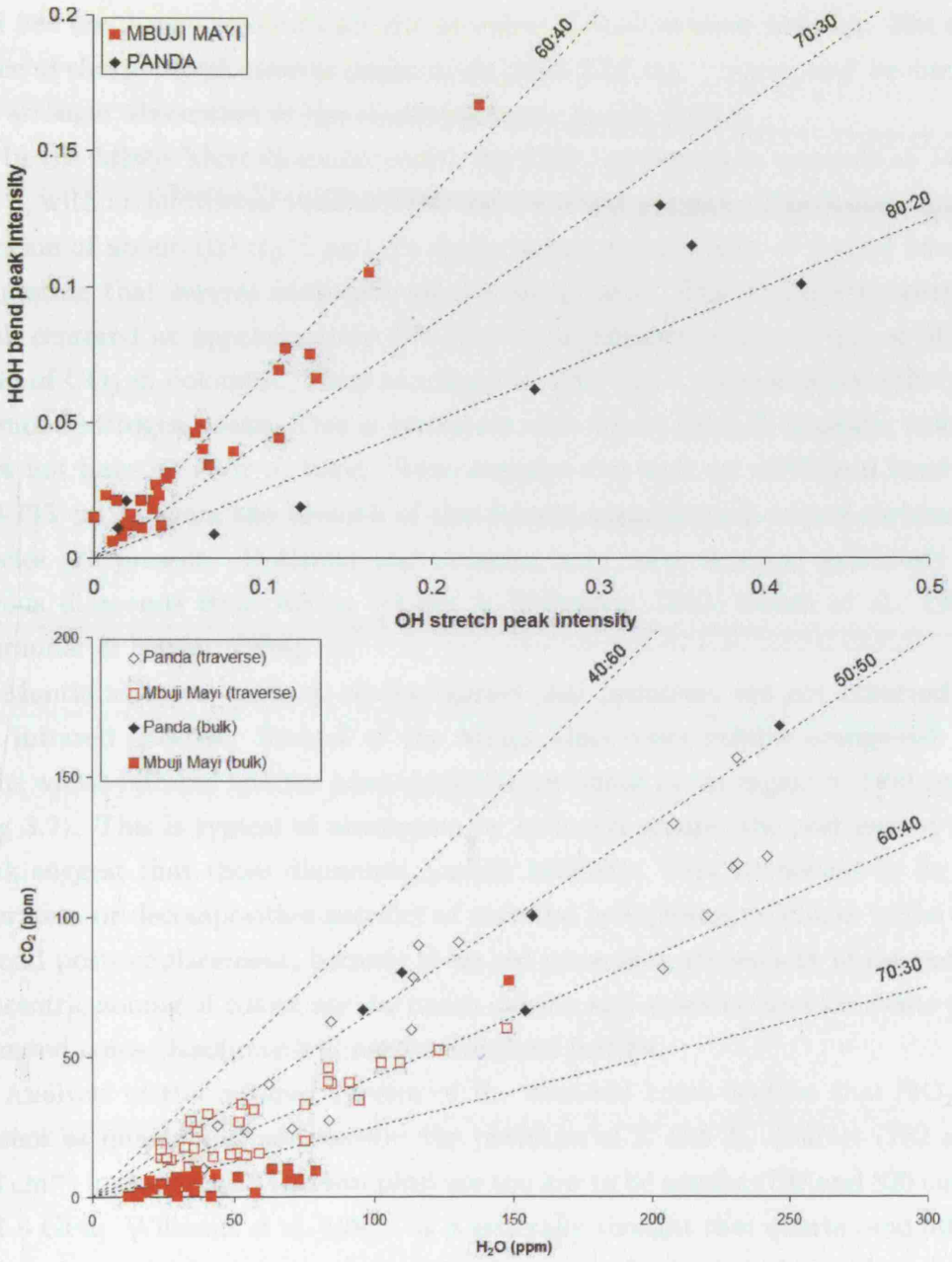

Figure 3.4: Volatile characteristics of the Mbuji Mayi (red) and Panda (black). The relationship between (a) the integral intensities of the H-O-H bend (≈1650 cm^{-1}) and the O-H stretch (≈3420 cm^{-1}); (b) correlation between the concentration of CO_2 and H_2O in traverse (open symbols) and bulk (solid symbols) data.

and 684 cm^{-1} may also indicate the presence of mica in some samples. The absence of sharp OH phlogopite peaks in the 3600-3700 cm^{-1} region may be due to the stronger absorption of the coexisting water in this region.

In the Mbuji Mayi diamond coats, the CO_3^{2-} ν_3 stretch is centered at 1447 cm^{-1}, with an additional peak at 1462 cm^{-1} in some samples. This feature spans a region of about 100 cm^{-1} and it's shape indicates an overlay of several bands, suggesting that several carbonate species are present. The strong symmetrical peak centered at approximately 877 cm^{-1} is attributed to the ν_2 out of plane bend of CO_3 in dolomite. There is a band at 1097 cm^{-1}, superimposed onto the diamond nitrogen peaks. This is consistent with the ν_1 peak of dolomite; calcite does not have an Ft-ir ν_1 band. Some samples also have an additional band at 729-735 cm^{-1}, again the breadth of this feature suggests that several carbonate species are present. Dolomite and ankerite have been observed previously in fibrous diamonds from Africa (Lang & Walmsley, 1983; Navon et al., 1988; Schrauder & Navon, 1994).

Mantle silicates, such as olivine, garnet and pyroxene, are not observed in the infrared spectra. Several of the Mbuji Mayi coats exhibit orange-red regions whose infrared spectra have sharp narrow bands in the region $\approx$ 3600 cm^{-1} (Fig 3.7). This is typical of absorption by hydroxyl groups, the positions of the peak suggest that these diamonds contain kaolinite. This is thought to be an alteration or decomposition product of material precipitated in cracks in the diamond post-emplacement, because these red areas are independent of the radial concentric zoning of colour and inclusion density and in some cases permeate the diamond cores. Kaolinite will not be discussed further.

Analysis of the infrared spectra of the diamond coats confirm that SiO_2 is present as quartz and not coesite: the positions of E and A_2 doublet (782 and 810 cm^{-1} in the Mbuji Mayi samples) are too low to be coesite (799 and 820 cm^{-1} at 1.6 GPa; Williams et al. 1993). It is generally thought that quartz (and other included minerals) are secondary minerals, on the basis that the uniform bulk composition of fluid in samples from a single location suggests that the components were dissolved in a fluid at the time of entrapment (Wyllie & Ryabchikov, 2000). However, analysis of individual fluid inclusions shows that the compositional variability within single diamond coat samples is wide (section 4.3).

Coesite-quartz transformation rates are slow at low temperature and high pressure (Mosenfelder & Bohen, 1997; Perrillat et al., 2003): Experimentally determined growth rates show an exponential dependence on temperature and growth is an order of magnitude slower within 0.5 GPa of the coesite-quartz line than at lower pressures. At 2.5 GPa, 200°C experimental growth rates of ≈1 micron per 3 Ma were reported by (Perrillat et al., 2003), and growth rates an order of magnitude slower were reported by (Mosenfelder & Bohen, 1997). Furthermore, both authors report a decrease in growth rate in the latter stages of transformation. Had coesite ever formed in the inclusions, then slow kinetics should mean that some remnant coesite should remain today. Therefore, it is likely that dissolved SiO_2 was precipitated from the trapped fluid following eruption and cooling of the host sample. At the conditions of diamond growth (≈1000°C, 4-5 GPa), the solute load of aqueous fluid in the system MgO-SiO_2-H_2O, which approximates the composition of hydrous peridotite (forsterite + enstatite) mantle, may be high. In experiments at 3 GPa and 1100°C, the solute load of H_2O was 30% and was dominated by SiO_2 (Ryabchikov et al., 1982). Stalder et al. (2001) suggests that convergence between the H_2O solubility in silicate melt and SiO_2 solubility in H_2O may occur between 4 and 5 GPa, therefore the amount of dissolved solute present in the trapped fluid may have been even higher. Once trapped, the composition of the fluid inclusion is constant, however SiO_2 solubility in H_2O decreases with decreasing temperature and pressure (Manning, 1994). In the experimental system CaO-SiO_2-H_2O, which is an analogue of the fluid inclusion composition in this study, silicate solubility fell from 4.2 to 0.5 mol % from 1400°C, 2 GPa to 1200°C, 0.8 GPa (Mysen, 2002). Therefore, SiO_2 dissolved in the fluid at the time of inclusion entrapment at ≈1000°C, 4-5 GPa in the mantle, will be exsolved from the fluid when the temperature and pressure of the inclusions drops due to cooling of the host diamond after kimberlite eruption. Rapid cooling means that SiO_2 would have been exsolved in the quartz stability field as a secondary mineral in the inclusions. This suggests that the other minerals.

The conclusion that quartz is a secondary mineral, rather than a transformed form of coesite, means that it cannot be used as a paragenetic indicator. It also means that the origional fluid was SiO_2-rich, this has implications for the

structure of water and the ability of the water-rich fluid to migrate through the mantle (section 7.3). It is likely that the other mineral phases present in the inclusions (carbonate, apatite, sheet silicates) are also secondary, in addition to quartz. This would mean that the origional fluid had a high solute load.

The presence of water is determined by the wide absorption bands in the MIR spectra at 3400-3200 cm^{-1} (produced by overlapping symmetric and antisymmetric OH stretches at 3220 cm^{-1} and 3445 cm^{-1} respectively) and at 1630 cm^{-1} (H_2O bend). There is a correlation between the intensities of the OH stretch and HOH bend, suggesting that most water is present as H_2O molecules (Fig 3.4). The maximum peak intensity of the H_2O band has 60% of the intensity of the OH stretch band, this is consistent with the presence of liquid water, in which the bending band of H_2O is just a bit weaker than the O-H stretch bands. The antisymmetric stretch is more intense than the symmetric stretch, this leads to an asymmetric OH envelope. The absorption near 3220 cm^{-1}, which is considered to be the overtone of the 1630 cm^{-1} bend ($\nu_{2_{a1}}$), is quite strong in the Mbuji Mayi relative to the 3445 cm^{-1} absorption.

There is a correlation between the concentrations of H_2O and CO_2 in the Mbuji Mayi diamond coat fluid (Fig 3.4. The ratio $H_2O\#$ ($100H_2O/(CO_2+H_2O)$) is $\approx$ 89 (71 to 93); for comparison, the ratios in fibrous diamonds from Botswana and Siberia are 30-90 % and 5-20 % respectively (Navon et al., 1988; Schrauder & Navon, 1994; Zedgenizov et al., 2004). The relationship between inclusion density and $H_2O\#$ is positive in the Mbuji Mayi diamond coats indicating a link between water and high inclusion densities (Fig. 3.5). Within samples, there is a decrease in the ratio $H_2O\#$ along a traverse from the core-coat boundary to the rim (Fig. 3.6), suggesting that there was a progressive geochemical evolution towards more carbonate-rich fluid compositions during the growth of the Mbuji Mayi diamond coats. There is also a decrease in inclusion density, suggesting that diamond growth rates were highest at the onset of coat growth and decreased as growth proceeded. Nitrogen concentrations along the sample traverses are correlated with inclusion density, suggesting that high levels of nitrogen uptake are associated with rapid diamond growth.

Navon (1991) has shown that the volume of fluid inclusions is conserved during diamond transport from the mantle to the surface, because of the low

thermal expansion coefficient and bulk modulus of diamond ($\alpha_D = 1.5\times10^{-6}$ K^{-1} and $\kappa_D = 5.83$ GPa respectively; Yoder 1993). Therefore, fluid inclusions in diamond retain a residual internal pressure from their formation in the mantle; this pressure is hydrostatic and is exerted by the trapped volatiles (water). The pressure induced infrared shift of quartz at room temperature may be used to estimate the residual internal pressure of inclusions in fibrous diamond (Navon, 1991). Using the 7 $cm^{-1}GPa^{-1}$ shift of the 800 cm^{-1} peak calibrated by Williams et al. (1993), the positions of the quartz peaks in the Mbuji Mayi sample set (809.9 and 812.5 cm^{-1}) correspond to internal pressures of 1.4 to 1.8 GPa. The pressure-temperature path of the Mbuji Mayi inclusions can be estimated using the equation of Rosenfeld & Chase (1961):

$$\frac{P}{T} = \frac{\alpha_D - \alpha_I}{\frac{1}{\kappa_D} - \frac{1}{\kappa_I}} \tag{3.1}$$

where α_I and κ_I are the thermal expansion coefficient and bulk modulus of water (8.6×10^{-4} K^{-1} and 53.2 GPa respectively Smith 1963). This gives a formation pressure of 6.4 to 6.8 at 1000°C.

Panda

In contrast, the Panda diamond coats have strong absorption bands in the region 1100-800 cm^{-1}, which are due to absorption by olivine, pyroxene and garnet (Fig 3.9). Parageneses have been assigned to the Panda diamond coats on the basis of the compositions of their mantle silicate inclusions (section 4.4). As in the DRC samples, carbonate and water are present in the infrared spectra of all the Panda diamond coats. In peridotitic samples, the ν_3 stretch of carbonate peak is centred at 1447 cm^{-1} suggesting the presence of dolomite, whilst the eclogitic sample (PAN4) has a second carbonate peak centred at 1423 cm^{-1} suggesting the additional presence of calcite or ankerite. Quartz is only observed in the single eclogitic sample. The residual internal pressure indicated by quartz in sample PAN4 is 1.8 GPa, which corresponds to a formation pressure of 6.8 at 1000°C

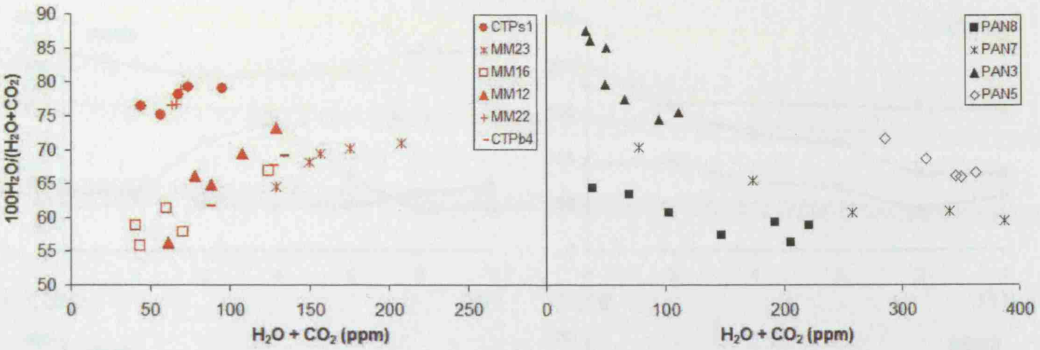

Figure 3.5: Relationship between inclusion density (represented by the concentration of H_2O+CO_2 in ppm) and volatile composition (H_2O#) within selected individual samples from Mbuji Mayi (red) and Panda (black).

using equation 3.1. No apatite was detected in the infrared spectra of any of the Panda diamond coats.

As in the Mbuji Mayi samples, there is a correlation between the intensities of the OH stretch and HOH bend, suggesting that most water is present as H_2O molecules (Fig 3.4). The maximum peak intensity of the H_2O band has only 30% of the intensity of the OH stretch. However, the absorption near 3220 cm^{-1}, which is considered to be the overtone of the 1630 cm^{-1} bend ($\nu_{2_{a1}}$), is weak in the Panda samples relative to the 3445 cm^{-1} absorption. The reduced intensity of the H_2O absorption band in the Panda samples suggests that either water is present as hydroxyl groups (OH^-) e.g. in hydrous minerals or in glass. However, the silicate inclusion population indentified during EMPA does not include hydrous minerals and there are no metal-OH bands or sharp hydroxyl bands in the region 3600 cm^{-1} of the infrared spectra. Alternatively, the structure of water has been modified by interaction with solutes. Dubessy et al. (2002) have shown that chlorine causes a reduction in the intensity of the OH stretch component at $\approx$3200 cm^{-1} and an increase in the intensity of the component at $\approx$3450 cm^{-1} in the vibrational spectra of water. EMPA shows that inclusions in the Panda diamond coats have a high concentration of KCl (section 4.3.2).

The Panda coat fluid, like the Mbuji Mayi fluid, shows a correlation between the concentration of H_2O and CO_2 (Fig 3.4). The ratio H_2O# ($100H_2O$/(CO_2+H_2O)) is $\approx$61 (58 to 70); this is lower than in the Mbuji Mayi inclusions

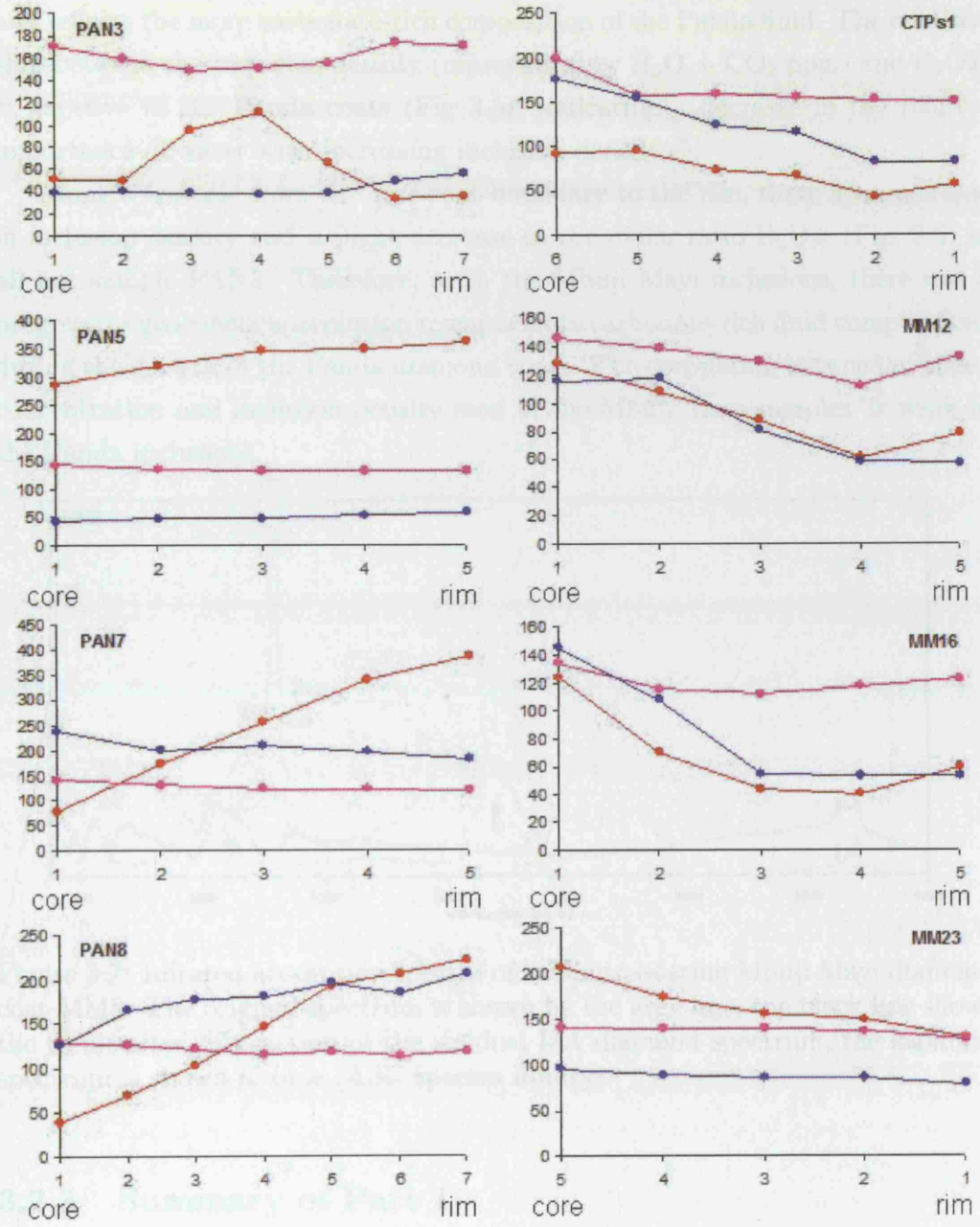

Figure 3.6: Variation in nitrogen concentration and volatile compositions along traverses through selected diamond coats from the core-coat boundary to the rim of the coat. Nitrogen concentration ($\div$ 10) in ppm (blue), total volatile concentration H_2O+CO_2 in ppm (red) and H_2O# ($\times 2$) (pink). Panda samples are in the left column, Mbuji Mayi samples in the right column.

and reflects the more carbonate-rich composition of the Panda fluid. The relationship between the inclusion density (represented by $H_2O + CO_2$ ppm) and $H_2O\#$ is negative in the Panda coats (Fig 3.5), indicating a decrease in the relative importance of water with increasing inclusion density.

Along a traverse from the core-coat boundary to the rim, there is an increase in inclusion density and a slight decrease in the molar ratio $H_2O\#$ (Fig. 3.6) in all but sample PAN3. Therefore, as in the Mbuji Mayi inclusions, there was a progressive geochemical evolution towards more carbonate-rich fluid compositions during the growth of the Panda diamond coats. The correlation between nitrogen concentration and inclusion density seen in the Mbuji Mayi samples, is weak in the Panda inclusions.

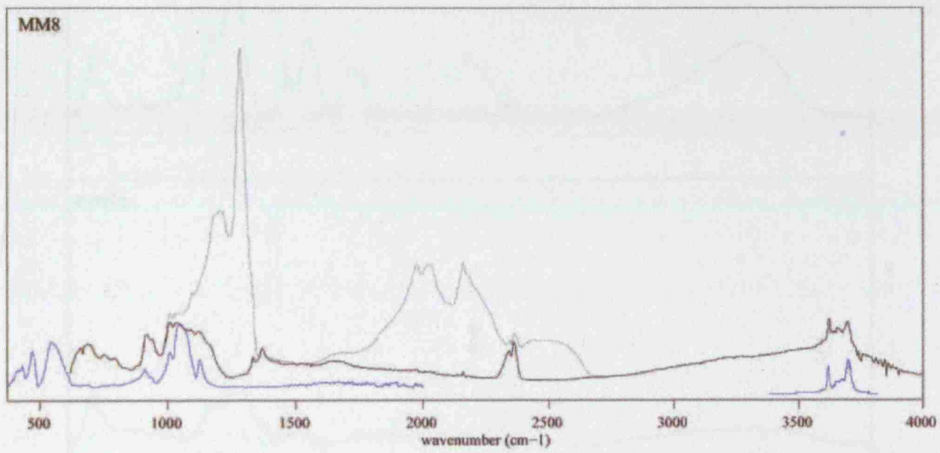

Figure 3.7: Infrared absorption spectra of kaolinite-bearing Mbuji Mayi diamond coat MM8. The original spectrum is shown by the grey line, the black line shows the result after subtraction of the residual IaA diamond spectrum, the kaolinite spectrum is shown in blue (ASU spectra library).

3.2.3 Summary of Part 1

There are some important similarities between the Mbuji Mayi and Panda diamond coats:

- Water and carbonate are present

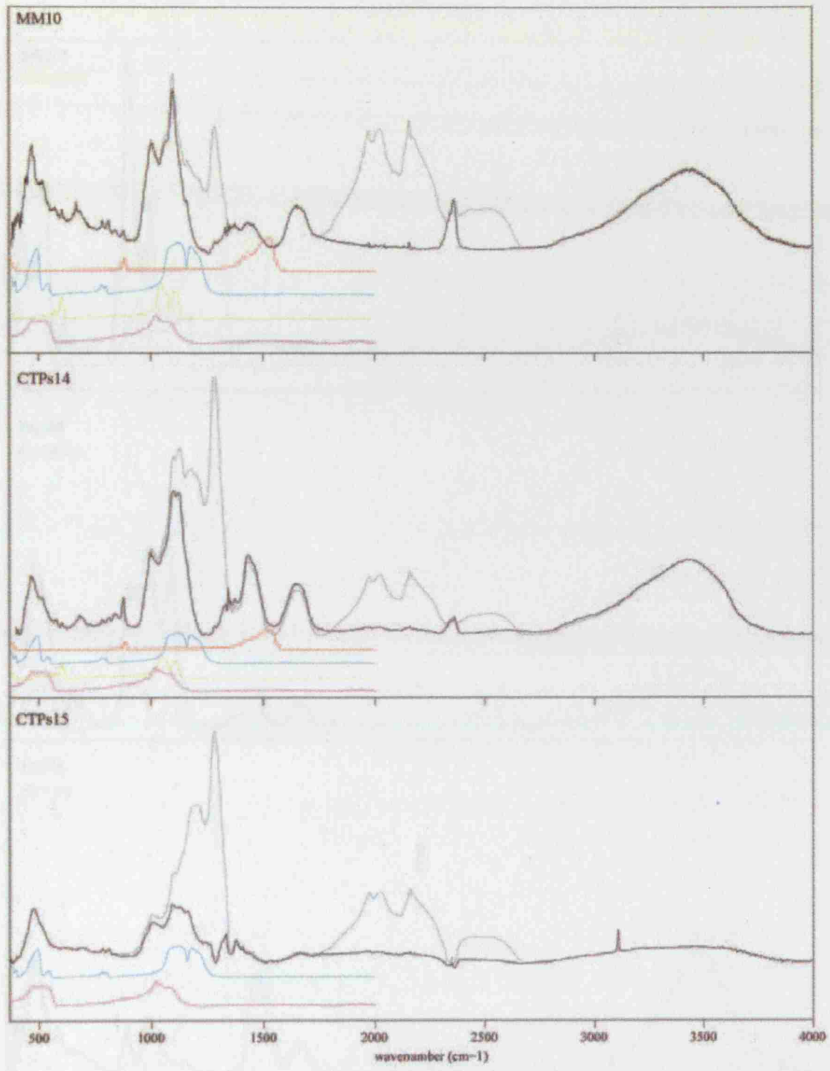

Figure 3.8: Infrared absorption spectra of selected Mbuji Mayi diamond coats. Original spectrum (grey line) and result after subtraction of the residual IaA diamond spectrum (grey line). Carbonate (red) is identified by the wide band at 1480-1410 cm^{-1} (ν_3 symmetric in plane stretch of CO_3) and the sharp peak at 890-860 cm^{-1} (ν_2 out of plane bend of CO_3). The intensities of these carbonate bands are correlated. Quartz (turquoise) is recognised by the sharp bands at $\approx$ 784 and $\approx$ 811 cm^{-1} (pressure shifted from the 1 atm positions of 779 and 798 cm^{-1}). Characteristic infrared absorption bands of phosphate (apatite, yellow) at 575 and 606 cm^{-1}. Sheet silicates (such as phlogopite, pink) are inferred from the bands at $\approx$ 1100, 1000, 840, 525 and 475 cm^{-1}. Example mineral spectra are from the ASU spectra library.

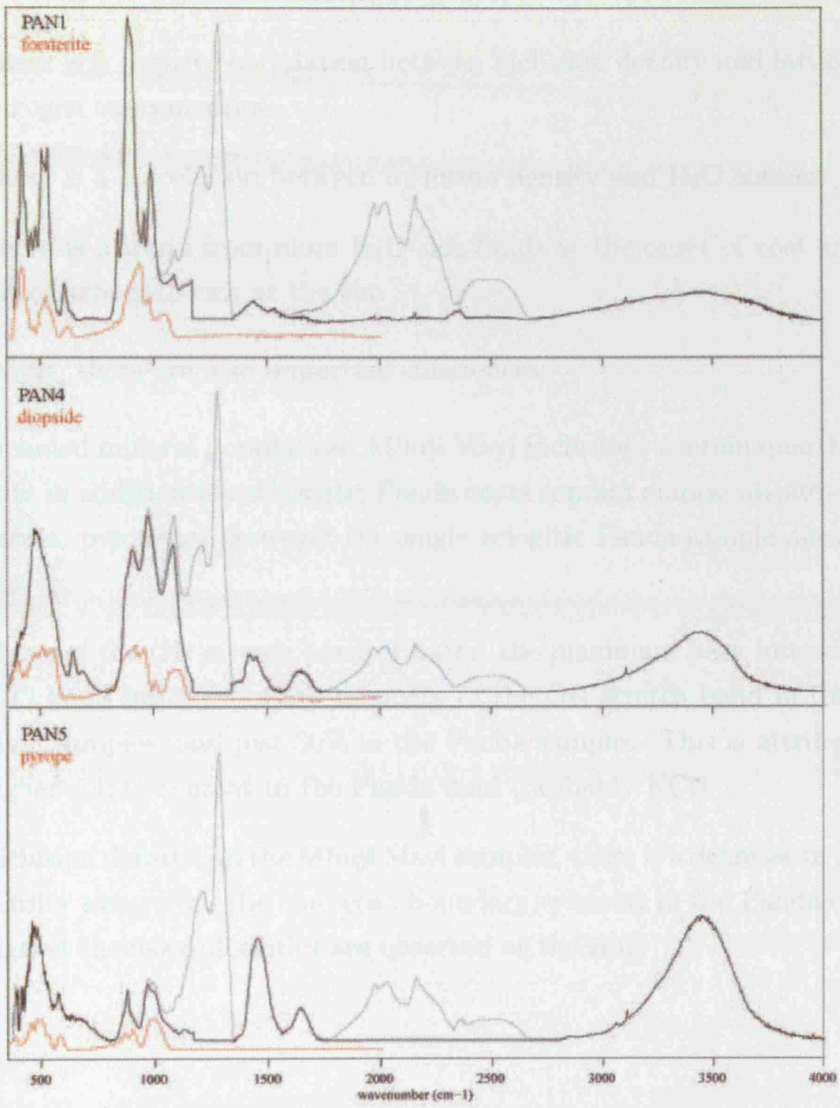

Figure 3.9: Infrared absorption spectra of selected Panda diamond coats. The original spectrum is shown by the grey line, the black line shows the result after subtraction of the residual IaA diamond spectrum. Minerals present include: olivine (PAN1: 887, 507, 987, 608, 532 and 843 cm^{-1}), pyroxene (PAN4: 1090, 480, 877 (shoulder), 520, 977, 908, 644 cm^{-1}), garnet (PAN5: 484, 877, 904 (shoulder), 575, 967, 993 cm^{-1}), quartz (PAN4: 812 and 784 cm^{-1}) and carbonate (all: $\approx$ 880 and 1460-1420 cm^{-1}). Example mineral spectra are from the ASU spectra library.

- Water is the dominant volatile at $\geq 50\%$
- There is a positive correlation between inclusion density and lattice bound nitrogen concentration
- There is a correlation between inclusion density and H_2O content
- There is a trend from more H_2O-rich fluids at the onset of coat growth to more carbonate-rich at the rim

However, there are also important differences:

- Included mineral population: Mbuji Mayi inclusions contain quartz and apatite in addition to carbonate; Panda coats contain mantle silicates (olivine, garnet, pyroxene), however the single eclogitic Panda sample does contain quartz.
- Shape of the OH stretch band of water: the maximum peak intensity of the H_2O band has 60% of the intensity of the OH stretch band in the Mbuju Mayi samples, and just 30% in the Panda samples. This is attributed to a higher solute content in the Panda fluid (probably KCl).
- Inclusion density: in the Mbuji Mayi samples, there is a decrease in inclusion density away from the core-coat boundary, whereas in the Panda coats the highest inclusion densities are observed at the rim.

3.3 Part 2: Structure

This part of the study investigates the changing shape of the infrared absorption spectra of a sample MM10 during infrared microthermometry. In fluid bearing inclusions such as those in cuboid diamond, the pressure in the inclusions is hydrostatic and is exerted by the trapped volatiles. Inclusions in diamonds retain a residual internal pressure from their formation at 4-7 GPa, 1000-1300°C as observed by Navon (1991). The internal pressure of the inclusions may be increased by heating the sample. The aim of this experiment is to investigate the phase assemblage of the inclusions and the changes in fluid phase along the pressure-temperature path. The structure of mantle fluid is of importance when considering the conditions of diamond growth and the diamond-forming reaction. The question of whether the fluids represented in cuboid diamonds are carbonate- or CO_2-bearing during diamond growth and of whether OH is present as water or in a melt at the upper mantle pressure and temperature conditions also has implications for mantle metasomatism and the generation of kimberlite magma and its apparently CO_2 driven ascent.

3.3.1 Samples and Analytical Method

Variable temperature experiments were carried out at the Earth Sciences Department, Cambridge University, U.K. Infrared absorption spectra were recorded over the range 7000 to 400 cm^{-1} using a Bruker IFS113v Fourier transform infrared (Ft-ir) spectrometer with an MCT detector. For mid-infrared (MIR) analyses, a silicon carbide Globar light source and a Ge/KBr beam splitter were used; for near-infrared (NIR) analyses, we used a tungsten halogen lamp and a CaF_2 beam splitter. The beam size was 10 mm, so the resultant spectrum represents the average sample composition. Instrumental measurements were carried out in absorption at a spectral resolution of 2 cm^{-1}, with one spectrum being the average obtained from 512 scans.

3.3.1.1 Low-Temperature Experiments (20-294 K)

Low temperature measurements were conducted under vacuum (10^{-3} Pa) using a Leybold two-stage close-cycle helium cryostat. For MIR measurements, the vac-

uum chamber was equipped with KRS5 windows; quartz windows were used for NIR analyses. Diamond samples were mounted on a high-thermal-conductivity oxygen-free copper plate, with a central gap. Where the sample was smaller than the gap, Indium foil was used to improve the contact between sample and holder and as a mask to ensure that only fibrous diamond was analysed. Temperature was measured using a calibrated Si-diode temperature sensor (LakeShore, DT-470-DI-13). Spectra were collected during cooling at 40 degree intervals. The experimental set up is show in in figure 3.10.

3.3.1.2 High-Temperature Experiments (298-1010 K)

High temperature measurements were conducted under vacuum after the completion of the low temperature experiments. The sample was surrounded by platinum foil and positioned in a cylindrical platinum wound resistance furnace with a recycle water-cooling system. The temperature of the sample was measured using a NiCr/NiAl thermocouple at the sample surface. The heating rate was 15 $Kmin^{-1}$, the sample was then held at each analysis temperature. Data was collected during heating and collection started when the sample temperature was reached. The uncertainty of measured sample temperature is ± 5 K at < 650 K and ± 10 at > 650 K. Spectra were collected during heating at 25 K intervals from 298 to 473 K (50 to 200°C) and at 50 degree intervals at higher temperatures.

3.3.1.3 Sample

Sample MM10 from the Democratic Republic of Congo (DRC) was used in this study. The 4 mm diameter sample was laser cut to a thickness of 0.4 mm and polished on both sides, the finished product weighs 0.08 ct. The sample was cleaned in acetone then HCl and distilled water prior to analysis. The sample is a type IaA diamond, so shows infrared absorption peaks of diamond and of substitutional nitrogen pairs. The room temperature infrared absorption spectrum shows that the sample contains OH, carbonate, quartz and apatite (Fig 3.8). The spectra of crystalline phases in diamond micro-inclusions are equivalent to powder spectra because the phases are randomly orientated in a multitude of inclusions. This sample was chosen on the basis of its high inclusion density and its strong quartz infrared absorption which provided an internal pressure calibration.

Figure 3.10: Photographs of (a) He-cryostat for low temperature infrared spectroscopy, this unit is lowered into the sample chamber of the Bruker IFS 66v spectrometer, which is then sealed and vacuuated. (b) Cylindrical platinum-wound furnace and recycle-water-cooling system in the vacuum sample chamber of the spectrometer.

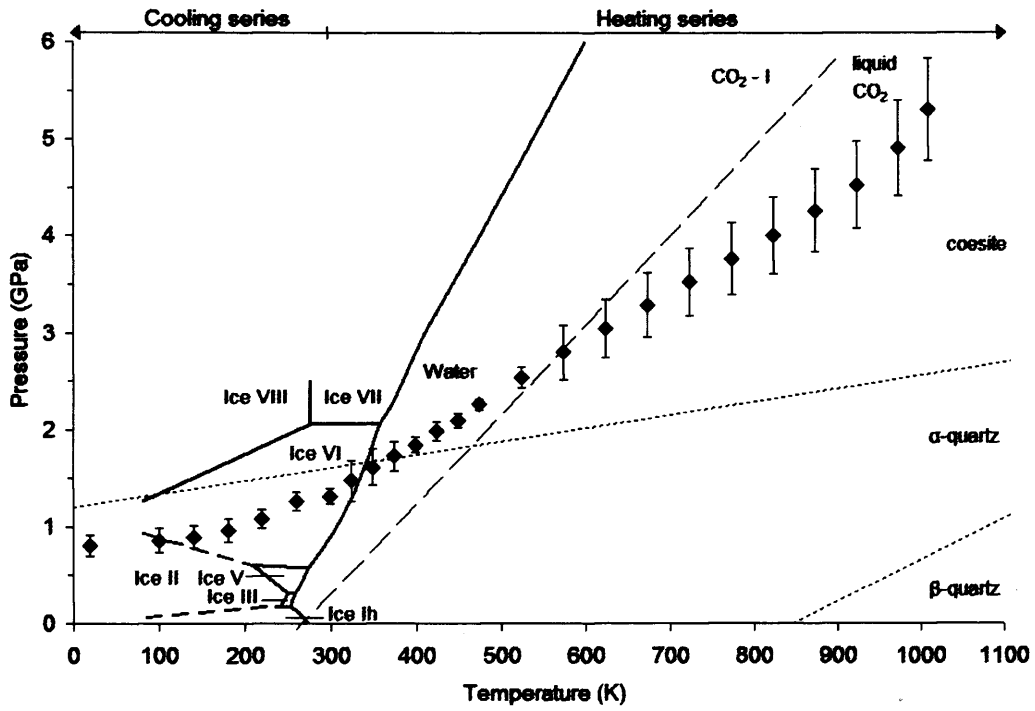

Figure 3.11: Temperature-pressure path for inclusions in sample MM10 during heating and cooling. Pressures are derived from the shift in the position of the quartz 800 cm^{-1} band (black diamonds). Also shown are the phase transitions in H_2O (heavy black lines) from Minceva-Sukarova et al. (1984) and high pressure H_2O solidus from Datchi et al. (2000), CO_2 (- - -) from Lu & Hofmeister (1995) and quartz from Mirwald & Massonne (1980).

3.3.1.4 Pressure Determination

The infrared spectra indicate that fibrous diamond sample MM10 contains quartz. Analysis of the infrared spectra of the diamond coats confirm that SiO_2 is present as quartz and not coesite because the positions of E and A_2 peaks (782 and 810 cm^{-1}) are too low to be coesite (799 and 820 cm^{-1} at 1.6 GPa; Williams et al. 1993). For the purpose of this study we assume that quartz occurs in micro-inclusions where it coexists with water. This is consistent with the observation that mineral phases occupy about 30% of the volume of an inclusion, the rest being a void (Guthrie et al., 1991). Therefore, pressure in the inclusions is assumed to be hydrostatic.

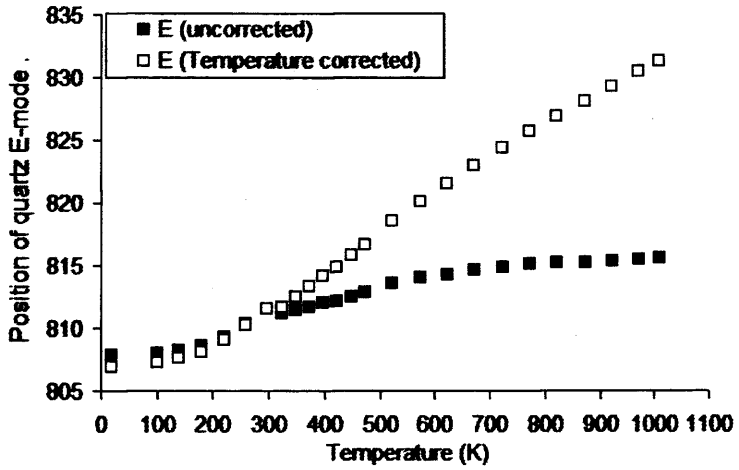

Figure 3.12: Plot of the variation in the measured position of the quartz E-mode with temperature during heating from 20 to 1010 K (solid squares) and of the temperature-corrected position of the quartz E-mode (open squares). Temperatures are corrected using the calibration of Gervais & Piriou (1975) for temperatures $\geq$300 K and the calibration of Ouillon et al. (2000) at temperatures $<$ 300 K.

The non-linear pressure-induced shift in the positions of various quartz infrared absorption bands has been calibrated by Wong et al. (1986) in the region of interest using a diamond anvil cell. At ambient conditions, the A_2 and E quartz peaks should be at 779.6 and 800.6 cm^{-1} respectively (Wong et al., 1986). At room temperature (298 K), the positions of the E and A_2 peaks in diamond sample MM10 are 783.4 and 811.5 cm^{-1}, this corresponds to an internal pressure of 1.49 GPa. Reference to the phase diagram for water shows that water in the inclusions should be present as ice VI at room temperature (Fig. 3.11).

Both the E and A_2 modes decrease in intensity during heating, but both persist to 1010 K. The E and A_2 modes of quartz shift to higher wavenumbers during the experiment (Fig. 3.12). Gervais & Piriou (1975) have shown that the position of the A_2 mode is independent of temperature, therefore the A_2 shift must reflect to the changing internal pressure of the inclusions during heating. The E-type vibrational mode of quartz is more sensitive to pressure than the A_2-mode (McMillan & Hess, 1990; Williams et al., 1993; Wong et al., 1986) therefore, the E-mode of quartz is used as an internal pressure determinant in

these experiments. The temperature dependence of the frequency of the E-mode is slightly negative (Gervais & Piriou, 1975). We have corrected for the negative shift in the position of the E-mode using the temperature calibration of Gervais & Piriou (1975) for temperatures $\geq$300 K and the calibration of Ouillon et al. (2000) at temperatures < 300 K. Temperature corrected band positions are shown in figure 3.12. The corrected band positions are then used to determine the internal pressure of the inclusions using the calibration of Wong et al. (1986). This method ignores the cross temperature-pressure coefficient. Figure 3.11 shows the pressure-temperature path seen by quartz during the experiment.

3.3.2 Results

The internal pressure of the inclusions recorded by the quartz barometer varies from 0.83 GPa at 20 K to 5.28 GPa at 1010 K. The quartz barometer records the average internal pressure of the inclusions; some inclusions may record slightly higher or lower internal pressures due to differences in their compositions and initial volumes. This may result in water and ice coexisting in different inclusions within the sample close to the ice-liquid water transition; this has been observed in inclusions in a cuboid diamond by Kagi et al. (2000).

According to the phase H_2O phase diagram, the temperature path of the inclusions crosses the transition from ice VI and liquid water, which occurs at 338 K at 1.6 GPa. Therefore, low-temperature infrared spectra of OH and HOH features of inclusions in sample MM10 give the spectrum of ice VI, these features are similar to ice VI spectra reported by Bertie et al. (1968) and Song et al. (2003). There is a kink in the pressure-temperature slope at 298 K indicating a small increase in the pressure on quartz between 298 and 323 K during cooling. This records the position of the phase transition from liquid water to ice VI.

3.3.2.1 Si-O Species

A strong, sharp peak occurs at 1090 cm^{-1}, along with a weaker feature at 1160 cm^{-1}, this is due to crystalline quartz present within the inclusions. The characteristic sharp peak of the E-mode, used as an internal pressure calibration in this study, is observed at 811 cm^{-1}. Other peaks at 474, 514 and 783 cm^{-1} are also

identified as quartz vibrations (Farmer, 1974b; Moenke, 1974; Williams et al., 1993).

There is an intense sharp peak at 1000 cm^{-1}, that could be due to the Si-O stretching vibration of phlogopite mica (Farmer, 1974b). The weak sharp peak at 840 cm^{-1} can also be assigned to mica (in addition to carbonate vibrations), as well as the broad band near 684 cm^{-1}, (Farmer, 1974b). There are no sharp peaks in the 3600-3700 cm^{-1} region that are usually associated with OH-containing layered silicates, however, the bands of phlogopite are unusually broad and could be hidden within the broad stretching band profile from the dominant H_2O phase.

3.3.2.2 O-H Species

In order to identify the phase of water (H_2O liquid, ice polymorph, OH), attention must be paid to the shape of the fundamental OH stretching absorption band in the region 2800-4000 cm^{-1}, which is sensitive to the extent of hydrogen bonding (Kagi et al., 2000). Figure 3.13 shows the evolution of the OH absorption envelope over the temperature range 20 to 1010 K (0.83 to 5.28 GPa). With increasing temperature, there is a decrease in the profile intensity and the position of the peak maximum shifts to higher wavenumbers (by +150 cm^{-1} from 20 to 1010 K) and becomes increasingly asymmetric. Figure 3.14 shows the results of deconvolution of the OH stretching band, revealing contributions from the OH symmetric stretch ($\nu_{1_{a1}}$), OH asymmetric stretch ($\nu_{3_{b1}}$) and OH bend overtone ($2\nu_{2_{a1}}$). The position of the H-O-H bending mode ($\nu_{2_{a1}}$) in the region 1750 to 1550 cm^{-1} shifts by +37 cm^{-1} during the experiments. Therefore, the bending mode is less sensitive to modification to the structure of water than the O-H stretch region. After the experiments the band shape and the position of the peak maximum returned to their pre-experiment form. Water in the micro-inclusions shows four distinctive structural regimes over the temperature range of the experiment. These will be discussed below.

20-220 K

At low temperature, the principal peak of the OH stretch region occurs at 3420 cm^{-1} and a second maximum occurs at 3240 cm^{-1}; the OH bend at 1600-

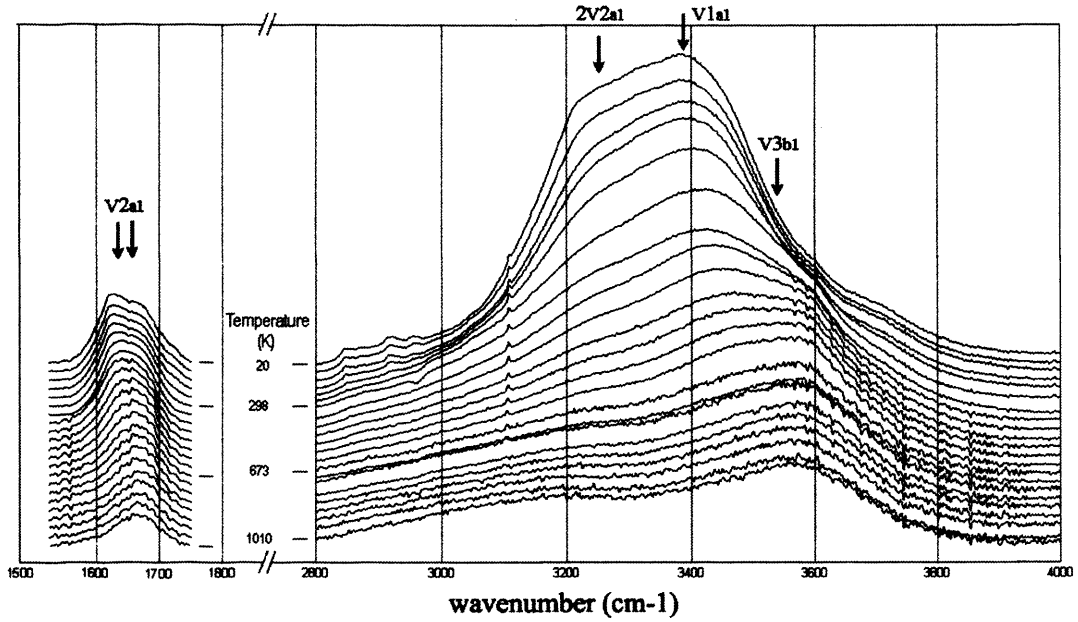

Figure 3.13: Evolution of the OH bending (fundamental $\nu_{2_{a1}}$ and overtone $2\nu_{2_{a1}}$) and stretching (symmetric $\nu_{1_{a1}}$ and asymmetric $\nu_{3_{b1}}$) infrared modes in diamond MM10 during heating. Low temperature spectra are at the top, significant temperatures are marked.

1680 cm^{-1} has a doublet form with maxima at 1625 and 1670 cm^{-1} (Fig. 3.13 and Fig. 3.14) and the 20 K NIR spectrum has a weak band at 5200 cm^{-1}. These features are characteristic of ice VI, which comprises OH stretch bands at 3245 cm^{-1} ($2\nu_{2_{a1}}$) and 3415 cm^{-1} ($\nu_{1_{a1}}$) (Bertie et al., 1968). Reference to the pressure-temperature diagram (Fig. 3.11) shows that temperature-pressure conditions are in the stability field for ice VI.

260-298 K

With increasing temperature, the bands at 3240 and 3420 cm^{-1} continue to decrease in intensity, and a high-frequency shoulder develops at 3550 cm^{-1}. The position of this new band is characteristic of liquid H_2O (Walrafen, 1972).

Figure 3.14a shows the results of deconvolution of the OH stretching components to distinguish the temperature at which the crystal-liquid transition occurs.

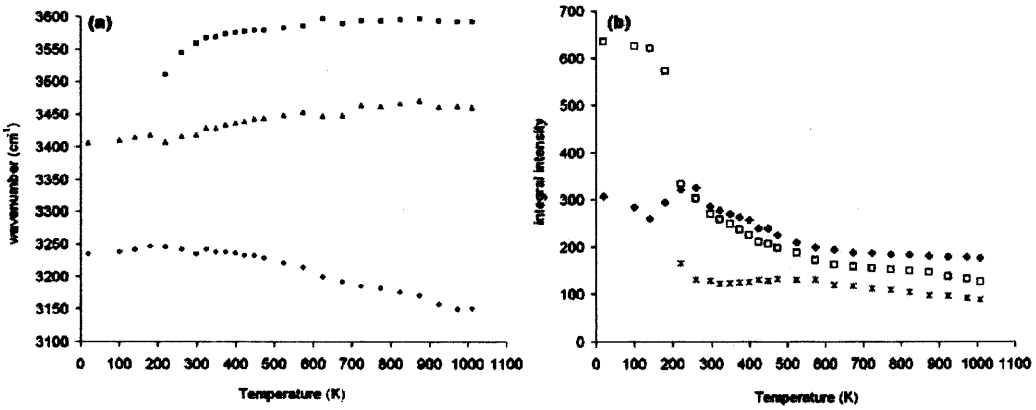

Figure 3.14: Results of curve fitting: $\nu_{1_{a1}}$ (open squares), $\nu_{3_{b1}}$ (closed triangles), $2\nu_{2_{a1}}$ (closed diamonds) and $\nu_{2_{a1}}$ (crosses); a) position of component curves in the OH stretch region, also shown is the position of the peak maximum. b) integral intensities of the OH band components against temperature.

This figure indicates that liquid and ice VI H_2O coexist in the inclusions in the temperature region 298 to 220 K. This is consistent with the anomalous pressure change recorded by the quartz barometer. Reference to the phase diagram (Fig. 3.11) shows that the pressure-temperature path of the inclusions crosses the solidus of pure water at 338 K (Datchi et al., 2000; Minceva-Sukarova et al., 1984). Therefore solidus temperature is depressed by ≈80 degrees. Solidus depression may be due to the solute load of the fluid e.g. at 1 bar, dissolved CO_2 suppress may the freezing point of water by 56 K (Roedder, 1984). Ice VI and liquid water have been detected in the room temperature NIR spectrum of fibrous diamonds by Kagi et al. (2000). The ability to freeze water ice indicates that the inclusions contain liquid water rather than hydrous melt or minerals.

323-623 K

This temperature region sees dramatic changes in the shape of the OH envelope. The high-frequency shoulder that developed in the 220 to 298 K region, becomes a new band, and the band at 3240 shifts to lower wavenumbers. The position of the overall OH envelope maximum progressively shifts to higher wavenumbers and the band broadens.

Figure 3.14b shows that the integral intensities of the $\nu_{1_{a1}}$ and $2\nu_{2_{a1}}$ components decrease with increasing temperature, their intensities have a positive correlation over the range 423 to 573. However, the integral intensity of the $\nu_{3_{b1}}$ asymmetric stretch band increases throughout this temperature range and do not correlate with the $\nu_{1_{a1}}$ and $2\nu_{2_{a1}}$ components. This means that the $\nu_{3_{b1}}$ band becomes increasingly dominant, this is reflected in the fact that the position of the peak maximum of the OH envelope shifts by +150 cm^{-1} from the position of the $\nu_{1_{a1}}$ component to that of the $\nu_{3_{b1}}$ component during heating from 323 K to 623 K (Fig. 3.14a). The OH bend ($2\nu_{2_{a1}}$) is now composed of a single peak, which shifts to higher wavenumbers with increasing temperature.

The 323-623 K temperature region tracks the decrease in the degree of H-bonding in the aqueous fluid as the temperature rises. At low temperatures, most H_2O is H-bonded in tetrahedral clusters, during heating intensified thermal motions loosen and destroy the H-bonded structure breaking up the tetrahedral network. This causes a reduction in the orientational correlation.

673-1010 K

At higher temperature the positions of the fundamental OH bands remain approximately constant (Fig. 3.14a), the only change is the decrease in OH band intensity. Above 673 K the trapped water is fully compressed and does not have much structure to destroy by heating and therefore there is no further H-bond breakage. Therefore, water in the inclusions now has a similar structure to what it would have had during diamond growth in the mantle.

3.3.2.3 C-O Species

Figure 3.15 shows the regions of the infrared spectra of sample MM10 relevant to C-O species over the temperature range 20 to 573 K.

CO_2

The existence of a CO_2 phase is indicated by a broad feature at 2337 cm^{-1} which is present below 298 K (Fig. 3.15). This peak is due to the ν_3 asymmetric stretching

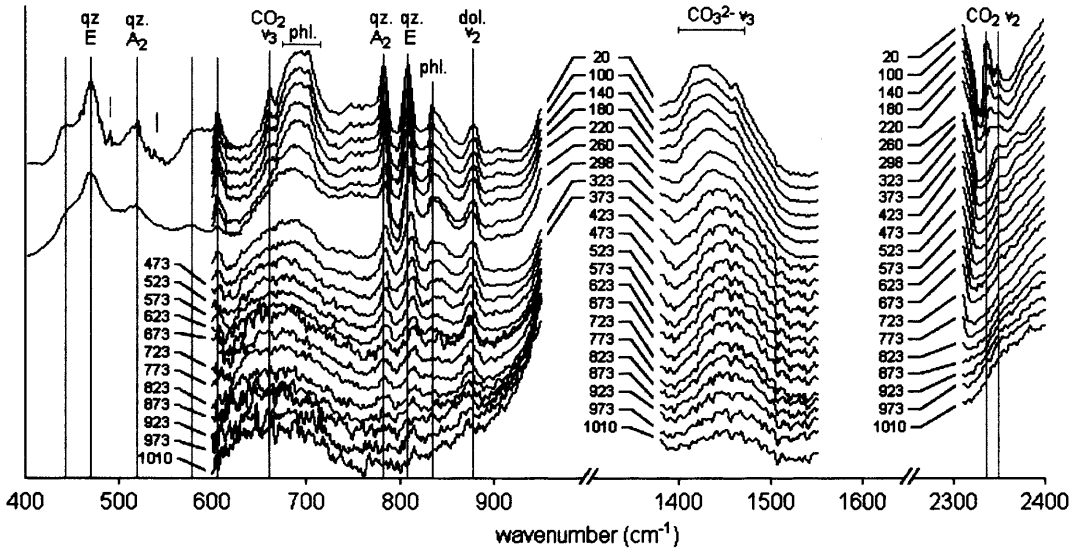

Figure 3.15: MIR spectra of sample MM10 showing regions relevant to CO_2, CO_3 and silicate minerals. Spectra have been displaced vertically according to temperature. Diamond absorption peaks have been subtracted. Temperatures above 573 K are not shown because of the high noise contribution.

vibration of molecular CO_2. These bands are sharp and occur at lower wavenumbers than atmospheric CO_2. At 220 K this peak developed a doublet structure with two components at 2334 and 2345 cm^{-1}, and it shifted abruptly to lower wavenumber. The pressure-temperature conditions recorded by the quartz calibration are within the stability field of CO_2 phase-I (Fig. 3.11) (Lu & Hofmeister, 1995) and the band positions are consistent with the fundamental ν_3 asymmetric stretch and ν_2 bend of solid CO_2 phase-I (Dows & Schettino, 1973). The existence of CO_2-I provides further evidence for a high internal pressure retained within the inclusions at ambient temperature. The ν_2 bending vibration of CO_2 near 670 cm^{-1} was also observed at 220 K and below (Fig. 3.15).

Melting of CO_2-I would normally occur at 550-600 K at 3 GPa on the temperature pressure path of the inclusions (Fig. 3.11) (Iota & Yoo, 2001). However, the crystalline CO_2 doublet is only present at and below 220 K and the CO_2 stretch disappears entirely above 298 K. This suggests that CO_2 becomes dissolved in water upon the melting of water ice VI. At 298 K, 1 bar, the maximum concentration of CO_2 that may be dissolved in liquid water is 5 wt%. CO_2 solu-

bility increases at high pressure and temperature because of the lower dielectric constant of water. The possible identification of CO_2 in the trapped mantle fluid may have implications for the carbon source for fibrous diamond growth and for the diamond forming reaction.

CO_3

Several bands that are attributed to carbonate are present in the spectra of MM10: those at 1490-1410, 1096 and 877 cm^{-1}. The most obvious feature is a broad band centered at 1431 cm^{-1}, that is due to the asymmetric stretching vibration (ν_3) of CO_3^{2-} groups (Fig. 3.15). This feature spans a region of about 100 cm^{-1} and the shape of the feature indicates an overlay of several bands. This suggests that several carbonate species are present. This band is due either to the ν_3 asymmetric stretching vibration of CO_3^{2-} groups dissolved with an aqueous fluid phase, or due to carbonate minerals. The wide band in the region 720-620 cm^{-1} is assigned to the ν_4 in plane bend of CO_3, in addition to phlogopite. The sharp peaks at 877 and 748 cm^{-1} can be assigned to the ν_2 and ν_4 modes of dolomite ($CaMg(CO_3)_2$) (White, 1974). The ν_2 peak at 877 cm^{-1} shifts linearly to lower wavenumber during heating, and is present over the entire range studied here. The position of this peak when extrapolated to 1 bar is 879 cm^{-1}, this is consistent with the presence of dolomite. The band at 1096 cm^{-1} is consistent with the ν_1 peak of dolomite; calcite does not have a ν_1 band in infrared.

A sharp peak appears at 1468 cm^{-1} at 260 K during cooling, correlated with the appearance of the CO2 features. The frequency of this band is consistent with CO_3 species. Characteristic vibrations of HCO^{3-} groups within hydrocalcite or hydromagnesite phases occur in this region (White, 1974). It is possible that some hydrated carbonate crystallises from the H_2O-CO_2 liquid phase, at the same time as the CO_2-I phase.

3.3.3 Discussion

This study shows that the inclusions in fibrous diamond MM10 contain aqueous water rather than hydrous minerals or melt. At T=298 K and P=1.5 GPa,

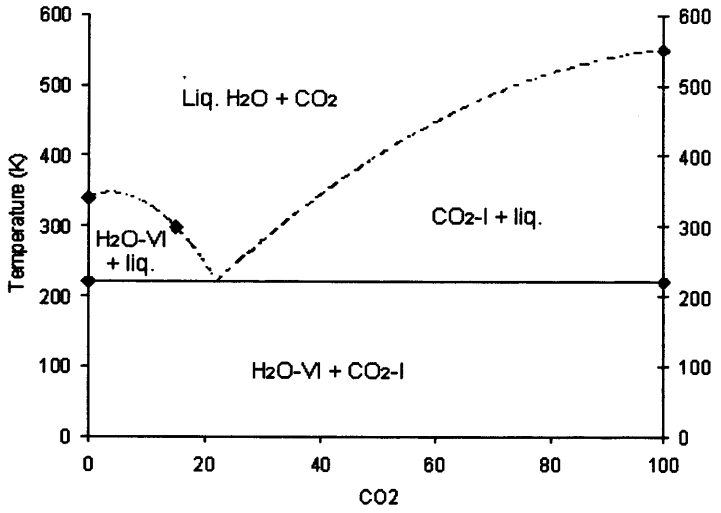

Figure 3.16: Temperature-composition plot for the system H_2O-CO_2 at ≈1.5 GPa. Black diamonds show points constrained by the infrared spectra of sample MM10 and published data for the melting point of pure H_2O-VI (Minceva-Sukarova et al., 1984) and pure CO_2-I (Lu & Hofmeister, 1995); dashed lines show the extrapolated T-X fields.

assuming that silicate or carbonate dissolution in the H_2O-CO_2 species is minimal, the system contains ice-VI and liquid H_2O close to the liquidus curve, as well as CO_2 species dissolved in the aqueous fluid. Therefore this is a pseudo-binary eutectic system (Fig. 3.16). Below 220 K CO_2-I coexists with ice VI. Above the solidus for ice VI, at approximately 220 K, ice VI begins to melt and CO_2 species dissolved in the liquid H_2O that is formed. Ice VI and liquid H_2O+CO_2 coexist over the temperature range 220 - 300 K. Above the liquidus at approximately 300 K, the remainder of the ice VI melts and the CO_2 species are so diluted that its infrared modes are no longer visible in the infrared spectra.

3.3.3.1 Thermodynamic Properties

Figure 3.17 illustrates some thermodynamic and transport properties of liquid water (calculated using the ChemicaLogic SteamTab) along the pressure-temperature path calculated from the position of the E-mode quartz peak. The peak temperature-pressure conditions during the experiment are similar to during diamond growth.

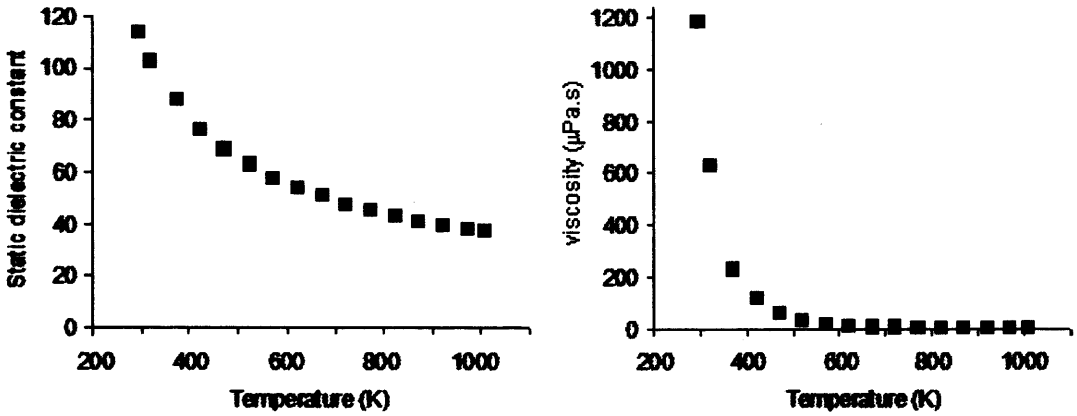

Figure 3.17: Dielectric constant and viscosity along the calculated pressure path during heating of MM10 from 298 to 1010 K, calculated using Chemlogics Steamtab program.

The reduction in the dielectric constant is consistent with the changing shape of the OH stretch in the infrared spectra during heating. The decrease in the dielectric constant at high temperature and pressure allows non-polar substances, such as CO_2, to be dissolved. The viscosity of water also decreases dramatically during heating, forming an asymptote towards zero μPa.s above 600 K; this increases the fluid mobility within the mantle.

3.3.3.2 Diamond Growth Conditions

Inclusions in diamond sample MM10 are dominated by H_2O and carbonate. The presence of free-water rather than silicate melt in the inclusions indicates that the mantle was sub-solidus or near-solidus during fibrous diamond growth. It also indicates that the fibrous diamond grew from a free fluid. Equilibria between the C-O-H fluids and neutral carbon species represented by diamond also occur at high pressure and temperature

High-pressure high-temperature diamond growth experiments have been conducted in the C-O-H fluid (Akaishi et al., 2000, 2001; Sokol et al., 2001) and carbonate-C-O-H fluid (Pal'yanov et al., 2002a; Sokol et al., 2001; Yamaoka et al., 2002) systems at $\geq$5.7 GPa and $\geq$1150 ^{o}C, i.e. at the conditions of diamond formation in the mantle. This work has shown that any combination of H_2O, CO_2,

H_2 and CH_4 are able to catalyse the growth of diamond from graphite; 3) elevated concentrations of H_2O-CO_2 enhance the catalytic effect of carbonate with respect to diamond nucleation and growth (Pal'yanov et al., 2002a); and 4) oxidising (H_2O-CO_2-C) fluids have a higher catalytic activity than reducing (CH_4-H_2-C and CH_4-H_2O-C) fluids (Sokol et al., 2001). High nucleation and growth rates are required for fibrous and polycrystalline diamond growth, therefore the experimental results are consistent with the presence of fluids in inclusions in fibrous diamonds.

It is thought that diamond formed by reducing reactions between an incoming H_2O-rich carbonate melt and the more reduced minerals of the host mantle. The occurrence of both oxidised (carbonate and CO_2) and neutral (diamond) carbon in fibrous diamond inclusion suggests that the local oxidation state was buffered by diamond. The most oxidising conditions that diamond can exist in an eclogite host rock are defined by reaction 3.2:

$$CaMg(CO_3)_2 + 2SiO_2(+H_2O) \rightleftharpoons CaMgSi_2O_6 + 2C + 2O_2(+H_2O) \quad (3.2)$$

Excess O_2 generated during the breakdown of carbonate may oxidise the host mantle e.g. in stabilising biotite or phlogopite at the expense of KCl (which was detected in the micro-inclusions by EMPA (section 4.3)) and water e.g. reaction 3.3:

$$2K(Mg,Fe)_3(Si_3Al)O_{10}(OH)_2 + 2SiO_2 \rightleftharpoons 3(MgFe)_2Si_2O_6 + KCl + 2H_2O + O_2 \quad (3.3)$$

The H_2O and carbonate-rich fluid inclusions represent the residual fluid after precipitation of diamond. The trapped minerals (carbonate, quartz, phlogopite) are thought to have crystallised from this residual fluid, either as products of fractional crystallisation from the original fluid (carbonate minerals), or as precipitates from dissolved species liberated during metasomatic reactions (quartz, phlogopite). CO_2 may be formed by reaction between diamond and the oxidised fluid ($C + O_2 = CO_2$), or may have been a component of the incoming metasomatic fluid.

3.3.3.3 Application to Whole Sample Set

Applying this discussion to the wider sample set: the co-existence of 1) Ca-Mg carbonate, SiO_2 and diamond (plus clinopyroxene in the Panda sample) in the Mbuji Mayi and eclogitic Panda samples suggests that fibrous diamond growth occurred by reaction reaction 3.3. The equivalent reaction in lherzolite is eqn 3.4:

$$CaMg(CO_3)_2 + 2Mg_2Si_2O_6 \rightleftharpoons 2Mg_2SiO_4 + CaMgSi_2O_6 + 2C + 2O_2 \quad (3.4)$$

The coexistence of Ca-Mg carbonate, orthopyroxene, olivine, clinopyroxene and diamond in the peridotitic Panda samples suggests that fibrous diamond growth in peridotite occurred at this buffer. The reaction between Ca-bearing carbonate and peridotite will convert harzburgite to lherzolite and may explain the absence of harzburgitic inclusions in the Panda diamond coats. Incomplete reaction in eclogite and lherzolite may lead a high solute load in the coexisting aqueous fluid; these solutes may be later precipitated forming daughter minerals such as quartz, as seen in the Mbuji Mayi and Panda sample sets (section 3.2.2.2).

3.3.4 Summary of Part 2

Micro-thermometry has been combined with infrared spectroscopy in a novel approach to study the structure of fluid inclusions in a fibrous diamond from the Democratic Republic of Congo. At 20 K, the inclusions contain H_2O ice VI, carbonate, phlogopite, quartz and minor phase I CO_2. The onset of melting of H_2O ice VI occurs $\approx$120 degrees below the predicted phase boundary (340 K at 1.6 GPa), suggesting that the fluid contains dissolved solutes. The solid CO_2 peak disappears upon melting of water ice VI, as CO_2 is dissolved in the liquid phase. H_2O-VI coexists with liquid H_2O+CO_2 between 220 and 300 K as this is a pseudo-binary eutectic system. The ability to freeze water ice shows that OH in the inclusions is dominantly present as free water. The structure of water is distorted at high pressure and temperature, causing a reduction in the dielectric constant and viscosity of the trapped mantle fluids. Dissolved CO_2 may be present because of the low dielectric constant of water at the pressure-temperature conditions of diamond growth.

Chapter 4

Major Elements

4.1 Introduction

This chapter presents the major element compositions of individual micro-fluid inclusions the Mbuji Mayi and Panda diamond coats. Previous work in this field is summarised in section 1.2.1.

There is currently no published data on the major element composition of fluids in micro-inclusions in Panda diamonds and only limited data for Canadian fibrous diamonds. The Panda diamond coats also contain macro-silicate inclusions and so provide an important link between studies of syngenetic mineral inclusions in diamond and studies of mantle fluids in fibrous diamonds. The results provide information on the paragenetic environment and pressure-temperature conditions of fibrous diamond growth at Panda. This chapter also re-examines the composition of fluid inclusions in African samples and find that a minor brine component is also present in addition to the recognised carbonatite-like and alkali-silicate end-member fluids.

4.2 Analytical Method

4.2.1 Micro-Inclusions

Electron Microprobe Analyses (EMPA) of individual micro-inclusions in the diamond coats were performed using a JEOL Superprobe 733 at Birkbeck College, University of London. The instrument is equipped with an Energy Dis-

Instrumental setup	
Collimator	yes
Elemental range	C to U
Resolution (FWHM peak width of Mn)	138 eV
Channel width of regions of interest	0.01 KeV (1024 channels with 0 - 10 KeV range)
Operational settings	
Accelerating voltage	15 eV
Beam current	10 nA
Spot diameter	2 μm
Count time	100 s
Counts per second	6 to 7 Kcps

Table 4.1: Instrumental operating conditions for EMPA analyses. FWHM - full width at half maximum.

persive Spectrometer (EDS), a collimator and a Si(Li)crystal detector with an atmospheric thin window (ATW). EDS is appropriate for the analysis of the micro-inclusions which give low totals, because peak intensities are an order of magnitude higher than can be achieved using a Wavelength Dispersive Spectrometer (WDS). However, the use of EDS does mean that the resolution is lower and the peak-to-background ratio higher than would be achieved by WDS. The same instrument was used to collect cathodoluminescence (CL) images of the coated diamond samples. The instrumental and operating conditions are given in table 4.1. Spectra were reduced using the Oxford Instruments Link ISIS SEM-Quant correction relative to a cobalt standard. The XY coordinates of each sampled inclusion was noted and the radial position calculated in order that any compositional zoning could be recognised and related to the CL image.

The following elements were analysed: SiO_2, TiO_2, Al_2O_3, Cr_2O_3, MgO, total Fe as reported FeO, CaO, P_2O_5, Na_2O, K_2O and Cl. Cl was analysed in the fluid micro-inclusions because KCl has been shown to be an important component of fluids trapped in Canadian diamonds (Johnson et al., 2000; Klein-BenDavid et al., 2004, 2002). SO_3 was also analysed but is not presented because it was below detection limit in all inclusions except in sample CTPb8. The full dataset of individual micro-inclusion compositions are shown in Appendix 1. The mean of the individual inclusion compositions measured in a sample was taken to represent the bulk major element composition of that sample.

Individual shallow sub-surface inclusions were identified using backscattered

electron imaging mode. The inclusions are completely enclosed in the diamond host and are not connected to the diamond surface by cracks. Because of the low mean atomic number of diamond, the electron beam shows a significant degree of penetration into the sample with an activation area of approximately 1.5 μm^2 at 15 KeV. This relatively large analytical volume allows statistically significant sampling of the inclusion volume. The analytical volume is larger than the average inclusion diameter ($\leq$ 1 μm). The fact that the inclusions are smaller than the activated region and that the inclusions have high volatile concentrations means that analysed totals are significantly lower than 100%. The average total oxide plus chlorine concentration is 18% (1 to 53 wt%) in the Mbuji Mayi coat inclusions 12 wt% (2 to 45 wt%) in the Panda coat inclusions. The sum of oxides plus chlorine was normalised to 100 wt% in order to remove the effect of variable inclusion size, depth and C-O-H content. The disadvantage of normalising to 100% is that it is not possible to evaluate data quality, because the mean and standard deviation are irrelevant when the totals are not equal and the errors are of variable magnitude when normalised. The full dataset of individual inclusion compositions is given in table A.1.

Schrauder & Navon (1994) estimate the accuracy of EMPA micro-inclusions in diamond to be 10-40% for various oxides in a given inclusion. Uncertainty arises from the low and variable oxide contents of the inclusions and the assumption of a uniform carbon matrix. Izraeli et al. (2004) analysed olivine micro-inclusions in diamond with restricted compositions and showed that accuracy is better than 15% for major elements in individual inclusions and precision is of the order of a few percent.

4.2.2 Macro-Inclusions

Silicate inclusions were exposed during polishing of six of the eight Panda coated diamonds. Both peridotitic (PAN1, PAN3, PAN5, PAN7, PAN8) and eclogitic parageneses (PAN4) are represented. The ratio of peridotitic to eclogitic diamonds in this small sample set approximates that in the inclusion population in octahedral diamonds from Panda (Tappert et al., 2005). Silicate inclusions in the coated diamonds are small (typically 2 to 10 μm) but abundant (Figure

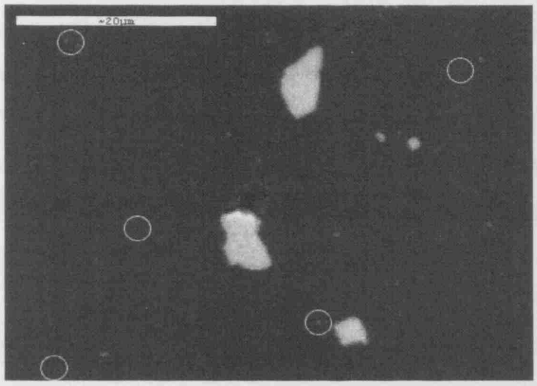

Figure 4.1: Backscatter electron image of sample PAN4 showing several macro-sized clinopyroxene inclusions. The dark region is the diamond host, the small indistinct white dots are fluid micro-inclusions (some indicated by white circles). Scale bar is 20 microns.

4.1), with approximately ten inclusions large enough for analysis being identified on each polished surface. Inclusions at the small end of the size range do not give 100% totals. Table 4.5 shows the analysed total and the normalised molecular proportions of these inclusions. Multiple analysis of a single clinopyroxene grain in PAN4 revealed good reproducibility, with the following standard deviations (1σ) in oxide wt%: SiO_2(0.22), Al_2O_3 (0.09), FeO(0.10), Cr_2O_3 (0.08), MgO(0.08), CaO(0.09), TiO_2(0.12). Mn was not analysed due spectral overlap with Cr.

In the following discussion, inclusions in the Panda diamond coats are compared to inclusions in octahedral Panda diamonds analysed by WDS. Only differences in the major element concentrations (mainly Mg, Fe, Ca) are considered, because the resolution of the WDS analyses is an order of magnitude better than of EDS analyses.

4.3 Results: Micro-Inclusions

Table 4.2 shows the average compositions of fluids in the Mbuji Mayi and Panda diamond coat inclusions. The bulk compositions of fluids in both sample sets define a tight range. The normalised major element patterns for the Mbuji Mayi fluids and the eclogitic Panda fluid are similar and are within an order of magni-

tude of the major element composition of eclogite (Fig. 4.2a). The Mbuji Mayi major element pattern is not similar to the peridotitic Panda diamond fluid (not shown) because of the markedly lower concentrations of Si and Al in the peridotitic Panda sample fluids. The main difference between the trapped fluid and eclogite is the elevated K (and Cl) content of the fluid. Figure 4.2b,c shows the bulk compositions of fluids from the two locations normalised to their kimberlite hosts. Fluids from both localities are strongly enriched in K and Na relative to their respective kimberlites; the Panda samples are also strongly enriched in Ti (Fig. 4.2b,c).

4.3.1 Mbuji Mayi Individual Inclusion Compositions

557 individual micro-inclusions were analysed in the 29 samples from the Mbuji Mayi kimberlite. The variance in intra-diamond inclusion compositions is greater than the inter-diamond variance in bulk composition (95% significant). This suggests that the fluid is strongly heterogeneous at the inclusion scale; however the bulk fluid compositions are relatively uniform suggesting that the regional fluid is relatively homogeneous. This local heterogenity may be a reflection of

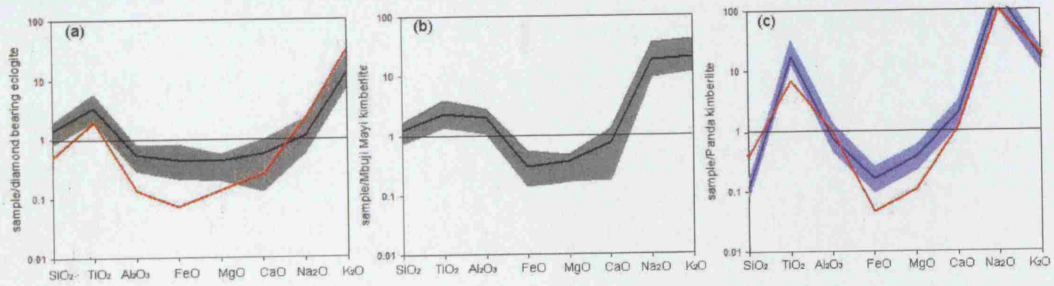

Figure 4.2: (a) Average major element composition (solid black line) and range of compositions (grey field) of Mbuji Mayi diamond coat fluids and eclogitic Panda sample PAN4 (red line) normalised to diamond bearing eclogite KEC-81-DB-1 from Koidu (Sierra Leone) (Hills & Haggerty, 1989); (b) Average (solid black line) and range (grey shaded area) of Mbuji Mayi diamond coat fluids normalised to Mbuji Mayi kimberlite (Fieremans et al., 1984); and (c) average (solid blue line) and range (blue shaded area) of peridotitic diamond micro-inclusions and average eclogitic diamond inclusions (red line) normalised to Panda kimberlite (Nowicki et al., 2004).

the heterogeneity of the metasomatic fluid. The fluid may be heterogeneous on a fine spatial scale because of local variation in the degree of equilibrium between the fluid and the various minerals of the host rock. The fluid will also have been hetergeneous on a temporal scale as the fluid compostion was changed by crystallisation of the diamond host and other minerals. Some heterogeneity may also be due to the entrapment of solid phases.

sample	no. inc.	SiO_2	TiO_2	Al_2O_3	FeO	MgO	CaO	BaO	Na_2O	K_2O	P_2O_5	Cl	total	Si	Ti	Al	Fe	Mg	Ca	Ba	Na	K	P	Cl
Mbuji Mayi																								
CTPs1	21	36.6	2.8	6.2	10.7	5.1	17.0	4.4	1.0	7.7	10.1	1.7	19.9	40.4	2.3	4.0	10.0	8.4	20.3	2.0	1.1	5.4	4.8	3.2
CTPs2	21	35.3	2.7	5.7	13.6	5.3	18.3	3.8	1.6	6.2	10.1	1.2	20.7	39.1	2.3	3.8	12.6	8.6	22.0	1.7	1.7	4.4	4.8	2.3
CTPs5	21	48.0	2.8	7.9	12.5	4.4	9.0	2.3	1.9	7.1	6.6	1.3	23.2	52.6	2.3	5.1	11.5	7.2	10.7	1.0	2.0	5.0	3.1	2.5
CTPs6	21	40.3	3.7	6.4	6.7	4.0	14.1	9.2	1.2	8.7	7.1	3.4	27.4	45.6	3.2	4.3	6.3	6.8	17.3	4.3	1.3	6.3	3.4	6.9
CTPs7	15	50.5	5.1	8.6	8.4	4.7	8.5	3.4	1.1	8.1	5.6	0.4	25.5	55.7	4.2	5.6	7.7	7.7	10.1	1.5	1.2	5.7	2.7	0.8
CTPs8	21	41.6	3.2	6.7	10.4	6.4	13.0	4.4	1.5	7.3	8.7	1.9	22.9	45.5	2.6	4.3	9.5	10.4	15.4	1.9	1.6	5.1	4.1	3.5
CTPs12	9	45.9	3.8	7.0	10.6	5.5	10.9	7.5	2.0	9.3	5.2	1.6	31.2	50.0	3.1	4.5	9.6	8.9	12.7	3.3	2.2	6.5	2.4	2.9
CTPs13	10	55.1	4.2	9.8	9.5	2.3	3.8	3.7	1.4	10.4	3.4	0.6	34.2	62.0	3.5	6.5	9.0	3.8	4.6	1.6	1.6	7.5	1.6	1.1
CTPs14	21	35.8	3.6	5.6	10.6	6.1	17.3	8.7	1.9	6.1	8.7	2.5	18.5	39.8	3.0	3.7	9.6	9.9	20.2	4.1	2.1	4.4	4.2	5.1
CTPs15	18	48.0	3.4	7.5	11.8	4.5	10.5	6.9	1.4	8.3	9.0	1.1	20.5	53.2	2.8	4.9	10.9	7.3	13.5	3.6	1.6	5.9	4.7	2.1
CTPb4	20	24.9	2.6	3.8	8.8	4.7	12.6	6.4	3.9	20.8	8.8	7.8	15.8	27.6	2.2	2.5	8.2	7.8	14.9	2.8	4.2	14.8	4.1	14.6
CTPb7	20	42.1	2.4	7.6	8.7	3.5	11.3	nd	2.4	14.6	5.6	5.0	29.3	45.6	2.0	4.9	7.9	5.6	13.1	nd	2.5	10.0	2.6	8.9
CTPb8	40	37.5	2.7	6.0	8.5	6.4	12.9	nd	2.5	14.2	6.6	5.1	23.1	39.6	2.2	3.7	7.6	10.0	14.6	nd	2.6	9.7	3.0	9.0
MM8	30	41.1	2.6	7.3	10.9	4.8	11.1	3.1	1.7	8.8	7.5	1.7	17.1	45.7	2.2	4.8	10.1	7.9	13.3	1.3	1.8	6.3	3.5	3.3
MM23	20	31.2	2.7	5.3	12.4	5.7	18.4	4.4	1.1	7.2	10.4	1.9	9.8	34.7	2.2	3.5	11.6	9.5	22.3	2.0	1.2	5.1	5.0	3.5
MM21	20	46.4	1.8	7.4	7.6	3.5	10.2	3.2	1.6	10.4	6.1	2.0	14.1	51.5	1.5	4.8	7.1	5.7	12.2	1.4	1.7	7.4	2.9	3.8
MM6	20	39.3	2.9	6.2	10.2	5.5	14.3	3.8	1.1	8.5	9.4	2.6	10.8	42.9	2.4	4.0	9.3	8.9	17.0	1.7	1.1	6.0	4.4	4.8
MM17	20	38.1	3.1	7.3	11.6	5.4	15.0	5.4	2.2	8.0	8.3	1.4	10.3	42.3	2.6	4.8	10.8	9.0	18.0	2.4	2.4	5.7	4.0	2.7
MM2	15	52.0	2.7	8.9	8.1	3.3	5.8	3.4	2.4	12.1	5.6	2.3	3.9	58.5	2.3	5.9	7.6	5.5	7.0	1.5	2.6	8.7	2.7	4.4
MM1	20	36.4	2.7	6.5	18.0	4.2	10.1	4.5	2.5	7.2	9.4	1.5	4.3	40.9	2.3	4.4	17.1	7.1	12.5	2.1	2.8	5.2	4.6	2.8
MM4	10	53.8	5.0	8.0	14.1	5.9	2.6	nd	1.2	8.4	2.3	nd	5.9	58.6	4.1	5.1	12.9	9.6	3.0	nd	1.2	5.9	1.1	nd
MM11	20	42.1	2.9	7.0	9.9	5.2	9.3	2.6	2.4	10.7	8.7	2.8	5.7	46.6	2.4	4.6	9.2	8.6	11.1	1.1	2.6	7.5	4.1	5.2
MM7	24	37.5	3.0	5.5	10.2	6.0	7.9	4.3	2.5	16.2	6.7	4.1	21.2	41.2	2.5	3.6	9.4	9.9	9.4	1.9	2.7	11.5	3.2	7.8
MM9	20	39.7	2.7	6.6	10.1	4.5	9.7	3.8	2.9	12.4	8.4	3.2	19.4	44.3	2.3	4.3	9.5	7.5	11.5	1.6	3.1	8.8	4.0	6.0
MM12	21	44.5	3.1	7.2	10.1	5.6	7.0	3.7	2.9	11.4	6.9	2.6	19.6	48.9	2.6	4.6	9.3	9.2	8.2	1.6	3.1	8.0	3.2	4.9
MM15	22	36.7	2.6	6.5	10.1	5.1	10.4	3.3	3.1	14.0	7.7	3.0	20.2	40.6	2.1	4.2	9.4	8.4	12.4	1.5	3.3	9.9	3.7	5.7
MM20	11	43.6	3.0	7.1	8.0	6.4	8.9	3.4	2.3	10.9	8.1	1.7	18.2	48.2	2.5	4.6	7.4	10.5	10.6	1.5	2.5	7.7	3.8	3.3
MM22	20	41.3	2.7	7.8	7.4	4.2	11.3	4.1	3.1	12.0	7.3	3.5	19.5	45.7	2.3	5.1	6.8	6.8	13.3	1.8	3.3	8.4	3.4	6.5
CDR3	20	48.1	2.4	6.2	4.8	5.8	4.2	3.0	3.2	14.6	9.3	nd	5.1	54.9	2.0	4.1	4.6	9.9	5.1	1.4	3.6	10.6	4.5	nd
Panda																								
PAN2	43	4.8	nd	nd	5.9	12.7	7.4	18.1	4.1	23.3	nd	22.1	13.5	5.0	nd	0.9	11.2	9.4	8.4	7.5	4.1	15.2	0.9	38.3
PAN3	17	3.2	nd	0.8	3.4	7.1	5.1	17.7	4.8	28.8	1.1	30.1	6.1	3.2	nd	0.5	6.0	5.0	5.5	7.0	4.6	18.3	0.5	50.7
PAN5	22	6.0	3.4	2.2	8.5	28.0	13.1	12.3	6.0	13.0	0.7	13.4	7.9	6.3	2.4	1.4	24.9	13.2	14.5	5.2	5.8	8.2	0.3	22.5
PAN7	28	3.5	nd	0.8	5.2	19.1	8.8	12.8	9.7	20.1	2.1	22.3	23.1	3.5	nd	0.5	16.6	7.9	9.6	5.2	9.0	12.7	1.0	36.8
PAN6	27	4.1	8.0	1.3	4.7	17.2	7.7	na	7.7	22.1	1.3	23.6	8.8	4.1	5.7	0.8	14.7	7.0	8.3	6.5	7.2	13.6	0.6	38.8
PAN8	19	4.5	6.1	1.3	5.9	14.6	7.9	na	11.8	22.6	0.9	26.8	7.1	4.3	4.3	nd	11.6	8.3	8.0	nd	10.4	13.1	0.4	41.0
PAN4	13	15.1	1.7	1.7	1.6	10.6	5.0	12.5	4.1	26.0	2.8	22.2	8.0	16.0	nd	1.1	9.4	2.5	5.7	5.2	4.2	17.3	1.3	39.2

Table 4.2: Average major element compositions of inclusions in Mbuji Mayi and Panda diamond coats. Abbreviations: no. inc. - number of inclusions analysed, nd - not detected, na - not analysed.

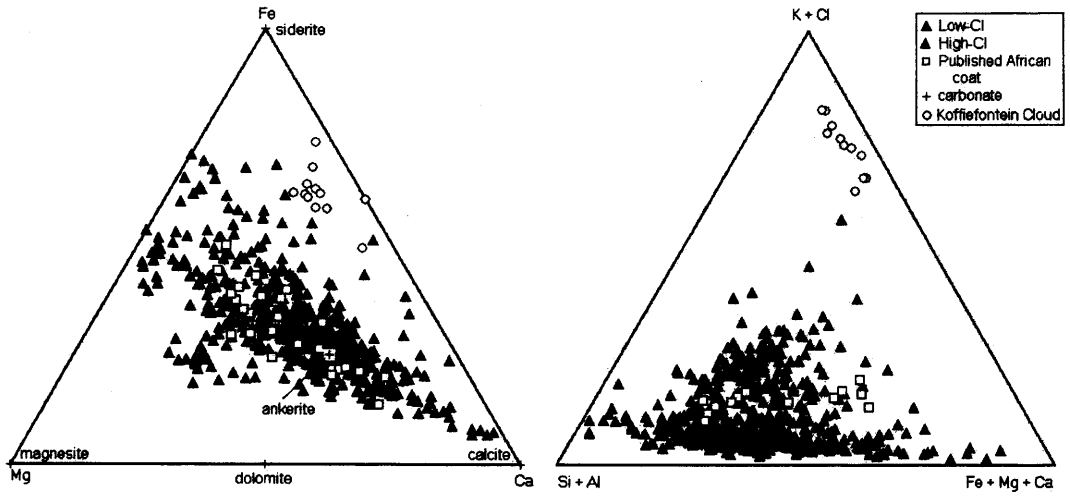

Figure 4.3: Compositions of micro-inclusions in African diamond fluids. The Low-Cl (grey triangles) and high-Cl (black triangles) from Mbuji Mayi diamond coats are compared to published data from fibrous diamonds from DRC and Botswana (Navon et al., 1988; Schrauder & Navon, 1994) (open squares) and to brine in cloudy diamonds from Koffiefontein (Izraeli et al., 2001, 2004) (Open circles).

The compositions of individual inclusions in the Mbuji Mayi diamond coats are not consistent with any single mineral phase, either mantle minerals (garnet, olivine, pyroxene), or minerals identified in the infrared spectra of these samples (quartz, carbonate, apatite). This is consistent with the findings of Guthrie et al. (1991), who observed that inclusion cavities contained multi-phase secondary mineral populations and a void that was assumed to have contained fluid. The samples do not show radial zoning in the major element compostion of fluid inclusions. Infrared spectroscopy has shown that the inclusions in the Mbuji Mayi samples are dominated by water and carbonate and contain quartz and apatite (section 3.2.2.2).

The Mbuji Mayi inclusion compositions are similar to those reported previously from Botswana (Schrauder & Navon, 1994) and the DRC (Navon et al., 1988) but widen the compositional field of African diamond fluids (Fig. 4.3). The range of individual inclusion compositions is shown in the variation diagrams in figure 4.4. Si has a negative linear correlation with Ca and P and positive linear correlation with Al in all inclusions. Potassium is enriched in all inclusions, those with <2 mol% Cl (low-Cl) also show a positive linear correlation

between Si and K. Therefore, the inclusions vary between Si-Al-K rich and Ca-P rich end-members (Navon et al., 1988; Schrauder & Navon, 1994); the calculated end-member compositions are given in table 4.3. Compositional vectors of phlogopite are seen in the low-Cl variation diagrams (Si vs K 4.4a, Si vs Al 4.4b), suggesting that phlogopite may be present in the inclusions. Recording this compositional vector suggests that the fluid was in equilibrium with phlogopite, or that phlogopite was trapped as a solid phase rather than precipitated as a daughter mineral from the trapped fluid. The concentrations of Ti and Na are variable but do not show a consistent trend with Si (not shown).

The Ca-P end-member is thought to be carbonatite-like because of the presence of carbonate and apatite in the infrared spectra. The relative proportions of Ca to P in the inclusions lie along the compositional vector of apatite (Fig. 4.4e). This suggests that apatite was trapped as a solid phase. Fe and Mg concentrations are scattered but have a slight negative correlation with Si, suggesting that Fe and Mg are dominantly associated with the carbonate end-member fluid. The average molar ratio Mg# (Mg/(Mg+Fe)) is 0.5 $\pm$0.1 and does not correlate with Si. The relative proportions of Fe, Mg and Ca in the inclusions are consistent with the presence of calcite and ankerite (Fig 4.3), with some Fe and Mg also present in non-carbonate phases e.g. silicates.

Inclusions with $\geq$2 mol% Cl (high-Cl) show a negative correlation between K and Si (Fig 4.4), in these inclusions K is correlated with Cl indicating the presence of a third fluid end-member: a KCl brine. The other major elements follow the same trends as in the low-Cl inclusions. The calculated end-member composition of the high-Cl fluid is given in table 4.3. The molar ratio K/Cl of the High-Cl end-member is 0.78, this is similar to the average K/Cl ratio of brine inclusions in a peridotitic coated diamond from Diavik, Canada (0.6$\pm$0.1 Klein-BenDavid et al. 2004) and those in cloudy diamonds from Koffiefontein, South Africa (average 0.64$\pm$0.1 Izraeli et al. 2001, 2004). This ratio is significantly higher than in the Panda samples (Fig. 4.4f). The molar ratio (Na+K)/Cl in the Mbuji Mayi fluid is close to 1, therefore the brine is approximately charge compensated by monovalent cations. The high-Cl end-member is similar to the composition of fluid inclusions in cloudy diamonds from Koffiefontein (Izraeli et al., 2001, 2004) (Fig. 4.3) except that the Mbuji Mayi coated diamond fluids have a higher Si

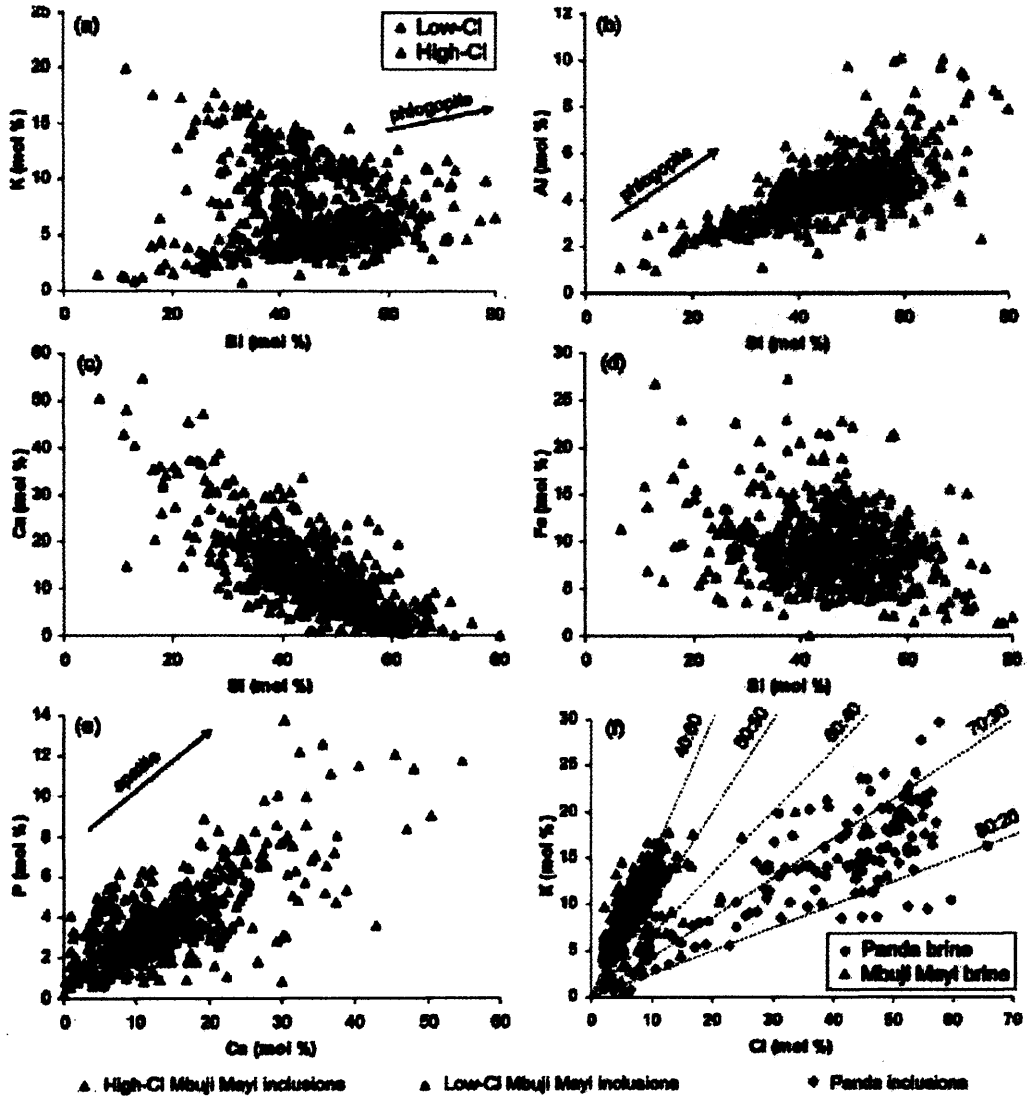

Figure 4.4: Variation diagrams showing the 100% normalised molecular proportions of various elements in the Mbuji Mayi diamond coat fluids. Low Cl inclusions (grey triangles) have <2 mol% Cl, high-Cl inclusions (black triangles) have $\geq$ 3 mol% Cl. (a) Low-Cl inclusions have a positive correlation between K and Si, high-Cl inclusions have a negative variation trend; (b) Positive correlation between Si and Al; (c) Ca is negatively correlated with Si; (d) Fe data is widely scattered, there is a very weak negative trend with Si; (e) Ca and P are correlated; (f) Cl and K are correlated in high-Cl inclusions at a Cl:K ratio of 40:60, this is compared to the Panda fluid data (grey diamonds) where the Cl:K ratio is 70:30. Vectors for apatite and phlogopite are also shown.

Origin	Mbuji Mayi			Panda			
Suite	Unknown			Peridotite		Eclogite	
End-member	Carb.	Si-Al-K	Brine	Brine	Low Cl	Brine	Low Cl
wt% oxide							
SiO_2	0.0	58.0	19.3	2.2	7.6	3.4	39.1
TiO_2	2.5	3.6	2.2	0.0	0.0	0.0	0.0
Al_2O_3	0.9	10.2	4.6	0.0	2.5	0.7	4.0
FeO	17.7	8.2	0.4	1.4	37.6	9.4	12.8
MgO	8.4	4.0	2.2	0.0	14.1	0.0	4.3
CaO	39.7	1.4	7.4	0.7	19.9	0.6	12.7
BaO	3.6	0.0	1.4	14.7	16.6	11.2	14.3
Na_2O	1.8	1.4	4.4	10.3	1.6	3.6	5.0
K_2O	0.5	9.7	39.2	34.3	0.0	37.4	0.0
P_2O_5	19.9	3.3	0.0	0.0	0.0	1.2	7.9
Cl	0.4	0.2	18.8	36.5	0.0	32.5	0.0
mol %							
Si	0.0	64.2	19.8	2.1	8.4	3.4	45.8
Ti	2.2	3.0	1.7	0.0	0.0	0.0	0.0
Al	0.6	6.6	2.8	0.0	1.6	0.4	2.7
Fe	17.1	7.6	0.4	1.1	34.6	7.9	12.5
Mg	14.5	6.6	3.5	0.0	23.1	0.0	7.4
Ca	49.1	1.7	8.2	0.7	23.4	0.7	16.0
Ba	3.6	0.0	0.6	5.6	7.2	4.4	6.6
Na	2.1	1.5	4.4	9.6	1.7	3.5	5.7
K	0.3	6.9	25.8	21.1	0.0	24.0	0.0
P	9.7	1.6	0.0	0.0	0.0	0.4	3.2
Cl	0.8	0.5	32.9	59.7	0.0	55.4	0.0
molar ratios							
K/Cl	0.4	15.2	0.8	0.4	-	0.4	-
Na+K/Cl	2.9	18.6	0.9	0.5	-	0.5	-

Table 4.3: Calculated end-member major element compositions of inclusions in Mbuji Mayi and Panda diamond coats.

and a significantly lower Fe concentration than the cloudy diamonds. High-Cl inclusions are concentrated at the core-coat boundary in the Mbuji Mayi samples but also occur randomly distributed througout the rest of the diamond coat. This high-Cl end-member was not recognised by Schrauder & Navon (1994).

Eight S-rich inclusions were analysed in sample CTPb8, these contained 14-44 mol% S. Sulphur is negatively correlated with Si and Cl and surprisingly also with Fe and Mg, suggesting that S is not present as sulphide. These fluids are different to Fe-Si-Ni sulfide melts coexisting with carbonate in K-, Ba-, Rb-, Sr-, HFSE- and Cl-rich cuboid diamonds from Yubileinaya (Yakutia, Siberia) (Klein-BenDavid et al., 2003). Unfortunately there are not enough S-rich inclusions to

draw conclusions about their characteristics.

4.3.2 Panda Individual Inclusion Compositions

The major element composition of 245 individual micro-inclusions in the Panda diamond coat reveals the presence of silicate minerals, K-Na-Cl brine and Fe-Ca-Mg carbonates; no sulphide inclusions were detected. The inclusions span a wide compositional range and the samples are not zoned in terms of major elements. Infrared spectroscopy has shown that the inclusions in the Panda samples are dominated by water and carbonate and contain mantle silicates (section 3.2.2.2).

In addition to their occurrence as macro-inclusions (section 4.4), olivine (PAN1, PAN2, PAN3, PAN6) and clinopyroxene (PAN1, PAN4, PAN5) are present in the micro-inclusions, where they coexist with K-Na-Cl fluid and/or carbonate. Olivine in micro-inclusions has Mg# $\approx$89 and clinopyroxene in both eclogitic and peridotitic samples has Mg# $\approx$71 and Ca# (Ca# = 100 $\times$ Ca/(Ca+Mg+Fe)) of $\approx$24. The compositions of these mineral phases are poorly constrained as they are present in very small, multi-phase inclusions. Peridotitic and eclogitic inclusions do not occur mutually within samples. Multi-phase micro-inclusions containing mantle silicates are ignored when considering the micro-inclusions in order to reveal the composition of the coexisting brine and carbonate in the peridotitic and eclogitic samples.

4.3.2.1 Peridotitic

Micro-inclusion compositions in the peridotitic coated diamonds from Panda contrast with inclusions in the Mbuji Mayi samples, in that the African fluids have higher concentrations of SiO_2 and Al_2O_3. The inclusions are similar to inclusion compositions described in a single fibrous diamond from Diavik (Klein-BenDavid et al., 2004) (Fig. 4.6). Fe, Mg and Ca are present in all Panda inclusions and often in the absence of Si and Al. This observation, combined with the presence of carbonate bands in the infrared spectra of all samples (section 3.2.2.2), indicates that the micro-inclusions contain carbonate. There is a strong correlation between Ca and Mg and a broad correlation with Fe, which is consistent with the presence of dolomite and some ankerite, probably in addition to mantle silicates.

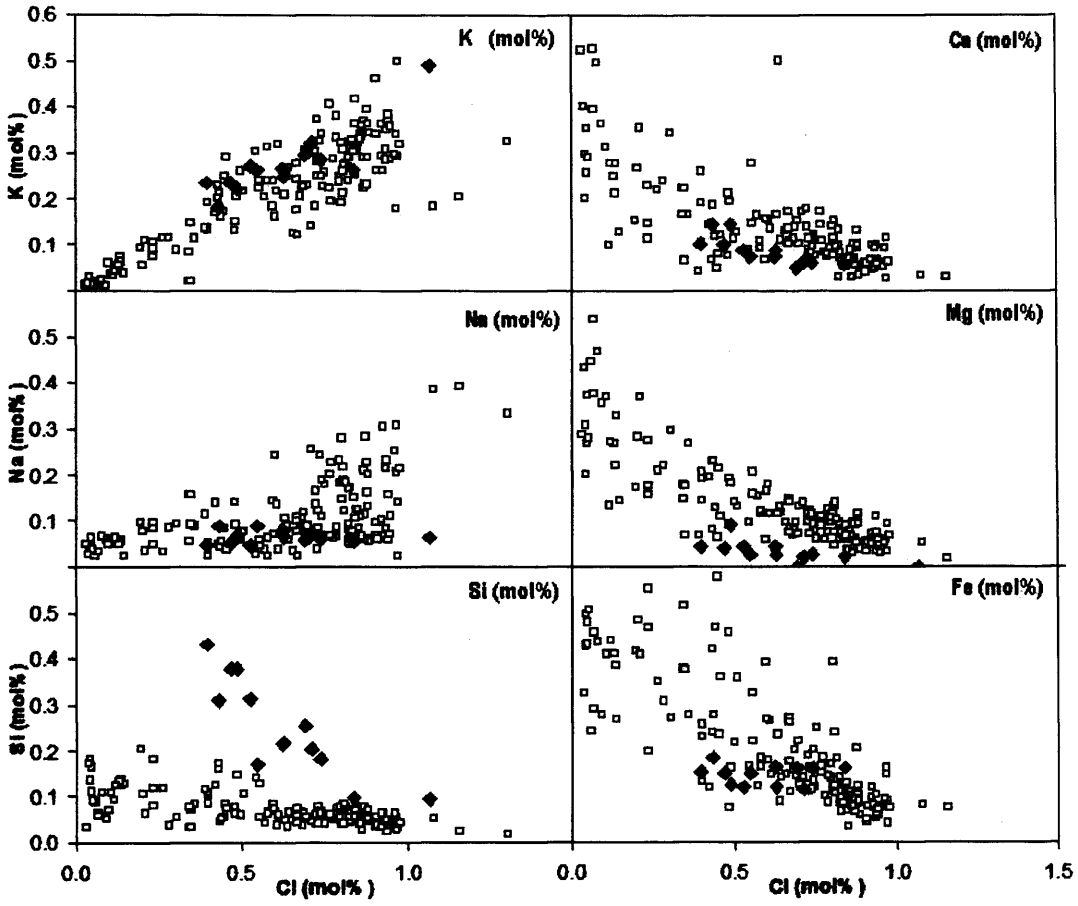

Figure 4.5: Variation diagrams showing the 100% normalised molecular proportions of various elements in relation to Cl in the peridotitic (open squares) and eclogitic (black diamonds) Panda diamond coat fluids.

The average Mg# is 0.42 ±0.1. The peridotitic diamond coat fluids also have high concentrations of Ba (5 - 8 mol%).

The chemistry of the micro-inclusions in the peridotitic diamonds shows that Cl is negatively correlated with Ca, Mg, Fe and Si and positively correlated with K and Na (Fig. 4.5). The average K/Cl molar ratio of the fluid is 0.37 (range 0.07 to 0.71) and the (K+Na)/Cl ratio is 0.61 (range 0.22 to 1.88), these ratios are significantly lower than in the Mbuji Mayi samples. The inclusion compositions fall along linear arrays from carbonate towards K-Na-Cl rich compositions, indicating the presence of a Cl-brine end-member. The calculated end-member

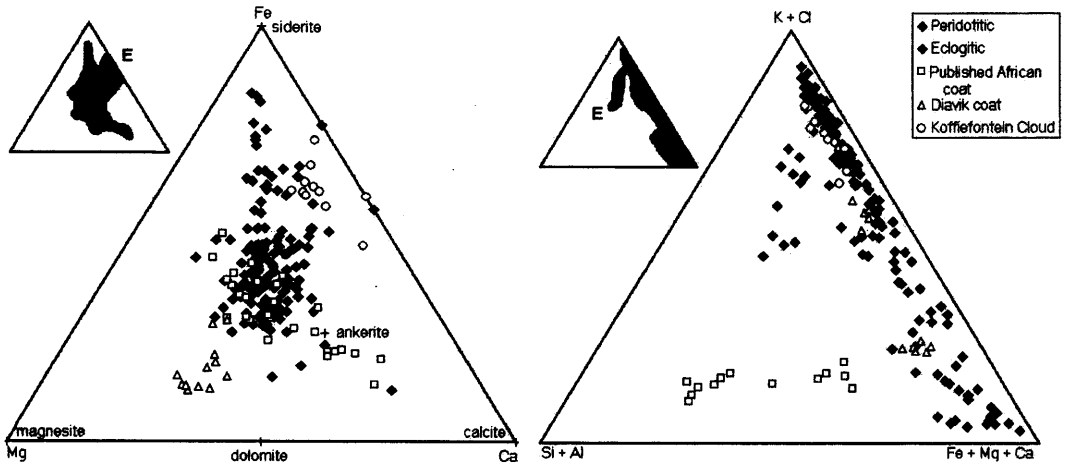

Figure 4.6: Compositions of micro-inclusions in peridotitic (grey diamonds; PAN1, PAN2, PAN3, PAN5, PAN6, PAN7, PAN8) and eclogitic (black diamonds; PAN4) coated diamonds from Panda. Also shown are published data from coated diamonds from Africa (Navon et al., 1988; Schrauder & Navon, 1994) (open squares) and Diavik (Canada) (Klein-BenDavid et al., 2004) (open triangles) cloudy diamonds from Koffiefontein (Izraeli et al., 2001) (open circles). Summary insets show the compositional fields of inclusions in the peridotitic (P, grey) and eclogite (E, black) samples.

carbonatite and brine compositions are given in table 4.3. The brine is similar to the composition of K-Cl rich fluid in cloudy diamonds from Koffiefontein (Izraeli et al., 2001) and to the brine end-member fluid in a fibrous diamond from Diavik (Canada) (Klein-BenDavid et al., 2004).

In most inclusions, the molar ratio Na+K/Cl is less than 1, therefore Cl in the inclusions is not fully charge balanced by the alkali cations. However, the sum of the charge associated with positive mono- and divalent (K, Na, Fe, Mg, Ca) ions is $\geq$100 (average 223) per 100Cl ions and it is thought that the charge is balanced by carbonate ions as suggested by Izraeli et al. (2001).

4.3.2.2 Eclogitic

Relative to the peridotitic fluid, the eclogitic fluid is Si- and Al-rich Fig. 4.6). The high Si-content is consistent with the presence of quartz in the infrared spectra in addition to carbonate (section 3.2.2.2). This chemical composition is similar

to that observed in the Mbuji Mayi coated diamonds and to published data for fibrous diamonds from Zaire and Botswana (Navon et al., 1988; Schrauder & Navon, 1994), but the Panda fluid has a higher concentration of K, Cl and Ba (Fig. 4.6). The eclogitic coat fluid is more Fe-rich (Mg# = 0.38 ±0.1) than that in the peridotitic samples, a result confirmed both by the observation of ankerite in addition to dolomite in the infrared spectra and the lower Mg-content of eclogite-suite minerals. The difference between the carbonate compositions observed in the peridotitic and eclogitic coated diamonds may be a reflection of the difference in host rock composition e.g. if carbonate is generated or modified by reactive chromatographic processes (section 2.2.3.1). The fluid coexisting with eclogite may be enriched in Si, Al and Fe relative to the fluid coexisting with peridotite, because the eclogite host rock is more rich in these elements and the fluid is tending towards equilibrium with this matrix. In addition, fluids in eclogite have a higher dihedral angle than they do in peridotite (Mibe et al., 2003), therefore fluids cannot percolate so deeply into eclogite and will crystallise over a shorter distance. Therefore, fractionation may not be so pronounced. The recognition that the fluid is more Si and Al rich in the eclogitic diamond sample may have implications for Tonalite-trondhjemite-granodiorite (TTG) genesis in the Archean. Recent experimental work has shown that partial melting (ca. 5-30%) of hydrous basalt (eclogite) at between 2 and 4 GPa can account for the majority of major and trace element characteristics of TTG suites (Rapp et al., 2003). The inclusions in this study provide evidence for hydrous basalt in the cratonic mantle, without the need to melt subducting slab. The experimental study by Rapp et al. (2003) generated low Nb/Ta and high Zr/Sm ratios from a source with initially subchondritic Nb/Ta, therefore the trace element signature is process driven rather than being controlled by tectonic environment.

The chemistry of the micro-inclusions in the single eclogitic diamond shows that Cl is negatively correlated with Ca, Mg, Fe and Si, and correlated with K (Fig. 4.5). In consequence, the inclusion compositions fall along linear arrays from carbonate towards K-Cl rich compositions, again indicating the presence of a Cl-brine end-member. Unlike the peridotitic micro-inclusions there is no correlation between Cl and Na (Fig. 4.5). The average K/Cl molar ratio of the fluid is 0.45 (range 0.07 to 0.60). The calculated composition of the low-Cl and

brine end-members is given in table 4.3. The end-member brine composition in the eclogitic suite micro-inclusions is similar to that in the peridotitic diamond micro-inclusions except for its higher Fe content (table 4.3).

Sample	Suite	Minerals present	T (°C)	P (GPa)
PAN1	P	olivine^{x,y,z}, cpx^{z}, carb^{x}.		
PAN2	P	olivine^{z}, carb.^{x}		
PAN3	P	pyroxene^{x} (cpx^{y},opx^{y}), carb^{x}.	935^{c}	4.2^{c}
PAN4	E	cpx^{x,y,z}, rutile^{y}, quartz^{x}, carb^{x}.		
PAN5	P	garnet^{x,y}, cpx^{y,z}, carb.^{x}	959^{b}, 980^{c}	4.6^{c}
PAN6	P	olivine^{z}, carb.^{x}		
PAN7	P	olivine^{y}, carb.^{x}		
PAN8	P	garnet^{y}, olivine^{y}, carb.^{x}	1006^{a}	

Table 4.4: Summary of Panda diamond coat characteristics determined from Ft-ir spectroscopy and EMPA. Nitrogen and H_2O concentrations are given in ppm and are normalised to a sample thickness of 1 mm. H_2O=100H_2O/(H_2O+CO_2). Mineral phases as detected in: ^{x}Ft-ir absorption spectra, EMPA as ^{y}single phase macro-inclusions ^{z}micro-inclusion phases. Pressure and temperature conditions are calculated from macro-inclusion compositions using the geotherometers of ^{a} O'Neill (1978), ^{b} Krogh (1988) and the geothermobarometer of ^{c} Nimis & Taylor (2000). Starting pressures for calculation were 4.6 GPa.

4.4 Results: Macro-Inclusions

Olivine, garnet, clinopyroxene and orthopyroxene were identified in the infrared spectra of the diamond coats and from EMPA (table 4.4), phlogopite was not detected. No silicate inclusions were observed in the diamond cores. Macro-silicate inclusions in the Panda diamond coats have sharp crystal outlines, but the resolution is not sufficient to determine the morphology (Fig. 4.1).

4.4.1 Garnet

Two diamond coats contain garnet inclusions (PAN8 and PAN5), with moderate Cr_2O_3 (7.3 to 8.9 wt%) and high CaO contents (5.1 to 6.7 ±0.09 wt%) and are classified as lherzolitic Cr-pyrope (Fig. 4.7). The chemistry of these garnet inclusions overlap with the compositions of garnet inclusions in gem diamonds from Panda (Stachel et al., 2003; Tappert et al., 2005) and extend the range to more Ca- and Fe-rich compositions. This is reflected in the high values of Ca# of 13.8 to 18.2.

Suite	Sample	SiO_2	TiO_2	Al_2O_3	Cr_2O_3	FeO	NiO	MgO	CaO	Na_2O	K_2O	total	Si	Ti	Al	Cr	Fe	Mg	Ca	Na	Mg#[a]	Ca#[b]
Garnet																						
lherz.	PAN8	41.4	0.2	16.7	8.5	7.4	0.2	17.9	5.4	0.3	0.7	66.1	6.1	0.02	2.9	1.0	0.9	3.9	0.8	0.1	81.1	14.87
lherz.	PAN8	41.9	nd	17.1	8.6	6.9	nd	18.1	5.4	0.3	0.4	91.2	6.1	-	2.9	1.0	0.8	3.9	0.8	0.1	82.3	15.06
lherz.	PAN8	41.8	0.2	17.5	7.6	7.5	nd	18.2	5.0	0.4	0.8	101.8	6.1	0.02	3.0	0.9	0.9	4.0	0.8	0.1	81.2	13.84
lherz.	PAN8	41.4	0.1	16.9	9.0	7.0	nd	18.0	5.7	0.4	0.1	79.7	6.0	0.01	2.9	1.0	0.9	3.9	0.9	0.1	82.1	15.60
lherz.	PAN5	42.8	0.1	18.0	7.3	6.1	nd	18.5	6.1	0.2	nd	99.8	6.2	0.01	3.1	0.8	0.7	4.0	0.9	0.1	84.3	16.75
lherz.	PAN5	42.5	nd	17.9	7.4	6.6	0.1	17.7	6.6	0.2	nd	101.1	6.2	-	3.1	0.8	0.8	3.8	1.0	0.1	82.7	18.17
lherz.	PAN5	41.2	nd	17.6	8.3	7.4	nd	17.3	6.0	0.3	0.5	59.3	6.0	-	3.0	1.0	0.9	3.8	0.9	0.1	80.6	16.78
lherz.	PAN5	42.1	nd	17.9	7.5	6.6	0.2	17.6	6.6	0.2	0.1	87.6	6.1	-	3.1	0.9	0.8	3.8	1.0	0.1	82.6	18.16
lherz.	PAN5	42.4	nd	17.9	7.6	6.7	nd	17.6	6.5	0.2	nd	99.7	6.2	-	3.1	0.9	0.8	3.8	1.0	0.1	82.4	18.02
lherz.	PAN5	42.8	nd	18.1	7.3	6.5	nd	17.7	6.3	0.2	0.1	101.1	6.2	-	3.1	0.8	0.8	3.8	1.0	0.1	82.9	17.54
Clinopyroxene																						
lherz.	PAN5	54.6	nd	1.0	1.9	2.1	nd	17.3	21.8	1.2	nd	55.2	2.0	-	0.0	0.1	0.1	0.9	0.8	0.1	93.6	45.87
lherz.	PAN5	55.4	nd	1.0	1.9	1.6	nd	17.0	21.7	1.1	nd	68.8	2.0	-	0.0	0.1	0.0	0.9	0.8	0.1	94.9	46.59
lherz.	PAN5	56.9	0.1	1.0	nd	1.7	nd	17.3	22.0	1.0	nd	83.8	2.0	0.00	0.0	-	0.0	0.9	0.8	0.1	94.9	46.41
lherz.	PAN5	56.2	nd	1.0	1.8	1.6	nd	16.9	21.3	1.0	nd	84.9	2.0	-	0.0	0.1	0.0	0.9	0.8	0.1	95.0	46.26
lherz.	PAN5	55.0	nd	1.4	1.7	1.8	nd	17.8	20.6	1.1	0.3	52.1	2.0	-	0.1	0.0	0.1	1.0	0.8	0.1	94.6	43.97
lherz.	PAN3	55.0	0.3	1.2	2.0	2.3	nd	16.6	21.2	1.0	0.1	87.7	2.0	0.01	0.0	0.1	0.1	0.9	0.8	0.1	92.8	45.97
lherz.	PAN3	56.0	0.3	2.5	2.9	1.7	nd	15.3	18.9	2.2	nd	85.4	2.0	0.01	0.1	0.1	0.1	0.8	0.7	0.2	94.2	45.48
lherz.	PAN3	56.2	0.2	0.9	1.7	2.2	nd	16.2	21.4	0.9	nd	91.5	2.0	0.01	0.0	0.0	0.1	0.9	0.8	0.1	93.1	46.88
lherz.	PAN3	55.4	0.4	2.5	2.7	2.1	nd	15.7	19.1	1.8	0.3	88.6	2.0	0.01	0.1	0.1	0.1	0.8	0.7	0.1	93.1	44.90
lherz.	PAN3	56.4	0.3	2.3	2.7	1.8	nd	15.3	18.9	2.1	nd	94.0	2.0	0.01	0.1	0.1	0.1	0.8	0.7	0.1	93.9	45.42
lherz.	PAN3	56.1	0.3	1.8	2.2	1.7	nd	16.4	19.7	1.5	nd	96.5	2.0	0.01	0.1	0.1	0.0	0.9	0.8	0.1	94.6	45.00
lherz.	PAN3	55.7	0.5	0.8	1.2	2.0	nd	17.1	21.7	0.7	0.1	94.3	2.0	0.01	0.0	0.0	0.1	0.9	0.8	0.0	94.0	46.08
ecl.	PAN4	55.7	0.4	7.4	nd	6.7	nd	9.8	15.5	4.6	nd	97.9	2.0	0.01	0.3	-	0.2	0.5	0.6	0.3	72.3	45.22
ecl.	PAN4	55.9	nd	7.3	nd	6.9	nd	9.6	15.6	4.7	nd	98.6	2.0	-	0.3	-	0.2	0.5	0.6	0.3	71.3	45.36
ecl.	PAN4	55.5	nd	7.3	nd	7.0	nd	9.8	15.6	4.8	nd	99.9	2.0	-	0.3	-	0.2	0.5	0.6	0.3	71.4	44.84
ecl.	PAN4	55.7	nd	7.3	nd	6.8	0.4	9.7	15.3	4.7	nd	100.4	2.0	-	0.3	-	0.2	0.5	0.6	0.3	71.8	44.90
ecl.	PAN4	55.6	nd	7.3	nd	6.9	nd	9.9	15.5	4.8	nd	99.8	2.0	-	0.3	-	0.2	0.5	0.6	0.3	71.9	44.77
ecl.	PAN4	55.5	nd	7.4	nd	7.0	nd	9.8	15.6	4.8	nd	96.6	2.0	-	0.3	-	0.2	0.5	0.6	0.3	71.2	44.90
ecl.	PAN4	55.8	0.3	7.1	nd	6.6	nd	9.9	15.7	4.6	nd	98.8	2.0	0.01	0.3	-	0.2	0.5	0.6	0.3	72.6	45.35
ecl.	PAN4	55.4	nd	7.3	nd	7.0	nd	9.8	15.6	4.9	nd	96.6	2.0	-	0.3	-	0.2	0.5	0.6	0.3	71.4	44.85
ecl.	PAN4	55.9	nd	7.3	nd	6.7	nd	9.8	15.6	4.7	nd	98.5	2.0	-	0.3	-	0.2	0.5	0.6	0.3	72.3	45.31
ecl.	PAN4	55.2	nd	6.3	nd	6.9	nd	10.4	16.9	4.3	nd	96.4	2.0	-	0.3	-	0.2	0.6	0.7	0.3	72.9	45.85
ecl.	PAN4	55.8	0.3	7.2	nd	6.7	nd	9.8	15.6	4.6	nd	99.9	2.0	0.01	0.3	-	0.2	0.5	0.6	0.3	72.2	45.35
ecl.	PAN4	55.9	nd	7.3	nd	6.5	nd	9.8	15.8	4.6	nd	100.2	2.0	-	0.3	-	0.2	0.5	0.6	0.3	72.8	45.64
ecl.	PAN4	55.0	nd	7.2	0.3	6.9	nd	10.0	15.9	4.7	nd	91.6	2.0	-	0.3	0.0	0.2	0.5	0.6	0.3	72.1	45.09
ecl.	PAN4	55.5	nd	7.1	nd	7.4	nd	9.7	15.6	4.7	nd	99.5	2.0	-	0.3	-	0.2	0.5	0.6	0.3	70.1	44.58
ecl.	PAN4	55.4	0.3	7.2	nd	7.2	nd	9.8	15.4	4.7	nd	102.0	2.0	0.01	0.3	-	0.2	0.5	0.6	0.3	70.8	44.52
ecl.	PAN4	55.7	nd	7.2	nd	6.7	nd	9.8	15.8	4.7	nd	100.3	2.0	-	0.3	-	0.2	0.5	0.6	0.3	72.2	45.50
ecl.	PAN4	55.7	0.4	7.3	nd	6.6	nd	9.7	15.5	4.8	nd	101.2	2.0	0.01	0.3	-	0.2	0.5	0.6	0.3	72.3	45.54
ecl.	PAN4	55.5	nd	7.3	nd	7.1	nd	9.8	15.6	4.7	nd	100.2	2.0	-	0.3	-	0.2	0.5	0.6	0.3	71.2	44.88
ecl.	PAN4	55.0	nd	7.0	0.3	7.4	nd	9.9	15.7	4.7	nd	99.6	2.0	-	0.3	0.0	0.2	0.5	0.6	0.3	70.3	44.49
ecl.	PAN4	55.3	0.3	7.3	nd	7.0	nd	9.9	15.4	4.7	nd	101.7	2.0	0.01	0.3	-	0.2	0.5	0.6	0.3	71.6	44.46
ecl.	PAN4	56.0	nd	7.2	nd	6.9	nd	9.8	15.5	4.7	nd	100.3	2.0	-	0.3	-	0.2	0.5	0.6	0.3	71.7	44.97
ecl.	PAN4	55.3	0.3	7.2	nd	6.5	0.4	9.8	15.7	4.8	nd	101.5	2.0	0.01	0.3	-	0.2	0.5	0.6	0.3	72.9	45.60

Suite	Sample	SiO_2	TiO_2	Al_2O_3	Cr_2O_3	FeO	NiO	MgO	CaO	Na_2O	K_2O	total	Si	Ti	Al	Cr	Fe	Mg	Ca	Na	Mg#[a]	Ca#[b]
Olivine																						
lherz.	PAN8	43.4	nd	0.3	nd	8.5	0.4	47.2	0.1	0.2	nd	65.5	1.6	-	0.0	-	0.3	2.6	0.0	0.0	90.9	-
lherz.	PAN8	44.1	nd	0.2	nd	8.5	0.4	46.4	nd	0.3	nd	79.4	1.6	-	0.0	-	0.3	2.5	-	0.0	90.6	-
lherz.	PAN8	45.2	nd	nd	nd	6.5	0.4	47.5	0.1	0.2	nd	95.6	1.6	-	-	-	0.2	2.5	0.0	0.0	92.8	-
	PAN7	44.0	nd	nd	0.1	6.4	0.5	48.8	nd	0.2	0.1	95.2	1.6	-	-	0.0	0.2	2.6	-	0.0	93.1	-
	PAN7	44.0	nd	nd	0.1	7.3	0.5	47.8	nd	0.3	nd	94.1	1.6	-	-	0.0	0.2	2.6	-	0.0	92.1	-
	PAN7	44.6	nd	nd	nd	6.8	0.4	47.9	nd	0.3	nd	94.3	1.6	-	-	-	0.2	2.6	-	0.0	92.6	-
	PAN7	43.9	nd	nd	0.1	6.7	0.4	48.6	0.1	0.2	nd	94.7	1.6	-	-	0.0	0.2	2.6	0.0	0.0	92.8	-
	PAN7	43.1	nd	0.2	0.2	9.5	0.4	46.3	nd	0.3	nd	59.8	1.6	-	0.0	0.0	0.3	2.5	-	0.0	89.7	-
lherz.	PAN1	43.7	nd	nd	nd	8.5	0.3	47.3	nd	0.3	nd	96.6	1.6	-	-	-	0.3	2.6	-	0.0	90.9	-
lherz.	PAN1	44.0	nd	nd	nd	8.1	0.3	47.4	nd	0.3	nd	97.9	1.6	-	-	-	0.2	2.6	-	0.0	91.3	-
lherz.	PAN1	44.7	nd	nd	nd	8.3	0.3	46.3	0.2	0.2	nd	94.1	1.6	-	-	-	0.3	2.5	0.0	0.0	90.8	-
lherz.	PAN1	43.9	nd	nd	nd	8.4	0.3	47.0	nd	0.3	nd	96.1	1.6	-	-	-	0.3	2.5	-	0.0	90.9	-
lherz.	PAN1	43.7	nd	nd	nd	8.8	0.3	47.0	nd	0.2	nd	85.6	1.6	-	-	-	0.3	2.5	-	0.0	90.5	-
lherz.	PAN1	43.9	nd	nd	nd	8.3	0.4	47.2	nd	0.3	nd	95.7	1.6	-	-	-	0.3	2.5	-	0.0	91.0	-
lherz.	PAN1	43.8	nd	nd	nd	8.4	0.3	47.3	nd	0.3	nd	94.7	1.6	-	-	-	0.3	2.6	-	0.0	91.0	-
lherz.	PAN1	43.9	nd	nd	nd	8.6	0.4	46.7	nd	0.3	nd	88.0	1.6	-	-	-	0.3	2.5	-	0.0	90.6	-
Orthopyroxene																						
lherz.	PAN3	63.0	nd	1.7	nd	5.5	0.4	28.7	0.3	0.2	0.2	61.5	2.1	-	0.1	-	0.2	1.4	0.0	0.0	90.3	0.67
lherz.	PAN3	64.1	nd	0.7	nd	5.4	0.4	28.8	0.2	0.2	0.2	59.8	2.2	-	0.0	-	0.2	1.4	0.0	0.0	90.6	0.55
lherz.	PAN3	66.2	nd	1.0	nd	4.1	0.3	27.5	0.3	0.1	0.2	43.8	2.2	-	0.0	-	0.1	1.4	0.0	0.0	92.2	0.63
lherz.	PAN3	60.6	nd	0.6	nd	6.2	0.4	30.8	0.8	0.3	0.3	47.4	2.1	-	0.0	-	0.2	1.6	0.0	0.0	89.8	1.64

Table 4.5: EMPA analyses of silicate inclusions in diamond coats from Panda. Totals are normalised to 100 wt%, the analysed totals are also given. [a]Mg# = Mg/(Mg+Fe), [b]Ca# = Ca/(Ca+Mg+Fe). Abbreviations: lherz. - lherzolite, ecl. - eclogite, nd - not detected.

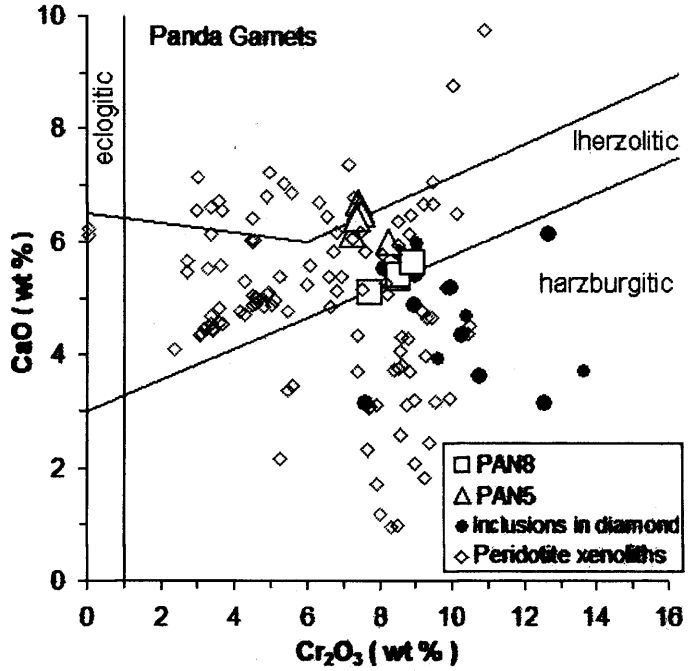

Figure 4.7: Cr_2O_3 verses CaO for garnet inclusions in diamond coats PAN5 (large open triangles) and PAN8 (large open squares). Also shown are compositions of garnet inclusions in gem diamonds from Panda, data from Stachel et al. (2003); Tappert et al. (2005) (small closed circles) and of garnets from Panda peridotite xenoliths from Menzies et al. (2004) (small diamonds).

The Mg# of the garnets varies between 80.6 and 84.3 (mean = 82). The effect of Ca on the MgFe partitioning between garnet and olivine was eliminated by recalculating all garnets to a Ca-free composition according to the method of Stachel et al. (2003). From the data of O'Neill (1978), it can be estimated that the Mg# of garnet decreases by 3.0 per cation Ca ([O]=24) at relevant conditions of 1000 to 1100°C and 5 GPa, when coexisting with olivine with an Mg# of 91. The recalculated Mg#'s of the Panda garnets vary between 83.4 and 87.1 (mean = 85); the mean Mg# for Slave Cr-pyrope inclusions in diamond is 87.0 and for worldwide samples 87.9 (Stachel et al., 2003). Therefore, the garnet Mg# values are indeed low. Low Mg# is indicative of a high source fertility (i.e. not significantly affected by depletion through partial melting) and low equilibration temperatures. The garnet inclusions also have high Na_2O concentrations (0.2 to 0.40 wt%), a characteristic shared by garnets in gem diamonds from Panda

(Tappert et al., 2005). In all the garnets, the TiO_2 concentrations are below the 0.4 wt% cut-off value used as an indicator of metasomatic activity by silicate melts (Gurney et al., 1975; Matthews et al., 1992). This may suggest that the metasomatic agent wasnot a silicate melt, or may be a reflection of the fine scale heterogeneity of the samples.

4.4.2 Olivine

Three of the coated diamonds contain olivine inclusions (PAN1, PAN7 and PAN8). The olivines have forsterite contents of 89.7 to 93.1 % (Fig. 4.8), this is within the lower half of the worldwide database for inclusions in diamonds and extends the range recorded in olivine inclusions in gem Panda diamonds (91.9-93.2) to lower Mg numbers. In consequence, there is an overlap between the Mg# values of olivine inclusions in the Panda diamond coats and olivine xenocrysts from Panda (generally 90-93, Menzies et al. 2004). NiO concentrations range from 0.3 to 0.5 wt% and are within the range of NiO content of inclusions in gem diamond from Panda (0.19 to 0.40 wt%; Tappert et al. 2005). Cr_2O_3 and CaO concentrations are generally below or within the detection limits.

4.4.3 Clinopyroxene

Eclogitic (PAN4) and peridotitic (PAN3, PAN1, PAN5 and PAN8) clinopyroxenes are represented in the Panda coated diamond inclusion population. Eclogitic clinopyroxene inclusions are found in sample PAN4 and have molar ratios of Mg# = 70.1 to 72.9 and Ca# = to 44.5 to 45.9 and so are omphacitic. The eclogitic clinopyroxenes in PAN4 are homogenous, all grains lie within one standard deviation of the mean. The clinopyroxenes have a very low Tschermak component (2-Si>0). They fall within group C of the MgO-Na_2O subdivisions of eclogitic pyroxene (Taylor & Neal, 1989). The majority of diamondiferous eclogites and eclogitic diamond inclusions have group B compositions (More MgO-rich and Na_2O-poor) (Taylor & Anand, 2004). The Al_20_3 and Na_2O concentrations are low (7.1 $\pm$ 0.3 wt% and 4.7 $\pm$ 0.2 wt% respectively) relative to eclogitic clinopyroxene inclusions from Snap Lake and from worldwide. Cr_2O_3 concentrations are generally below detection limits.

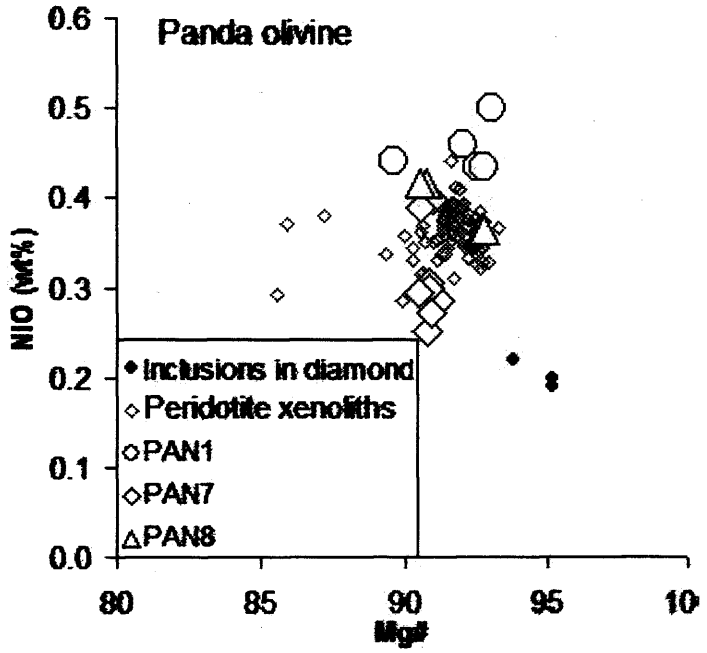

Figure 4.8: Mg# (molar Mg/(Mg + Fe)) verses NiO wt% for olivine inclusions in Panda coated diamonds (large open symbols), gem Panda diamonds (small closed circles) (Tappert et al., 2005) and mantle xenoliths from Panda (small open diamonds) (Menzies et al., 2004).

Peridotitic clinopyroxenes have molar ratios of Mg# = 92.8 to 95.0 and Ca# = 43.8 to 46.7; they have high Cr_2O_3 concentrations (1.2 to 2.9 wt%) and so are Cr-diopsides. Peridotitic clinopyroxene inclusions are classified as lherzolitic on the basic of their Al_2O_3 and Cr_2O_3 compositions (Fig. 4.9). These compositions are less magnesian and more Ca-rich than the world average and overlap both with those of clinopyroxene inclusions in gem diamonds and clinopyroxene inclusions in xenoliths from Panda (Menzies et al., 2004; Tappert et al., 2005).

The Cr-diopside inclusions have Al_2O_3 contents of 0.8 to 2.5 wt% and Na_2O concentrations of 0.7 to 2.3 wt%. Clinopyroxene inclusions in sample PAN3 are compositionally heterogeneous, showing a range of CaO, Al_2O_3, FeO, MgO and Na_2O contents. K_2O concentrations in clinopyroxene inclusions coexisting with KCl brine in the Panda diamond coats are generally below the detection limit (0.05 wt%). Interaction between clinopyroxene and K-rich fluid was suggested to

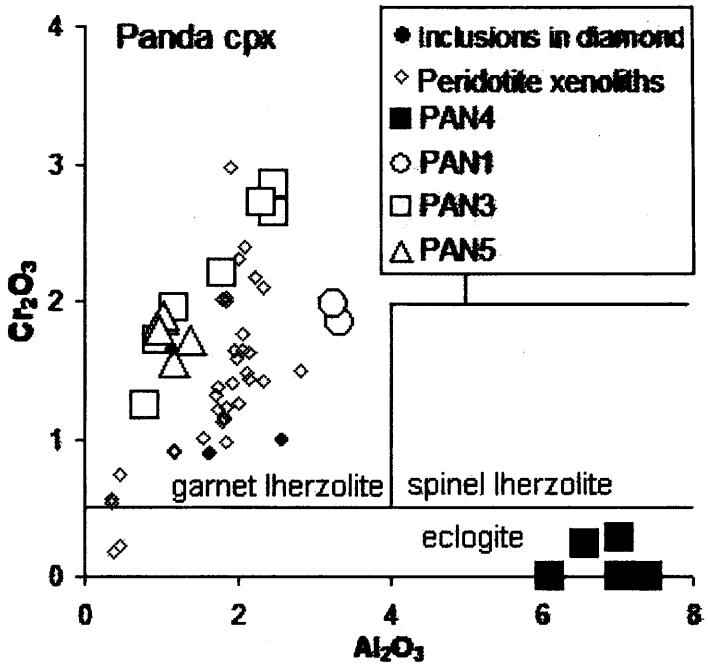

Figure 4.9: Al_2O_3 verses Cr_2O_3 for clinopyroxene inclusions in Panda coated diamonds (large symbols). Also shown are compositions of clinopyroxene inclusions in gem diamonds from Panda, data from Stachel et al. (2003) (closed circles) and mantle xenoliths from Panda (small open diamonds) Menzies et al. (2004).

explain the high K_2O-contents of many clinopyroxenes in mantle xenoliths and as inclusions in diamonds (up to 0.37 wt% in lherzolite (Perchuk et al., 2002) and up to 2 wt% in eclogitic and ultra-high pressure clinopyroxenes (Harlow & Veblen, 1991; Taylor et al., 2000, 1996a)).

4.4.4 Orthopyroxene

Four orthopyroxene inclusions were analysed, all from PAN3. Like the Cr-pyrope and olivine inclusions, orthopyroxenes have relatively low values of Mg# (89.8-92.2). The low Mg# of lherzolitic orthopyroxene is indicative of low source temperatures.

4.4.5 Inclusion Geothermobarometry

We have estimated the temperature of fibrous diamond growth using the non-touching inclusions assemblages in peridotitic samples PAN8 (garnet-olivine; O'Neill 1978, 1980), PAN5 (garnet-clinopyroxene Krogh 1988), PAN1 and PAN5 (enstatite-in-clinopyroxene; Nimis & Taylor 2000). Pressure was estimated using the Cr-in-clinopyroxene barometer of Nimis & Taylor (2000) in samples PAN3 and PAN5. The results are given in figure 4.10 and summarised in table 4.4.

Geothermobarometry indicates that the peridotitic diamond coats grew at an average temperature of 930-1010 $\pm 50^{o}$C and pressures of 4.2 to 4.5 GPa. These conditions are right on the diamond stability line, and overlap with pressure-temperature estimates from xenocrysts in the Panda kimberlite. These temperatures are slightly lower than those calculated for non-touching pairs of inclusions in non-fibrous diamonds from Panda (1061 to 1233^{o}C; Tappert et al. 2005). The calculated PT conditions place the Panda coats on a geotherm of 37 to 40 mW/m^2 (Pollack & Chapman, 1977), this is slightly lower than for world-wide diamond sources, where geothermal gradients of about 40-42 mW/m^2 have been deduced (Boyd & Gurney, 1986; Griffin et al., 1992; Stachel & Harris, 1997a). The geothermal gradient of the diamond coats are similar to the geothermal gradient indicated by touching garnet and orthopyroxene pairs in Panda octahedral diamonds (Stachel et al., 2003; Tappert et al., 2005), which have re-equilibrated to the lower mantle temperatures after entrapment in the diamond.

Compositional disequilibrium in PAN8 leads to wide variations in temperature: calculated temperatures ranging from 730 to 1090^{o}C depending whether low-Mg or high-Mg garnet-olivine pairs were used. The maximum temperature variation calculated within the other samples is $\leq$100^{o}C. This wide range calculated temperature in PAN8 is unlikely to be the true temperature range because it is not recorded in the other samples, more likely this reflects varying degrees of disequilibrium between coexisting minerals.

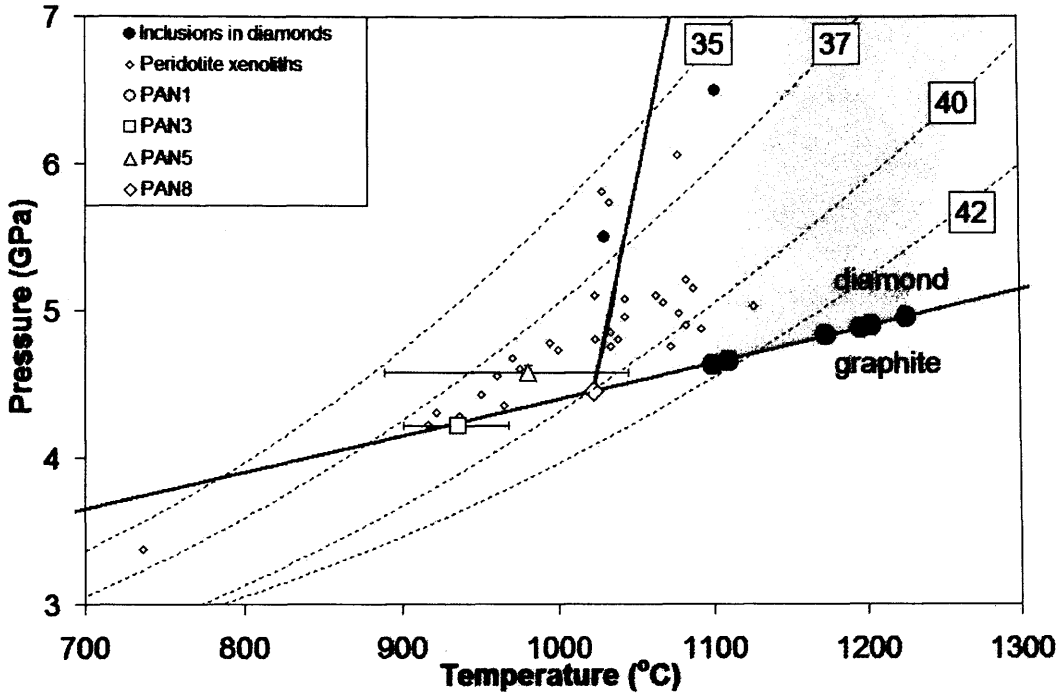

Figure 4.10: Average pressure-temperature conditions of clinopyroxene equilibration in samples PAN3 and PAN5 calculated using the geochermobarometer of Nimis & Taylor (2000) (error bars show the range of conditions calculated using the full range of compositions), and the temperature of PAN8 calculated for a range of pressures (dark grey line) calculated using the garnet-olivine geothermometer of O'Neill (1978, 1980). Black circles are the temperatures of formation of non-touching pairs of garnet-olivine inclusions in gem diamonds from Panda calculated at 5 GPa; the light shaded area represents the range of temperatures at given pressures (Tappert et al., 2005) and of clinopyroxene crystals (solid black circles) in mantle xenoliths from Panda (open diamonds) (Menzies et al., 2004) calculated using Nimis & Taylor (2000). Dashed lines show conductive geotherms (in mW/m^2) for various surface heat flow values are calculated after Pollack & Chapman (1977), the graphite-diamond stability boundary is shown as a solid black line (Berman & Simon, 1955).

4.5 Discussion

4.5.1 Conditions of Fibrous Diamond Growth

The compositions of the silicate inclusions in the Panda diamond coats indicates that fibrous diamond can grow in both peridotitic and eclogitic host rocks. Therefore, fibrous diamonds grow in the same paragenetic environments as octahedral diamonds. Harzburgitic inclusions were not found in the Panda coats, this is in contrast to inclusions in 'normal' Panda diamonds which are dominantly harzburgitic. The absence of harzburgitic inclusions may be a sampling artefact due to the fact that there are only eight Panda coated diamonds in this study; however, harzburgitic inclusions may not be expected in the diamond coats because of the coexisting Ca-rich fluid, which will re-fertilise the host mantle converting harzburgite to lherzolite.

In most models of upper mantle magmatism, garnet lherzolite is the starting material; partial melting and extraction of mafic and ultramafic liquids gives rise to a range of depleted residual rocks ranging from depleted lherzolite to harzburgite (Dawson, 2004). Frey & Green (1973) first proposed the two stage model of primary depletion (to form harzburgite) and secondary re-enrichment for the origin of some lherzolite. O'Hara et al. (1975) added the alternative proposal that once the primitive mantle had been completely freed of garnet and clinopyroxene by partial melting to produce harzburgite, minor amounts of garnet and clinopyroxene were generated by exsolution from orthopyroxene on cooling. While the modal compositions (5-10% garnet, 2-5% diopside) of many garnet lherzolites does suggest that they may be of exsolution origin, metasomatic addition of Ti, Zr, the LREE and Sr is required to account for the high incompatible element compositions (Dawson, 2004). Several authors have proposed an origin of lherzolitic diamond sources through metasomatic enrichment of former harzburgite (e.g. Griffin et al. 1999; Stachel et al. 1998, 2004). Stachel et al. (2004) identified two styles of metasomatic re-enrichment: 1) subsolidus infiltration of strongly fractionated C-H-O fluids with a very high ratio of LREE to MREE, HREE and other HFSE and 2) supersolidus percolation of melts that refertilize the diamond sources both in major and trace elements and that are characterized

by a moderate enrichment of LREE over MREE, HREE and other HFSE. Conversion of harzburgite to lherzolite is accompanied by introduction of increasing modal clinopyroxene which leads to an apparent depletion in LREE relative to harzburgitic garnet (Stachel et al., 2004).

The similarity between the average major element compositions of fluid inclusions in the Mbuji Mayi samples and those in the eclogitic Panda samples suggests that the African diamond coats may also be also eclogitic. This is consistent with the observation of quartz in the infrared spectra of many of these samples (chapter 3) and with high abundance of eclogite xenoliths ($\geq$90%) in the Mbuji Mayi kimberlite (El Fadili & Demaiffe, 1999).

Geothermometry of silicate macro-inclusions indicates that the Panda diamonds grew over a narrow temperature range of 930 to 1010°C. These calculated temperatures from EDS analyses are lower than indicated by inclusions in non-fibrous diamonds from Panda (1100-1250°C; Tappert et al. 2005). These low temperatures have strong implications for the age of the diamond coats. Fibrous diamonds are generally thought to have grown shortly before their entrainment and eruption in kimberlite, on the basis that their nitrogen is only mildly aggregated (type IaA). However, this low degree of aggregation may also be due to storage at low temperatures, as is suggested by the geothermometry of the Panda crystalline inclusions. Diamond growth at lower temperatures may be possible because of the high level of fluid supersaturation, which is consistent with the development of a fibrous morphology. Diamond growth rates in the system carbonate-water varied in the range 1.7 μm/h at 1420°C to 0.10 μm/h at 1150°C (Pal'yanov et al., 2002a). Diamond growth in KCl (Litvin, 2003) and carbonate-KCl (Tomlinson et al., 2004) (chapter 6) exhibit skeletal forms, again testifying to high crystallisation rates in KCl-bearing systems. For the amount of nitrogen present, the low degree of nitrogen aggregation is also consistent with temperatures $\leq$1200°C. The low equilibration temperatures for inclusions in the coated diamonds from Panda suggest fibrous diamond formation occurred in a solid host rock at this location. The dominance of water in the infrared spectra of the inclusions (sections 3.2.2.2 3.2.2.2) and absence of silicate melt in the peridotitic Panda diamond coats, would further support such a growth mechanism. However, whether or not the diamond could form in this way is dependent on

the eutectic of the carbon-bearing fluid in the presence of the other metasomatic components. These parameters are as yet not well understood.

Geobarometry gives calculated equilibration pressures of 4.2-4.6 GPa for Panda coat inclusions. The lack of silicate inclusions in the Mbuji Mayi diamond coats means that geothermometric estimates cannot be made, however the residual internal pressures of the inclusions (1.4 to 1.8 GPa) correspond to formation pressures of 6.4 to 6.8 at 1000°C (Chapter 3). Therefore, both the Panda and Mbuji Mayi diamond coats grew at similar pressures to normal octahedral diamonds.

4.5.2 Nature of the Trapped Fluid

The presence and abundance of fluid inclusions in both the Panda and Mbuji Mayi fibrous diamonds give a clear indication that they had a fluid growth medium. The chemical compositions of these inclusions reveal the presence of three fluid components:

4.5.2.1 Carbonate End-Member

Both the Panda and Mbuji Mayi diamond fluid inclusions contain carbonate, this is the only fluid component that all the fibrous diamonds have in common suggesting that carbonate plays an important role in the growth of these diamonds.

At Panda, both parageneses contain Fe-Mg-Ca carbonate. The similarity between the calculated end-member compositions of carbonate in the peridotitic and eclogitic samples suggests that this fluid was derived externally and percolated through both paragenetic environments. In this scenario, the peridotitic and eclogitic diamond coats grew in the same metasomatic event. The eclogitic carbonates are slightly more enriched in Fe and contain detectable P relative to the peridotitic carbonates, this is probably due to reaction between the carbonate and the eclogite host rock. The compositions of fluid inclusions are a product of metasomatic reactions (and of a diamond precipitating redox reaction, section 3.3.3.2) between an incoming fluid and the host mantle and do not represent the 'original' composition of the fluid percolating through the peridotite and eclogite mantle.

Carbonate in the Mbuji Mayi diamonds varies between calcite and a 50:50 mix of Mg- and Fe-carbonate. Apatite is thought to have been precipitated from the carbonate melt and incorporated into the micro-inclusions as a solid phase, rather than precipitated as a daughter mineral from the trapped fluid.

4.5.2.2 Brine End-Member

The brine end-members are characterised by high K and Cl concentrations and low K/Cl ratios. K/Cl = 0.4 in the Panda brine and 0.8 at Mbuji Mayi, relative to a ratio of 15.2 in the silicate end-member fluid. High K/Cl ratios in diamond brines have previously been attributed to crystallisation of Cl-rich phases (e.g. apatite) in the diamond forming region of the mantle (Johnson et al., 2000). This may be appropriate for the Mbuji Mayi samples which have relatively high concentrations of P and apatite in the infrared spectra. However, apatite fractionation is unlikely to have been influential in forming the Panda fluids because inclusions in the Panda coats have low P concentrations and apatite is not seen in the infrared spectra. Klein-BenDavid et al. (2004) suggests that the carbonatite melt is parental and that this evolves towards a brine composition following crystallisation of carbonate minerals. Extreme fractionation is required to generate Cl-concentrations of up to 60 mol% and strong enrichment in Ba and K. Navon et al. (2004) suggests that both brine and silicte melt may separate from the carbonatite melt by forming two separate immiscible fluids. Each fluid then continues to evolve separately by fractional crystallisation of minerals, including diamond.

All of the above models require the presence of a carbonatite melt. The amount of brine present in the fluid may be a reflection of the degree of carbonatite melt present. This will only occur during late stage crystallisation of the the residual fluid/melt (e.g. chromatographic fractionation distal to the point of fluid/melt input) or at very low degrees of carbonatite partial melting. Therefore, the Panda diamond fluid may be the result of the presence of low degree carbonatite melts, while the Mbuji Mayi fluids represent less fractionated melts. The residual melt may still be mobile, allowing lower K/Cl fluids to continue to permeate into and metasomatise the mantle. Metasomatism by K-rich fluid

containing H_2O, CO_2 and Cl is invoked to explain an alteration assemblage of K-feldspar, calcite, sodalite and djerfisherite in eclogite xenoliths from Udachnaya, Siberia (Misra et al., 2004).

The high K and Cl concentrations of the Mbuji Mayi, and particularly the Panda fluids suggest that the brine was not sourced locally, but from a large volume of the mantle. This is consistent with the similarity between the compositions of brines in the peridotitic and eclogitic Panda diamonds indicating that the fluid percolated through both lithologies. Burgess et al. (2005) measured halogen ratios in coated diamonds from Panda and concluded that high I/Cl and Br/Cl ratios also require the fluids to have acquired halogens from a large volume of the mantle.

4.5.2.3 Silicate End-Member

The low content or absence of a silicate component in the peridotitic Panda fluid and the dominance of water in the infrared spectra of the peridotitic Panda samples (section 3.2.2.2) indicates that pressure-temperature conditions were below or close to the lherzolite + H_2O solidus. This is consistent with the low equilibration temperatures of silicate minerals in the peridotitic Panda coats. It also indicates that the metasomatic carbonate-brine fluid did not have a silicate component. Therefore, the alumnosilicate fluid component in the eclogitic Panda sample was generated locally.

In the eclogitic Panda fluid, the minor silicate component may be due to either: 1) partial melting of the eclogite host rock as a result of the lower temperature of the eclogite + H_2O solidus; or 2) to the greater availability of Al and Si in alumnosilicate minerals in the solid eclogite host rock, which may be liberated by metasomatic reactions between fluid and host rock minerals. In both these scenarios, the silicate fluid component is generated locally. The dominance of water in the infrared spectra of the eclogitic Panda samples (section 3.2.2.2) suggests that conditions were below the eclogite + H_2O solidus, therefore dissolution of Si and Al from the host rock by the trapped fluid is preferred. Ryabchikov & Boettcher (1980); Ryabchikov et al. (1982) have shown that the SiO_2 content of the vapour phase may reach 35 wt% at 3 GPa, 1100°C in the $MgSiO_4$-SiO_2-H_2O system. During experiments at 2 GPa, changes in the fluid H_2O# caused

a increase in the solubility of SiO_2 and a decrease in the solubility of MgO, FeO and CaO (Schneider & Eggler, 1986). Therefore, the intra-diamond compositional variability may reflect fine scale equilibrium as a result of the variable solubility of oxides, depending on the immediate mineralogy and fluid composition. Micro-inclusions in cloudy diamonds from Koffiefontein contain phlogopite or high-Si mica depending on whether the host is peridotitic or eclogitic (Izraeli et al., 2004), supporting the suggestion that Si-fluids may be generated locally by metasomatism. The higher Si and Al content of the eclogitic fluid relative to peridotitic fluids may be due to the fact that the concentrations of these elements is higher in eclogite than in peridotite: this means that more Si and Al will enter the fluid as it equilibrates with the wall rock during reactive chromatographic processes. Experiments in the diamond stability field (at 5 GPa) in the basalt-H_2O system indicate that at up to 1000 °, residual eclogite coexists with a fluid containing 80% H_2O with a nepheline- to quartz-normative, peralkaline character (Kessel et al., 2005). This fluid may be a source of Si, Al and K in the diamond micro-inclusions. The eclogite+ H_2O solidus lies between 1000 and 1050°C but terminates at a second critical endpoint between 5 and 6 GPa; both the hydrous melt and the supercritical liquid evolve from rhyolitic to trachytic/andesitic with increasing liquid fraction (Kessel et al., 2005). Therefore, the trapped fluid composition is more consistent with the sub-solidus scenario than with a hydrous basalt melt.

The high concentration of the silicate end-member in the Mbuji Mayi fluid may be generated locally by reaction with the host mantle or partial melting of the host rock. However, detailed infrared spectroscopy of Mbuji Mayi sample MM10 (section 3.3) indicated that quenched silicate melt is absent in this sample, whose inclusions contain a high concentration of the silicate end-member fluid in EMPA. Therefore, a reaction mechanism is favoured to explain the presence of the silicate end-member. These reactions may have led to the precipitation of secondary phlogopite (and quartz from infrared, section 3.2.2.2) which may then have been incorporated into the micro-inclusions. Alternatively, these minerals may have been precipitated directly from the carbonate melt, in which case their presence reflects differences in the composition of the metasomatic fluid between Panda and Mbuji Mayi.

4.5.3 Origin of the Trapped Fluid

Schrauder & Navon (1994) suggested three models to explain the range of fluids observed in fibrous diamonds from Botswana:

1. Partial melting of carbonated source rock
2. Fractional crystallisation
3. Mixing between hydrous silicate fluid and carbonatite melt

4.5.3.1 Partial Melting

Mantle carbonate melts may be formed locally by solidus and low-degree partial melting of carbonated lherzolite (Dalton & Presnall, 1998; Moore & Wood, 1998) and carbonated eclogite (Yaxley & Brey, 2004). In these experiments, higher degrees of partial melting lead to more silicate-rich melt compositions (Dalton & Presnall, 1998; Moore & Wood, 1998; Yaxley & Brey, 2004). According to this model, higher Si and Al concentrations in the Mbuji Mayi and eclogitic Panda samples would reflect higher degrees of partial melting, or may be a reflection of the higher Si and Al content of the eclogite protolith. However, the similarity between carbonate and brine in the eclogitic and peridotitic Panda samples indicates that this fluid was not derived locally. The Mg# of the peridotitic Panda fluid ($\approx$0.42) is too low to be in equilibrium with mantle minerals. Experimental carbonatite melt and hydrous fluid in equilibrium with peridotite at lower pressures have Mg# of 0.85 and 0.78 respectively (Schneider & Eggler, 1986). This suggests that the fluid was not produced by low degree partial melting. Finally, the extreme K and Cl enrichment (up to 60 mol% Cl) in the Panda samples is also unlikely to be generated locally by partial melting. Therefore, it is considered unlikely that the trapped fluid in the Mbuji Mayi and Panda fibrous diamonds formed locally by partial melting of a carbonated host rock.

4.5.3.2 Fractional Crystallisation

In the fractionation model of Schrauder & Navon (1994) a silicate melt, similar to the Si-Al-K end-member fluid, crystallises silicate minerals and leaves a

residual volatile- and incompatible-rich carbonate melt. The lack of a silicate component in the Panda samples and silicate melt in MM10 indicates that the inclusion contents are not igneous precipitates from silicate melt. Furthermore, fractional crystallisation of silicates is unlikely to generate the linear correlations seen between all major elements in the individual inclusion data.

Klein-BenDavid et al. (2004); Navon et al. (2004); Schrauder & Navon (1994) suggest that the 3 end-member fluids may be derived by fractionation of carbonate and apatite from carbonatite melt and by the subsequent separation of residual melt into two immiscible fluids: brine and hydrous-silicate melt. This is based on the observations of Izraeli et al. (2001); Klein-BenDavid et al. (2002); Navon et al. (1988); Schrauder & Navon (1994) that, while carbonate is present in all samples, silicate melts and brine were never detected together in any single diamond and no mixing lines were observed between these end-members. However, this study has shown that the Si-Al-rich Mbuji Mayi samples do also contain a component of KCl.

Fractional crystallisation of an incoming carbonate fluid is a viable means of generating the continuous compositional array between the carbonatite melt and KCl brine. Johnson (1991) provides experimental evidence that CO_2 and H_2O-NaCl liquid are immiscible up to high temperatures (940oC) at 7.5 kbar in the CO_2-H_2O-NaCl at moderate to low salinities (>23 wt%). However, there is no experimental evidence at higher pressures, however mixed CO_2-H_2O-NaCl fluid and a silicate/silicocarbonatite melt in natural fluid inclusions in spinel harzburgite and lherzolite xenoliths from Tenerife were attributed to the separation and heterogeneous trapping of the original siliceous carbonatite melt by Frezzotti et al. (2002). The effect of water and chloride on carbonate is not constrained by experiments. It may, however, be assumed that sodium will, to some extent, be partitioned into a supercritical CO_2-H_2O-(K,Na)Cl fluid, and that the carbonate melt will be correspondingly enriched in $CaCO_3$, $FeCO_3$ and $MgCO_3$, once a water-bearing brine has formed.

Fractional crystallisation does not require the residual fluid to be in equilibrium with host rock, instead it is in equilibrium with mineral precipitates. This local equilibrium allows for the intra-diamond scale compositional variability observed in both sample sets. It is unlikely that the fractional crystallisation of

carbonate minerals generated the silicate end-member fluid seen in the eclogitic Panda sample, because the silicate component is not observed in the peridotitic sample and so is not though to be present in the parental fluid. However, this process cannot be ruled out for the Mbuji Mayi samples if the metasomatic fluid was more enriched in Si.

4.5.4 End-Member Mixing

Mixing between carbonate and silicate melts (Schrauder et al., 1996) does not explain the observed range of fluids, because Si-rich sample MM1 does not contain silicate melt. However, mixing between externally derived carbonate melt and a locally derived silicate component may explain the linear variation exhibited between Si and the other major elements in the Mbuji Mayi and eclogitic Panda diamond fluids. A mixing model is supported by the negative linear relationship between Si and the incompatible elements observed by Schrauder et al. (1996).

4.5.5 Origin of the Panda Silicates

Navon (1991) suggested that silicate inclusions in diamond coats may be part of the the kimberlite megacryst suite. However, the present evidence shows that the silicate inclusions are more magnesian than equivalent minerals in the kimberlite megacryst suite, and additionally, that both peridotitic and eclogitic mineral inclusions are observed. Thus, fibrous diamond growth does not appear to be related to the formation of the megacryst suite.

The silicate macro-inclusions in the Panda diamond coats may either be secondary minerals precipitated from the trapped fluid, or protogenetic inclusions from the mantle host. In the first instance, the silicate inclusions would have crystallised from the fluid in the early stages of chromatographic fractionation e.g. in the vein or proximal wall rock. This study has established that the inclusions do not contain silicate melt, but solute-rich aqueous fluid and carbonate. Therefore,garnet, pyroxene and olivine crystallised from the carbonate melt. However, the precipitation of demonstrably peridotitic and eclogitic minerals from carbonatite melt is not expected. Unlike the macro-inclusions, olivine and clinopyroxene

within the micro-inclusions may have been precipitated directly from the carbonate melt.

The second possibility is that the silicate macro-inclusions are protogenetic. In this scenario, the diamond coat inclusions may be compared with equivalent minerals in octahedral diamonds from Panda. The low Mg# of lherzolitic orthopyroxene is indicative of low source temperatures, this is corroborated by low calculated equilibration temperatures (930 to 1010°C). These temperatures are lower than inclusions in non-fibrous diamonds from Panda (1100-1250°C; Tappert et al. 2005). This shift may imply that the source region underwent cooling by about 200°C between the time of octahedral and fibrous diamond formation. Tappert et al. (2005) suggest that the high temperatures during gem diamond growth are a transient feature. Transient heating of the cratonic mantle may be due to a rising plume, or a result of a high geothermal gradient due to proximity to the lithosphere-asthenosphere boundary. Bedini et al. (1997) suggests that metasomatic agents are formed during reaction between plume derived melts and lithospheric peridotities. In this model, the plume causes thermomechanical erosion of the mantle lithosphere enabling infiltration of basaltic melts, which then react with peridotities. Reaction occurs at decreasing melt masses, generating small fractions of volatile rich residual melt (including carbonatite) because of the conductive thermal gradient; these melts have low viscosity and solidification tempertures and migrated upwards and infiltrate lithosphere perisotites (Bedini et al., 1997).

The relatively low Mg# of garnet and olivine in the coat are indicative of a high source fertility. The coat inclusions extend the compositional range of Panda diamond inclusion compositions from relatively undepleted inclusions in gem diamonds to more fertile Fe- and Ca-rich compositions (lower Mg# and higher Ca#). When compared to the composition of the trapped fluid (Fig 4.11), it can be seen that the compositions of garnet, olivine and orthopyroxene inclusions in the diamond coat trend away from the composition of equivalent minerals in gem diamond moving in the direction of the composition of the trapped fluid. This suggests that these samples provide a snap-shot of mantle metasomatism. This is consistent with the disequilibrium observed between inclusions in individual diamonds e.g. garnet in PAN8 and clinopyroxene in PAN3. This heterogeneity

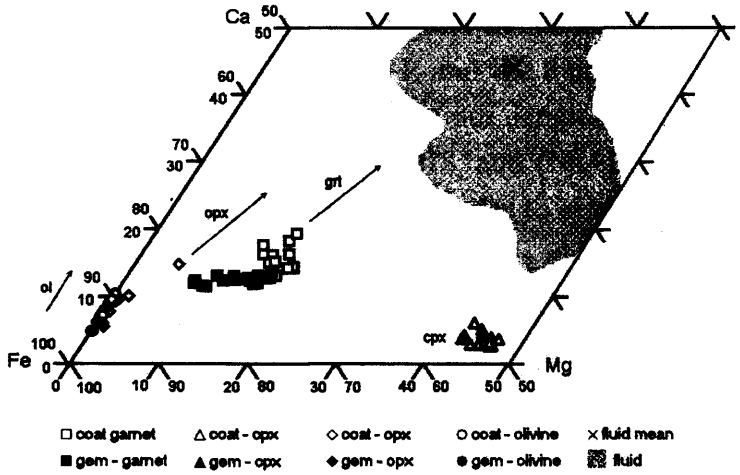

Figure 4.11: Ternary diagram showing the compositions of garnet (squares), olivine (circles), orthopyroxene (diamonds) and clinopyroxene (triangles) inclusions in gem diamonds (grey-filled symbols) (Stachel et al., 2003; Tappert et al., 2005) and the fibrous diamond coats (open symbols) and of the average fluid composition (cross) and field of measured fluid compositions (grey filled area) in micro-inclusions in the coat. Garnet, opx and olivine in the diamond coat trend away from the composition of equivalent minerals in gem diamond in the direction of the trapped fluid composition.

is not thought to reflect contamination during sample preparation because the compositions of garnet and clinopyroxene in other samples are uniform. The lack of zoning and truncation in the CL image indicates that the diamond coats grew in a single event. This is also unlikely to be due to changes in temperature over the course of diamond growth, because the fibrous morphology indicates that the diamond coats grew rapidly. Therefore, it is thought that this is a mantle feature possibly reflecting disequilibrium between the trapped fluid and clinopyroxene. Rapid growth is required to preserve such chemical disequilibrium. Therefore, non-equilibrium between co-existing phases is more likely to be due to varying degrees of equilibrium during metasomatism.

4.6 Summary of EMPA Study

Fluid inclusions in the Mbuji Mayi and Panda diamond coat populations are distinctly different, but contain the similar end-member fluids: 1) Fe-Mg-Ca car-

bonate, 2) K-rich alumnosilicate, 3) K-Cl brine. In the Mbuji Mayi samples, the carbonate end-member is also enriched in P and the fluid compositions vary between carbonate and alumnosilicate with a minor component of KCl. The K/Cl molar ratio of the high-Cl end-member is 0.78, and (Na+K)/Cl close to 1. The bulk composition of the Mbuji Mayi fluid is similar to eclogite (except for strong enrichment in K and Cl relative to eclogite) and is also similar to the fluid in the eclogitic Panda sample. In the absence of more conclusive evidense, this may suggest that the Mbuji Mayi diamond coats may also be also eclogitic. This is consistent with the high abundance of eclogite xenoliths ($\geq$90%) in the Mbuji Mayi kimberlite (El Fadili & Demaiffe, 1999).

The Panda coats are dominated by brine and Ca-Fe-Mg carbonate. All inclusions are also enriched in Ba. The average K/Cl molar ratio of the fluid is 0.4 to 0.5, indicating much higher Cl-contents than in the African samples. The calculated end-member compositions of carbonate are similar for both the peridotitic and eclogitic samples. This suggests that the parental fluid was derived externally and percolated through both paragenetic environments. In this scenario, the peridotitic and eclogitic diamond coats grew in the same metasomatic event. Peridotitic Panda samples contain low to zero concentrations of the Si-Al end-member; eclogitic samples contain higher concentrations of Si-Al fluid and bear a closer resemblance to the Mbuji Mayi fluid. This suggests that the Si-Al fluid is derived locally in the eclogite host rock.

It is thought that the observed fluid composition is the result of fractional crystallisation of an incoming metasomatic carbonate melt. This led to an array of fluid compositions between carbonate and KCl brine. Reactions between this fluid an the minerals of the host rock led to the generation of a Si-Al fluid component, particularly in the eclogite paragenesis.

In addition to micro-fluid inclusions, the Panda coats contain macro-inclusions of olivine, garnet, orthopyroxene and clinopyroxene. Both peridotitic (lherzolitic) and eclogitic suite minerals are represented, therefore fibrous diamonds grow in the same paragenetic environments as octahedral diamonds. The inclusions are small, euhedral and numerous. Equilibration temperatures of inclusions in the diamond coats (930 to 1010°C) are lower than indicated by inclusions in non-fibrous diamonds from Panda (1100-1250°C; Tappert et al. 2005). This suggests

that the low degree of nitrogen aggregation seen in fibrous diamond (IaA) may be due to temperatures, and therefore the diamond coats are not necessarily young. The inclusions indicate a more fertile source mantle than for the growth of octahedral diamond at Panda. They have lower Mg# and higher Ca# values than equivalent phases in gem diamonds. The inclusion compositions are more similar to xenocrysts from the Panda kimberlite. The inclusion compositions trend away from their equivalent gem diamond inclusion compositions in the direction of the trapped fluid phase, suggesting growth during a metasomatic event.

Chapter 5

Trace Element Composition

5.1 Introduction

Here I report trace element compositions of both the core and coat of six coated diamonds from the Mbuji Mayi sample set analysed by laser ablation inductively coupled plasma mass spectrometry (LA-ICP-MS). Unfortunately, this study was completed before the Panda samples were received. Most of the impurities measured reside in micro-inclusions rather than in lattice sites, even in the gem quality diamond cores. The novelty of this work is in the determination of the composition of the fluid from which the cores have grown. Fluid compositions for diamond coats have been determined by Schrauder et al. (1996) by instrumental neutron activation analysis (INAA). However, this work does add to the small database and serves as a useful comparison between LA-ICP-MS and INAA. This chapter also address the question of whether there is a genetic relationship between the coat fluid and kimberlite magma.

Bibby (1982); Fesq et al. (1975) used INAA to study the geochemistry of 1500 non-fibrous diamonds from South Africa, concluding that diamond contained submicroscopic mineral and melt inclusions. Subsequently, Damarupurshad et al. (1997) showed that eclogitic diamonds are characterized by high Sc/Cr ratios $\geq$0.02, and are enriched in Fe, Mn, Na, Ca, K, Ga, Au and heavy rare earth elements relative to peridotitic diamonds; while peridotitic diamonds are enriched in Ni, Co, Ir and the light rare earth elements. The compositions of inclusions in fibrous diamonds have also been analysed by INAA, (Schrauder et al., 1996)

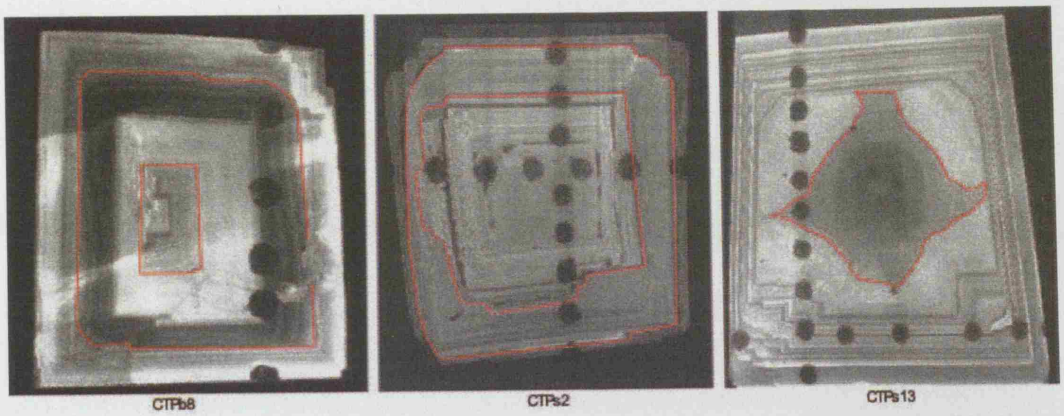

Figure 5.1: Cathodoluminescense image of DRC diamond cores showing location of laser ablation pits relative to oscillatory growth zoning. Red lines delineate growth zones defined by truncated zoning. Ablation pits are 120μm in diameter.

found that incompatible element concentrations in the trapped fluid are higher than in mantle minerals and in melt inclusions, and that carbonate-rich fluids are enriched in incompatible elements over hydrous fluids by 2 orders of magnitude.

LA-ICP-MS is a relatively new technique in diamond research. Resano et al. (2003) have demonstrated the capability of LA-ICP-MS for analysing trace impurities in diamonds, in order to use geochemically fingerprint diamonds from different geographic sources. This work is of interest to government and non-governmental organisations hoping to recognise diamonds from conflict regions and remove them from the diamond market. Rege et al. (2003) used LA-ICP-MS to analyse peridotitic and eclogitic diamonds from worldwide sources. Both paragenesis show rare earth element patterns that are generally flatter than in fibrous diamonds and show wide geographical variation. Wang et al. (2003a) analysed the trace element composition a large coated diamond from the DRC by LA-ICP-MS. These authors detected high concentrations of Ba, Sr, Zr and light rare earth in the coat, but none of these elements were detected in the core.

ICP-mass spectrometer	
RF power	1200 W
Plasma Ar flow rate	17 L min^{-1}
Auxillary Ar flow rate	1.2 L min^{-1}
Carrier Ar flow rate	1.3 L min^{-1}
Sampling cone and skimmer	Pt
Lens voltage	6.25 v
laser ablation unit	
Output energy	200 mJ
Frequency	20 Hz
Spot size	120 μm
Number of cleaning pulses	10
Number of analytical pulses	600
Ablation time	30 s

Table 5.1: Instrumental operating conditions for LA-ICP-MS analyses.

5.2 Analytical Method

5.2.1 Samples

Five DRC coated diamonds were selected on the basis of high inclusion content (from Ft-ir spectroscopy): CTBb8, CTPs14, CTPs13, CTPs2, CDR3. The diamond cores record numerous growth events, distinguished by truncated zoning due to resorption and overgrowth (as can be seen in Fig. 5.1). Samples were cleaned in concentrated H_2SO_4 and rinsed with Milli-Q water prior to analysis.

5.2.2 Apparatus

Trace element compositions were analysed by Laser Ablation Inductively Coupled Plasma Mass Spectrometry (LA-ICP-MS) at Ghent University, Belgium. The instrument used was a Perkin-Elmer SCIEX Elan 6100 quadropole based ICP-MS, equipped with a Lambda Physik COMPex 100 excimer laser and a GeoLas illumination system. The excimer laser operates at a wavelength of 193 nm and uses a gas mixture of Ar with 5% F_2 and small amounts of Ne. Analyses were performed by Isabel De Schrijver, Ghent University.

5.2.3 Analytical Procedure

In view of the low trace element concentrations in diamond, the maximum spot size (120 m), the maximum frequency (20 Hz) and the maximum attainable

energy (200 mJ energy output, which is reduced to 2.5 mJ on the substrate due to absorption of radiation through the optical path) were used. Other parameters were optimised on a daily basis, selected settings are shown in table 5.1. The optimal ablation time is a trade off between: 1) the need for long ablation times to reduce elemental detection limits, and 2) the need for short ablation periods to minimise the reduction in signal intensity that occurs over during ablation. A time of 30 s (600 shots) was considered appropriate; the stability of the ^{13}C in figure 5.2 (RSD$\approx$10%) shows that it is possible to achieve controlled ablation of the sample over a period of 30 s. Surface contamination was avoided by cleaning the sample surface with 10 laser pulses before counting. Ablation generated sharp craters 45 - 50 μm in depth. The ability to produce a regular, flat bottomed crater is due to the high absorption of diamond in the far-UV region and the homogenous beam profile of the 193 nm system (Resano et al., 2003).

UV-LA-ICP-MS is used to analyse elements with atomic numbers greater than 12 that occur in low concentrations. The following isotopes were analysed in the coated diamonds: ^{23}Na, ^{27}Al, ^{39}K, ^{45}Sc, ^{47}Ti, ^{55}Mn, ^{57}Fe, ^{58}Ni, ^{59}Co, ^{69}Ga, ^{88}Sr, ^{90}Zr, ^{93}Nb, ^{138}Ba, ^{139}La, ^{181}Ta and ^{238}U. Masses 57 and 58 are subject to interference from Ar-O molecular species (e.g. $ArO(H)^+$) in the carrier gas (e.g. $^{18}O+^{40}Ar$, $^{17}O+^{40}Ar$), however only ^{58}Ni is likely to be significantly affected by such interference because the natural abundances of ^{17}O, ^{16}O, ^{36}Ar and ^{38}Ar are $\leq$0.4%. We have corrected for the effect of this contribution by subtracting the gas blank, which was measured for 30 s prior to ablation.

The 120 μm sample spot encompassed a multitude of micro-inclusions, therefore this is a bulk analytical technique. Traverses were taken across each specimen, with at least 4 sample positions in each coat and core. An example of a time-resolved plot of the raw data is shown in figure 5.2. Data collected from ablation pits straddling fractures or the core-coat boundary were discarded. The median of the 4+ analysis in each sample region (core or coat) was taken as the representative value for that region; the median was used in preference to the mean in order to minimise the possible influence of outliers. The full dataset is given in table A.2.

A halo of redeposited particles appears around the crater following ablation of the diamond cores (non-fibrous). Resano et al. (2003) have analysed the

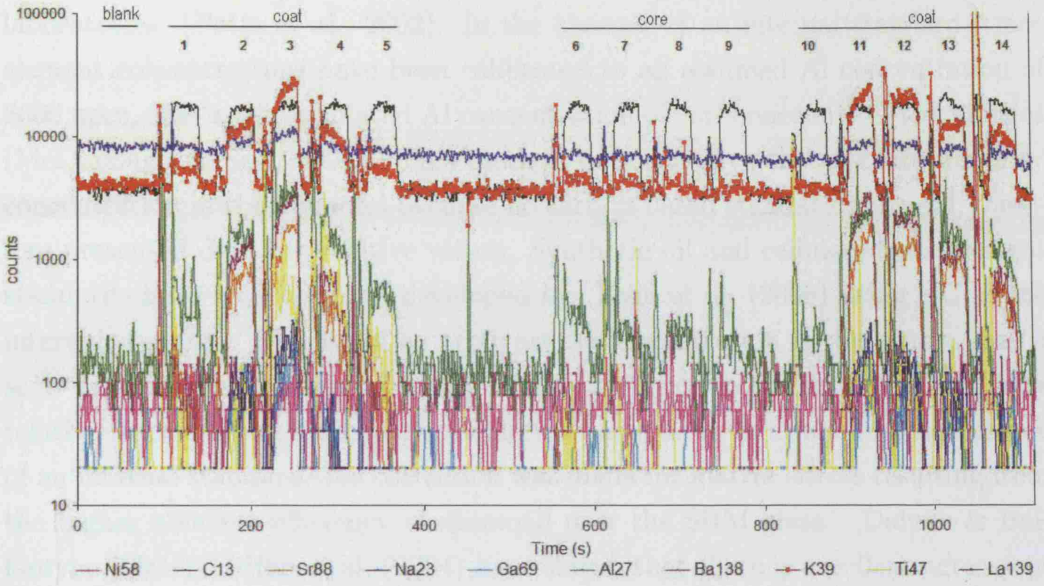

Figure 5.2: Time resolved output from analysis along traverse C of sample CTPs2. The plot starts with 30 s of counting on the gas blank, each spot is then ablated for 30 s. Each analysis is preceded by a sharp peak, this is due to pre-ablation cleaning of the sample spot.

structure of these deposits by micro-raman spectrometry and conclude that it is micro-crystalline graphite or nano-crystalline carbon. This carbon halo does not form during ablation of the fibrous diamond coat, possibly due to the high oxygen content of inclusions in the coat.

5.2.4 Standards and Calibration

Prior to sample analysis, the NIST Standard Reference Material 612 (glass) was analysed at the same operating conditions as the diamond analysis. This was used to correct for possible sensitivity variations during different laser ablation sessions.

In calculating trace element concentrations, all impurities are assumed to be located in micro-inclusions and not in the diamond lattice. LA-ICP-MS intensities (I, in counts per second) were calibrated to element concentrations (in ppm) using NIST Standard Reference Material (SRM) 612 (equation 6.1) and the G-PROBE1 glass, a silicate glass designed as an international proficiency test for microprobe

laboratories (Potts et al., 2002). In the absence of an internal standard, trace element concentrations have been calibrated to an assumed Al concentration of 8600 ppm, this is the estimated Al concentration of carbonaceous (CI) chondrites (McDonough & Sun, 1995). This method does not give the absolute impurity concentration in the diamond because no carbon-based standard was used, therefore presented data are relative values. Synthetic oil and cellulose trace element standards have recently been developed by Rege et al. (2005) using ^{13}C as the internal standard. The use of an arbitrary Al concentration in this study, gives a semi-quantitative estimate of composition of inclusion in the diamond and allows relative trace element enrichment/depletion patterns to be studied in the absence of an internal standard. No correction was made for matrix effects resulting from the higher ablation efficiency of diamond over the SRM glass. Dalphe & Ballantyne (2004); Griffin et al. (2004) have shown that there is excellent agreement between results derived calibration with carbon standards (cellulose and oil) and calibration using the NIST612 glass, indicating that matrix effects are not too significant.

$$Conc^{element}_{sample} = \left[\frac{\left(\frac{I^{element}_{sample}}{I^{Al}_{sample}}\right) \times Conc^{Al}_{sample}}{\left(\frac{I^{element}_{NIST}}{I^{Al}_{NIST}}\right) \times \left(\frac{Conc^{Al}_{NIST}}{Conc^{element}_{NIST}}\right)} \right] \tag{5.1}$$

With this method of calculation, the analytical error on the concentration of each element is dependent on the absolute abundance of Al at a given ablation spot. The errors presented in table 5.2 (core fluid data) and table 5.3 (coat fluid data) are calculated using the average Al intensity in those regions; this gives higher errors for the core fluid than the coat fluid. An element may be below the detection limit because either it has a low concentration in the fluid, or the fluid inclusion density is low at the sampled point.

5.3 Results

The compositions of inclusions in the diamond cores (Fig. 5.3a) and coats (Fig. 5.3b) show a general 2-4 fold enrichment in incompatible elements (Ba, U, Nb, Ta, La,

sample	spot	Na	K	Sc	Ti	Mn	Fe	Co	Ni	Ga	Sr	Zr	Nb	Ba	La	Ta	U
CTPb8	average	9312	11545	3837	5215	nd	6708	102	2068	84	385	90	50	276	62	nd	nd
	8a	nd	16197	3325	3103	nd	nd	nd	nd	69	1016	na	nd	2840	143	na	na
	9a	nd	9959	4305	nd	nd	13567	147	3439	99	424	na	nd	1765	55	na	na
	10a	7090	13131	3369	4093	nd	6708	76	1169	126	385	na	56	312	62	na	na
	11a	11535	1305	5216	6337	nd	3461	61	1129	55	83	na	43	241	43	na	na
	1d	nd	nd	nd	nd	nd	5402	nd	nd	nd	nd	90	nd	46	68	nd	nd
	2d	nd	nd	nd	15738	nd	11083	128	2967	nd	222	nd	nd	175	nd	nd	nd
CTPs13	average	5990	14593	630	34642	nd	3450	29	525	14	69	218	23	137	31	27	31
	2a	2330	nd	396	39503	nd	601	30	nd	nd	67	na	19	451	38	na	na
	3a	nd	nd	984	23572	nd	5731	nd	nd	nd	68	na	25	152	29	na	na
	4a	nd	nd	807	40889	nd	3376	28	nd	nd	70	na	nd	78	nd	na	na
	5a	nd	nd	966	63937	nd	4682	36	nd	nd	46	na	nd	42	26	na	na
	6a	nd	nd	1117	29621	nd	3524	nd	nd	nd	41	na	nd	15	8	na	na
	8a	7010	8418	nd	71142	nd	nd	38	nd	nd	176	na	12	26	nd	na	na
	9a	3000	4713	120	15987	nd	447	12	194	14	nd	na	16	138	9	na	na
	10a	4993	14635	596	9558	nd	1600	24	913	nd	nd	na	46	118	nd	na	na
	11a	29932	25008	359	5499	nd	nd	21	681	37	342	na	13	2324	95	na	na
	3c	12172	21809	374	64566	nd	nd	nd	nd	nd	nd	na	22	282	nd	na	na
	4c	5990	14842	2553	53306	nd	nd	nd	46	nd	nd	na	nd	224	nd	na	na
	5c	615	5591	561	34642	nd	nd	nd	nd	nd	nd	na	46	103	nd	na	na
	6c	1901	9157	665	74276	nd	nd	nd	370	nd	nd	na	27	119	nd	na	na
	3d	16106	31337	nd	23122	nd	20074	327	8570	nd	341	nd	nd	1507	77	27	46
	4d	8742	14552	nd	15372	nd	nd	nd	nd	14	nd	218	27	137	33	nd	16
CTPs2	average	2910	10731	3216	7933	nd	8962	117	3081	86	101	251	25	45	11	13	8
	5a	nd	10731	1362	32707	nd	nd	nd	nd	nd	nd	na	37	nd	nd	na	na
	6a	4394	11597	2606	7991	nd	nd	89	707	33	223	na	19	420	21	na	na
	7a	1425	10977	2064	30203	nd	6274	70	3081	103	41	na	nd	45	nd	na	na
	8a	1038	14753	4998	1424	nd	9273	117	3265	20	20	na	37	117	nd	na	na
	9a	nd	7168	6918	7874	nd	8650	154	2442	86	nd	na	49	nd	110	na	na
	10a	nd	6443	3826	3518	nd	15427	nd	3534	90	nd	na	nd	37	47	na	na
	1d	774	545	nd	nd	nd	nd	5	nd	nd	nd	nd	nd	nd	nd	1	nd
	2d	74097	26636	nd	23525	nd	nd	126	nd	nd	519	nd	nd	17	nd	57	16
	3d	120590	10182	nd	3489	nd	nd	182	nd	nd	160	251	52	62	nd	13	nd

Table 5.2: DRC Diamond core trace element data analysed by LA-ICP-MS and normalised to an Al concentration of 8600 ppm (Carbonaceous chondrites; McDonough & Sun 1995). Data for individual sample spots is given along with the sample medium taken to be the bulk composition of the micro-inclusions (highlighted grey). Abbreviations: na - not analysed, nd - not detected.

sample	spot	Na	K	Sc	Ti	Mn	Fe	Co	Ni	Ga	Sr	Zr	Nb	Ba	La	Ta	U
CTPb8	average	4543	22330	357	3404	nd	12245	14	198	87	1877	156	45	5038	382	nd	20
	1a	1411	7418	818	2816	nd	nd	33	nd	45	479	na	44	1646	100	na	na
	2a	4524	16233	841	5792	nd	nd	9	231	76	2089	na	121	5689	434	na	na
	3a	3039	12589	1259	3923	nd	nd	nd	nd	89	1877	na	134	3778	367	na	na
	4a	5349	19517	524	4400	nd	nd	nd	222	78	2591	na	110	5424	449	na	na
	5a	4722	22330	769	3970	nd	nd	8	71	84	2328	na	43	5228	392	na	na
	6a	2751	23230	191	2425	nd	nd	19	111	87	1915	na	12	5038	400	na	na
	7a	2616	23232	333	3268	nd	nd	7	30	119	1787	na	14	6383	363	na	na
	12a	4543	25493	181	2877	nd	nd	nd	198	143	1993	na	35	7229	401	na	na
	13a	7019	28231	222	3002	nd	nd	nd	202	87	1850	na	25	4952	373	na	na
	14a	5416	23514	357	2705	nd	nd	24	419	87	2172	na	51	4851	382	na	na
	15a	5551	22478	354	5016	nd	nd	25	111	142	2779	na	73	5805	432	na	na
	16a	5357	29139	755	4061	nd	nd	nd	291	88	1658	na	63	3078	271	na	na
	17a	2027	6521	466	nd	nd	nd	5	168	34	584	na	45	1093	70	na	na
	3d	nd	19453	43	3540	nd	14923	nd	nd	324	1849	216	45	6802	390	nd	29
	4d	nd	5861	26	1805	nd	9567	nd	nd	104	1146	96	25	2651	213	nd	10
CTPs13	average	1117	17261	217	12182	147	5275	6	77	33	154	118	24	1781	100	1	4
	1a	2492	617	283	16264	nd	nd	10	nd	24	212	na	12	1735	88	na	na
	12a	1121	17601	30	4605	nd	nd	5	76	34	153	na	nd	1840	101	na	na
	1c	836	17911	37	3006	nd	nd	nd	62	32	155	na	nd	1846	99	na	na
	2c	839	38645	378	18896	nd	nd	nd	nd	31	149	na	20	1462	71	na	na
	6c	1901	9157	665	74276	nd	nd	nd	370	nd	43	na	27	119	nd	na	na
	7c	835	20322	150	8100	nd	nd	6	126	36	219	na	nd	1827	105	na	na
	1d	3434	5396	nd	68990	214	1742	nd	54	nd	136	38	41	135	nd	1	1
	2d	1113	16921	nd	3529	79	8808	6	78	125	281	198	nd	2553	131	nd	8
CTPs2	average	1948	15239	435	6450	nd	11585	15	287	81	1815	197	48	4195	330	5	50
	1a	nd	11533	171	19111	nd	nd	nd	937	nd	911	na	40	1646	75	na	na
	2a	1778	14450	nd	2758	nd	nd	nd	329	76	1578	na	28	4148	335	na	na
	3a	1876	15546	nd	13565	nd	nd	nd	92	71	1363	na	16	4243	324	na	na
	4a	174	11678	302	42005	nd	nd	nd	323	18	815	na	48	2099	118	na	na
	11a	2273	22380	321	6111	nd	nd	nd	251	100	2086	na	nd	6625	424	na	na
	12a	2292	22109	349	3705	nd	nd	10	252	81	1929	na	23	5393	339	na	na
	13a	1948	14931	520	3050	nd	nd	9	228	58	1818	na	73	3754	277	na	na
	14a	1336	19261	654	3466	nd	nd	15	642	78	1731	na	78	3544	213	na	na
	2c	nd	52076	795	6789	nd	nd	nd	nd	266	4502	na	nd	12513	873	na	na
	9c	nd	69658	3979	18042	nd	nd	nd	nd	461	8758	na	nd	21585	1892	na	na
	4d	7647	6659	nd	19297	nd	9621	96	nd	159	1812	209	144	3932	251	5	49
	5d	4431	13873	nd	5955	nd	13549	30	nd	237	2820	184	99	6184	441	4	51
CTPs14	average	3221	17198	21	4113	nd	10958	19	178	203	1597	391	15	4418	298	1	15
	1a	2187	14813	21	2768	nd	8412	19	180	317	1066	459	nd	6738	222	1	22
	2a	2824	17625	35	3794	nd	11284	nd	218	195	1638	391	12	4405	319	1	18
	3a	3475	17403	53	5062	nd	13529	nd	188	230	1797	364	14	4584	375	1	26
	4a	3414	16993	19	4474	nd	11856	nd	95	195	1613	392	18	4421	339	2	12
	5a	3028	16326	nd	4121	nd	10088	nd	176	202	1430	399	22	4264	279	nd	9
	6a	3618	17905	20	4106	nd	10633	nd	98	204	1581	280	15	4077	248	2	3
CDR3	average	2553	2467	38	3166	nd	nd	20	137	90	3899	na	89	7039	498	na	na
	1a	1863	2198	38	2213	nd	nd	nd	111	21	2286	na	86	5679	397	na	na
	2a	2621	2702	nd	3397	nd	nd	23	105	28	3194	na	145	8001	535	na	na
	3a	2486	2231	nd	2935	nd	nd	15	164	14	2605	na	78	6070	458	na	na
	4a	3299	3063	nd	3431	nd	nd	20	489	20	3526	na	85	8046	590	na	na

Table 5.3: DRC Diamond coat trace element data analysed by LA-ICP-MS and normalised to an Al concentration of 8600 ppm (Carbonaceous chondrites; McDonough & Sun 1995). Data for individual sample spots is given along with the sample medium taken to be the bulk composition of the micro-inclusions (highlighted grey). Abbreviations: na - not analysed, nd - not detected.

Sr, Zr) relative to major elements (Na, Al, Fe) when normalised to CI chondritic meteorites (McDonough & Sun, 1995). This high level of enrichment is unlikely to be due to the entrapment of mantle minerals and is more consistent with the presence of a fluid or quenched melt in the inclusions. Fesq et al. (1975) referred to such sub-microscopic inclusions as "magma droplets". On cooling, daughter minerals may precipitate from this quenched fluid (e.g. quartz, apatite and carbonate seen in the Ft-ir spectra) and a trapped melt will quench to glass and may crystallise mineral phases. However this will not alter the bulk composition of the inclusions.

Nickel and Cobalt have been detected as lattice impurities in synthetic diamonds grown from metal solvent catalysts at concentrations of $\leq$ 30 ppm and $\leq$ 1 ppm respectively (Hayakawa et al., 2000). Griffin et al. (2004) have determined absolute Ni and Co concentrations in fibrous diamond as 18.9 and 16.8 ppm respectively, using a carbon-based LA-ICP-MS standard. In this study we have calculated the relative concentrations of trace elements in inclusions in the diamond, not the bulk diamond composition. However lattice bound Ni and Co are not considered to be a significant component of the measured composition of the coated diamonds, because these elements are correlated with Fe in the core; Fe was not detected in the synthetic diamond lattice.

5.3.1 Diamond Core Fluids

The median compositions of the fluids in the diamond cores and the fluid data for individual analytical points are given in table 5.2.

5.3.1.1 Incompatible Elements

Inclusions in the diamond cores are generally enriched in high field strength elements (HFSE: Nb, Ta, Ti, Zr) over chondritic meteorites when Al-normalised (Fig. 5.3a): Ta by $\geq$3 orders of magnitude, Nb by $\geq$2 orders of magnitude and Zr and Ti by $\geq$1 order of magnitude. Although the Ta data is sparse, there appears to be a correlation between Ta and Ti, but not between Ti and Nb or Zr. HFSE enrichment may be due to the presence of rutile, titanates, sphene or ilmenite either as trapped crystalline phases or contributors to the glass/fluid. The diamond

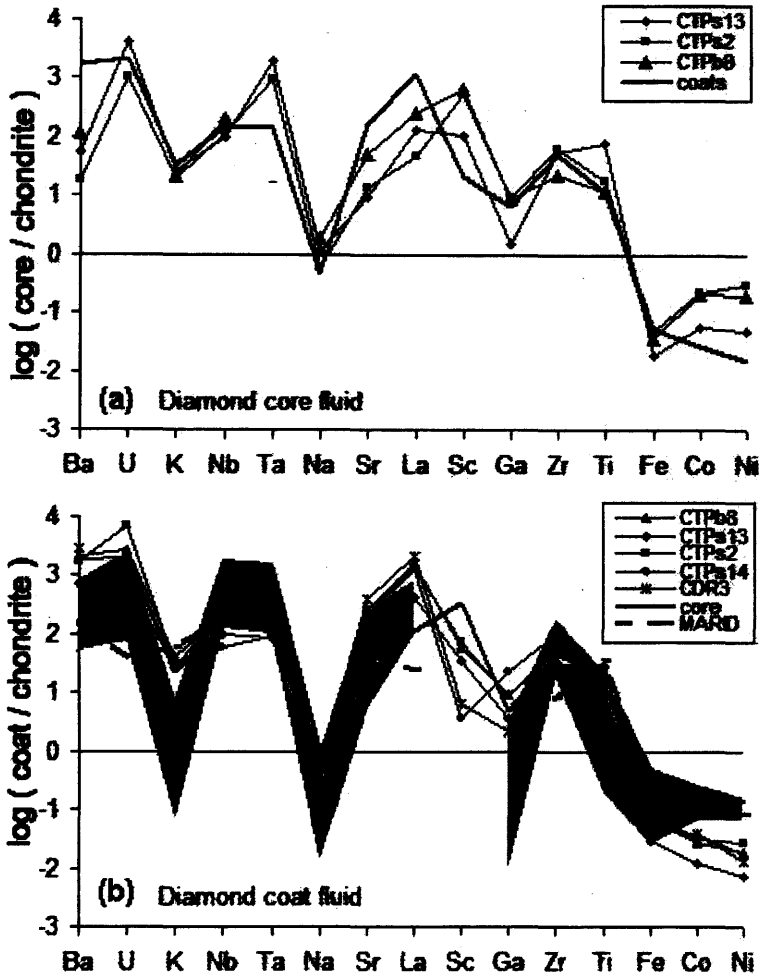

Figure 5.3: Average trace element abundance patterns of diamond fluid (normalised to chondritic Al) normalised to carbonaceous chondrite (McDonough & Sun, 1995). (a) Average sample core fluids compositions (black lines) compared to the average coat fluid (grey line). (b) Average composition of diamond sample coat fluids (black lines) and the compositional range of kimberlite (light grey shaded area; Dawson 1980) and MARID (heavy dashed line; Gregoire et al. 2002) and the average core fluid composition (dark grey line). Sample symbols: CTPb8 (triangle), CTPs13 (diamond), CTPs2 (square), CTPs14 (circle), CDR3 (cross).

coat inclusions also contain very high concentrations of U, $\geq$3 times the concentration of U in chondritic meteorites for an equal Al content. This U-enrichment may be due to the influence of U-bearing minerals (apatite, zircon, monazite) either as included minerals or as constituents of the trapped glass/fluid; Zr may also be due to the presence of zircon. The other large ion lithophile elements (LILE: Ba, Sr, K) and La are enriched by 1 to 2 orders of magnitude over chondritic mantle (for the same Al content) in the diamond core fluid, the exception to this is Na which is present at approximately chondritic level (Fig. 5.3a). La, Ba and Sr are inter-correlated, but are not correlated with K or Na (Fig. 5.4a-c).

The enrichment of HFSE such as Ti, Zr and Ta in the diamond core fluid precludes carbonatite as the fluid trapped during diamond core growth, because carbonatite is typically low in HFSE (Ionov et al., 1993). When compared to natural carbonatite (Woolley & Kempe, 1989), La, Ba, Sr and Nb are depleted and the trace element pattern of the inclusions is different from that of carbonatite (Fig. 5.5). Therefore, we conclude that carbonatite-like fluid/melt was not important during core growth. This is relevant because carbonate-rich melts are commonly thought to be one of the main carbon sources and catalysts for diamond growth in the mantle and are the focus of diamond growth research in high-pressure high-temperature experiments (Akaishi et al., 1990; Arima & Kozai, 2003; Litvin et al., 1998a; Pal'yanov et al., 1999a).

Hydrous fluids are expected to show strong enrichment of highly soluble LILE (Sr, K, Ba) at the expense of insoluble HFSE (Ti, Zr, Nb, Ta). This is at odds with the observation that the diamond core fluids are enriched in HFSE relative to LILE. CO_2 reacts with silicate mantle minerals to form carbonate. Since there is no trace element evidence for carbonate involvement in the growth of the diamond cores, CO_2 is also not considered to be a dominant component of the diamond core fluid. This suggests that C-O-H fluids are unlikely to be the dominant fluid present in the diamond core inclusions.

High Field Strength Element enrichment is often characteristic of silicate melt, while high Sr, Ba and Zr concentrations are expected in H_2O-rich silicate melts (Harte et al., 1993). Melt composition controls melt structure, which in turn controls trace element partitioning: HFSE become increasingly soluble with decreasing SiO_2 content of silicate melts and are therefore more enriched in mafic

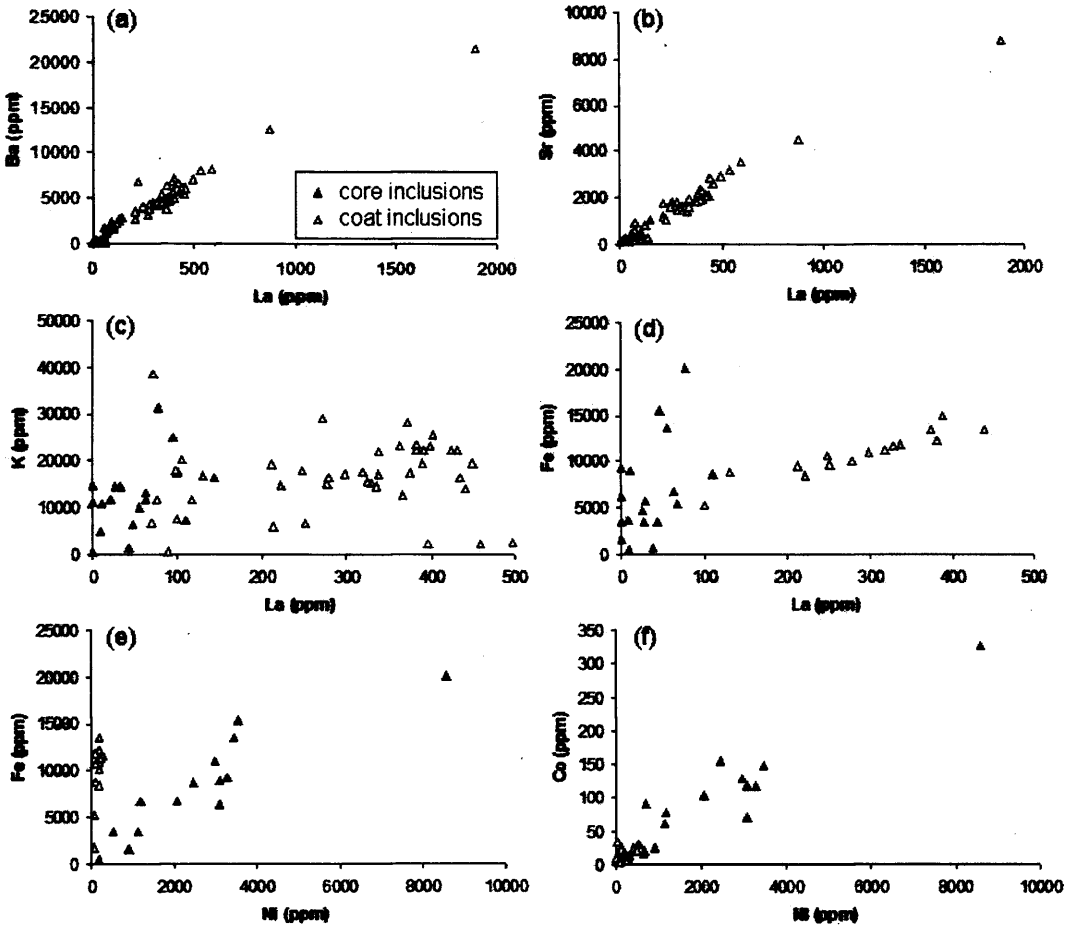

Figure 5.4: Compositional variation of individual sample spots in diamond coat fluids (open triangles) and diamond core fluids (solid triangles). (a) La and Ba are correlated in core and coat fluid; (b) La and Sr are correlated in core and coat fluid; (c) La and K are not correlated in either core or coat fluid; (d) La is correlated with Fe in the coat but not in the core fluid; (e) Ni and Fe are correlated in the core fluid; (f) Ni and Co are correlated in the core fluid.

melts (Mysen, 2004). Therefore, we favour a mafic silicate melt as the dominant component of the diamond core inclusions. However, HFSE elements may also be sequestered into mica (e.g. phlogopite) or zircon, apatite and sphene. HFSE-rich minerals may have contributed to the HFSE-enriched signature of the diamond core inclusions, either directly by being entrapped, or by reactions between the fluid and these mineral in the host rock matrix.

We have calculated the trace element compositions of mantle silicate minerals that would be in equilibrium with a silicate melt with the trace element composition of the diamond core fluids, normalised to 14 wt% Al_2O_3, using the partition coefficients of Klemme et al. (2002); Latourrette et al. (1995) (table 5.4). The value of 14 wt% Al_2O_3 is the average Al concentration of the silicate melts generated during those partitioning experiments. The concentrations of most incompatible elements (K, Sr, Nb, Ba, La and U) are approximately within the range observed in natural mantle garnet and clinopyroxene and therefore concentration of these elements may have been generated locally by partial melting processes. However, the calculated concentrations of Zr and Ti are very high and are therefore unlikely to have been generated by closed system partial melting of unmetasomatised mantle. The calculated range of incompatible element concentrations in phlogopite are significantly higher than observed in mantle samples, therefore phlogopite is unlikely to have been present at the time of diamond core growth.

5.3.1.2 Compatible Elements

Diamond cores contain higher concentrations of compatible elements than their coats relative to chondritic Al. In the core region, Fe, Ni and Co are intercorrelated (Fig. 5.4e-f) and are depleted relative to chondritic meteorites for the same Al concentration (Fig. 5.3a). The Ni/Fe ratios of sample spots in the core range from 0.2 to 0.6, this is an order of magnitude higher than the average Ni/Fe ratio in peridotite-pyroxenite suite xenoliths ($\approx$0.04) and two orders of magnitudes higher than in eclogite xenoliths ($\leq$0.001; calculated from Dawson 1980). The ratios Ni/Co and Fe/Co are similarly high ($\approx$23 and $\approx$78 respectively). We have calculated the concentration of Ni in olivine in equilibrium with a silicate melt with the average Ni concentration of the diamond core fluids normalised to 14 wt% Al_2O_3, using $D_{Ni}^{olivine/melt} = 10$ (Green, 1994). The calculated Ni concentration in olivine is 57720 to 335749 ppm, an order of magnitude higher than Ni in pyrolite mantle (1960 ppm Ni; McDonough & Sun 1995) and in olivine diamond inclusions (2000 to 4000 ppm; Stachel et al. 2003). Therefore the high Ni/Fe and Co/Fe ratios may indicate the presence of a sulphide or metallic component in addition to the silicate melt in the diamond core inclusions. The trapped fluid

mineral	sample	K	Na	Ti*	Ba	U	Nb	La	Sr	Zr*	Ta	Ni*
diamond core fluids												
phl	CTPb8	383257	34976	60233	11083	-	42	19	667	17	-	-
	CTPs13	484470	8219	400100	5511	0.4	20	8	119	40	-	-
	CTPs2	356241	4790	90937	1800	0.09	27	3.3	174	47	-	-
cpx	CTPb8	881	-	20458	6	-	10	23	335	92	-	-
	CTPs13	1113	-	135891	2.8	2.7	5	10	60	220	3.5	-
	CTPs2	818	-	30886	0.9	0.7	6	4	88	255	2	-
grt	CTPb8	38	-	11934	0.12	-	3.8	0.5	21	394	-	-
	CTPs13	48	-	79270	0.06	2.0	1.8	0.2	3.8	948	1.2	-
	CTPs2	35	-	18017	0.02	0.5	2.4	0.09	5.5	1095	0.6	-
ol	CTPb8	-	-	-	-	-	-	-	-	-	-	225329
	CTPs13	-	-	-	-	-	-	-	-	-	-	57220
	CTPs2	-	-	-	-	-	-	-	-	-	-	335749
Observed mantle minerals												
phl[1]	Max	90071	3338	6165	470	0.4	15.5	0.6	30	20	1.6	1445
	Min	55205	223	1980	140	0.01	0.35	0.07	1.5	0.75	0.05	480
cpx[2]	Max	4068	31084	14564	19	-	1.49	8.91	200	20	-	-
	Min	332	5564	240	0.04	-	0.00	0.34	39.8	0.29	-	-
grt[2]	Max	0	2967	6833	3.22	-	8.52	0.74	31.3	176	-	-
	Min	0	668	14.2	0.00	-	0.00	0.00	0.12	1.54	-	-
ol[3]	Max	-	-	-	-	-	-	-	-	-	-	2000
	Min	-	-	-	-	-	-	-	-	-	-	4000

Table 5.4: Calculated trace element compositions of silicate minerals in equilibrium with hydrous silicate melt with the average trace element composition of the diamond core fluids (normalised to 14 wt% Al_2O_3). Concentrations are in ppm, elements marked with * are unreasonably high concentrations for mantle minerals. Partition coefficients for core fluid calculation: phlogopite and amphibole from Latourrette et al. (1995) clinopyroxene and garnet from Klemme et al. (2002); olivine from Green (1994) for hydrous silicate melts in equilibrium with basanite, eclogite and peridotite respectively. Abbreviations: phl - phlogoptite, cpx - clinopyroxene, grt - garnet, ol - olivine. Observed mineral concentrations from: 1 - Gregoire et al. (2002), 2 - Stachel et al. (2004), 3 - Stachel et al. (2003).

has non-chondritic Ni/Fe and Ni/Co ratios, therefore the Ni and Co signature is unlikely to be due to metallic phases in the diamond cores. The Ni/Fe ratio of the diamond core inclusions (Ni/Fe = 0.2 to 0.6) are similar to those of sulphide inclusions in African diamonds (0-0.9; Deines & Harris 1995).

In low pressure partitioning experiments between olivine and MORB melt, Li et al. (2003) found that Ni partition coefficients in S-bearing silicate systems were up to 50% lower than those derived from S-free experiments due to the formation of Ni-S complexes. Thompson & Barnes (1984) investigated the distribution of Ni and Fe between sulphides and olivine, and calculated a Ni/Fe partition coefficient of ≈9.8 ($KD^{sulphide/olivine}$ = sulphide$^{X_{Ni}/X_{Fe}}$/olivine$^{X_{Ni}/X_{Fe}}$, where X

denotes mole fractions). The calculated Ni/Fe ratio of olivine in equilibrium with a sulphide melt with the compatible element composition of the core fluid (Ni/Fe = 0.2 to 0.6) is 0.02 to 0.06. This is within the range observed for olivine inclusions in natural diamond (0.02 - 0.06, Hervig et al. 1980). Fleet & MacRae (1988) have determined this partition coefficient experimentally and give a higher value of ≈30, which they suggest is appropriate to the upper mantle. Using this higher value, olivine in equilibrium with the core fluid has a calculated Ni/Fe ratio of 0.007 to 0.02. Therefore, we suggest that Ni and Co in the trapped fluid/glass may be present as a sulphide phase.

Sulphide is the predominant diamond inclusion worldwide and is over abundant when compared to mantle peridotite and eclogite (Gurney, 1989). This study suggests that sulphide should also be expected as sub-microscopic inclusions, as is the case with glass and minerals (e.g. Damarupurshad et al. 1997; Fesq et al. 1975). The presence of a sulphide component in silicate melt is not contrary to evidence from metasomatised xenoliths, where sulphide minerals are common in eclogite xenoliths, often as inclusions in clinopyroxene and garnet (Taylor & Anand, 2004). Oxide-sulphide-silicate inclusion assemblages have been described in the centre of single diamonds from Yakutia (Bulanova et al., 1998). Therefore, we favour a silicate-sulphide melt as the fluid present in sub-microscopic inclusions in the diamond core.

5.3.1.3 Paragenesis

The Ni/Fe ratios of the trapped sulphide give a FeNiS sulphide phase with 8 to 27 mol% Ni, this is intermediate between the Ni content of peridotitic (>12%) and eclogitic (<12%) sulphides (Deines & Harris, 1995), so it is not possible to assign a paragenesis to the diamond cores on the basis of inferred sulphide composition. Rege et al. (2003) showed that eclogitic and super-deep diamonds typically have negative HFSE (Nb, Zr, Ti) anomalies, while peridotitic diamonds from different global locations show variable degrees of HFSE enrichment. The ratio Nb/La in the diamond core fluid is ≈0.8, this is similar to the Nb/La ratio in peridotitic diamonds from global locations (Nb/La ≈0.66 in peridotitic diamonds, Nb/La ≈0.02 eclogitic diamonds, calculated from Rege et al. 2003). This suggests that the diamond cores in this study may possibly be peridotitic.

5.3.2 Diamond Coat Fluids

The median compositions of the diamond coat fluids and the data for individual analytical points are given in table 5.3. Inclusions in the diamond coat are enriched in La, Ba and Sr and depleted in Ta, Ti, Sc, Ni and Co relative to the diamond core fluids when the data are Al-normalised. Relative to Al, the concentrations of the other incompatible elements (U, K, Nb, Na, Ga, Zr) and Fe are approximately equal in both the diamond core and coat fluids.

5.3.2.1 Incompatible Elements

When normalised to CI chondrites and baselined to chondritic Al, Na is present at approximately chondritic concentrations; the remaining LILE and La are enriched by approximately 1.5 to 3.3 orders of magnitude, in the order K<Sr<La<Ba<U (Fig. 5.3b). There is a positive correlation between La, Ba, Sr and Fe in the diamond coat inclusions (Fig. 5.4a-c). The chondrite-normalised trace element pattern is similar to that of fibrous diamonds from Botswana (Schrauder et al., 1996), Canada and Siberia (Griffin et al., 2004). The HFSE (Ta, Nb, Zr) concentrations of the extrapolated diamond coat fluids are enriched by a factor of $\approx$2 over CI chondrites; Ti is only moderately enriched relative to chondritic Al. The HFSE ratios in the diamond coat fluids are generally similar to those in the diamond core inclusions, the ratio Nb/Zr ranges from 0.04 to 0.29 in the coat (mean 0.16), in the core the range is 0.09 to 0.48 (mean 0.23); Zr/Ti = 0.01 to 0.1 (mean 0.02) in the coat inclusions and 0.01 to 0.03 (mean 0.02) in the diamond core inclusions. The elements K, Na and U are also present in similar ratios in the coat fluid as in the core fluid: Zr/K = 0.007 to 0.023 (0.008 to 0.023 in the diamond core fluid); Nb/Na = 0.005 to 0.024 (0.004 to 0.013 in the diamond core fluid). Therefore, the fluid trapped in inclusions in the diamond coat may contain a component of silicate melt similar to that in the diamond core inclusions. The presence of a hydrous silicate fluid component is consistent with H_2O and quartz in the infrared spectra of the diamond coats (section 3.2.2.2).

The main difference between the diamond core fluid and that trapped in inclusions in the diamond coat appears to be the LILE- and La-enrichment of the latter. In figure 5.5 we compare the Al-normalised LILE plus La, Fe Nb

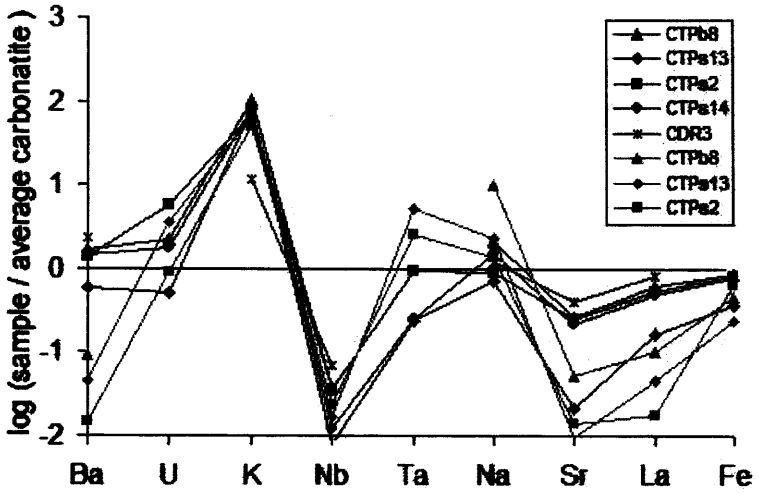

Figure 5.5: Average composition of diamond coat fluids (black lines) and core fluids (grey lines) relative to chondritic Al, normalised to natural carbonatite (Woolley & Kempe, 1989). Sample symbols: CTPb8 (triangle), CTPs13 (diamond), CTPs2 (square), CTPs14 (circle), CDR3 (cross).

and Ta composition of the diamond coat fluids to natural carbonatite (data from Woolley & Kempe 1989); these elements are commonly enriched in carbonatite. Most elements deviate by less than one order of magnitude from the carbonatite axis, the exception to this is K, which is enriched by two orders of magnitude over natural carbonatite and Nb which is depleted by two orders of magnitude (Fig. 5.5). The similarity between the coat fluid and carbonatite may be expressed by ratios Na/Ba≈0.66, La/Ta≈130 (0.71 and 122 respectively in carbonatite (Woolley & Kempe, 1989). The presence of a carbonatite component in the diamond coat fluids is consistent with carbonate and apatite in the Ft-ir spectra (section 3.2.2.2). The Nb depletion of the coat fluid relative to carbonatite may reflect competition for Nb, for example with rutile. The high K-content relative to the other LILE may be due to the presence of a K-rich mineral such as phlogopite, or due to a component of KCl brine in the inclusions. The presence of KCl has been detected in individual fluid inclusions in fibrous diamonds from Canada by EMPA (Klein-BenDavid et al., 2004, 2002), while fibrous diamonds from Botswana (Schrauder & Navon, 1994) contain detectable concentrations of Cl, which shows a positive correlation with K. Furthermore, studies of the

noble gas and halogen geochemistry of fibrous diamond fluids have also reveal high and correlated K and Cl contents (18 - 59 and 6 - 19 ppm respectively) in diamonds from the DRC (Johnson et al., 2000). Brine may be an evolved form of carbonatitic fluid formed by crystallisation of mantle phases.

We infer suggest that the diamond coats contain inclusions of carbonatite-like fluid and a component of hydrous-silicate melt similar to that in the diamond core inclusions. Silicate and carbonatitic fluid end-members have previously been identified in fluid inclusions in fibrous diamonds from the DRC and Botswana (Navon et al., 1988; Schrauder & Navon, 1994). Schrauder et al. (1996) show that incompatible element concentrations are a factor of two higher in the carbonatitic end-member than in the silicate fluid.

The overall normalised trace element pattern of the diamond coat inclusions is broadly similar to that of group I kimberlite (Fig. 5.3b); the diamond coat fluid ratios of Nb/Zr = 0.04 to 0.29 and Nb/Ta = 7.9 to 11.3 are within the kimberlite range. The similarity to kimberlite has been noted previously (Akagi & Masuda, 1988; Griffin et al., 2004; Schrauder et al., 1996). However, there are important differences; the trapped fluid is more enriched in LILE (Ba, K, U, Sr,) and La and is relatively depleted in HFSE (Nb, Ta, Ti and to a lesser extent Zr) when baselined to chondritic-Al. This is demonstrated by comparing trace element ratios in the diamond coat to those from the Mbuji Mayi kimberlite. The diamond coat has Nb/Ba = 0.003 to 0.012 and Nb/La = 0.05 to 0.17, which are an order or magnitude lower than in the Mbuji Mayi kimberlite (Nb/La = 0.45 $\pm$ 0.25, Nb/La = 3.0 $\pm$ 1.1; data from Fieremans et al. 1984; Taylor et al. 1994) Ta/K = 0.0001 to 0.0003 and Ta/U = 0.086 to 0.26, also order of magnitude lower than the Mbuji Mayi kimberlite (Ta/K = 0.004 $\pm$ 0.003, Ta/U = 4.5 $\pm$ 3; data from Fieremans et al. 1984; Taylor et al. 1994).

The chondrite-normalised trace element pattern of the diamond coat inclusions is also similar to MARID (Mica-Amphibole-Rutile-Ilmenite-Diopside), the main difference being the higher relative concentrations of Ba, Sr and La in the diamond coat inclusions (Fig. 5.3b). Gregoire et al. (2002) proposed that MARID is a highly alkaline melt genetically linked to Group II kimberlite, which percolated through and metasomatised the upper mantle (Jones, 1989). Therefore, MARID may be a relevant melt/fluid source for the fluid trapped as inclusions in

the diamond coats. PIC (Phlogopite-Ilmenite-Clinopyroxene) is the Group I kimberlite equivalent of MARID (Gregoire et al., 2002) and therefore may be more relevant to fibrous diamond growth, because coated diamonds are only known from group I kimberlites (Boyd et al., 1992).

5.3.2.2 Compatible Elements

Concentrations of compatible elements (Fe, Ni, Co) in the diamond coat fluid are depleted relative to CI chondrites for a given Al concentration (Fig. 5.3b). While the concentration of Fe in the diamond cores is correlated with Ni and Co and is attributed to the presence of sulphide, this is not the case in the diamond coats. Iron is generally positively correlated with the LIL elements in the diamond coats and is associated with the carbonatite component (this may mask any contribution from Fe-sulphides). The average sample Ni/Co ratio is ≈16 (range 7 to 23), this is lower than in the diamond cores where Ni/Co ≈ 23. The Ni concentration of olivine in equilibrium with a carbonate melt with the Ni-content of the diamond coat fluid (calculated using $KD_{Ni}^{olivine/melt} = 19.1$; from Sweeney et al. 1995), varies between 1323 and 5490 ppm (average 3268 ppm). This largely overlaps with the range of Ni concentrations in olivine diamond inclusions is 2000 to 4000 ppm (Stachel et al., 2003), so Ni may reside in the carbonate melt in the diamond coat inclusions.

5.3.3 Zoning

The diamond cores do not show systematic zoning in fluid composition. Trace element zoning was not expected because all of the cores show evidence for growth during more than one event. However zoning is also not apparent within single growth zones (e.g. in sample CTPs13 the traverse sampled several points within a single growth zone, Fig. 5.6). Fluid inclusions appear to be compositionally zoned in the diamond coats. In sample CTPs13 (Fig. 5.6) and CDR3 inclusions become more enriched in carbonatite components (Ba, La, Sr) towards the rim, relative to Al; Nb initially increases then decreases perhaps reflecting competition of Nb between accessory silicate minerals (e.g. rutile) and carbonatite. In CTPb8, CTPs14 and CTPs2 (Fig. 5.6) the carbonatite components initially increase away

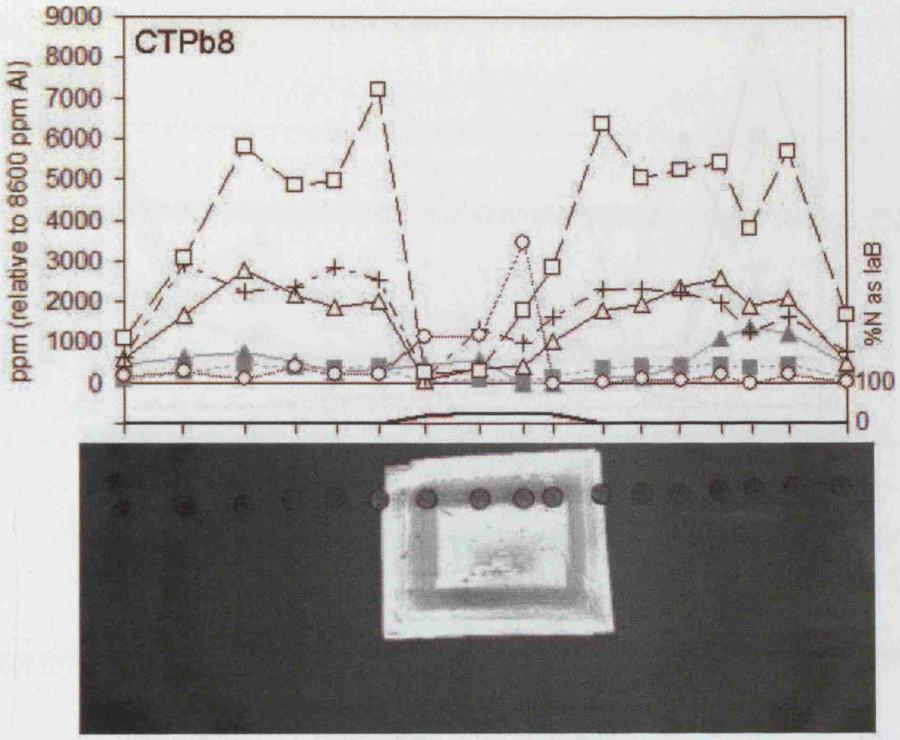
CTPb8
ppm (relative to 8600 ppm Al)
9000
8000
7000
6000
5000
4000
3000
2000
1000
0
%N as laB
100
0

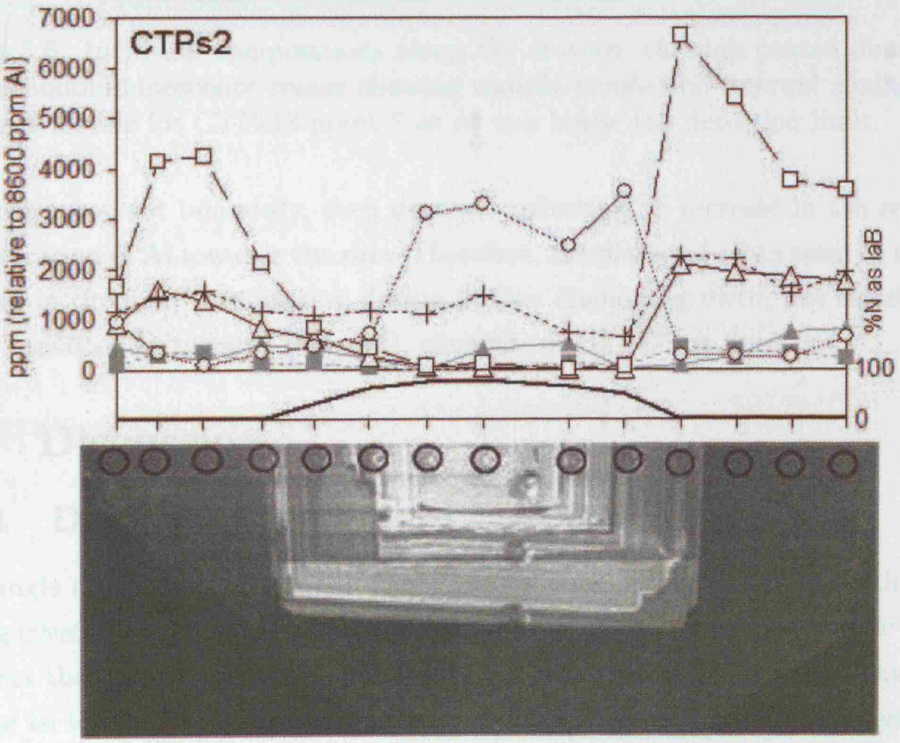
CTPs2
ppm (relative to 8600 ppm Al)
7000
6000
5000
4000
3000
2000
1000
0
%N as laB
100
0

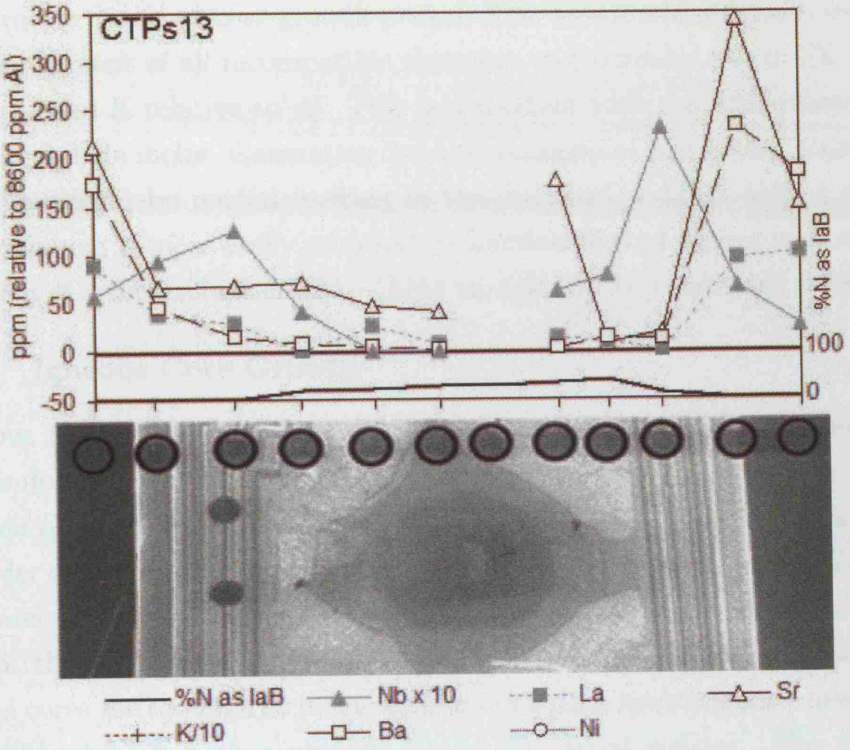

Figure 5.6: Inclusion compositions along the traverse through coated diamonds and cathodoluminescence image showing sample points and internal zoning. No data is available for CTPs13 point 7 as Al was below the detection limit.

from the core-coat boundary, then decrease reflecting an increase in the relative concentration of Al towards the rim. Therefore, the diamond coats seem to record changes in the fluid composition during fibrous diamond growth, but the change is not consistently towards more LIL element- or HFSE-rich fluid.

5.4 Discussion

5.4.1 Diamond Core Fluid Formation

The single crystal morphology of the diamond cores indicates that growth rates during crystallisation of the cores were lower than during formation of their coats and that the system was saturated (but not supersaturated) in carbon. This may be due to lower volatile concentrations and/or differences in carbon speciation

relative to the diamond coat growth period. The core fluids are characterised by strong enrichment of all incompatible elements, in particular the HFSE (Ti, Ta, Zr, Nb), U and K relative to Al. This is consistent with the entrapment of silicate and sulphide melts. Generating 2-4 fold enrichment across the incompatible element spectrum by partial melting in the diamond stability field is unlikely; such enrichment is more easily achieved by fractionation of silicate melt or by the infiltration of a metasomatic fluid. These models will be considered below.

5.4.1.1 Igneous Core Growth

Bulanova (1995) suggested that diamond may crystallise from a fractionating silicate-sulphide melt. This model is consistent with the high concentration of transition elements in diamond cores. The solubility of carbon in sulphide melts is an order of magnitude higher than in silicate melts (Saxena, 1989). Therefore, this model provides a means of saturating the growth environment in carbon. However, the concentrations of Ti, Zr and K in the fluid/glass inclusions in the diamond cores are too high to be in equilibrium with a mantle silicate assemblage, and so cannot have been generated locally by partial melting. The fractional crystallisation model is also inconsistent with the lack of systematic trace element trends across growth zones in the diamond cores. Therefore, there is no clear signal that the diamond cores grew during igneous fractionation.

5.4.1.2 Metasomatic Core Growth

Fluids and melts percolating through the mantle are a potential source of both incompatible elements and carbon. Migrating fluids are heterogeneous because they may only achieve equilibrium on a very local scale, which means that fluid compositions may vary within single growth zone. Single gem diamonds, comparable to the diamond cores, may record the full range of $\delta^{13}C$ isotopic variability observed in bulk analyses of individual diamonds (Hauri et al., 2002). The high Zr and Ti concentrations of the diamond core fluids suggest an open system during diamond core growth. These elements may be supplied by a metasomatising silicate melt. Infiltration of silicate melts into subsolidus peridotite requires H_2O-rich compositions to prevent the melt from crystallising and stagnating (Stachel

& Harris, 1997a). The introduction of this fluid lowers the mantle solidus temperature, dissolves alumnosilicate components from the wall rock minerals, and may lead to partial melting. Diamond may crystallise directly from the metasomatic fluid, or from these partial melts, or from a reaction product of the two. Almost all eclogites from the Yakutian kimberlites show evidence of having experienced partial melting (e.g. spongy clinopyroxene, kelphytic rims on garnet and K-rich alumnosilicate glass (Spetsius, 1995)). Phlogopite is not thought to have formed during this metasomatic event, as it would not be in equilibrium with the trace element composition of the silicate melt.

5.4.2 Diamond Coat Fluid Formation

The symmetrical and fibrous morphology and the presence of volatile-filled cavities in the diamond coats indicate rapid diamond growth under conditions of fluid and carbon supersaturation. This situation may be achieved by diamond growth in a carbonatitic fluid. The striking morphological difference between cores and the coats, and the difference in age recorded by the nitrogen aggregation state in these samples, argue in favour of a 2-stage process for the growth of coated diamond.

The diamond coat inclusions contain a carbonatite-like component. This is expressed as enrichment in Ba, Sr and La relative to the core fluid (normalised to the same Al-concentration). The presence of this carbonate component may be explained by two models: (1) fractional crystallisation of a metasomatic melt; (2) low degree partial melting of the pre-enriched mantle, as proposed by Schrauder et al. (1996).

5.4.2.1 Carbonate Influx and Fractional Crystallisation

An influx of carbonate into the peridotite or eclogite mantle would introduce additional LILE. In-situ crystallisation of carbonates and apatite (as seen in the Ft-ir spectra of the diamond coats) would then drive the fluid towards a more water-rich and possibly silicate-rich composition, depending on the composition of the incoming fluid. The different zoning patterns observed in the diamond coats may reflect the timing of diamond growth in relation to fractionation. This

model assumes that the carbon source for diamond coat growth was different from that for diamond core growth and so is in agreement with the general observation that fibrous diamonds have restricted and globally uniform range of $\delta^{13}C$ values of -5 to -8 ‰ (Boyd et al., 1992). This model is in agreement with the dominance of H_2O over CO_2 ($CO_2/(CO_2 + H_2O) \leq 0.4$) in the coat. The incoming carbonate melt will also react with the minerals of the host mantle (both primary minerals and those formed during previous metasomatic events, possibly including the diamond core event(s)). This will modify the composition of the metasomatic fluid and add silicate components.

5.4.2.2 Partial Melting of Enriched Mantle

Dalton & Presnall (1998) and Moore & Wood (1998) demonstrated that solidus melting of carbonated lherzolite within the diamond stability field (3-7 GPa) produces carbonatite melts. In similar experiments using carbonated eclogite, Yaxley & Brey (2004) show that solidus (1310°C at 5 GPa) and low degree ($\leq$0.3%) partial melting of carbonate-bearing eclogite also produces carbonate melts. The eclogite melts are markedly more calcic than those produced during melting of carbonated peridotite. Ryabchikov et al. (1991) showed that carbonate melts generated near the peridotite solidus can dissolve appreciable amounts of apatite (up to 10 wt% P_2O_5), this can explain the presence of apatite in the Ft-ir spectra of diamond coats. Low degree partial melting of the pre-enriched host may generate Ba, Sr, La and U-bearing volatile-rich fluids. In this scenario, the trapped fluid represents an in-situ melt generated from pre-existing metasomatic phases. The zoning patterns recorded in individual diamond coats would depend on the phases present in the local growth region. The main argument against this model is the global uniformity in the range of $\delta^{13}C$ values for fibrous diamond. Carbon introduced during the diamond core-forming event and later released by local partial melting for diamond coat formation, should form a coat with a similar isotopic composition as the core, unless $\delta^{13}C$ is fractionated during partial melting of carbonate or by the separation of a CO_2-rich fluid from the carbonate melt. This model also requires a change in pressure and/or temperature to initiate melting by decompression, dehydration or at the solidus. Alternatively, melting may be initiated by the injection of a fluid (e.g. from a

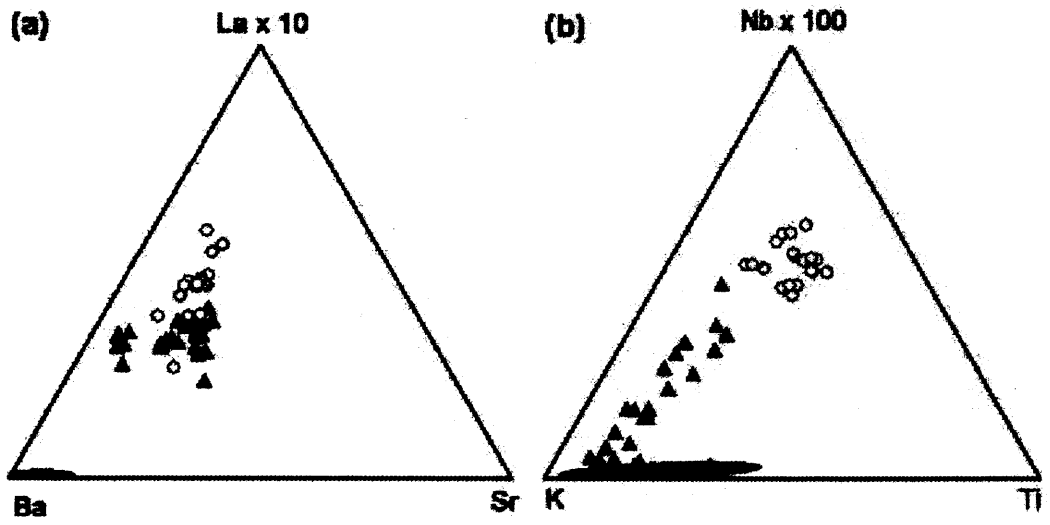

Figure 5.7: Ternary diagram showing the incompatible element concentrations in the diamond coat fluids (black triangles) compared to the composition of the Koidu group-I kimberlite (open circles), data from Taylor et al. (1994). (a) La-Ba-Sr; (b) Nb-K-Ti. The phlogopite field is shown in grey. Kimberlite may be obtained by crystallising phlogopite from the trapped fluid in diamond coats.

plume, subducted slab, or leaked from mantle convection cells). This fluid may supply carbon for diamond growth. An influx of C-O-H fluid is supported by the high concentrations of H_2O and CO_2 determined from the infrared spectra of the diamond coats. With increasing degrees of partial melting, experimental lherzolite and eclogite melts (Dalton & Presnall, 1998; Yaxley & Brey, 2004) evolve smoothly from carbonate-rich to silicate-rich melts similar to kimberlite (at $\approx$1% partial melting).

5.4.2.3 Comparison Between Coat Fluid and Kimberlite Magma

Akagi & Masuda (1988) used the similarity between the $^{87}Sr/^{86}Sr$ ratios (0.7038 - 0.7252) of fibrous diamonds from Mbuji Mayi and the Mbui Mayi kimberlite magma, to suggest that fluid inclusions in fibrous diamonds were trapped as the diamond grew, either in the kimberlite melt, or in the kimberlite source. This is supported by the similarity between the $\delta^{13}C$ composition of fibrous diamond and that of carbonate in kimberlite (Kirkley et al., 1989) and by the fact that fibrous diamonds are only known from group 1 (basaltic) kimberlites (Boyd et al., 1992).

This would suggest that the diamond coat was young (the diamond cores may be much older). Phenocrystic growth of fibrous diamond is not consistent with the composition of the trapped fluids (high LILE concentrations, Ti-rich) or with the ubiquitous IaA nitrogen aggregation state of fibrous diamond, which requires the diamond to be resident in the mantle for a period of time (albeit short) prior to kimberlite eruption (Boyd et al., 1994). Furthermore, inclusions in fibrous diamonds retain a residual internal pressure of 1.4 to 2.0 GPa, corresponding to a formation pressure of 4-7 GPa (Navon, 1991). Therefore, these fibrous diamonds must have grown at depth rather than during kimberlite ascent. Therefore, fibrous diamond is a xenocryst in kimberlite magma (Boyd et al., 1987). However, the diamond coat may have grown in the kimberlite source region, perhaps during the early stages of kimberlite melt generation (and is later entrained in the same kimberlite), or from a fluid separated from kimberlite melt (and is extracted in a later kimberlite eruption).

In order to evaluate whether the fluid/melt trapped in the coat is related to the kimberlite source, I have compared the incompatible element composition of the fluid in the diamond coat with that of unaltered kimberlite from Koidu, Sierra Leone (data from Taylor & Anand 2004). Koidu was chosen, in the absence of complete trace element data from Mbuji Mayi, because it is a similar group-I kimberlite. If the trapped fluid is genetically related to kimberlite, then kimberlite should lie along an extension of the compositional trend of the diamond coat inclusions in the ternary diagrams in figure 5.7. This is true for Sr-Ba-La (Fig. 5.7a), for which there is an overlap between the fluid composition and that of the Koidu kimberlite, the main difference being the stronger Ba enrichment of the fluid in the diamond coats. The relationship is also true for Nb-Ti-K (Fig. 5.7b); here the trapped fluid contains a higher concentration of K, resulting in lower element/K ratios for the fluid than for kimberlite. Therefore, much of the trace element composition of the diamond coat fluid in these samples is consistent with a genetic relationship with the kimberlite source. This implies a possible relationship between fibrous diamond growth and kimberlite petrogenesis. This would suggest that fibrous diamond growth occurred either immediately pre- or syn- kimberite genesis. In the first case, the trapped fluid may represent an intermediate stage of evolution between metasomatic fluid and kimberlite melt.

In the second case, the three end-member fluids may have been derived from a failed parental kimberlite, as it underwent fractional crystallisation in the mantle.

The composition of the Koidu kimberlite may be obtained by crystallising phlogopite from the fluid/melt trapped in the diamond coat, for example by metasomatic reaction with the wall rock. This may lead to the formation of phlogopite-rich PIC suite mantle rocks (Gregoire et al., 2002), which later become disrupted and entrained in ascending kimberlite melt. Alternatively, K-concentrations in the fluid may also be reduced by the formation and separation of a KCl fluid similar to the brine described in cloudy diamonds (Izraeli et al., 2001).

5.5 LA-ICP-MS Summary

Coated diamonds allow investigation of the environment and process of both octahedral and fibrous diamond growth.

The diamond core and coat inclusions show a general 2-4 fold enrichment in incompatible elements relative to Al. This strong enrichment is unlikely to be due to the entrapment of silicate mantle minerals (olivine, garnet, clinopyroxene, phlogopite) alone, therefore sub-microscopic fluid or glass inclusions are inferred to be present. The diamond core fluids are strongly enriched in HFSE (Nb, Ti, Ta, Zr) and U relative to Al, and moderately enriched in LILE (Ba, Sr, K). This trace element composition is consistent with the trapped fluid being a silicate melt. I favour a model in which incompatible element enrichment is achieved by the introduction of a metasomatic silicate fluid/melt and the diamond cores crystallised either directly from this metasomatic fluid or from the interaction between the incoming melt and the host mantle. However, the Ni content and Ni/Fe ratio of the trapped fluid are very high for a silicate melt in equilibrium with mantle minerals; the Ni and Co signature of the diamond core fluid is thought to be dominated by a sulphide phase.

In contrast, the diamond coats grew in the presence of a fluid that is strongly enriched in LILE (U, Ba, Sr, K) and La, and only moderately enriched in HFSE (Ta, Nb, Zr) when normalised to chondritic Al. LILE and La enrichment is

interpreted as due to the presence of a carbonatitic fluid in the diamond coat inclusions, which is mixed with a HFSE-rich hydrous silicate fluid similar to that in the core. The carbonate may be an externally derived metasomatic carbonatite or may have been derived locally by low degree partial melting of the diamond-core host mantle. Sulphide is not detected in the coat fluid. Much of the composition of the coat fluid is consistent with a genetic link to group-1 kimberlite, the high Ba and K content of the fluid relative to kimberlite may be reduced by the crystallisation of phlogopite.

Laser Ablation ICP-MS is a valuable tool for determining the composition and variability of very low level (ppm to ppb) impurities included in diamond. The 'chemically transparent' nature of diamond allows direct observation of the mantle melt inclusions. The use of relative concentrations enables the trace element patterns of diamond inclusions to be studied in the absence of an internal standard. This has led to the recognition of discrete signatures that we have interpreted in terms of various proportions of silicate (core and coat), sulphide (core only) and carbonatite (coat only) melts in coated diamonds from the DRC. Awareness of the types of fluids that are involved in diamond growth is important for understanding diamond growth and interpreting the wide variability of diamond trace element compositions (e.g. Rege et al. 2003). Information about the relative importance of fluid types during diamond growth at different localities can provide the basis for statistical 'fingerprinting' of diamonds (De Corte et al., 2004; Resano et al., 2003).

Chapter 6

HP-HT experiments

6.1 Introduction

This chapter describes the results of diamond growth experiments using C-K_2CO_3-KCl. This system is an analogue for Cl-rich mantle fluids in the natural diamond coats. The purpose of this study is to extend the range of fluids used to experimentally model diamond growth in the carbonate-fluid system.

Diamond synthesis has been successful using KCl-C at 6 GPa, 1620°C (Wang, 1998) and KCl-H_2O-C at 7-8 GPa, 1200-1700°C (Litvin, 2003). Halogens are of interest because of the profound effect they have on the phase relations of carbonate-rich systems (e.g. Williams & Knittle 2003); and because of the occurrence of KCl in inclusions in fibrous diamond (Izraeli et al., 2001, 2004; Klein-BenDavid et al., 2004, 2002). Chlorine has been shown to be an important component of mantle fluids, by comparisons of experimentally derived Cl partition coefficients for apatite with the Cl-content of mantle-derived apatite (Brenan, 1993). High-pressure experiments (1.5-2.0 GPa) indicate that Cl forms complexes with alkalies (K, Na, Ba, Rb), altering their partition coefficients $KD^{fluid/melt}$ and causing them to fractionate into the fluid phase (Ayers & Eggler, 1995). There is a good correlation between the concentration of Cl and K in micro-inclusions in natural-coated diamond (Fig 4.4 and Fig 4.5).

6.2 Previous Work

High-pressure high-temperature (HPHT) diamond growth experiments aim to replicate the process of natural diamond formation in the mantle. These experiments use transition metals and inorganic catalysts, the latter are chosen to represent natural compositions e.g. carbonates, alkali-silicates, sulphides, C-O-H fluids. This section will describe the progress made in HPHT diamond synthesis.

6.2.1 High-Pressure High-Temperature Experiments

HPHT experimental diamond growth methods subject graphite to conditions similar to those under which natural diamonds are formed in the Earth's mantle. The General Electric (GE) team of Francis Bundy, Tracy Hall, Herbert Strong, and Robert Wentorf claimed the first authenticated synthesis of diamond in December 1954, using their belt-type high-pressure device. This work followed a successful, but unpublicised experiment by Baltazar von Platen, at the Allmanna Svenska Elektriska Aktiebolaget (ASEA) Laboratory in Stockholm, Sweden, in 1953. Elemental carbon is dissolved into a metallic solvent catalyst then re-precipitated as diamond. The HPHT conditions of diamond synthesis are clearly defined by the metal-carbon eutectic temperature and the diamond-graphite phase boundary (Bundy et al., 1961). General Electric reported 12 transition metals (Fe, Co, Ni, Ru, Rh, Pa, Ir, Os, Pt, Cr, Mn, Ta) and their alloys that act as successful solvent catalysts. Binary alloys e.g. Cu-Nb have also been shown to have a catalytic effect (Wakatsuk, 1966). Carbon has a high solubility in molten metals, however these melts are not petrologically significant.

6.2.1.1 Carbonates

In the 1990's non-metallic catalysts were added to the list of solvent catalysts. Akaishi et al. (1990) reported the first experimental results of diamond growth in a carbonate-carbon system (Na_2CO_3 and $CaCO_3$) at 7.7 GPa and >2000°C. Akaishi et al. (1996) showed that molten carbonates are also effective sintering agents for the synthesis of polycrystalline diamond. Since the work of Akaishi et al. (1990), a variety of inorganic compounds have been used in experimental investigations of diamond growth and nucleation, including kimberlitic melt

(Arima et al., 1993), halides (Wang, 1998), carbonates (Kanda et al., 1990; Litvin et al., 1999, 1997, 1998a,b; Pal'yanov et al., 1999a, 1998, 1999b; Sato et al., 1999; Sokol et al., 1998, 2000; Taniguchi et al., 1996) and multi-component carbonate-silicate melts (Litvin & Zharikov, 1999; Pal'yanov et al., 2002b). GE also identified many of these as solvent catalysts, but this work is not published in the scientific literature. Carbonates have remained the centre of attention, because of the occurrence of carbonates as inclusions in natural diamond coat (Guthrie et al., 1991; Lang & Walmsley, 1983; Walmsley & Lang, 1992b). Higher pressures and temperatures are required for synthesis with carbonate synthesis than when using metal catalysts, typically >7 GPa, ≥1600°C. The melting temperature of carbonate is lowered by adding an alkali component due to the eutectic/peritectic relationship; this was shown experimentally by Taniguchi et al. (1996). The addition of C-O-H fluid to carbonate also substantially decreases the minimum temperature required for diamond synthesis (from ≈1700°C in dolomite-carbon to ≈1420°C in dolomite-fluid-carbon (Sokol et al., 2001). Relatively low temperature conditions of 1150°C at 5.7 GPa were first achieved in the system alkali-carbonate-H_2O by Pal'yanov et al. (2002a).

6.2.1.2 Other Natural Fluid Analogues

C-O-H fluids have also been successfully used as solvent catalysts for diamond growth (Akaishi et al., 2000; Sokol et al., 2001). C-O-H fluids actively react with solid carbon, graphite dissolves into the fluid and is then precipitated as octahedral diamond under the high-pressure and high-temperature conditions (≥5.7 GPa, ≥1200°C). The advantage of such fluids is that they are supercritical in the diamond stability field; therefore the melt temperature of the catalyst does not control the minimum diamond growth temperature.

Recently, metallic sulphide-carbon melts (FeS-C, NiS-C, CuS-C, Ag_2S-C) have been used to grow octahedral diamond at conditions of ≥6 GPa (Bobrov et al., 2004). Sulphide melts are of interest because of the abundance of sulphides as diamond inclusions and in mantle xenoliths; however they are not known to occur in diamond coat.

6.2.1.3 Growth Mechanism in Natural Analogues

All these experiments provide important insights into diamond formation, but they cannot elucidate the mechanism of formation because they are based on quench methods. Okada et al. (2002); Solozhenko et al. (2002); Turkevich et al. (2002); Utsumi et al. (2004) are the first to have directly observed the process of diamond growth, in real time with both metallic and natural-type fluid catalysts respectively, using synchrotron x-ray diffraction. These experiments showed that high temperature growth is interface controlled, while the diamond growth rate is controlled by the rate of carbon diffusion in the melt at temperatures close to the catalyst solidus. These experiments also confirm earlier results in carbonate (e.g. Pal'yanov et al. 1998), C-O-H (e.g. Akaishi et al. 2000) that diamond growth in a range of catalysts is characterised by an induction period prior to diamond growth. The length of this induction period is temperature and pressure dependent, and may reach tens to hundreds of hours at low PT conditions.

In most diamond growth experiments, graphite is converted to diamond in the presence of catalytic compounds. However, diamond growth from graphite is unlikely to be the case for natural diamond growth. Various authors have produced diamond as a decomposition product of carbon bearing compounds e.g. C-O-H fluids (Yamaoka et al., 2002), cellulose (Yamaoka et al., 2002) and metal carbonates ($MgCO_3$, Pal'yanov et al. 2002a; $CaCO_3$, Yamaoka et al. 2002; $CaMg(CO_2)_3$, Arima et al. 2002). The first step in diamond synthesis from metal carbonates is the decomposition of carbonate to metallic oxide + CO_2. A reductant is then needed to convert CO_2 to elemental carbon. All these studies find that metastable graphite is formed first, which is then transformed to diamond. This means that studies using graphite as the carbon source are valid.

The morphology of the grown diamond is dependent on the pressure - temperature conditions: at low temperature, grown diamonds are cubes, the morphology changes through cubo-octahedron at intermediate to octahedral at high temperature. The nature of the solvent catalyst also affects the growth morphology, largely because of the varying catalyst melt temperature.

6.3 Experimental Method

6.3.1 Calibration

The pressure exerted by the press on the multi-anvil module is shown on a hydraulic oil pressure scale. This primary pressure scale was calibrated experimentally on the basis of fixed pressure points caused by identifiable and precisely measurable phase changes whose PT position is well known. The ideal calibration marker has a polymorphic transformation is in the correct pressure range which is marked by a large change (i.e. resistance, structure), it is chemically pure and stable and easy to handle and has minimal hysteresis and temperature dependence. Pressure was calibrated at room temperature by measuring the large electrical resistance discontinuity associated with the phase transformations Bi(I)-Bi(II) at 2.55 GPa and Bi(III)-Bi(V) at 7.7 GPa; and Ba (5.5 G Pa). Pressure was calibrated at 1100 °C using the $\alpha - \gamma$ phase transition of Fe_2SiO_4. The fixed-point static calibration curve was calculated by interpolation between and extrapolation from these fixed points (Fig 6.1). Temperatures were estimated from the calibration between applied electrical power and temperature using a $W_{97\%}Re_{3\%}$-$W_{75}\%Re_{25\%}$. The accuracy of the pressure and temperature determinations was ± 0.5 GPa and ± 100 °C respectively.

6.3.2 Starting Materials and Preparation

The carbon source for experiments was high purity graphite powder (UCP1-100; Ultra Carbon Group, impurity concentration <5 ppm). The solvent catalyst was composed of K_2CO_3 (BDH limited AnalaR, 99.9%), KCl (Fisons Analytical Reagents, 99.8%) in varying proportions. Starting materials were weighed and mixed by lightly grinding together under acetone in an agate mortar, and then stored in a desiccating oven at 130°C. The materials were loaded into the capsule as a homogenous mix. K_2CO_3 is strongly hygroscopic; in order to minimise this effect in anhydrous experimental runs, the capsule was stored in the oven for a minimum of 24 hours between loading and crimping, and between crimping and welding of the capsule.

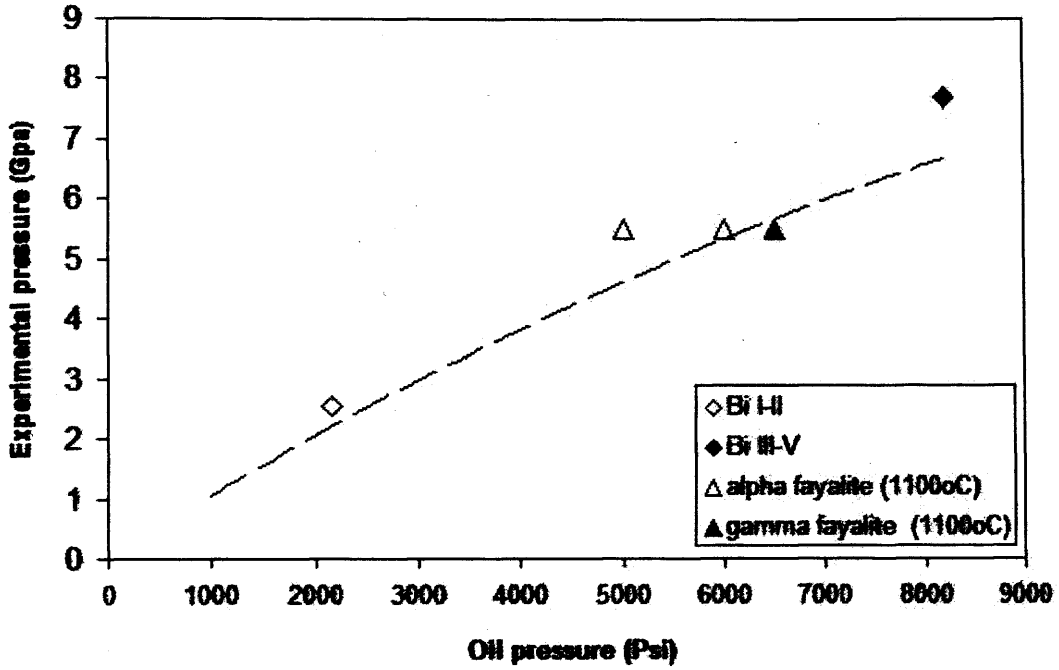

Figure 6.1: Oil pressure to experimental pressure calibration line for 14/8 assembly.

The diamond seeds were synthetic cubo-octahedra (0.9-1.1 mm diameter), characterised by sharp edges and dendritic texturing on the cubic (100) faces which may have aided nucleation and growth on these faces. The size, shape and surface texture of seed crystals were examined by Scanning Electron Microscopy (SEM) prior to experiments. Seeds were also weighed and cleaned in HCl and acetone. They were embedded in the powdered mix in the centre of the capsule.

6.3.3 High-Pressure Experiments

Multi Anvil Press (MAP) experiments were carried out in the Haskel lab at University College London. Experiments were conducted using a Walker module (modified double-stage HP apparatus similar to 6/8 type HP devices) in combination with a 1000 ton four post press.

For experiments in the range 5-7 GPa, a 14/8 assembly was used. This comprised 8 WC cubic inner anvils of 26 mm edge length with a truncated edge length

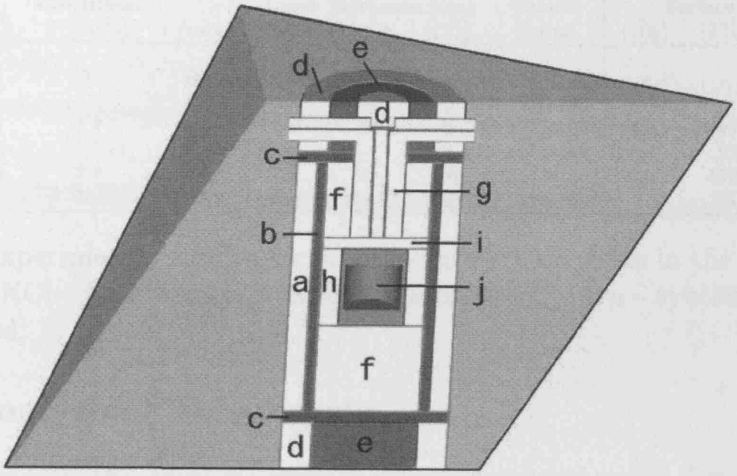

Figure 6.2: Cross-section of cell assembly in the 14 mm MgO octahedra. (a) ZrO sleeve, (b) Graphite heater, (c) Graphite discs, (d) ZrO end caps, (e) Cu contact, (f) Al_2O_3 pressure medium and spacer parts, (g) Thermocouple tube, (h) MgO jacket, (i) MgO Cap, (j) Pt capsule.

of 8 mm. The pressure-transmitting medium was MgO-Cr_2O_3 octahedra with an edge length of 14 mm and a 5 mm diameter cylindrical hole. The octahedra were combined with pyrophyllite fin gaskets. Figure 6.2 shows a cross section of the octahedral sample cell assembly. Within the octahedral sits a cylindrical graphite furnace (length 7.8 mm, outer diameter 4 mm, inner diameter 3.4 mm) within a ZrO thermal insulating sleeve. A platinum sample capsule of length 3 mm and inner diameter 1.7 mm was positioned so that its centre was at the hottest region in the furnace. The thermocouple was aligned axially and positioned immediately above the Pt capsule.

The heating rate for all experiments was $50^oC\ min^{-1}$. The temperature distribution within the capsule was not measured, however thermal gradients were minimised by the use of a highly conductive capsule, and by the positioning of the hotspot at the centre of the sample. Quenching was achieved by shutting of the electric power supply, while the system maintained experimental pressure.

Run	Conditions			Layer Thickness (μm)			Growth	Surface coverage		
	T (°C)	P (GPa)	t (min)	Seed	(100)	(111)	Morph.	(100)	(111)	size (μm)
SK-1	1050	7	60	syn	>2	<2	111>100	-	-	-
				nat	-	0	111>100	-	-	-
SK-3	1420	7.7	<5	syn	5	5	111>100	5%	<2%	5-10
				nat	-	3	111>100	-	<2%	5-10
SK-4	1260	7.7	60	syn	10	10	111>100	60%	45%	10-30
				nat	-	8	111>100	-	5%	5-20

Table 6.1: Experimental results for diamond growth on seeds in the system 50C-35K_2CO_3-15KCl. Abbreviations: Morph - morphology, syn - synthetic seed, nat - natural seed.

6.3.4 Analytical Techniques

After experiments, the capsules were sliced open using a razor. The smaller part of the filled capsule was mounted in epoxy resin and polished under acetone. This was used to investigate the texture and grain size of the solvent catalyst and the graphite. The run product was then cleaned with 10% HCl solution to remove carbonate and KCl, and a hot mixture of HNO_3 and H_2SO_4 to remove graphite. SEM images were collected using a JEOL superprobe 733, with an accelerating voltage of 15V.

6.4 Results

Carbonate crystals in the recovered sample are irregularly shaped with acicular and dendritic forms, while KCl forms small spherules (Fig. 6.3h). These textures are typical of quench crystals, indicating that the K_2CO_3-KCl mix melted in all experimental runs. Large ($\approx$20 μm) graphite flakes are also present, and the seed diamond had sunk to the bottom of the capsule in all runs.

Diamond growth took place on the octahedral (111) faces of both the natural and synthetic diamond, and also on the cubic (100) face of the synthetic seed (table 6.1). Two growth morphologies are observed: (1) Development of numerous epitaxial octahedra {111} up to 20 μm in size. On the natural seed, the new octahedra have nucleated along the edges of the seed facets (Fig. 6.3c-f); on the synthetic seed, octahedra appear to be aligned and in places are so densely packed that they form a growth layer parallel to the seed surface (Fig. 6.3d). The apparent alignment of growth features and presence of areas of high nucleation density

for octahedra {111} may be related to the original dendritic surface texture of the synthetic seed, because defects and steps at the surface of the seed face will provide low-energy nucleation sites. Many octahedra {111} on both the natural and synthetic seeds from SK-4 display skeletal forms (Fig. 6.3f); the development of skeletal morphologies testifies to high crystallisation rates. (2) Layered growth occurred on both seed types in all runs. Layers generally grow inwards from the edge of the seed faces (Fig. 6.3g); however, they also developed away from the crystal edge (again this may be related to textures on the original seed face). In both cases, the edges of the layers are aligned parallel to the edges of the seed face (Fig. 6.3g). In SK-3, layered growth is the dominant growth mechanism; this is surprising since peak temperatures in SK-3 were ≈200°C higher than in SK-4 (1420 and 1260°C, respectively), in which skeletal growth is prevalent. This may be because SK-3 spent a greater proportion of its total run time at lower temperatures. All the developed growth features show flat surfaces with sharp edges, these features are characteristic of solution growth.

The development of octahedra and growth layers are characteristics similar to those observed using K_2CO_3-H_2O-CO_2 at 5.7 GPa, 1150-1420°C during experiments in excess of 20 h (Pal'yanov et al., 2002a). Skeletal growth forms have been observed in experiments using KCl-C at 1200-1600°C at 7-8 GPa (Litvin, 2003).

6.5 Discussion

The straight edges and flat surfaces of grown diamond indicate a solution process, i.e. growth was by precipitation process from a liquid. It is likely that graphite was preserved as a metastable phase in the starting mix, until the conditions of eutectic melting of KCl-K_2CO_3 were reached. Graphite is more soluble than diamond because it is thermodynamically metastable at the experimental conditions. The dissolution of graphite leads to formation of carbon-saturated melt solutions, from which carbon is precipitated as diamond. In practice, levels of carbon concentration in the sample capsule are also likely to be affected by temperature gradients.

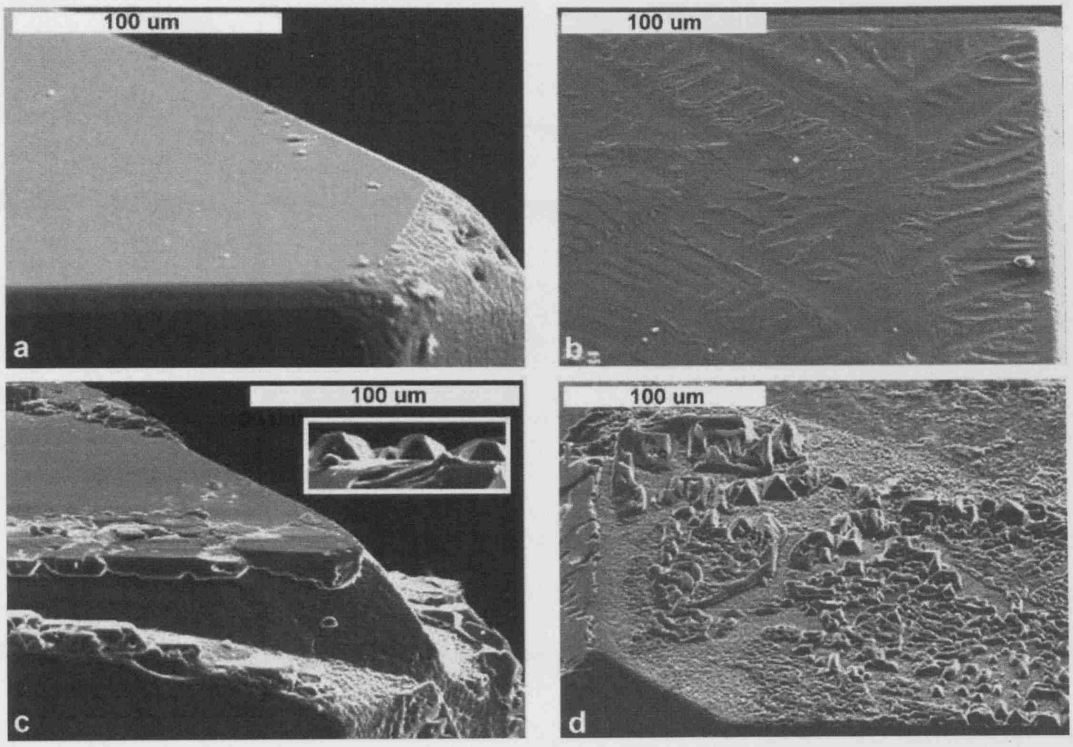

Figure 6.3: SEM images of diamond growth in 50C-35K_2CO_3-15KCl. (a) Surface of pre-run natural seed; (b) dendritic texture on pre-run synthetic seed (100) face; (c) growth on natural seed octahedral face (111) in SK-4, inset (width 50 μm) shows growth at the seed apex; (d) high density epitaxial octahedra on synthetic cube (100) face from SK-4.

Halides are known to reduce carbonate liquidus temperatures: at 1 bar, 15 mol% KF and KCl lower the K_2CO_3 liquidus temperature from 896, to 840 and 800°C, respectively (Levin et al., 1956). Williams & Knittle (2003) used F to reduce the liquidus temperature of carbonate to 700°C at 1.6 GPa, in experiments investigating the structural complexity of carbonate. These authors observe a shift of the C-O symmetric stretch (from 1050-1075 cm^{-1} in non-fluorinated carbonate glasses to 970 cm^{-1}) in the Raman spectra, which they suggest is most likely to be due to disruption of the carbonate group by F, which allows extensive bridging between C-O bond units and cations (in this case K^+) in the melt. It is likely that chlorine has a similar affect on the carbonate liquidus, and is responsible for the reduction of the K_2CO_3 liquidus temperature of potassium carbonate

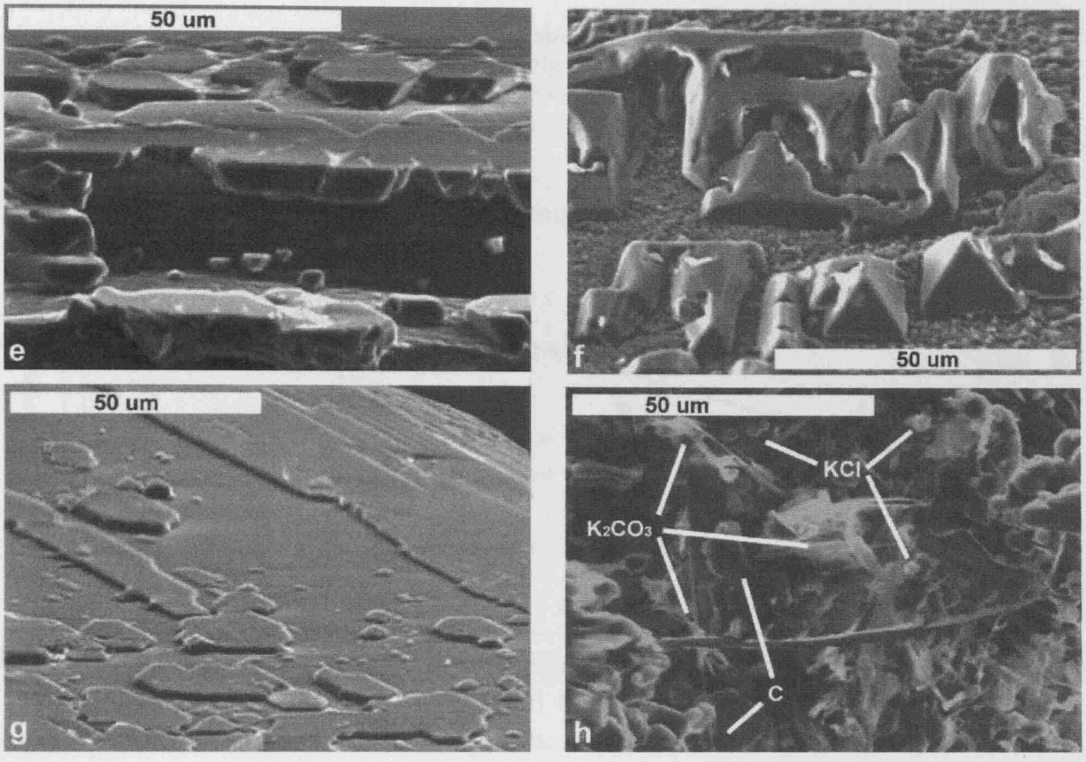

Figure 6.3: (e) epitaxial octahedra on a natural seed octahedral face in SK-4; (f) skeletal morphology of octahedra on the synthetic seed in SK-4; (g) layered growth and octahedra on the natural seed from SK-3, aligned along (111); (h) graphite flakes, KCl spherules and needles of K_2CO_3 from SK-1.

from ≈1300 to 1000°C at 7.7 GPa. Therefore, the presence of liquid KCl allows K_2CO_3 to act as a solvent catalyst at conditions below the continental geotherm (Fig. 6.4).

Diamond growth at a temperature of 1050°C at 7.7 GPa is a reduction of the minimum growth temperature reported in the alkali-carbonate-C-O-H system (Pal'yanov et al., 2002a). Furthermore, 1050°C cannot be considered a minimum temperature, i.e. diamond growth occurred in all experimental runs so I cannot rule out the possibility of growth at even lower temperatures. Furthermore, the experiments in this study were conducted in a narrow pressure range and are limited to durations of 1 hour or less, the minimum growth temperature will be reduced at lower pressures. Minimum synthesis temperatures are likely to be controlled by phase relations in the system K_2CO_3-KCl, which remain to be

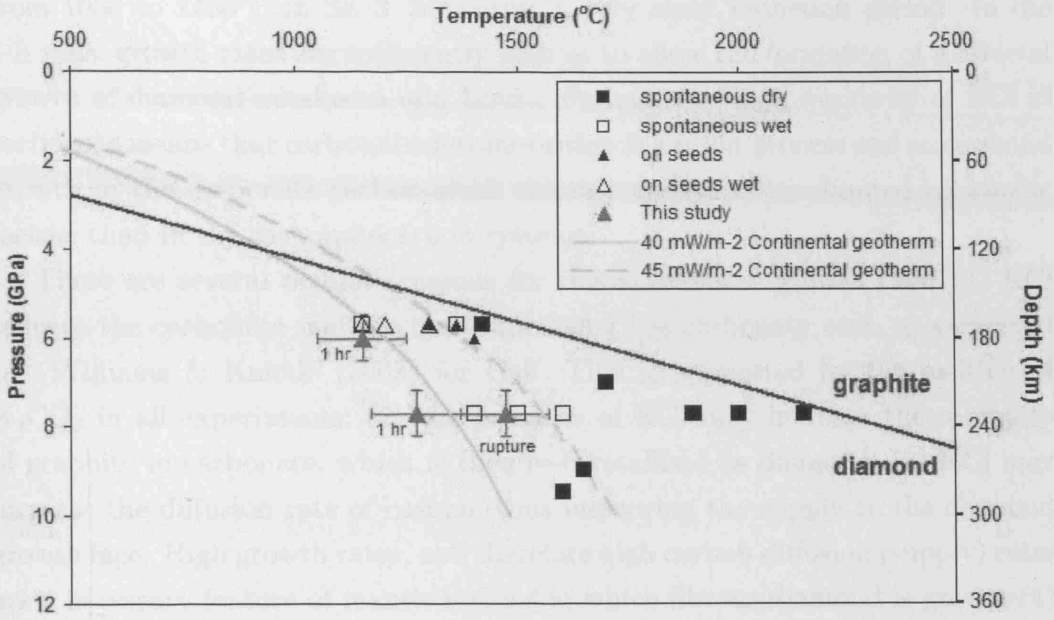

Figure 6.4: PT conditions of successful diamond growth experiments (grey triangles). Error bars are 100°C, 0.5 GPa. Also shown, continental geotherms 35 mW/m^2 ( ) and 40 mW/mm^2 (- - -), and published conditions of diamond synthesis in carbonate on seeds (triangles) and spontaneous (squares). Solid symbols show synthesis in carbonate only (Akaishi et al., 1990; Pal'yanov et al., 2002a, 1999a, 1998; Sato et al., 1999; Sokol et al., 2001, 1998, 2000; Taniguchi et al., 1996); Open symbols show synthesis using carbonate-fluid (CO_2, H_2O, H_2O-CO_2; Pal'yanov et al. 2002a, 1999b; Sokol et al. 2001; Yamaoka et al. 2002 systems).

determined.

Previous diamond growth experiments in carbonate-carbon systems below 1500°C (Pal'yanov et al., 2002a, 1999a,b, 2002b; Sokol et al., 2001, 2000) suggest that diamond growth is characterised by a relatively long induction period before diamond nucleation (<30 h at 5.7 GPa and 1420°C using K_2CO_3 Pal'yanov et al. 2002a). C-O-H fluids reduce, but do not eliminate, this induction period (<20 h at 5.7 GPa, 1420°C in the K_2CO_3-$H_2C_2O_4.2H_2O$-C system Pal'yanov et al. 2002a). However, diamond growth in carbonate has been achieved in 20 mins at conditions above 1500°C (Taniguchi et al., 1996). The concept of an induction period is completely at odds with our experimental data; In the K_2CO_3 KCl system, significant growth occurred in 5 mins as the temperature was increased

from 1050 to 1460°C in SK-3, indicating a very short induction period. In the 1-h runs, growth rates are sufficiently high as to allow the formation of a skeletal growth of diamond octahedra and layers. Perhaps the high reactivity of KCl in carbonate means that carbonate decomposition is a rapid process and so diamond growth in the carbonate-carbon-alkali chloride system is less limited by kinetic factors than in the carbonatecarbon systems.

There are several possible reasons for this accelerated growth rate: (1) KCl reduces the carbonate melting by destabilising the carbonate unit, as suggested by Williams & Knittle (2003) for CaF. This is supported by the melting of K_2CO_3 in all experiments; (2) the presence of KCl may increase the solubility of graphite in carbonate, which is then re-crystallised as diamond; (3) KCl may increase the diffusion rate of carbon, thus improving the supply to the diamond growth face. High growth rates, and therefore high carbon diffusion (supply) rates are a necessary feature of mantle regions in which fibrous diamond is grown; (4) There may be compositional effects at the carbonate-diamond interface, caused by a change in the anion ligands at the surface. Further work is needed to identify which mechanism(s) is responsible for the dramatically accelerated diamond growth rates in these experiments.

6.6 Summary of HPHT Experiments

The presence of KCl reduces the potassium carbonate liquidus to ≈1000°C at 7.7 GPa, allowing it to act as a solvent catalyst for diamond growth at temperatures below the continental geotherm. This is a significant reduction on the minimum diamond growth temperature reported in the alkali-carbonateCOH system (Pal'yanov et al., 2002a). Synthetic diamond growth in the KCl-carbonate system occurred rapidly, leading to the development of skeletal diamond morphologies. The addition of KCl also reduced the period for diamond growth in carbonate to $\leq$ 5 min. It is suggested that KCl destabilises carbonate, allowing greater solubility and diffusion of carbon. Further work needs to be done to demonstrate spontaneous diamond growth and establish the lower temperature boundary of diamond growth in the carbonate-KCl system, as well as to investigate the effect of Cl on the structure of carbonate.

Chapter 7

Conclusions

7.1 Results Summary

In an attempt to develop a model for the genesis of coated diamonds, the main features of the Panda and Mbuji Mayi diamonds are first summarised.

- Micro-inclusion in diamond coats are dominated by liquid water and carbonate.
- A minor component of CO_2 may be dissolved in water in the inclusions.
- Micro-inclusions in diamond coats do not contain silicate melt, but solute-rich aqueous fluid.
- Equilibration temperatures of silicate inclusions in Panda diamond coats are 930 to 1010°C, ≈200°C cooler than those those of minerals in octahedral diamonds from Panda.
- Coated diamonds form in a solid host rock (sub-solidus or near-solidus).
- Diamond coats form in both peridotitic and eclogitic paragenetic environments.
- The host mantle reservoir below Panda was more fertile during growth of the diamond coat than it had been during growth of the diamond cores.

- Garnet, olivine, clinopyroxene and orthopyroxene macro-inclusions in Panda coats are thought to be protogenetic (pre-date diamond coat growth) and therefore record metasomatism by the diamond-growth fluid.
- Varying proportions of three end-members can explain all the fluid inclusion compositions:
  1. Fe-Mg-Ca carbonate
  2. KCl brine
  3. Alumnosilicate fluid
- At Panda, the silicate end-member fluid is thought to have been derived locally by dissolution of the host rock because it is only present in the eclogitic sample.
- The carbonate and KCl fluids are derived externally and percolate through and metasomatise the mantle hosting diamond cores.
- The trace element composition of the fluid in the diamond coat is consistent with it being essentially a carbonatite melt.
- Diamond formed by redox reactions between the host mantle and the incoming carbonate fluid.
- KCl reduced the solidus temperature of the carbonatite melt and may have increased the amount of carbon dissolved.
- Apatite and possibly phlogopite in the Mbuji Mayi micro-inclusions are also thought to have been incorporated into the micro-inclusions as solid phases, either as secondary minerals generated by reaction between the fluid and host rock or as direct precipitates from the incoming carbonatite.
- The trace element composition of the Mbuji Mayi coat fluid suggests a broad genetic link with kimberlite, but is not consistent with diamond precipitation directly from kimberlite because of the high K and Ba content of the fluid inclusions.

- The trace element composition of the core is consistent with it containing some micro-inclusions of silicate melt and some sulphide, which are below the limits of optical petrography.

7.2 Growth Conditions

The growth conditions of the Panda and Mbuji Mayi samples are summarised below, the two sample sets are then compared and contrasted in table 7.1.

7.2.1 Panda

The Panda diamond coats contain macro-inclusions of peridotitic (olivine, Cr-pyrope, orthopyroxene, Cr-diopside) and eclogitic (omphacite) minerals. Therefore, the diamond coats grew in both peridotitic and eclogitic host rocks, and these diamonds may share the same petrologic environments as octahedral diamond. Silicate macro-inclusions in the Panda diamond coats are more fertile than equivalent minerals in Panda octahedral diamond, and trend away from the octahedral diamond inclusions in the direction of the composition of the trapped fluid. This suggests that the fibrous diamond coats likely formed during the metasomatic influx of fluids.

Both eclogitic and peridotitic fluid micro-inclusions are dominated by carbonate and KCl brine; silicate minerals olivine and clinopyroxene were also observed in micro-inclusions in both types. The similarity between the eclogitic and peridotitic end-member brine and carbonate compositions suggests that these components were externally derived and pervaded through both petrogenic environments. The Si-rich fluid component is virtually absent in the peridotitic

samples, but is abundant in the eclogite sample where it coexists with quartz, suggesting that this silicate end-member fluid component was derived locally by reaction between the incoming fluid and the host rock minerals. Experimental melting of hydrous eclogite has been shown to generate granitoid melts with major- and trace-element compositions similar to arc basalts and equivalent to Archean TTG (Rapp et al., 2003). The H_2O and carbonate-rich fluid inclusions represent the residual fluid after precipitation of diamond. The trapped minerals are thought to have crystallised from this residual fluid, either as products of fractional crystallisation from the original fluid (carbonate, olivine, clinopyroxene), or as precipitates from dissolved species liberated during metasomatic reactions (quartz).

Geothermometry indicates that the inclusions equilibrated at around 930 to 1010°C. This low temperature is consistent with the unaggregated state of nitrogen in the diamond coats, which contain medium to high nitrogen concentrations, and requires a low geothermal gradient. These low temperatures also suggest that fibrous diamonds growth at Panda was not the result of a thermal event and favours a growth model driven by open system arrival of externally derived metasomatic fluids. This temperature is cooler than the equilibration temperature of inclusions in octahedral diamonds at Panda (1100-1250 °C; Tappert et al. 2005). Formation pressures of 4 to 5 GPa are indicated by geobarometry of clinopyroxene inclusions, high residual internal pressures of fluid inclusions are recorded by quartz in the eclogitic diamond coat sample.

	Mbuji Mayi (DRC)	Panda (Canada)
Differences	No single phase macro-inclusions	Single phase macro-inclusions
	No mantle silicates	Mantle silicate inclusions
	Paragenesis unknown	Peridotitic and eclogitic
	Low-KCl content	High-KCl content
	SiAlK to carbonate array (minor KCl)	KCl to carbonate array
	Inclusion density decreases to rim	Inclusion density increases to rim
Similarities	High-carbonate content	High-carbonate content
	Water-rich	Water-rich
	No silicate melt	No silicate component in P-type
	Quartz in inclusions	Quartz in inclusions in E-type
	N ppm and inclusion density correlate	N ppm and inclusion density correlate
	Type-IaA	Type-IaA
	High internal pressure in inclusions	High internal pressure in inclusions

Table 7.1: Comparison between Panda and Mbuji Mayi diamond coats.

7.2.2 Mbuji Mayi

The Mbuji Mayi fluid inclusions are dominated by carbonate and aluminosilicate end-member fluids, with only minor KCl fluid component. Carbonate, apatite, quartz and mica, possibly phlogopite were identified as solid phases by infrared spectroscopy. The trace element chemistry of the Mbuji Mayi diamond coats indicates that the dominant constituent is a carbonatite-melt. The H_2O and carbonate-rich fluid inclusions represent the residual fluid after precipitation of diamond. The trapped minerals are thought to have crystallised from this residual fluid, either as products of fractional crystallisation from the original fluid (carbonate minerals), or as precipitates from dissolved species liberated during

metasomatic reactions (quartz, phlogopite). In contrast, the diamond core formed in the presence of a silicate melt.

The paragenesis of these samples is unknown, but the similarity with eclogite and with the fluid in the eclogitic Panda sample suggests an eclogitic paragenesis for this sample set.

Sample MM10 has a high proportion of the silicate end-member fluid, however detailed analysis of the infrared spectra indicates that its inclusions are dominated by liquid water; hydrous-silicate melt was not detected. This indicates that the host mantle was sub-solidus or near-solidus during the MM10 diamond coat growth. All Mbuji Mayi samples are type IaA, indicating that they formed and were stored at relatively low mantle temperatures ($\leq$ 1100°C). Geobarometry of quartz inclusions in Mbuji Mayi diamond coats indicates formation pressures of 6.4 to 6.8 GPa, calculated at 1000°C.

7.3 Diamond Growth Window in PTfO_2

The above discussion shows that the diamond coats in this study formed in a solid host rock. This indicates that conditions were below or close to the wet solidus of the host rock. This is consistent with the relatively low formation and storage temperatures of these samples. The presence of a carbonate melt places a lower limit on the temperature in the mantle at the time of coat growth. Figure 7.1 shows the pressure-temperature region of fibrous diamond growth in the mantle at Panda and Mbuji Mayi.

The pressure-temperature conditions indicated by inclusion geothermobarometry of the lherzolitic Panda diamond coats fall below, but close to the lherzolite

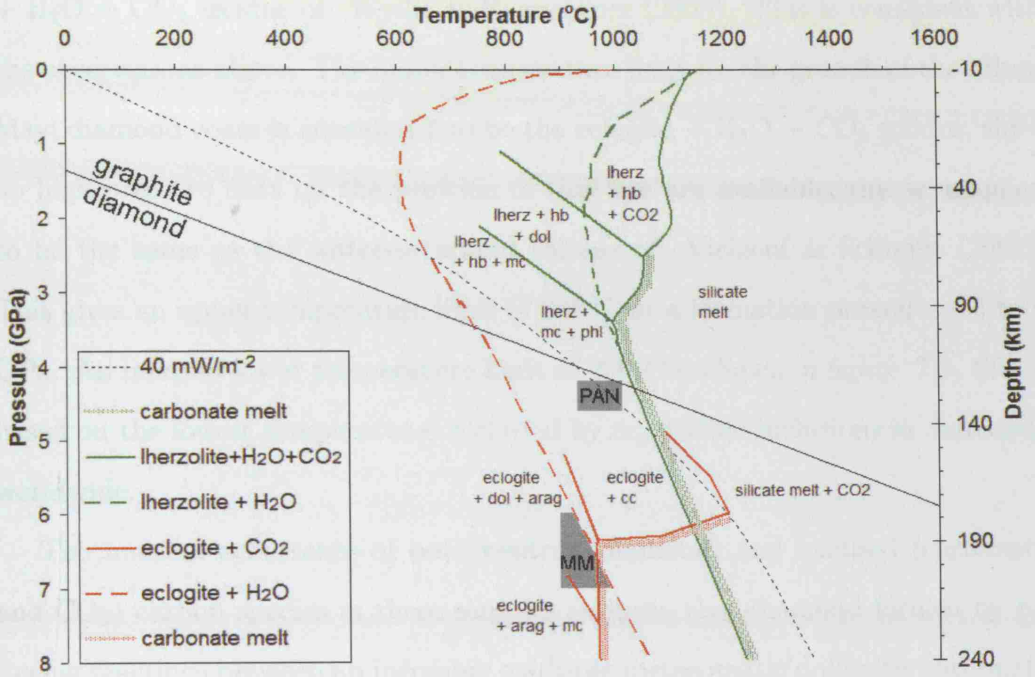

Figure 7.1: Pressure-temperature characteristics of fibrous diamond growth at Panda and Mbuji Mayi (grey boxes). The green dashed line is the solidus curve of lherzolite+H_2O and the solid green line shows the stability fields of carbonate phases in lherzolite + H_2O + CO_2 (Wyllie & Ryabchikov, 2000); the green dotted area on the high-temperature side of the lherzolite solidus line is the region of low degree carbonate melt. The red dashed line is the eclogite + H_2O solidus (Vielzeuf & Schmidt, 2001); the solid red line is the stability field of carbonate phases in eclogite + CO_2 (Hammouda, 2003), these fields are likely to shift to lower temperatures with the addition of H_2O. The red dotted area on the high-temperature side of this line is the region of low degree melting of eclogite. Also shown are the diamond-graphite line (Berman & Simon, 1955) and a shield geothermal gradient of 40 mW/m^{-2} calculated after Pollack & Chapman (1977). Abbreviations, lherz - lherzolite, cc - calcite, arag - aragonite, dol - dolomite, ms - magnesite, phl - phlogopite, hb - hornblende.

+ H_2O + CO_2 solidus of Wyllie & Ryabchikov (2000). This is consistent with the observations above. The upper temperature limit for the growth of the Mbuji Mayi diamond coats is considered to be the eclogite + H_2O + CO_2 solidus, since no high pressure data on the position of this line are available, this is assumed to be the same as the water-saturated solidus of Vielzeuf & Schmidt (2001). This gives an upper temperature limit of 990°C at a formation pressure of 6 to 7 GPa. An inferred lower temperature limit of 900°C is shown in figure 7.1, this is based on the lowest temperatures recorded by crystalline inclusions in diamonds worldwide.

The unusual occurrence of both neutral (diamond) and oxidised (carbonate and CO_2) carbon species in these samples suggests that diamond formed by reducing reactions between an incoming oxidising metasomatic dolomitic carbonate melt and the more reduced minerals of the host mantle reservoir e.g. in eclogite dolomite - coesite $\rightleftharpoons$ clinopyroxene - diamond (DCDD, eqn. 3.2); in peridotite dolomite - enstatite $\rightleftharpoons$ forsterite - diopside - diamond (DMFDD; eqn. 3.4). Figure 7.2 shows the temperature - f_{O_2} region of fibrous diamond growth in the mantle at Panda and Mbuji Mayi (Stachel et al., 2003).

The upper limit of oxygen fugacity of the incoming carbonate fluid is ≈0.3 log f_{O_2} at the temperature of fibrous diamond growth. In the Mbuji Mayi eclogite, fibrous diamond growth occurred in a window close to the FsMC buffer (ferrosilite to magnetite + coesite; the high pressure equivalent of the fayalite - magnetite - quartz buffer FMQ). In the Panda lherzolite, the oxygen fugacity during fibrous diamond growth may have extended down to approximately -1.5 log f_{O_2} below FsMC, the lower limit of carbonate stability in lherzolite. These oxidising conditions are consistent with the dominance of H_2O and absence of CH_4 in the

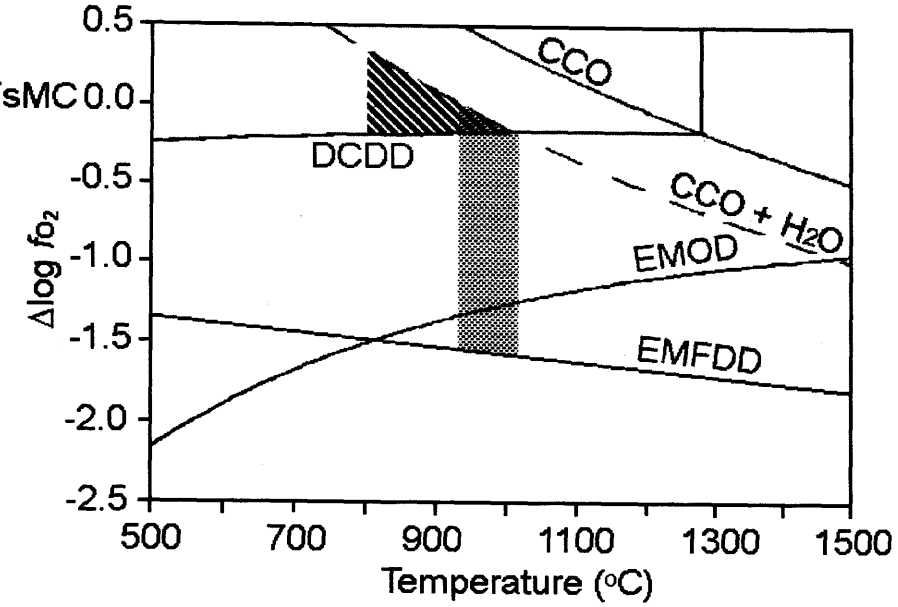

Figure 7.2: Isobaric temperature - δlog f_{O_2} section showing FO_2 characteristics of fibrous diamond growth in the peridotitic Panda coats (black spotted area) and at Mbuji Mayi (grey striped area) at 5 GPa relative to the f_{O_2} of FsMC (ferrosilite to magnetite + coesite; the high pressure equivalent of the fayalite - magnetite - quartz buffer FMQ). The reaction lines separating the stability fields of carbonate (high f_{O_2} side) and diamond (low f_{O_2} side) in fluid (CCO) and in eclogite (DCDD), lherzolite (EMFDD) and harzburgite (EMOD) are from Luth (1993). The position of the CCO buffer in the presence of water has been corrected using the data of Sokol et al. (2001) extrapolated to 1000°C.

inclusions, according to the thermodynamic modelling of Sokol et al. (2001).

Liquids can migrate through rocks by self generating hydraulic fracture [1], or

[1]Hydraulic fracture is extensional fracture caused by the pressure exerted by the fluid/melt. At the tip of the injecting fluid/melt is a transient low pressure cavity, which sucks volatiles and pore fluids from the wall rocks.

by porous flow. The latter involves the movement of liquid along grain boundaries and is dependent on the dihedral angle [1] Lower dihedral angles allow greater porous flow, and interconnectivity of a liquid can be maintained along grain edges up to 60°; at dihedral higher angles, liquid forms pools at three-grain corners. Dihedral angles increase in the order carbonatite <mafic melt< H_2O-CO_2 (Best, 2003). This means that carbonatitic and mafic silicate melts are stable along intergrain edges at melt fractions as low as 0.1 and 1% respectively, whereas H_2O-CO_2 fluids infiltrate grain edges only at high volumes ($\geq$8%) (Best, 2003). SiO_2-rich melts have low mobility, in experiments at $\leq$1.5 GPa using nepheline-normative, SiO_2-rich melts Maumus et al. (2004) showed that the median dihedral angles at olivine-olivine-melt contacts are $\approx$50°. However the olivine-melt interfacial energy is anisotropic so that connectivity is only achieved at $\geq$ 0.3 vol%; since SiO_2-rich melts are only present at low volume fraction in peridotites, these melts either occur as isolated pockets or have a low degree of connectivity. Furthermote, the high viscosity of SiO_2-rich melts means that they have very reduced mobility in the upper mantle (Maumus et al., 2004). Where silicate and carbonate melts coexist in a solid-dominated assemblage, the silicate melt selectively wets the grain-edge channels between solid phases, pushing the carbonate melt away from the grain edges and into the center of the melt pockets (Minarik, 1998). This prevents the carbonate melt from migrating independently and separating from the silicate melt, and may help explain the close association

[1]The dihedral angle is the angle formed by intersecting liquid/crystal interfaces. It is dependant on the crystal-crystal interfacial energy (and hence on the mineralogy of the host rock) and on the liquid-crystal interfacial energy (and hence on the type of liquid) and on temperature and pressure.

of carbonate and silicate melts (Minarik, 1998). Dihedral angle studies suggest that the different fluid components in the inclusions have varying degrees of mobility in the mantle. The high mobility of carbonate is consistent with this being the parental metasomatic fluid in the diamond coat system; brine and silicate-rich melt are less mobile and are thought to be enriched or generated locally.

Liquid connectivity is also dependent on the composition of the host rock; at 5 GPa the dihedral angle of aqueous fluid is 41 ± 2^{o} in forsterite (Mibe et al., 1998) and 52 ± 6^{o} aqueous fluid in pyrope (Ono et al., 2002). Toramaru & Fujii (1986) conducted experiments in lherzolite and showed that dihedral angles are much lower for melt in contact with olivine-olivine boundaries than for olivine-pyroxene and pyroxene-pyroxene boundaries. Therefore, the modal proportion of olivine in the host rock is an important factor in liquid connectivity, and so connectivity will decrease in the order dunite<harzburgite<lherzolite<eclogite. The dihedral angle of aqueous fluid is 62 to 68^{o} in eclogite (garnet and clinopyroxene, mono- and bi-mineralic) at 5 GPa, indicating that aqueous fluid in eclogite exists in isolated pores and does not migrate by porous flow (Mibe et al., 2003).

In conclusion, the diamond coats formed during metasomatic interaction between an incoming H_2O-bearing carbonate fluid and the solid eclogitic and peridotitic host mantle.

7.4 Model for the Growth of Coated Diamond

A schematic sketch of the following model is shown in figure 7.3. The starting point for this model is lithospheric mantle (peridotitic and eclogitic) containing ancient octahedral diamonds with a range of histories, parageneses, nitrogen

contents and aggregation states and carbon and nitrogen isotopic compositions. These various diamond populations later form the cores of the coated diamonds. It is thought that at least some of the cores in the Mbuji Mayi sample set may have grown in the presence of a silicate-sulphide melt. No further information is given on the origin of the diamond cores, as it is beyond the scope of this study.

At a significantly later date, the lithospheric mantle had cooled and was about 200°C cooler than it was during the growth of the normal octahedral diamonds, and no silicate melt is present. We are developing a model for diamond growth related to solid state brittle fracture of the mantle under an applied strain, such as a tectonic or shock event. Fractures are likely to have followed lines of weakness in the lithospheric mantle, such as pre-existing cracks and veins, along which ancient diamonds are located. At mantle pressures, reaction and dissolution is envisaged to have been concentrated at compressional nodes of the transient shear surfaces.

Lateral movement (shear) between fracture surfaces leads to the development of stress nodes focused on rough features. Many xenoliths show faceted surfaces that must reflect pre-existing planes of weakness and brittle fracture surfaces within the mantle. Small-scale transient high pressure points (compressional nodes) and low pressure points (extensional nodes) lead to the transient and localised pressure gradients. Mineral dissolution occurs under high-pressure regimes, this widens the crack/vein and allows the infiltration of metasomatic fluid. C-O-H fluids can move effectively around the mantle if they move through fractures, as there is no need to wet grain boundary surfaces. Areas of transient low pressure may suck out grain boundary fluids/melts lodged in the wall rock. Therefore, the composition of the metasomatic fluid is modified by fluid/melt addition and my mineral dissolution. Vein extension may also proceed via the

melting of hydrous and incompatible-rich solid solution minerals (phlogopite, Cr/Al spinel and apatite) by intergranular porous fluid flow into the pre-existing vein assemblage as the solidus is lowered by fluid infiltration (e.g. Foley 1992). Metasomatism widens the vein and may allow tributary veins to develop in the wall rock. The microscopic extension of veins allows the invasion of carbonate-H_2O±KCl fluid into the solid eclogitic and peridotitic host mantle region.

From these veins, the fluid propagates into the wall rock by intergranular porous flow. Porous flow is associated with fluid-rock reactions, such as interstitial crystallization of the melt fraction and dissolution and partial melting of wall rock minerals as well as reactive chromatographic processes. Some of the dominant carbonate component was reduced by metasomatic interaction with the various wall rocks and wall rock minerals. Fractional crystallisation of the modified carbonate led to the precipitation of secondary olivine, clinopyroxene (present in carbonate- and KCl-bearing micro-inclusions in the Panda samples), carbonate (both sample sets), phlogopite and apatite (Mbuji Mayi samples). This enriches the residual fluid in CO_2, which was available for further reduction to diamond, and also H_2O and KCl. In peridotite, free CO_2 would only have been present when the wall rocks were carbonated, armouring them against further intrusion by CO_2. C-O-H-rich fluids have high dihedral angles, so do not infiltrate far into the wall rock, but instead pool at grain boundaries where then enhance mineral dissolution and catalyse the growth of diamond. Diamond precipitated on the pre-existing diamond cores, which provided a low surface energy interface for nucleation. The low temperature and high levels of carbon supersaturation led to high levels of diamond nucleation on the diamond cores. Growth of individual nuclei was rapid (ca. minutes) because of the volatile-rich carbonate-H_2O-KCl

growth medium, as shown in the carbonate-KCl diamond growth experiments.

Dissolution of wall-rock minerals (at temperatures lower than their melting temperatures) occurs during the initial infiltration of the melt fraction into wall-rock, due to the dominance of surface energy minimization on melt flow at the intergranular scale (Foley, 1992). Dissolution of olivine and/or orthopyroxene occurs preferentially because these minerals are furthest from equilibrium with the alkaline-rich metasomatic fluid, this imparts a refractory wall-rock component on to the melt composition (Foley, 1992). This may lead to the conversion of harzburgite to lherzolite, as suggested in the study of peridotitic macro-silicate inclusions in the Panda diamond coats (section 4.5.1). The higher dihedral angle of fluids in eclogite relative to peridotite (Mibe et al., 2003) means that the metasomatic fluid remains in contact with the eclogite wall rock for longer, therefore matrix dissolution may proceed further. This, combined with the higher SiO_2 and Al_2O_3 content of eclogite relative to peridotite, leads to the enrichment in the silicate end-member fluid observed in the eclogitic sample from Panda, and possibly also in the Mbuji Mayi fluid inclusions and in inclusions. This process may eventually lead to the generation of alkaline magma, such as kimberlite. Zhang et al. (2003) describes polymict peridotite xenoliths from the Kaapvaal craton (South Africa), which are thought to have been variably affected by melt-assisted deformation/crack propagation, possibly associated with kimberlite precursors. Reaction between pyroxene and the KCl-bearing H_2O-rich fluid may have formed biotite or phlogopite in the host mantle.

The concentration of volatiles by fractional crystallisation and carbonate reduction and crystallisation may have enhanced vein propagation and so assisted the extension of the vein network and propagation of the carbonate-$H_2O\pm$KCl

fluid. If contemporaneous with a strain event, this process could have been aided by dissolution and reaction at compressional nodes distributed on a grain-scale. By this iterative method, the vein network was likely able to propagate, utilising existing lines of weakness.

Metasomatism is limited to a distance of << 1 meter from the propagating vein and proceeds via chromatographic reactive processes (Bodinier et al., 2004). Similarities between the samples from the Slave and Congo-Kasai cratons suggests that this process may be widespread and repeatable. A coupled structural and geochemical study of the Ronda peridotite (Spain) has revealed km scale percolation in the subcontinental lithosphere associated with melt-rock reactions (Van der Wal & Bodinier, 1996).

7.5 Octahedral and Fibrous Diamond Compared

This section addresses the possible reasons for the morphological difference between the diamond core (octahedral) and the coat (fibrous). The fibrous morphology, the uptake of inclusions and the symmetrical morphology indicate that fibrous diamond growth was rapid and occurred in the presence of a fluid (Boyd et al., 1994). Rapid growth is consistent with the generally high lattice nitrogen content of fibrous relative to octahedral diamond; nitrogen is unstable in the diamond lattice and would be replaced by carbon during slow diamond growth (Boyd et al., 1994). Octahedral diamonds are also thought to grow from a fluid phase based on the low density of crystallographic dislocations in the lattice (Sunagawa, 1984) and the polyhedral shape of diamond (Bulanova, 1995). This study provides additional information that may be used to investigate why growth rates

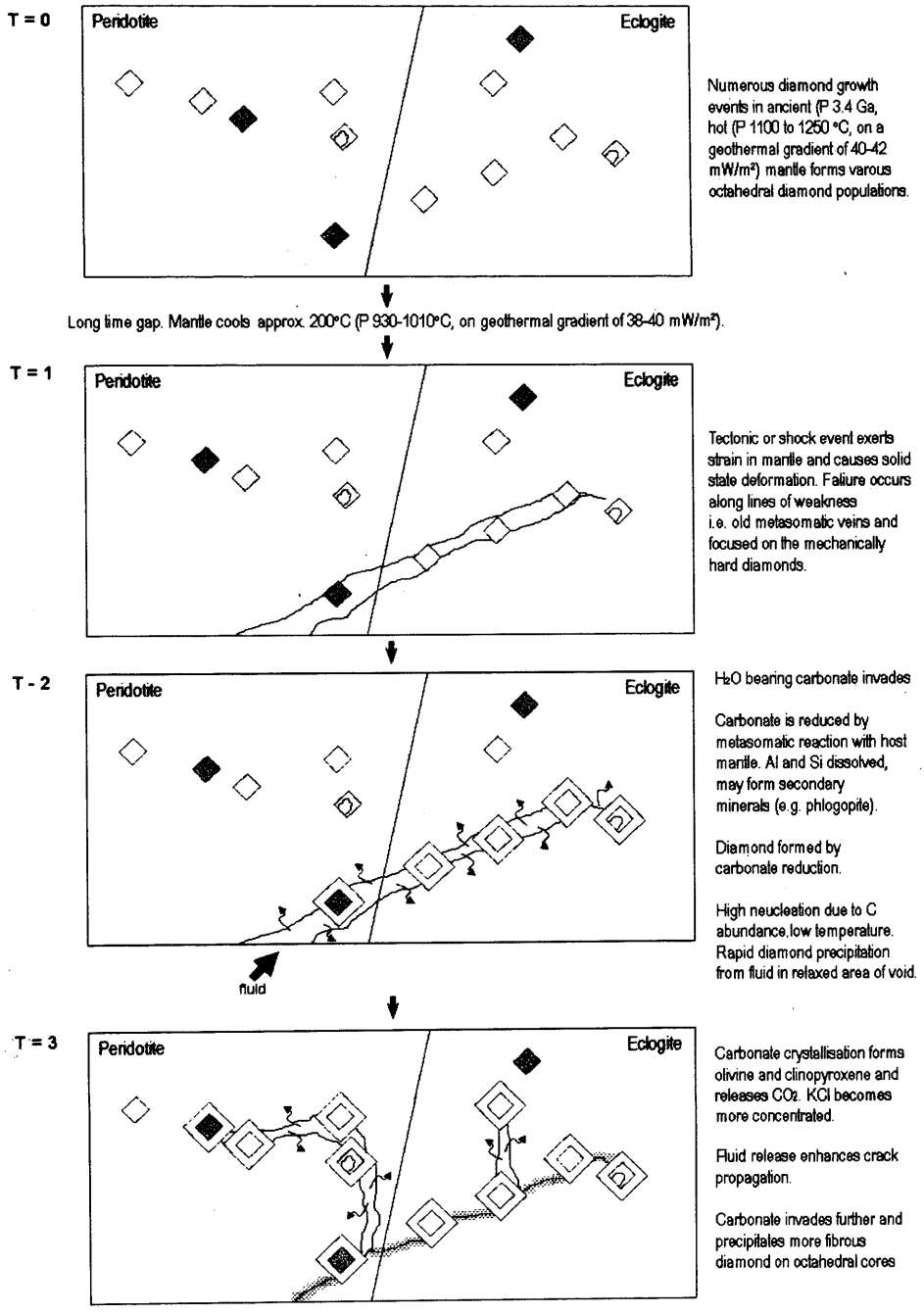

Figure 7.3: Schematic sketch of the coated diamond growth model.

of the coat are higher than of the core.

7.5.1 Chemical Effect

The LA-ICP-MS study of diamond cores and coats from Mbuji Mayi identified two different fluids; the core grew in the presence of a silicate melt (probably hydrous) while the coat grew in a water-rich carbonatite. Differences in the speciation of carbon (CO_2 in the silicate melt, CO_3 in carbonate) in these different fluids will cause differences in the reactivity of the diamond surface. There may also have been differences in the levels of carbon and volatile saturation between the two fluids causing differences in the rate of carbon diffusion the the diamond growth surface. The fluid in the fibrous coats is dominated by water and carbonate and therefore has a high level of volatile saturation. Under conditions of fluid and carbon supersaturation, an adhesive-type growth method occurs and there is an increase in the rate of diamond nucleation and precipitation, leading to an irregular atomic arrangement of carbons in the diamond lattice, a rough crystal-fluid interface and the formation of micro- and poly-crystalline diamond aggregates (Sunagawa, 1990). Fibrous diamond growth may be the result of a highly reactive diamond surface and a ready supply of carbon to the growth surface. This immediate reaction of carbon species to form diamond is unlikely to cause isotope fractionation. In contrast, the volatile concentration of the diamond core fluid is likely to be lower than the coat fluid, therefore carbon diffusion to the growth surface will be slower. The diamond surface may also be less reactive to the carbon-species present in the silicate melt.

7.5.2 Temperature Effect

Inclusion geothermometry of the Panda diamond coats indicates that they equilibrated at low temperatures (930 to 1010°C), compared to octahedral peridotitic diamond growth at Panda (1100 to 1250°C; Tappert et al. (2005)). Lower temperatures are consistent with the IaA state of nitrogen in the coats. Low temperatures favour high rates of nucleation and so are more likely to lead to the development of polycrystalline morphologies. The temperature difference between octahedral and fibrous diamond growth may indicate different types of growth event: octahedral Panda diamonds may have grown during a thermal event (suggested by Tappert et al. (2005) on the basis of the low aggregation state of nitrogen relative to the high equilibration temperatures) and may be igneous precipitates; while the Panda coats grew during a metasomatic event.

Bibliography

Akagi, T. & Masuda, A. (1988). Isotopic and Elemental Evidence for a Relationship between Kimberlite and Zaire Cubic Diamonds. *Nature*, 336(6200), 665–667. 1.2, 1.2.1, 5.3.2.1, 5.4.2.3

Akaishi, M., Kanda, H., & Yamaoka, S. (1990). Synthesis of Diamond from Graphite-Carbonate Systems under Very High Temperature and Pressure. *Journal of Crystal Growth*, 104, 578–581. 5.3.1.1, 6.2.1.1, 6.4

Akaishi, M., Kumar, M., Kanda, H., & Yamaoka, S. (2000). Formation Process of Diamond from Supercritical H2O-CO2 Fluid under High Pressure and High Temperature Conditions. *Diam Relat Mater*, 9(12), 1945–1950. 3.3.3.2, 6.2.1.2, 6.2.1.3

Akaishi, M., Kumar, M. D. S., Kanda, H., & Yamaoka, S. (2001). Reactions between Carbon and a Reduced C-O-H Fluid under Diamond-Stable Hp-Ht Condition. *Diam Relat Mater*, 10(12), 2125–2130. 3.3.3.2

Akaishi, M., Yamaoka, S., Ueda, F., & Ohashi, T. (1996). Synthesis of Polycrystalline Diamond Compact with Magnesium Carbonate and Its Physical Properties. *Diam. Relat. Mat.*, 5(1), 2–7. 6.2.1.1

Anders, E. & Zinner, E. (1993). Interstellar Grains in Primitive Meteorites: Diamond, Silicon Carbide and Graphite. *Meteoritics*, 28, 490–514. 2.1.3

Arima, M. & Kozai, Y. (2003). Diamond Crystallization from Carbonatitic Melts by Metasomatic Reducing Reactions. *Geochim Cosmochim Ac*, 67(18), A23–A23. 5.3.1.1

Arima, M., Kozai, Y., & Akaishi, M. (2002). Diamond Nucleation and Growth by Reduction of Carbonate Melts under High-Pressure and High-Temperature Conditions. *Geology*, 30(8), 691–694. 6.2.1.3

Arima, M., Nakayama, K., Akaishi, M., Yamaoka, S., & Kanda, H. (1993). Crystallisation of Diamond from a Silicate Melt of Kimberlite Composition in High-Pressure High-Temperature Experiments. *Geology*, 21, 968–970. 6.2.1.1

Ayers, J. C. & Eggler, D. H. (1995). Partitioning of Elements between Silicate Melt and H2O-NaCl Fluids at 1.5 and 2.0 GPa Pressure - Implications for Mantle Metasomatism. *Geochim Cosmochim Ac*, 59(20), 4237–4246. 6.1

Bedini, R., Bodinier, J., Dautria, J., & Morten, L. (1997). Evolution of LILE-enriched small melt fractions in the lithospheric mantle: a case study from the East African Rift. *Earth and Planetary Science Letters*, 153, 67–83. 4.5.5

Berman, R. & Simon, R. (1955). On the Graphite-Diamond Equilibrium. *Zeit. Elektrochem.*, 59, 333–338. 4.10, 7.1

Bertie, J. E., Labbe, H. J., & Whalley, E. (1968). Infrared Spectrum of Ice 6 in Range 4000-50 Cm-1. *J. Chem. Phys.*, 49(5), 2141. 3.3.2, 3.3.2.2

Best, M. (2003). *Ingeous and Metamorphic Petrology.* Blackwell Publishing. 7.3

Bibby, D. (1982). Impurities in Natural Diamond. *Chemistry and Physics of Carbon*, 18, 3–91. 2.2.1.1, 2.2.3.3, 5.1

Bleeker, W. & Davis, W. (1999). The 1991-1996 Natmap Slave Province Project: Introduction. *Can. J. Earth Sci.*, 36(7), 1033–1042. 1.3

Bobrov, A. V., Litvin, Y. A., & Divaev, F. K. (2004). Phase Relations and Diamond Synthesis in the Carbonate-Silicate Rocks of the Chagatai Complex, Western Uzbekistan: Results of Experiments at P=4-7 GPa and T=1200-1700 Degrees C. *Geochem. Int.*, 42(1), 39–48. 6.2.1.2

Bodinier, J. L., Menzies, M. A., Shimizu, N., Frey, F. A., & McPherson, E. (2004). Silicate, Hydrous and Carbonate Metasomatism at Lherz, France: Contemporaneous Derivatives of Silicate Melt-Harzburgite Reaction. *J. Petrol.*, 45(2), 299–320. 2.2.3.1, 7.4

Boyd, F. R. & Gurney, J. (1986). Diamonds and the African Lithosphere. *Science*, 232, 472–477. 2.1.1, 4.4.5

Boyd, F. R., Gurney, J. J., & Richardson, S. H. (1985). Evidence for a 150-200-km Thick Archean Lithosphere from Diamond Inclusion Thermobarometry. *Nature*, 315(6018), 387–389. 2.1.1

Boyd, S. R., Mattey, D. P., Pillinger, C. T., Milledge, H. J., Mendelssohn, M. J., & Seal, M. (1987). Multiple Growth Events During Diamond Genesis: An Integrated Study of Carbon and Nitrogen Isotopes and Nitrogen Aggregation State in Coated Stones. *Earth Planet Sc Lett*, 86, 341–353. 2.2.1.1, 2.2.2.2, 3.2.2.1, 5.4.2.3

Boyd, S. R., Pillinger, C. T., Milledge, H. J., & Seal, M. J. (1992). C-Isotopic and N-Isotopic Composition and the Infrared- Absorption Spectra of Coated Diamonds - Evidence for the Regional Uniformity of CO2-H2O Rich Fluids in Lithospheric Mantle. *Earth Planet Sc Lett*, 108(1-3), 139–150. 2.2.1.1, 2.2.2.2, 3.2.2.1, 5.3.2.1, 5.4.2.1, 5.4.2.3

Boyd, S. R., Pineau, F., & Javoy, M. (1994). Modeling the Growth of Natural Diamonds. *Chem Geol*, 116(1-2), 29–42. 1.2, 2.1.1.1, 2.2.1.1, 2.2.2.1, 3.2.2.1, 5.4.2.3, 7.5

Brenan, J. (1993). Partitioning of Fluorine and Chlorine between Apatite and Aqueous Fluid at High Pressure and Temperature: Implications for the F and Cl Content of High P-T Fluids. *Earth Planet Sc Lett*, 117, 251–263. 6.1

Brey, G. P., Kogarko, L. N., & Ryabchikov, I. D. (1991). Carbon-Dioxide in Kimberlitic Melts. *Neues Jahrb. Mineral.-Mon.hefte*, 4, 159–168. 2.1.1.1

Bulanova, G. P. (1995). The Formation of Diamond. *J. Geochem. Explor.*, 53, 1–23. 1.1, 5.4.1.1, 7.5

Bulanova, G. P., Griffin, B. J., Ryan, C. G., Shestakova, O., & Barnes, S. (1996). Trace Elements in Sulfide Inclusions from Yakutian Diamonds. *Contrib Mineral Petr*, 124(2), 111–125. 2.2.3.1

Bulanova, G. P., Griffin, W. L., & Ryan, C. G. (1998). Nucleation Environment of Diamonds from Yakutian Kimberlites. *Mineral Mag*, 62(3), 409–419. 5.3.1.2

Bundy, F. (1989). Pressure-temperature phase diagram of elemental carbon. *Physica A*, 156(1), 169–177. 2.5

Bundy, F. P., Strong, H. M., Bovenkerk, H. P., & Wentorf, R. H. (1961). Diamond-Graphite Equilibrium Line from Growth and Graphitization of Diamond. *J. Chem. Phys.*, 35(2), 383. 6.2.1

Burgess, R., Harrison, D., Hobson, E., Cartigny, P., & Harris, J. (2005). Volatile Composition of Canadian Fibrous Diamonds: Implications for the Origin and Fractionation of Halogens in the mantle. In *in prep.* 1.2.1, 4.5.2.2

Burgess, R., Johnson, L. H., Mattey, D. P., Harris, J. W., & Turner, G. (1998). He, Ar and C Isotopes in Coated and Polycrystalline Diamonds. *Chem Geol*, 146(3-4), 205–217. 1.2.1

Cartigny, P. (2005). Stable Isotopes and the Origin of Diamond. *Elements*, 1(2), 79–84. 2.2.2.1

Cartigny, P., Boyd, S. R., Harris, J. W., & Javoy, M. (1997). Nitrogen Isotopes in Peridotitic Diamonds from Fuxian, China: The Mantle Signature. *Terr. Nova*, 9(4), 175–179. 2.2.2.2

Cartigny, P., Harris, J. W., & Javoy, M. (1998). Eclogitic Diamond Formation at Jwaneng: No Room for a Recycled Component. *Science*, 280(5368), 1421–1424. 2.2.2.1, 2.2.2.2

Chinn, I. L., Gurney, J. J., Milledge, H. J., Taylor, W., & Woods, A. (1995). Cathodolumiencence Properties of CO2-Bearing and CO2-Free Diamonds from the George Creek K1 Kimberlite Dike. *Int Geol Rev*, 37, 254–258. 2.2.3.3, 2.4.2, 3

Chrenko, R. M., McDonald, R. S., & Darrow, K. A. (1967). Infra-Red Spectra of Diamond Coat. *Nature*, 213(5075), 474. 1.2.1

Chrenko, R. M., Tuft, R. E., & Strong, H. M. (1977). Transformation of State of Nitrogen in Diamond. *Nature*, 270(5633), 141–144. 2.2.1.1

Clausing, R. (1997). Diamond Morphology. In M. Prelas, A. Popovici, & L. Bigelow (Eds.), *Handbook of Industrial Diamonds and Diamond Films* (pp. 19–45). Kluwer Academic Publishers. 2.3, 2.3.1.2

Clifford, T. (1966). Tectono-Metallogenic Units and Metallogenic Provinces of Africa. *Earth and Planetary Science Letters*, 1, 421–434. 2.1.1

Collins, A. T. (2000). Spectroscopy of Defects and Transition Metals in Diamond. *Diam. Relat. Mat.*, 9(3-6), 417–423. 2.2.1.2

Collins, R. J. & Fan, H. Y. (1954). Infrared Lattice Absorption Bands in Germanium, Silicon, and Diamond. *Physical Review*, 93(4), 674–678. 3.1.1

Coltorti, M., Beccaluva, L., Bonadiman, C., Salvini, L., & Siena, F. (2000). Glasses in Mantle Xenoliths as Geochemical Indicators of Metasomatic Agents. *Earth Planet. Sci. Lett.*, 183(1-2), 303–320. 2.2.3.1

Creaser, R. A., Grutter, H., Carlson, J., & Crawford, B. (2004). Macrocrystal Phlogopite Rb-Sr Dates for the Ekati Property Kimberlites, Slave Province, Canada: Evidence for Multiple Intrusive Episodes in the Paleocene and Eocene. *Lithos*, 76(1-4), 399–414. 1.3.2

Dalphe, C. & Ballantyne, D. (2004). Quantitative Analysis of Ultra-Trace Im-

purities in Carbon-Based Materials by La-Icp-Ms: Application to Diamond Profiling. In *55th Diamond Conference* (pp. 7.1–7.2). Warwick, U.K. 5.2.4

Dalton, J. A. & Presnall, D. C. (1998). The Continuum of Primary Carbonatitic-Kimberlitic Melt Compositions in Equilibrium with Lherzolite: Data from the System CaO-MgO-Al2O3-SiO2-CO2 at 6 GPa. *J. Petrol.*, 39(11-12), 1953–1964. 2.1.1.1, 4.5.3.1, 5.4.2.2

Damarupurshad, A., Hart, R., Sellschop, J., & Meyer, H. O. A. (1997). The Application of Inaa to the Geochemical Analysis of Single Diamonds. *Journal of Radioanalytical and Nuclear Chemistry*, 219(1), 33–39. 1.2.1, 5.1, 5.3.1.2

Datchi, F., Loubeyre, P., & LeToullec, R. (2000). Extended and Accurate Determination of the Melting Curves of Argon, Helium, Ice (H2O), and Hydrogen (H-2). *Phys. Rev. B*, 61(10), 6535–6546. 3.11, 3.3.2.2

Davies, G. (1976). A-Nitrogen Aggregate in Diamond - Its Symmetry and Possible Structure. *Journal of Physics C-Solid State Physics*, 9(19), L537–L542. 2.2.1.1

Dawson, J. (1980). *Kimberlites and Their Xenoliths*, volume 15. Chicago: Springer Verlag. 1.2.1, 2.1.1.1, 5.3, 5.3.1.2

Dawson, J. (2004). A fertile harzburgitegarnet lherzolite transition: possible inferences for the roles of strain and metasomatism in upper mantle peridotites. *Lithos*, 77, 553–569. 4.5.1

Dawson, J. B. (1984). Contrasting Types of Upper-Mantle Metasomatism. In J. Kornprobst (Ed.), *Kimberlites II: The Mantle and CrustMantle Relationships* (pp. 289294). Amsterdam: Elsevier. 2.1

De Corte, K., De Schrijver, I., Vanhaecke, F., & Moens, L. (2004). Is There a Correlation between the Chemical Fingerprint of Gem Diamonds from a Single Mine and Their Nitrogen Content or Paragenesis? An La-Icp-Ms Case Study of Diamonds from Premier (South Africa), De Beers Pool (South Africa) Abd Udachnaya (Russia). In *55th Diamond Conference* (pp. 8.1). Warwick, U.K. 5.5

Deines, P. (1980). The Carbon Isotopic Composition of Diamonds - Relationship to Diamond Shape, Color, Occurrence and Vapor Composition. *Geochim. Cosmochim. Acta*, 44(7), 943–961. 2.2.2.1

Deines, P. (2002). The Carbon Isotope Geochemistry of Mantle Xenoliths. *Earth-Sci. Rev.*, 58(3-4), 247–278. 1.2.1, 2.2.2.1

Deines, P. & Harris, J. W. (1995). Sulfide Inclusion Chemistry and Carbon Isotopes of African Diamonds. *Geochim Cosmochim Ac*, 59(15), 3173–3188. 2.2.3.1, 2.2.3.1, 2.2.3.2, 5.3.1.2, 5.3.1.3

Deines, P., Harris, J. W., & Gurney, J. J. (1987). Carbon Isotopic Composition, Nitrogen-Content and Inclusion Composition of Diamonds from the Roberts Victor Kimberlite, South-Africa - Evidence for C-13 Depletion in the Mantle. *Geochim. Cosmochim. Acta*, 51(5), 1227–1243. 2.2.2.1

Deines, P., Harris, J. W., & Gurney, J. J. (1993). Depth-Related Carbon-Isotope and Nitrogen Concentration Variability in the Mantle Below the Orapa Kimberlite, Botswana, Africa. *Geochim Cosmochim Ac*, 57(12), 2781–2796. 2.2.2.1

Dows, D. A. & Schettino, V. (1973). Two-phonon infrared absorption spectra in crystalline carbon dioxide. *J. Chem. Phys.*, 54(11), 5009–5016. 3.3.2.3

Dubessy, J., Lhomme, T., Boiron, M. C., & Rull, F. (2002). Determination of Chlorinity in Aqueous Fluids Using Raman Spectroscopy of the Stretching Band of Water at Room Temperature: Application to Fluid Inclusions. *Appl. Spectrosc.*, 56(1), 99–106. 3.2.2.2

Eggler, D. (1983). Upper mantle oxidation state: evidence from olivine-orthopyroxene-ilmenite assemblages. *Geophysical Research Letters*, 10, 365–368. 2.4.2

Eggler, D. H. (1987). Solubility of Major and Trace Elements in Mantle Metasomatic Fluids: Experimental Constraints. In M. Menzies & C. Hawkesworth (Eds.), *Mantle Metasomatism*, volume 2 (pp. 21–39). London: Academic Press Inc. 2.2.3.1

El Fadili, S. & Demaiffe, D. (1999). Petrology of Eclogite and Granulite Nodules from the Mbuji Mayi Kimberlites (Kasai, Congo): Significance of Kyanite-Omphacite Intergrowths. In J. Gurney, M. Gurney, S. Pascoe, & S. Richardson (Eds.), *Proceedings of the Viith International Kimberlite Conference*, volume 1 (pp. 205–213). Red Roof Design cc. 1.3.1, 4.5.1, 4.6

Ernst, W. G. & Liou, G. (1995). Contrasting Tectonic Styles of the Qinling-Dhabie-Sulu and Franciscan Metamorphic Belts. *Geology*, 23, 353–356. 2.1.2

Evans, T. & Qi, Z. (1982). The Kinetics of the Aggregation of Nitrogen-Atoms in Diamond. *Proc. R. Soc. London Ser. A-Math. Phys. Eng. Sci.*, 381(1780), 159. 2.2.1.1

Evans, T. & Sauter, D. (1961). Etching of diamond surfaces with gases. *Phil. Mag.*, 6, 429–440. 2.3.1.2

Farmer, V. (1974a). *Infrared Spectra of Minerals.* London: Mineralogical Society of London. 3.1

Farmer, V. (1974b). The Layer Silicates. In V. Farmer (Ed.), *Infrared Spectra of Minerals* (pp. 331–364). Mineralogical Society. 3.3.2.1

Fesq, H., Bibby, D., Erasmus, C., Kable, E., & Sellschop, J. (1975). Determination of Trace Element Impurities in Natural Diamonds by Instrumental Neutron Activation Analysis. In L. Aherns, J. Dawson, A. Duncan, & A. Erlank (Eds.), *Phys. Chem. Earth*, volume 9 (pp. 817). Oxford: Pergamon Press. 2.2.3.3, 5.1, 5.3, 5.3.1.2

Fieremans, J., Hertogen, J., & Demaiffe, D. (1984). Petrology, Geochemistry and Strontium Isotopic Composition of the Mbuji Mayi and Kundelungu Kimberlites (Zaire). In J. Kornprobst (Ed.), *Kimberlites, I: Kimberlites and Related Rocks* (pp. 107–120). Elsevier Science Publishers B.V. Amsterdam. 1.3.1, 4.2, 5.3.2.1

Fine, G. & Stolper, E. (1985). The Speciation of Carbon-Dioxide in Sodium Aluminosilicate Glasses. *Contrib. Mineral. Petrol.*, 91(2), 105–121. 3.2.1

Fleet, M. E. & MacRae, N. D. (1988). Partition of Ni between Olivine and Sulfide - Equilibria with Sulfide-Oxide Liquids. *Contrib Mineral Petr*, 100(4), 462–469. 5.3.1.2

Foley, S. (1992). Vein-plus-wall-rock melting mechanisms in the lithosphere and the origin of potassic alkaline magmas. *Lithos*, 28, 435–453. 7.4

Frey, F. & Green, D. (1973). The mineralogy, geochemistry and origin of Iherzolite

inclusions in Victorian basanites. *Geochimica et Cosmochimica Acta*, 38, 1023–1059. 4.5.1

Frezzotti, M., Andersen, T., Neumann, E., & Simonsen, S. (2002). Carbonatite melt-CO2 fluid inclusions in mantle xenoliths from Tenerife, Canary Islands: a story of trapping, immiscibility and fluid-rock interaction in the upper mantle. *Lithos*, 64, 77–96. 4.5.3.2

Galimov, E. M. (1991). Isotope Fractionation Related to Kimberlite Magmatism and Diamond Formation. *Geochim Cosmochim Ac*, 55(6), 1697–1708. 2.2.2.1

Gervais, F. & Piriou, B. (1975). Temperature-Dependence of Transverse and Longitudinal Optic Modes in Alpha-Phases and Beta-Phases of Quartz. *Physical Review B*, 11(10), 3944–3950. 3.12, 3.3.1.4

Giardini, A. & Tydings, J. (1962). Diamond Synthesis: Observations on the Mechanism of Formation. *American Mineralogist*, 47, 1393–1421. 2.3.1.1

Girnis, A. V., Brey, G. P., & Ryabchikov, I. D. (1995). Origin of Group 1a Kimberlites - Fluid-Saturated Melting Experiments at 45-55 Kbar. *Earth and Planetary Science Letters*, 134(3-4), 283–296. 2.1.1.1

Green, T. H. (1994). Experimental Studies of Trace-Element Partitioning Applicable to Igneous Petrogenesis - Sedona 16 Years Later. *Chem Geol*, 117(1-4), 1–36. 5.3.1.2, 5.4

Gregoire, M., Bell, D. R., & Le Roex, A. P. (2002). Trace Element Geochemistry of Phlogopite-Rich Mafic Mantle Xenoliths: Their Classification and Their Re-

lationship to Phlogopite-Bearing Peridotites and Kimberlites Revisited. *Contrib Mineral Petr*, 142(5), 603–625. 5.3, 5.4, 5.3.2.1, 5.4.2.3

Grgoire, M., Lorand, J., O'Reilly, S., & Cottin, J.-Y. (2000). Armalcolite-bearing, Ti-rich metasomatic assemblages in harzburgitic xenoliths from the Kerguelen Islands: implications for the oceanic mantle budget of high-field strength elements. *Geochimica et Cosmochimica Acta*, 64, 673694. 1.2.1

Griffin, W., Shee, S.R.and Ryan, G., Win, T., & Wyatt, B. (1999). Harzburgite to lherzolite and back again: metasomatic processes in ultramafic xenoliths from the Wesselton kimberlite, Kimberley, South Africa. *Contributions to Mineralogy and Petrology*, 134, 232–250. 4.5.1

Griffin, W. L., Gurney, J., & Ryan, C. (1992). Variations in Trapping Temperatures and Trace Elements in Peridotite-Suite Inclusions from African Diamonds - Evidence for Two Inclusion Suites, and Implications for Lithosphere Stratigraphy. *Contrib Mineral Petr*, 110, 1–15. 2.2.3.1, 4.4.5

Griffin, W. L., Jaques, A. L., Sie, S. H., Ryan, C. G., Cousens, D. R., & Suter, G. F. (1988). Conditions of Diamond Growth - a Proton Microprobe Study of Inclusions in West Australian Diamonds. *Contrib. Mineral. Petrol.*, 99(2), 143–158. 2.2.3.1

Griffin, W. L., Rege, S., Davies, R., Jackson, S., & O'Reilly, S. Y. (2004). Trace Element Analysis of Diamond by LAM ICPMS: Standardisation, Results and Direction. In *55th Diamond Conference* (pp. 6.1–6.5). Warwick, U.K. 1.2.1, 5.2.4, 5.3, 5.3.2.1, 5.3.2.1

Gurney, J., Harte, B., & Cox, K. (1975). Mantle Xenoliths in the Matsoku Kimberlite Pipe. *Phys. Chem. Earth*, 9, 507–529. 4.4.1

Gurney, J. J. (1989). Diamonds. *Geological Society of Australia Special Bulletin*, 14, 936–965. 2.2.3.1, 5.3.1.2

Guthrie, G. D., Veblen, D. R., Navon, O., & Rossman, G. R. (1991). Sub-Micrometer Fluid Inclusions in Turbid-Diamond Coats. *Earth Planet Sc Lett*, 105(1-3), 1–12. 1.2, 1.2.1, 3.3.1.4, 4.3.1, 6.2.1.1

Haggerty, S. (1986). Diamond Genesis in a Multiply Constrained Model. *nature*, 320, 34–38. 2.1.1

Hammouda, T. (2003). High-Pressure Melting of Carbonated Eclogite and Experimental Constraints on Carbon Recycling and Storage in the Mantle. *Earth Planet Sc Lett*, 214(1-2), 357–368. 7.1

Harlow, G. (1998). *The Nature of Diamonds*. Cambridge: Cambridge University Press. 2.1, 2.1.1

Harlow, G. & Davies, R. (2005). Diamonds. *Elements*, 1(2), 67–70. 2.2

Harlow, G. & Veblen, D. R. (1991). Potassium in Clinopyroxene Inclusions from Diamonds. *Science*, 251, 652–655. 4.4.3

Harris, J. W. (1968). Recognition of Diamond Inclusions .1. Syngenetic Mineral Inclusions. *Ind. Diam. Rev.*, 28(334), 402. 2.2.3.1

Harris, J. W. (1979). Inclusions in Diamond. In J. Field (Ed.), *The Properties of Diamond* (pp. 555–591). London: Academic Press. 2.2.3.1, 2.3.1.2

Harris, J. W. (1992). Diamond Geology. In J. E. Field (Ed.), *The Properties of Natural and Synthetic Diamonds* (pp. 384385). Oxford, UK: Academic Press,. 2.2.3.1

Harte, B., Hunter, R. H., & Kinny, P. D. (1993). Melt Geometry, Movement and Crystallization, in Relation to Mantle Dykes, Veins and Metasomatism. *Philos. Trans. R. Soc. Lond. Ser. Â-Math. Phys. Eng. Sci.*, 342(1663), 1–21. 5.3.1.1

Hauri, E. H., Wang, J., Pearson, D. G., & Bulanova, G. P. (2002). Microanalysis of Delta C-13, Delta N-15, and N Abundances in Diamonds by Secondary Ion Mass Spectrometry. *Chem Geol*, 185(1-2), 149–163. 5.4.1.2

Hayakawa, S., Jia, X. P., Wakatsuki, M., Gohshi, Y., & Hirokawa, T. (2000). Analysis of Trace Co in Synthetic Diamonds Using Synchrotron Radiation Excited X-Ray Fluorescence Analysis. *Journal of Crystal Growth*, 210(1-3), 388–394. 2.2.1.2, 5.3

Heaman, L. M., Kjarsgaard, B. A., & Creaser, R. A. (2003). The Timing of Kimberlite Magmatism in North America: Implications for Global Kimberlite Genesis and Diamond Exploration. *Lithos*, 71(2-4), 153–184. 1.3.2

Hervig, R., Smith, J., Steele, I., Gurney, J., Meyer, H., & Harris, J. (1980). Diamonds: Minor Elements in Silicate Inclusions: Pressure Dependent Implications. *Journal of Geophysical Research*, 8, 6919–6929. 5.3.1.2

Hills, D. & Haggerty, S. E. (1989). Petrochemistry of Eclogites from the Koidu Kimberlite Complex, Sierra Leone. *Contrib Mineral Petr*, 103, 397–422. 4.2

Ionov, D. A., Dupuy, C., Oreilly, S. Y., Kopylova, M. G., & Genshaft, Y. S.

(1993). Carbonated Peridotite Xenoliths from Spitsbergen - Implications for Trace-Element Signature of Mantle Carbonate Metasomatism. *Earth Planet Sc Lett*, 119(3), 283–297. 5.3.1.1

Iota, V. & Yoo, C. S. (2001). Phase Diagram of Carbon Dioxide: Evidence for a New Associated Phase. *Phys. Rev. Lett.*, 86(26), 5922–5925. 3.3.2.3

Ireland, T. R., Rudnick, R. L., & Spetsius, Z. (1994). Trace-Elements in Diamond Inclusions from Eclogites Reveal Link to Archean Granites. *Earth Planet Sc Lett*, 128(3-4), 199–213. 2.2.3.1

Izraeli, E. S., Harris, J. W., & Navon, O. (1999). Raman Barometry of Diamond Formation. *Earth Planet Sc Lett*, 173(3), 351–360. 4

Izraeli, E. S., Harris, J. W., & Navon, O. (2001). Brine Inclusions in Diamonds: A New Upper Mantle Fluid. *Earth Planet Sc Lett*, 187(3-4), 323–332. 1.2.1, 2.4.2, 4.3, 4.3.1, 4.6, 4.3.2.1, 4.5.3.2, 5.4.2.3, 6.1

Izraeli, E. S., Harris, J. W., & Navon, O. (2004). Fluid and Mineral Inclusions in Cloudy Diamonds from Koffiefontein, South Africa. *Geochim Cosmochim Ac*, 68(11), 2561–2575. 4.2.1, 4.3, 4.3.1, 4.5.2.3, 6.1

Jakobsson, S. & Oskarsson, N. (1990). Experimental determination of fluid compositions in the system C-O-H at high P and T and low f o 2. *Geochim Cosmochim Ac*, 54, 355–362. 2.4.2

Javoy, M., Pineau, F., & Demaiffe, D. (1984). Nitrogen and Carbon Isotopic Composition in the Diamonds of Mbuji Mayi (Zaire). *Earth Planet Sc Lett*, 68, 399–412. 1.3.1, 1.3.1, 1.2, 2.2.2.1

Johnson, E. (1991). Experimentally determined limits for H2O-CO2-NaCl immiscibility in granulates. *Geology*, 19, 925–928. 4.5.3.2

Johnson, L. H., Burgess, R., Turner, G., & Harris, J. W. (2000). Noble Gas and Halogen Geochemistry of Mantle Fluids: Comparison of African and Canadian Diamonds. *Geochim Cosmochim Ac*, 64(4), 717–732. 1.2.1, 4.2.1, 4.5.2.2, 5.3.2.1

Jones, A. (1989). Upper Mantle Enrichment by Kimberlitic or Carbonatitic Magmatism. In K. Bell (Ed.), *Carbonatites, Genesis and Evolution* (pp. 448–463). Unwin Hyman. 5.3.2.1

Jones, R., Briddon, P. R., & Oberg, S. (1992). 1st-Principles Theory of Nitrogen Aggregates in Diamond. *Philos. Mag. Lett.*, 66(2), 67–74. 2.2.1.1

Kagi, H., Lu, R., Davidson, P., Goncharov, A. F., Mao, H. K., & Hemley, R. J. (2000). Evidence for Ice VI as an Inclusion in Cuboid Diamonds from High P-T near Infrared Spectroscopy. *Mineral Mag*, 64(6), 1089–1097. 1.2.1, 2, 3.3.2, 3.3.2.2, 3.3.2.2

Kamiya, Y. & Lang, A. (1965). On the Structure of Coated Diamonds. *Philosophical Magazine*, 11, 347–357. 1.2, 1.2.1, 1.3.1, 2.3.2

Kanda, H., Akaishi, M., & Yamaoka, S. (1990). Morphology of Synthetic Diamonds Grown from Na2CO3 Solvent-Catalyst. *Journal of Crystal Growth*, 106, 471–475. 6.2.1.1

Kessel, R., Ulmer, P., Pettke, T., Schmidt, M., & Thompson, A. (2005). The waterbasalt system at 4 to 6 GPa: Phase relations and second critical endpoint

in a K-free eclogite at 700 to 1400 oC. *Earth and Planetary Science Letters*, 237, 873–892. 4.5.2.3

Kinny, P. D. & Meyer, H. O. A. (1994). Zircon from the Mantle - a New Way to Date Old Diamonds. *J Geol*, 102(4), 475–481. 1.3.1

Kirkley, M. B., Gurney, J. J., & Rickard, R. (1991). Jwaneng Framesites: Carbon Isotopes and Intergrowth Composition. In *5th International Kimberlite Conference* (pp. 127–135). Araxa: CPRM Spec Publ. 2.2.2.1

Kirkley, M. B., Smith, H., & Gurney, J. J. (1989). Kimberlite Carbonates - a Carbon and Oxygen Isotope Study. In J. Ross (Ed.), *Kimberlites and Relates Rocks*, Geol. Soc. Aust. Spec Publ. (pp. 264–281). Blackwell, 14 edition. 5.4.2.3

Klein-BenDavid, O., Izraeli, E. S., Hauri, E., & Navon, O. (2004). Mantle Fluid Evolutiona Tale of One Diamond. *Lithos*, 77, 243–253. 1.2.1, 4.2.1, 4.3.1, 4.3.2.1, 4.6, 4.5.2.2, 4.5.3.2, 5.3.2.1, 6.1

Klein-BenDavid, O., Izraeli, E. S., & Navon, O. (2002). Volatile-Rich Brine and Melt in Canadian Diamonds. *Geochim Cosmochim Ac*, 66(15A), A403–A403. 4.2.1, 4.5.3.2, 5.3.2.1, 6.1

Klein-BenDavid, O., Logvinova, A., Izraeli, E., Sobolev, N., & Navon, O. (2003). Sulfide Melt Inclusions in Yubileinaya (Yakutia) Diamonds. In *8th International Kimberlite Conference* (pp. FLA–0111). Victoria, Canada. 1.2.1, 4.3.1

Klemme, S., Blundy, J. D., & Wood, B. J. (2002). Experimental Constraints on Major and Trace Element Partitioning During Partial Melting of Eclogite. *Geochim Cosmochim Ac*, 66(17), 3109–3123. 5.3.1.1, 5.4

Koeberl, C., Schrauder, M., Andreoli, M., Brandsttter, F., Lengauer, C., & Gilmour, I. (1997). Carbonados from Central Africa and Brazil - Are They Related to Impact Events? A Geological, Spectroscopical and X-Ray Study. Tucson, Arizona. 2.1.3

Koga, K. T., Van Orman, J. A., & Walter, M. J. (2003). Diffusive Relaxation of Carbon and Nitrogen Isotope Heterogeneity in Diamond: A New Thermochronometer. *Phys. Earth Planet. Inter.*, 139(1-2), 35–43. 2.2.3.2

Krogh, E. J. (1988). The Garnet-Clinopyroxene Fe-Mg Geothermometer - a Reinterpretation of Existing Experimental-Data. *Contrib Mineral Petr*, 99(1), 44–48. 4.4, 4.4.5

Lang, A. R. (1974). Space-Filling by Branching Columnar Single-Crystal Growth - Example from Crystallization of Diamond. *J. Cryst. Growth*, 23(2), 151–153. 2.3.2

Lang, A. R. & Walmsley, J. C. (1983). Apatite Inclusions in Natural Diamond Coat. *Phys. Chem. Miner.*, 9(1), 6–8. 1.2.1, 3.2.2.2, 6.2.1.1

Lang, A. R., Yelisseyev, A. P., Pokhilenko, N. P., Steeds, J. W., & Wotherspoon, A. (2004). Is Dispersed Nickel in Natural Diamonds Associated with Cuboid Growth Sectors in Diamonds That Exhibit a History of Mixed- Habit Growth? *J. Cryst. Growth*, 263(1-4), 575–589. 2.2.1.2

Latourrette, T., Hervig, R. L., & Holloway, J. R. (1995). Trace-Element Partitioning between Amphibole, Phlogopite, and Basanite Melt. *Earth Planet Sc Lett*, 135(1-4), 13–30. 5.3.1.1, 5.4

Le Roex, A. P., Bell, D. R., & Davis, P. (2003). Petrogenesis of Group I Kimberlites from Kimberley, South Africa: Evidence from Bulk-Rock Geochemistry. *J. Petrol.*, 44(12), 2261–2286. 2.1.1.1

Levin, E., McMurdie, H., & Hall, F. (1956). *Phase Diagrams for Ceramists.* Waterville, Ohio, USA: The American Ceramic Society. 6.5

Li, C., Ripley, E. M., & Mathez, E. A. (2003). The Effect of S on the Partitioning of Ni between Olivine and Silicate Melt in Morb. *Chem Geol*, 201(3-4), 295–306. 5.3.1.2

Litvin, Y. A. (2003). Alkaline-Chloride Components in Processes of Diamond Growth in the Mantle and High-Pressure Experimental Conditions. *Dokl Earth Sci*, 389(3), 388–391. 4.5.1, 6.1, 6.4

Litvin, Y. A., Aldushin, K. A., & Zharikov, V. A. (1999). Synthesis of Diamond at 8.5-9.5 GPa in the System K2Ca(CO3)2-Na2Ca(CO3)2-C Corresponding to the Composition of Fluid-Carbonatitic in Inclusions Diamond from Kimberlites. *Dokl Akad Nauk+*, 367(4), 529–532. 6.2.1.1

Litvin, Y. A., Chudinovskikh, L. T., & Zharikov, V. A. (1997). Crystallization of Diamond and Graphite in the Mantle Alkaline-Carbonate Melts in the Experiments at Pressure 7-11 GPa. *Dokl Akad Nauk+*, 355(5), 669–672. 6.2.1.1

Litvin, Y. A., Chudinovskikh, L. T., & Zharikov, V. A. (1998a). Crystallization of Diamond in the System Na2Mg(CO3)2-K2Mg(CO3)2-C at 8-10 GPa. *Dokl Akad Nauk+*, 359(5), 668–670. 5.3.1.1, 6.2.1.1

Litvin, Y. A., Chudinovskikh, L. T., & Zharikov, V. A. (1998b). Seed Growth

of Diamond in the System Na2Mg(CO3)2-K2Mg(CO3)2-C at 8-10 GPa. *Dokl Akad Nauk+*, 359(6), 818–820. 6.2.1.1

Litvin, Y. A. & Zharikov, V. A. (1999). Primary Fluid-Carbonatitic Inclusions in Diamond Simulating by the System K2O-Na2o-CaO-MgO-FeO-CO2 as a Diamond-Producing Medium in Experiment at 7-9 GPa. *Dokl Akad Nauk+*, 367(3), 397–401. 6.2.1.1

Lu, R. & Hofmeister, A. M. (1995). Infrared Fundamentals and Phase-Transitions in CO2 up to 50 GPa. *Phys. Rev. B*, 52(6), 3985–3992. 3.11, 3.3.2.3, 3.16

Luth, R. W. (1993). Diamonds, Eclogites, and the Oxidation-State of the Earths Mantle. *Science*, 261(5117), 66–68. 7.2

Machado, W. (1985). On the Dodecahedral Growth of Coated Diamonds. *Journal of Crystal Growth*, 71, 718–727. 1.2, 2.3.2

Manning, C. (1994). The Solubility of Quartz in H2O in the Lower Crust and Upper-Mantle. *Geochimica Et Cosmochimica Acta*, 58, 4831–4839. 3.2.2.2

Matthews, M., Harte, B., & Prior, D. (1992). Mantle Garnets - a Cracking Yarn. *Geochim Cosmochim Ac*, 56(7), 2633–2642. 4.4.1

Maumus, J., Laporte, D., & Schiano, P. (2004). Dihedral angle measurements and infiltration property of SiO2-rich melts in mantle peridotite assemblages. *Contributions to Mineralogy and Petrology*, 148, 1–12. 7.3

McDonough, W. & Sun, S.-S. (1995). The Composition of the Earth. *Chem Geol*, 120(228-253). 5.2.4, 5.2, 5.3, 5.3, 5.3, 5.3.1.2, A.2

McMillan, P. F. & Hess, A. C. (1990). Abinitio Valence Force-Field Calculations for Quartz. *Phys. Chem. Miner.*, 17(2), 97–107. 3.3.1.4

Melton, C., Salotti, C. A., & Giardini, A. A. (1972). The Observation of Nitrogen Water, Carbon Dioxide, Methane and Argon as Impurities in Natural Diamonds. *Am. Miner.*, 57(3-4), 1518 –1523. 2.2.3.3

Mendelssohn, M. J. & Milledge, H. J. (1995a). Geologically Significant Information from Routine Analysis of the Mid-Infrared Spectra of Diamonds. *Int Geol Rev*, 37, 95–110. 2.2, 2.2.1.1

Mendelssohn, M. J. & Milledge, H. J. (1995b). Morphological Characteristics of Diamond Populations in Relation to Temperature-Dependent Growth and Dissolution Rates. *Int Geol Rev*, 37, 285–312. 2.2, 2.3.1.2, 3.2.1

Menzies, A., Westerlund, K., Grutter, H., Gurney, J., Carlson, J., Fung, A., & Nowicki, T. (2004). Peridotitic Mantle Xenoliths from Kimberlites on the Ekati Diamond Mine Property, Nwt, Canada: Major Element Compositions and Implications for the Lithosphere beneath the Central Slave Craton. *Lithos*, 77(1-4), 395–412. 4.7, 4.4.2, 4.8, 4.4.3, 4.9, 4.10

Meyer, H. (1987). Inclusions in Diamond. *Mantle Xenoliths, Published by Wiley-Interscience, Editors Nixon P.H.*, (pp. 501–522). 2.2.3.1

Meyer, H. O. A. & Boyd, F. R. (1972). Composition and Origin of Crystalline Inclusions in Natural Diamonds. *Geochim. Cosmochim. Acta*, 36(11), 1255. 2.2.3.1

Meyer, H. O. A., Milledge, H. J., Sutherland, F. L., & Kennewell, P. (1997).

Unusual Diamonds and Unique Inclusions from New South Wales, Australia. *Russian Geology and Geophysics*, 38(2), 305–331. 2.2.1.1

Mibe, K., Fujii, T., & Yasuda, A. (1998). Connectivity of aqueous fluid in the Earth's upper mantle. *Geophysical Research Letters*, 25, 1233–1236. 7.3

Mibe, K., Yoshino, T., Ono, S., Yasuda, A., & Fujii, T. (2003). Connectivity of Aqueous Fluid in Eclogite and Its Implications for Fluid Migration in the Earth's Interior. *J. Geophys. Res.-Solid Earth*, 108(B6), art. no.–2295. 4.3.2.2, 7.3, 7.4

Milledge, H. (2004). Morphology of Diamond Inclusions. 2.2.3.1

Minarik, W. (1998). Complications to carbonate melt mobility due to the presence of an immiscible silicate melt. *Journal of Petrology*, 39, 1965–1973. 7.3

Minceva-Sukarova, B., Sherman, W., & Wilkinson, G. (1984). The Raman Spectra of Ice (Ih, Ii, Iii, V, Vi and Ix) as Functions of Pressure and Temperature. *Journal of Chemical and Solid State Physics*, 17, 5883–5850. 3.11, 3.3.2.2, 3.16

Mirwald, P. W. & Massonne, H. J. (1980). The Low-High Quartz and Quartz-Coesite Transition to 40 Kbar between 600-Degrees-C and 1600-Degrees-C and Some Reconnaissance Data on the Effect of Naalo2 Component on the Low Quartz-Coesite Transition. *Journal of Geophysical Research*, 85(NB12), 6983–6990. 3.11

Misra, K. C., Anand, M., Taylor, L. A., & Sobolev, N. V. (2004). Multi-Stage Metasomatism of Diamondiferous Eclogite Xenoliths from the Udachnaya Kim-

berlite Pipe, Yakutia, Siberia. *Contrib Mineral Petr*, 146(6), 696–714. 2.2.3.1, 4.5.2.2

Moenke, H. (1974). Silicates. In V. Farmer (Ed.), *Infrared Spectra of Minerals* (pp. 365–382). Mineralogical Society. 3.3.2.1

Moore, K. & Wall, F. (2003). A Novel Type of Diamond-Bearing Rock. In G. Rosatelli & F. Wall (Eds.), *4th Eurocarb* (pp. 19–20). Canary Islands, Spain: European Science Foundation. 2.1.1.3

Moore, K. R. & Wood, B. J. (1998). The Transition from Carbonate to Silicate Melts in the CaO-MgO- SiO2-CO2 System. *J. Petrol.*, 39(11-12), 1943–1951. 4.5.3.1, 5.4.2.2

Moore, M. & Lang, A. R. (1972). Internal Structure of Natural Diamonds of Cubic Habit. *Philosophical Magazine*, 26(6), 1313. 2.3.2

Mosenfelder, J. & Bohen, S. (1997). Kinetics of the Coesite to Quartz Transformation. *Earth and Planetary Science Letters*, 153(1-2), 133–147. 3.2.2.2

Mysen, B. (2002). Solubility behavior of alkaline earth and alkali aluminosilicate components in aqueous fluids in the Earth's upper mantle. *Geochimica Et Cosmochimica Acta*, 66, 2421–2438. 3.2.2.2

Mysen, B. (2004). Element partitioning between minerals and melt, melt composition, and melt structure. *Chemical Geology*, 213, 1–16. 5.3.1.1

Nadolinny, V. A., Yelisseyev, A. P., Baker, J. M., Newton, M. E., Twitchen, D. J., Lawson, S. C., Yuryeva, O. P., & Feigelson, B. N. (1999). A Study of C-13 Hyperfine Structure in the Epr of Nickel- Nitrogen-Containing Centres

in Diamond and Correlation with Their Optical Properties. *J. Phys.-Condes. Matter*, 11(38), 7357–7376. 2.2.1.2

Nakamoto, K. (1997). *Infrared and Raman Spectra of Inorganic and Coordination Compounds*. New York: Wiley-Interscience, 5th edition. 3.1

Navon, O. (1991). High Internal-Pressures in Diamond Fluid Inclusions Determined by Infrared-Absorption. *Nature*, 353(6346), 746–748. 1.2.1, 4, 3.2.2.2, 3.3, 4.5.5, 5.4.2.3

Navon, O., Hutcheon, I., Rossman, G. R., & Wasserburg, G. (1988). Mantle-Derived Fluids in Diamond Micro-Inclusions. *Nature*, 335, 784–789. 1.2.1, 2.4.2, 3, 3.2.1, 3.2.2.2, 4.3, 4.3.1, 4.6, 4.3.2.2, 4.5.3.2, 5.3.2.1

Navon, O., Klein-BenDavid, O., & Izraeli, E. (2004). Diamond Forming Fluids. *Geochim Cosmochim Ac*, 68(11), A277. 1.2.1, 4.5.2.2, 4.5.3.2

Navon, O. & Stoppler, E. (1987). Geochemical consequences of melt percolation: The upper mantle as a chromatographic column. *Journal of Geology*, 95, 285–307. 2.2.3.1

Nielson, J. E. & Wilshire, H. G. (1993). Magma Transport and Metasomatism in the Mantle - a Critical- Review of Current Geochemical Models. *Am. Miner.*, 78(11-12), 1117–1134. 2.2.3.1

Nimis, P. & Taylor, W. R. (2000). Single Clinopyroxene Thermobarometry for Garnet Peridotites. Part I. Calibration and Testing of a Cr-in-Cpx Barometer and an Enstatite-in-Cpx Thermometer. *Contrib Mineral Petr*, 139(5), 541–554. 4.4, 4.4.5, 4.10

Nixon, P. H. (1995). A Review of Mantle Xenoliths and Their Role in Diamond Exploration. *J Geodyn*, 20(4), 305–329. 2.1.1.1, 2.1.3, 2.2.3.1

Nowicki, T., Crawford, B., Dyck, D., Carlson, J., McElroy, R., Oshust, P., & Helmstaedt, H. (2004). The Geology of Kimberlite Pipes of the Ekati Property, Northwest Territories, Canada. *Lithos*, 76(1-4), 1–27. 1.3, 1.3.2, 4.2

O'Hara, M., Saunders, M., & Mercy, E. (1975). Garnet peridotite, primary ultrabasic magma and eclogite; interpretation of upper mantle processes in kimberlite. *Physics and Chemistry of the Earth*, 9, 571–604. 4.5.1

Okada, T., Utsumi, W., & Shimomura, O. (2002). In Situ X-Ray Observations of the Diamond Formation Process in the C-H2O-MgO System. *J. Phys.-Condes. Matter*, 14(44), 11331–11335. 6.2.1.3

O'Neill, H. (1978). An Experimental Study of FeMg Partitioning between Garnet and Olivine and Its Calibration as a Geothermometer. *Contrib Mineral Petr*, 70, 59–70. 4.4, 4.4.1, 4.4.5, 4.10

O'Neill, H. S. (1980). An Experimental Study of FeMg Partitioning between Garnet and Olivine and Its Calibration as a Geothermometer: Corrections. *Contrib Mineral Petr*, 72, 337. 4.4.5, 4.10

Ono, S., Mibe, K., & Yoshino, T. (2002). Aqueous fluid connectivity in pyrope aggregates: water transport into the deep mantle by a subducted oceanic crust without any hydrous minerals. *Earth and Planetary Science Letters*, 203, 895–903. 7.3

Orlov, Y. (1977). *The Mineralogy of Diamond.* New York: Wiley. 2.3.1, 2.3.1.2

Osagawara, Y. (2005). Microdiamonds in Ultrahigh-Pressure Metamorphic Rocks. *Elements*, 1(2), 91–96. 2.1.2

Ouillon, R., Pinan-Lucarre, J. P., & Ranson, P. (2000). Anharmonicity of Zone-Centre Optical Phonons: Raman Spectra of the Isomorphous Alpha-Quartz, Berlinite and Gallium Phosphate in the Temperature Range 8-300 K. *J. Raman Spectrosc.*, 31(7), 605–613. 3.12, 3.3.1.4

Pal'yanov, Y. N., Sokol, A. G., Borzdov, Y. M., & Khokhryakov, A. F. (2002a). Fluid-Bearing Alkaline Carbonate Melts as the Medium for the Formation of Diamonds in the Earths Mantle: An Experimental Study. *Lithos*, 60(3-4), 145–159. 3.3.3.2, 4.5.1, 6.2.1.1, 6.2.1.3, 6.4, 6.5, 6.4, 6.6

Pal'yanov, Y. N., Sokol, A. G., Borzdov, Y. M., Khokhryakov, A. F., Shatsky, A. F., & Sobolev, N. V. (1999a). The Diamond Growth from Li2CO3, Na2CO3, K2CO3 and Cs2CO3 Solvent-Catalysts at P=7 GPa and T=1700-1750 Degrees C. *Diam Relat Mater*, 8(6), 1118–1124. 5.3.1.1, 6.2.1.1, 6.4, 6.5

Pal'yanov, Y. N., Sokol, A. G., Borzdov, Y. M., Khokhryakov, A. F., & Sobolev, N. V. (1998). Crystallization of Diamond in the CaCO3-C, MgCO3-C and CaMg(CO3)(2)-C Systems. *Dokl Akad Nauk+*, 363(2), 230–233. 6.2.1.1, 6.2.1.3, 6.4

Pal'yanov, Y. N., Sokol, A. G., Borzdov, Y. M., Khokhryakov, A. F., & Sobolev, N. V. (1999b). Diamond Formation from Mantle Carbonate Fluids. *Nature*, 400(6743), 417–418. 6.2.1.1, 6.4, 6.5

Pal'yanov, Y. N., Sokol, A. G., Borzdov, Y. M., Khokhryakov, A. F., & Sobolev,

N. V. (2002b). Diamond Formation through Carbonate-Silicate Interaction. *Am. Miner.*, 87(7), 1009–1013. 6.2.1.1, 6.5

Pearson, D., Shirey, S. B., Carlson, R. W., Boyd, F. R., Pokhilenko, N. P., & Shimizu, N. (1995). Re—Os, Sm—Nd, and Rb—Sr Isotope Evidence for Thick Archaean Lithospheric Mantle beneath the Siberian Craton Modified by Multistage Metasomatism. *Geochimica Et Cosmochimica Acta*, 59(5), 959–977. 2.2.3.2

Pearson, D. G., Shirey, S. B., Harris, J. W., & Carlson, R. W. (1998). Sulphide Inclusions in Diamonds from the Koffiefontein Kimberlite, S Africa: Constraints on Diamond Ages and Mantle Re-Os Systematics. *Earth Planet Sc Lett*, 160(3-4), 311–326. 2.2.3.2

Pell, J. A. (1998). Lamproite-Hosted Diamonds. In *Geological Fieldwork 1997*, volume 1998-1 (pp. 24M–1 to 24M–4). British Columbia Ministry of Employment and Investment. 2.1.1.2

Perchuk, L. L., Safonov, O. G., Yapaskurt, V. O., & Barton, J. M. (2002). Crystal-Melt Equilibria Involving Potassium-Bearing Clinopyroxene as Indicator of Mantle-Derived Ultrahigh-Potassic Liquids: An Analytical Review. *Lithos*, 60(3-4), 89–111. 4.4.3

Perrillat, J.P. Daniel, I., Lardeaux, J., & Cardon, H. (2003). Kinetics of the coesite-quartz transition: Application to the exhumation of ultrahigh-pressure rocks. *Journal of Petrology*, 44, 773–788. 3.2.2.2

Pollack, H. N. & Chapman, D. (1977). On the Regional Variation of Heat Flow,

Geotherms, and Lithospheric Thickness. *Tectonophysics*, 38, 279–296. 2.5, 4.4.5, 4.10, 7.1

Potts, J., Thompson, M., & Wilson, S. (2002). Gprobe1 - an International Proficiency Test for Microprobe Laboratories. *Geostandards Newsletter*, 26, 197–235. 5.2.4

Prinz, M., Mason, D., Hlava, P., & Keil, K. (1975). Inclusions in Diamonds: Garnet Lherzolite and Eclogite Assemblages. *Physics and Chemistry of the Earth*, 9, 797–815. 2.2.3.1

Rapp, R., Shimizu, N., & Norman, M. (2003). Growth of early continental crust by partial melting of eclogite. *Nature*, 425, 605–609. 4.3.2.2, 7.2.1

Rege, S., Davies, R., Griffin, W., Jackson, S., & OReilly, S. (2003). Trace Element Analysis of Diamond by Lam Icpms: Preliminary Results. In *8th International Kimberlite Conference* (pp. Extended abstracts, FLA–0087). Vancouver, Canada. 5.1, 5.3.1.3, 5.5

Rege, S., Jackson, S., Griffin, W., Davies, R., Pearson, N., & O'Reilly, S. (2005). Quantitative trace-element analysis of diamond by laser ablation inductively coupled plasma mass spectrometry. *J. Anal. At. Spectrom*, 20, 601–611. 5.2.4

Resano, M., Vanhaecke, F., Hutsebaut, D., De Corte, K., & Moens, L. (2003). Possibilities of Laser Ablation-Inductively Coupled Plasma-Mass Spectrometry for Diamond Fingerprinting. *J. Anal. At. Spectrom.*, 18(10), 1238–1242. 5.1, 5.2.3, 5.5

Richardson, S. (1986). Latter-Day Origin of Diamonds of Eclogitic Paragenesis. *Nature*, 322, 623–626. 2.2.3.2

Richardson, S., Erlank, A., Harris, J., & Hart, S. (1990). Eclogitic Diamonds of Proterozoic Age from Cretaceous Kimberlites. *Nature*, 346, 54–56. 2.2.3.2

Richardson, S. H., Gurney, J., Erlank, A., & Harris, J. W. (1984). Origin of Diamonds in Old Enriched Mantle. *Nature*, 310, 198–202. 2.1.1

Richardson, S. H., Harris, J. W., & Gurney, J. J. (1993). 3 Generations of Diamonds from Old Continental Mantle. *Nature*, 366(6452), 256–258. 2.2.3.2

Ringwood, A. E., Kesson, S. E., Hibberson, W., & Ware, N. (1992). Origin of Kimberlites and Related Magmas. *Earth and Planetary Science Letters*, 113(4), 521–538. 2.1.1.1

Rivalenti, G., Zanetti, A., Mazzucchelli, M., Vannucci, R., & Cingolani, C. A. (2004). Equivocal Carbonatite Markers in the Mantle Xenoliths of the Patagonia Backarc: The Gobernador Gregores Case (Santa Cruz Province, Argentina). *Contrib Mineral Petr*, 147(6), 647–670. 2.2.3.1

Robertson, R., Fox, J., & A.E., M. (1934). Two Types of Diamond. *Philosophical Transactions of the Royal Society*, A323, 463. 2.2.1.1

Robinson, D., Scott, J., Van Niekerk, A., & Anderson, V. (1989). The Sequence of Evens Reflected in the Diamonds of Some Southern African Kimberlites. In J. Ross (Ed.), *Kimberlites and Related Rocks*, volume 2 (pp. 990–1000). Melbourne: Blackwell Scientific Publications. 2.3.1.2

Rocco, G. G., Garzon, O. L., & Cali, J. P. (1966). Non-Destructive Determination of Nitrogen in Diamond by Photoactivation. *International Journal of Applied Radiation and Isotopes*, 17(8), 433. 2.2.1.1

Roedder, E. (1984). *Fluid Inclusions*, volume 12 of *Reviews in Mineralogy*. Washington: Mineralogical Society of America. 3.3.2.2

Rosenfeld, J. & Chase, A. (1961). Pressure and Temperature of Crystallisation from Elastic Efects around Solid Inclusions in Minerals. *American Journal of Science*, 259, 519–541. 3.2.2.2

Rossini, F. D. & Jessup, R. S. (1938). Heat and Free Energy of Formation of Carbon Dioxide and of the Transition between Graphite and Diamond. *J. Res. Nat. Bur. Stand.*, 21, 491. 2.4.1

Ryabchikov, I. D. & Boettcher, A. L. (1980). Experimental Evidense at High Pressure for Potassic Magmatism in the Mantle of the Earth. *American Mineralogist*, 65, 915–919. 4.5.2.3

Ryabchikov, I. D., Edgar, A. D., & Wyllie, P. J. (1991). Partial Melting in the System Carbonate Phosphate Peridotite at 30 kbar. *Geokhimiya*, 2, 163–168. 5.4.2.2

Ryabchikov, I. D., Schreyer, W., & Abraham, K. (1982). Compositions of Aqueous Fluids in Equilibrium with Pyroxenes and Olivines at Mantle Pressures and Temperatures. *Contrib. Mineral. Petrol.*, 79(1), 80–84. 3.2.2.2, 4.5.2.3

Sato, K., Akaishi, M., & Yamaoka, S. (1999). Spontaneous Nucleation of Diamond

in the System MgCO3-CaCO3-C at 7.7 GPa. *Diam Relat Mater*, 8(10), 1900–1905. 6.2.1.1, 6.4

Saxena, S. K. (1989). The Oxidation State of the Mantle. *Geochim Cosmochim Ac*, 53, 98–95. 5.4.1.1

Scharer, U., Corfu, F., & Demaiffe, D. (1997). U-Pb and Lu-Hf Isotopes in Baddeleyite and Zircon Megacrysts from the Mbuji-Mayi Kimberlite: Constraints on the Subcontinental Mantle. *Chem Geol*, 143(1-2), 1–16. 1.3.1, 1.3.1

Schneider, M. & Eggler, D. (1986). Fluids in Equilibrium with Peridotite Minerals: Implications for Mantle Metasomatism. *Geochimica Et Cosmochimica Acta*, 50(5), 711–724. 4.5.2.3, 4.5.3.1

Schrauder, M., Koeberl, C., & Navon, O. (1996). Trace Element Analyses of Fluid-Bearing Diamonds from Jwaneng, Botswana. *Geochim Cosmochim Ac*, 60(23), 4711–4724. 1.2.1, 4.5.4, 5.1, 5.3.2.1, 5.3.2.1, 5.4.2

Schrauder, M. & Navon, O. (1993). Solid Carbon-Dioxide in a Natural Diamond. *Nature*, 365(6441), 42–44. 2.2.3.3, 2.4.2, 3

Schrauder, M. & Navon, O. (1994). Hydrous and Carbonatitic Mantle Fluids in Fibrous Diamonds from Jwaneng, Botswana. *Geochim Cosmochim Ac*, 58(2), 761–771. 1.2.1, 2.4.2, 3, 3.2.2.2, 4.2.1, 4.3, 4.3.1, 4.3.1, 4.6, 4.3.2.2, 4.5.3, 4.5.3.2, 5.3.2.1

Shimobayashi, N. & Kitamura, M. (2001). Growth Habit of Needle Crystals in Coats of Coated Diamonds. *Journal of Mineralogical and Petrological Sciences*, 96(5), 188–196. 2.3.2

Shirey, S. B., Richardson, S. H., & Harris, J. W. (2004). Age, Paragenesis and Composition of Diamonds and Evolution of the Precambrian Mantle Lithosphere of Southern Africa. *S. Afr. J. Geol.*, 107(1-2), 91–106. 2.1.1

Smith, C. B. (1983). Pb, Sr and Nd Isotopic Evidence for Sources of Southern African Cretaceous Kimberlites. *Nature*, 304, 51–54. 2.1.1.1

Smith, C. B., Gurney, J. J., Harris, J. W., Otter, M. L., Kirkley, M. B., & Jagoutz, E. (1991). Neodymium and Strontium Isotope Systematics of Eclogite and Websterite Paragenesis Inclusions from Single Diamonds, Finsch and Kimberley Pool, Rsa. *Geochim Cosmochim Ac*, 55(9), 2579–2590. 2.2.3.2

Smith, F. (1963). *Physical Geochemistry.* Addison Wesley Publishing. 3.2.2.2

Sobolev, A. V., Hofmann, A. W., & Nikogosian, I. K. (2000). Recycled Oceanic Crust Observed in 'Ghost Plagioclase' within the Source of Mauna Loa Lavas. *Nature*, 404(6781), 986–990. 4

Sobolev, N., Botkunov, A., Bakumenko, I., & Sobolev, V. (1972). Crystalline Inclusions with Octahedral Facets in Diamonds. *Doklady Akademii Nauk Sssr*, 204(1), 192–195. 2.2.3.1

Sobolev, N. V. (1977). *Deep-Seated Inclusions in Kimberlites and the Problem of the Composition of the Upper Mantle.* Washington D.C.: American Geophysics Union. 2.2.3.1

Sobolev, N. V. & Efimova, E. S. (1998). Compositional Range of Chromite Inclusions as Indicator of a Zoning of Diamond Crystals. *Dokl Akad Nauk+*, 358(5), 649–652. 2.2.3.1

Sobolev, N. V., Kaminsky, F. V., Griffin, W. L., Yefimova, E. S., Win, T. T., Ryan, C. G., & Botkunov, A. I. (1997). Mineral Inclusions in Diamonds from the Sputnik Kimberlite Pipe, Yakutia. *Lithos*, 39(3-4), 135–157. 2.2.3.1

Sobolev, N. V. & Shatsky, A. F. (1990). Diamond Inclusions in Garnets from Metamorphic Rocks: A New Environment for Diamond Formation. *Nature*, 343, 742–746. 2.1.2

Socrates, G. (2001). Inorganic and Coordination Complexes. In G. Socrates (Ed.), *Infrared and Raman Characteristic Group Frequencies: Tables and Charts* (pp. 283–327). Chichester: Wiley, 3rd edition. 3.1

Sokol, A. G., Borzdov, Y. M., Pal'yanov, Y. N., Khokhryakov, A. F., & Sobolev, N. V. (2001). An Experimental Demonstration of Diamond Formation in the Dolomite-Carbon and Dolomite-Fluid-Carbon Systems. *Eur J Mineral*, 13(5), 893–900. 3.3.3.2, 6.2.1.1, 6.2.1.2, 6.4, 6.5, 7.2, 7.3

Sokol, A. G., Pal'yanov, Y. N., Borzdov, Y. M., Khokhryakov, A. F., & Sobolev, N. V. (1998). Crystallization of Diamond from Na2CO3 Melt. *Dokl Akad Nauk+*, 361(3), 388–391. 6.2.1.1, 6.4

Sokol, A. G., Tomilenko, A. A., Pal'yanov, Y. N., Borzdov, Y. M., Pal'yanova, G. A., & Khokhryakov, A. F. (2000). Fluid Regime of Diamond Crystallisation in Carbonate-Carbon Systems. *Eur J Mineral*, 12(2), 367–375. 2.4.2, 6.2.1.1, 6.4, 6.5

Solozhenko, V. L., Turkevich, V. Z., Kurakevych, O. O., Crichton, W. A., & Mezouar, M. (2002). Kinetics of Diamond Crystallization from the Melt of the Fe-Ni- C System. *J. Phys. Chem. B*, 106(26), 6634–6637. 6.2.1.3

Song, M., Yamawaki, H., Fujihisa, H., Sakashita, M., & Aoki, K. (2003). Infrared Observation of the Phase Transitions of Ice at Low Temperatures and Pressures up to 50 Gpa and the Metastability of Low-Temperature Ice Vii. *Phys. Rev. B*, 68(2), art. no.–024108. 3.3.2

Spetsius, Z. (1995). Diamondiferous Eclogites from Yakutia: Evidence for a Late and Multistage Formation of Diamonds (Abstract). *6th INternational Kimberlite Conference*, (pp. 572–574). 5.4.1.2

Spetsius, Z. V., Belousova, E. A., Griffin, W. L., O'Reilly, S. Y., & Pearson, N. J. (2002). Archean Sulfide Inclusions in Paleozoic Zircon Megacrysts from the Mir Kimberlite, Yakutia: Implications for the Dating of Diamonds. *Earth Planet Sc Lett*, 199(1-2), 111–126. 2.2.3.1

Stachel, T.and Viljoen, K., Brey, G., & Harris, J. (1998). Metasomatic processes in lherzolitic and harzburgitic domains of diamondiferous lithospheric mantle: REE in garnets from xenoliths and inclusions in diamonds. *Earth and Planetary Science Letters*, 159, 1–12. 4.5.1

Stachel, T. (2001). Diamonds from the Asthenosphere and the Transition Zone. *Eur J Mineral*, 13(5), 883–892. 2.2.3.1

Stachel, T., Aulbach, S., Brey, G. P., Harris, J. W., Leost, I., Tappert, R., & Viljoen, K. S. (2004). The Trace Element Composition of Silicate Inclusions in Diamonds: A Review. *Lithos*, 77(1-4), 1–19. 4.5.1, 5.4

Stachel, T., Brey, G., & Harris, J. W. (2005). Inclusions in Sublithospheric Diamonds. *Elements*, 1(2), 73–78. 2.2.3.1

Stachel, T. & Harris, J. W. (1997a). Diamond Precipitation and Mantle Metasomatism - Evidence from the Trace Element Chemistry of Silicate Inclusions in Diamonds from Akwatia, Ghana. *Contrib Mineral Petr*, 129(2-3), 143–154. 2.2.3.1, 4.4.5, 5.4.1.2

Stachel, T. & Harris, J. W. (1997b). Syngenetic Inclusions in Diamond from the Birim Field (Ghana) - a Deep Peridotitic Profile with a History of Depletion and Re-Enrichment. *Contrib Mineral Petr*, 127(4), 336–352. 2.2.3.1

Stachel, T., Harris, J. W., Tappert, R., & Brey, G. P. (2003). Peridotitic Diamonds from the Slave and the Kaapvaal Cratons - Similarities and Differences Based on a Preliminary Data Set. *Lithos*, 71(2-4), 489–503. 1.3.2, 4.4.1, 4.7, 4.4.1, 4.9, 4.4.5, 4.11, 5.3.1.2, 5.4, 5.3.2.2, 7.3

Stalder, P., Ulmer, P., Thompson, A. B., & Gunther, D. (2000). Experimental Approach to Constrain Second Critical End Points in Fluid/Silicate Systems: Near-Solidus Fluids and Melts in the System Albite-H2O. *Am. Miner.*, 85(1), 68–77. 1

Stalder, R., Foley, S. F., Brey, G. P., & Horn, I. (1998). Mineral Aqueous Fluid Partitioning of Trace Elements at 900- 1200 Degrees C and 3.0-5.7 GPa: New Experimental Data for Garnet, Clinopyroxene, and Rutile, and Implications for Mantle Metasomatism. *Geochim Cosmochim Ac*, 62(10), 1781–1801. 2.2.3.1

Stalder, R., Ulmer, P., & Gunther, D. (2001). Fluids in the System Forsterite-Phlogopite-H2O at 60 kbar. *Contrib Mineral Petr*, 140(1), 607–618. 3.2.2.2

Sunagawa, I. (1984). Morphology of Natural and Synthetic Diamond Crystals.

In I. Sunagawa (Ed.), *Materials Science of the Earth's Interior* (pp. 303–330). D. Reidel Publishing Co. 1.1, 7.5

Sunagawa, I. (1990). Growth and Morphology of Diamond Crystals under Stable and Metastable Conditions. *Journal of Crystal Growth*, 99(1-4), 1156–1161. 2.3.1.1, 2.4, 2.3.2, 7.5.1

Sweeney, R. J., Prozesky, V., & Przybylowicz, W. (1995). Selected Trace and Minor Element Partitioning between Peridotite Minerals and Carbonatite Melts at 18-46 Kb Pressure. *Geochim Cosmochim Ac*, 59(18), 3671–3683. 5.3.2.2

Talnikova, S. (1995). Inclusions in natural diamonds of different habits. In N. Sobolev (Ed.), *International Kimberlite Conference* (pp. 603–605). 1.2.1

Taniguchi, T., Dobson, D., Jones, A., Rabe, R., & Milledge, H. J. (1996). Synthesis of Cubic Diamond in the Graphite-Magnesium Carbonate and Graphite-K2Mg(CO3)2 Systems at High Pressure of 9-10 GPa Region. *Journal of Materials Research*, 11(10), 2622–2632. 6.2.1.1, 6.4, 6.5

Tappert, R., Stachel, T., Harris, J. W., Shimizu, N., & Brey, G. P. (2005). Mineral Inclusions from the Panda Kimberlite, Stave Province, Canada. *Eur J Mineral*, 17(3), 423–440. 1.3.2, 4.2.2, 4.4.1, 4.7, 4.4.1, 4.4.2, 4.8, 4.4.3, 4.4.5, 4.10, 4.5.1, 4.5.5, 4.11, 4.6, 7.2.1, 7.5.2

Taylor, L. & Neal, C. (1989). Eclogites with oceanic crustal and mantle signatures from the Bellsbank kimberlite, South Africa, Part 1: mineralogy, petrography and whole rock chemistry. *Journal of Geology*, 97, 551–567. 4.4.3

Taylor, L. A. & Anand, M. (2004). Diamonds: Time Capsules from the Siberian

Mantle. *Chem Erde-Geochem.*, 64(1), 1–74. 2.2.2.1, 2.2.3.1, 2.3.1.2, 4.4.3, 5.3.1.2, 5.4.2.3

Taylor, L. A., Anand, M., Promprated, P., Floss, C., & Sobolev, N. V. (2003). The Significance of Mineral Inclusions in Large Diamonds from Yakutia, Russia. *Am. Miner.*, 88(5-6), 912–920. 2.2.3.1

Taylor, L. A., Keller, R. A., Snyder, G. A., Wang, W. Y., Carlson, W. D., Hauri, E. H., McCandless, T., Kim, K. R., Sobolev, N. V., & Bezborodov, S. M. (2000). Diamonds and Their Mineral Inclusions, and What They Tell Us: A Detailed Pull-Apart of a Diamondiferous Eclogite. *Int Geol Rev*, 42(11), 959–983. 2.2.3.1, 4.4.3

Taylor, L. A., Snyder, G. A., Crozaz, G., Sobolev, V. N., Yefimova, E. S., & Sobolev, N. V. (1996a). Eclogitic Inclusions in Diamonds: Evidence of Complex Mantle Processes over Time. *Earth Planet Sc Lett*, 142(3-4), 535–551. 2.2.3.1, 2.2.3.2, 4.4.3

Taylor, W. R. (1990). The Dissolution Mechanism of CO2 in Aluminosilicate Melts - Infrared Spectroscopic Constraints on the Cationic Environment of Dissolved CO3 2. *Eur J Mineral*, 2(5), 547–563. 2.2.3.2

Taylor, W. R., Bulanova, G., & Milledge, H. (1995). Quantitative Nitrogen Aggregation Study of Some Yakutian Diamonds: Constraints on Growth, Thermal and Deformation History of Peridotitic and Eclogitic Diamonds. 2.2.1.1

Taylor, W. R., Canil, D., & Milledge, H. J. (1996b). Kinetics of Ib to IaA Nitrogen Aggregation in Diamond. *Geochim Cosmochim Ac*, 60(23), 4725–4733. 2.2.1.1

Taylor, W. R., Jaques, A. L., & Ridd, M. (1990). Nitrogen-Defect Aggregation Characteristics of Some Australasian Diamonds - Time-Temperature Constraints on the Source Regions of Pipe and Alluvial Diamonds. *Am. Miner.*, 75(11-12), 1290–1310. 2.2.1.1

Taylor, W. R., Tompkins, L. A., & Haggerty, S. E. (1994). Comparative Geochemistry of West-African Kimberlites - Evidence for a Micaceous Kimberlite Endmember of Sublithospheric Origin. *Geochim Cosmochim Ac*, 58(19), 4017–4037. 5.3.2.1, 5.7

Thompson, J. & Barnes, S. (1984). The Distribution of Nickel and Iron between Olivine and Magmatic Sulphides in Some Natural Assemblages. *Can Mineral*, 22, 55–66. 5.3.1.2

Thompson, W. (1965). Infra-Red Spectroscopic Studies of Aqueous Systems. Part 1.Molar Extinction Coefficients of Water, Deuterium Oxide, Deuterium Hydrogen Oxide, Aqueous Sodium Chloride and Carbon Disulphide. *Transactions of the Faraday Society*, 61, 2635–2640. 3.2.1

Tomilenko, A. A., Chepurnov, A. I., Turkin, A. I., Shebanin, A. P., & Sobolev, N. V. (1997). Fluid Inclusions in Crystals of Synthetic Diamond. *Dokl Akad Nauk+*, 353(2), 237–240. 2.2.3.3

Tomilenko, A. A., Ragozin, A. L., Shatsky, V., & Shebanin, A. P. (2001). Fluid Inclusions in Natural Diamond. In A. G. F. Noronha, A. Doria (Ed.), *XVI ECROFI European Current Research on Fluid Inclusions* Porto. 2.2.3.3

Tomlinson, E., Jones, A., & Milledge, J. (2004). High-Pressure Experimental

Growth of Diamond Using C-K2CO3-KCl as an Analogue for Cl-Bearing Carbonate Fluid. *Lithos*, 77(1-4), 287–294. 4.5.1

Toramaru, A. & Fujii, N. (1986). Connectivity of melt phase in a partially molten peridotite. *Journal of Geophysical Research*, 91, 9239–9252. 7.3

Turkevich, V., Okada, T., Utsumi, W., & Garan, A. (2002). Kinetics of Diamond Spontaneous Crystallization from the Melt of the Fe-Al-C System at 6.5 GPa. *Diam Relat Mater*, 11(10), 1769–1773. 6.2.1.3

Turner, G., Burgess, R., & Bannon, M. (1990). Volatile-Rich Mantle Fluids Inferred from Inclusions in Diamond and Mantle Xenoliths. *Nature*, 344, 653–655. 1.2.1

Utsumi, W., Okada, T., Taniguchi, T., Funakoshi, K., Kikegawa, T., Hamaya, N., & Shimomura, O. (2004). In Situ X-Ray Diffraction of Graphite-Diamond Transformation Using Various Catalysts under High Pressures and High Temperatures. *J. Phys.-Condes. Matter*, 16(14), S1017–S1026. 6.2.1.3

Van der Wal, D. & Bodinier, J. (1996). Origin of the recrystallisation front in the Rhonda peridotite by km-scale pervasive porous melt flow. *Contributions to Mineralogy and Petrology*, 122, 387–405. 7.4

Vasseur, G., Vernieres, J., & Bodinier, J.-L. (1991). Modelling of trace element transfer between mantle melt and heterogranular peridotite during melt segregation. *Journal of Petrology*, Special Lherzolites Issue, 41–54. 2.2.3.1

Vielzeuf, D. & Schmidt, M. W. (2001). Melting Relations in Hydrous Systems Re-

visited: Application to Metapelites, Metagreywackes and Metabasalts. *Contrib Mineral Petr*, 141(3), 251–267. 7.1, 7.3

Wakatsuk, M. (1966). New Catalysts for Synthesis of Diamond. *Japanese Journal of Applied Physics*, 5(4), 337. 6.2.1

Walmsley, J. C. & Lang, A. R. (1992a). On Sub-Micrometer Inclusions in Diamond Coat - Crystallography and Composition of Ankerites and Related Rhombohedral Carbonates. *Mineral Mag*, 56(385), 533–543. 1.2.1

Walmsley, J. C. & Lang, A. R. (1992b). Oriented Biotite Inclusions in Diamond Coat. *Mineral Mag*, 56(382), 108–111. 1.2.1, 6.2.1.1

Walrafen, G. (1972). Raman and Infrared Spectral Investigations of Water Structure. In F. Frank (Ed.), *Water: A Comprehensive Treatise.* London: Plenum. 3.3.2.2

Wang, A., Pasteris, J. D., Meyer, H. O. A., & Dele-Duboi, M. L. (1996). Magnesite-Bearing Inclusion Assemblage in Natural Diamond. *Earth and Planetary Science Letters.* 2.4.2

Wang, Q., Zhao, Z. H., Bai, Z. H., Bao, Z. W., Xiong, X. L., Mei, H. J., Xu, J. F., & Wang, Y. X. (2003a). Carboniferous Adakites and Nb-Enriched Arc Basaltic Rocks Association in the Alataw Mountains, North Xinjiang: Interactions between Slab Melt and Mantle Peridotite and Implications for Crustal Growth. *Chin. Sci. Bull.*, 48(19), 2108–2115. 5.1

Wang, W. (1998). Formation of Diamond with Mineral Inclusions of Mixed Eclog-

ite and Peridotite Paragenesis. *Earth Planet Sc Lett*, 160(3-4), 831–843. 2.2.3.1, 6.1, 6.2.1.1

Wang, W., Moses, T. M., Hall, M., Shigley, J. E., & Hsi-Tien Shen, A. (2005). Carbonate and Solid CO2 Micro-Inclusions in a Large Faceted Gem Diamond. In M. Newton (Ed.), *56th Diamond Conference* (pp. 4.1). Oxford. 2.4.2, 3

Wang, W., Moses, T. M., & Shigley, J. E. (2003b). Physical and Chemical Features of a Large Coated Natural Diamond Crystal. *Diam Relat Mater*, 12(3-7), 330–335. 1.2.1

Westerlund, K., Shirley, S., Richardson, S. H., Gurney, J., & Harris, J. W. (2003). Re-Os Systematics of Diamond Inclusion Sulfides from the Panda Kimberlite, Slave Craton. 1.3.2

White, W. (1974). The Carbonate Minerals. In V. Farmer (Ed.), *Infrared Spectra of Minerals* (pp. 227–284). Mineralogical Society. 3.3.2.3

Williams, Q. (1995). Infrared, Raman and Optical Spectroscopy of Earth Materials. In T. Ahrens (Ed.), *Mineral Physics and Cruystallography: A Handbook of Physical Constants*, volume 2 (pp. 291–302). Washington: American Geophysical Union. 3.1

Williams, Q., Hemley, R. J., Kruger, M. B., & Jeanloz, R. (1993). High-Pressure Infrared-Spectra of Alpha-Quartz, Coesite, Stishovite and Silica Glass. *J. Geophys. Res.-Solid Earth*, 98(B12), 22157–22170. 3.2.2.2, 3.3.1.4, 3.3.1.4, 3.3.2.1

Williams, Q. & Knittle, E. (2003). Structural Complexity in Carbonatite Liquid

at High Pressures. *Geophysical Research Letters*, 30(1), art. no.–1022. 6.1, 6.5, 6.5

Wong, P. T. T., Baudais, F. L., & Moffatt, D. J. (1986). Hydrostatic-Pressure Effects on to-Lo Splitting and Softening of Infrared Active Phonons in Alpha-Quartz. *J. Chem. Phys.*, 84(2), 671–674. 3.3.1.4, 3.3.1.4

Wood, B. J., Bryndzia, L. T., & Johnson, K. E. (1990). Mantle Oxidation-State and Its Relationship to Tectonic Environment and Fluid Speciation. *Science*, 248(4953), 337–345. 2.4.2

Woods, G. S. (1986). Platelets and the Infrared-Absorption of Type-Ia Diamonds. *Proc. R. Soc. London Ser. A-Math. Phys. Eng. Sci.*, 407(1832), 219–238. 2.2.1.1

Woods, G. S. & Collins, A. T. (1983). Infrared-Absorption Spectra of Hydrogen Complexes in Type-I Diamonds. *J. Phys. Chem. Solids*, 44(5), 471–475. 2.2.1.2

Woolley, A. & Kempe, D. (1989). Carbonatites: Nomenclature, Average Chemical Compositions and Element Distribution. In K. Bell (Ed.), *Carbonatites Genesis and Evolution* (pp. 105148). London: Unwin Hyman. 5.3.1.1, 5.5, 5.3.2.1

Wyllie, P. J. & Ryabchikov, I. D. (2000). Volatile Components, Magmas, and Critical Fluids in Upwelling Mantle. *J. Petrol.*, 41(7), 1195–1206. 1.2.1, 3.2.2.2, 7.1, 7.3

Yamaoka, S., Kumar, M. D. S., Kanda, H., & Akaishi, M. (2002). Formation of Diamond from CaCO3 in a Reduced C-O-H Fluid at Hp- Ht. *Diam Relat Mater*, 11(8), 1496–1504. 3.3.3.2, 6.2.1.3, 6.4

Yaxley, G. M. & Brey, G. P. (2004). Phase Relations of Carbonate-Bearing Eclogite Assemblages from 2.5 to 5.5 GPa: Implications for Petrogenesis of Carbonatites. *Contrib Mineral Petr*, 146(5), 606–619. 4.5.3.1, 5.4.2.2

Yelisseyev, A. P., Pokhilenko, N. P., Steeds, J. W., Zedgenizov, D. A., & Afanasiev, V. P. (2004). Features of Coated Diamonds from the Snap Lake/King Lake Kimberlite Dyke, Slave Craton, Canada, as Revealed by Optical Topography. *Lithos*, 77(1-4), 83–97. 2.2.1.2

Yoder, M. (1993). Diamond Properties and Applications. In R. Davis (Ed.), *Diamond Films and Coatings: Development, Properties, and Applications* (pp. 1–30). New Jersey: Noyes Publications. 3.2.2.2

Zedgenizov, D. A., Kagi, H., Shatsky, A. F., & Sobolev, N. (2004). Carbonatitic Melts in Cuboid Diamonds from Udachnaya Kimberlite Pipe (Yakutia): Evidence from Vibrational Spactroscopy. *Mineral Mag*, 68(1), 61–73. 2.4.2, 3, 3.2.2.2

Zedgenizov, D. A., Reutsky, V. N., Shatsky, V. S., & Fedorova, E. N. (2003a). Impurities and Carbon Isotope Compositions of Microdiamonds with Extra Faces from the Udachnaya Kimberlite Pipe. *Geol Geofiz*, 44(9), 872–878. 1.2.1

Zedgenizov, D. A., Shiryaev, A. A., Kagi, H., & Navon, O. (2003b). Water-Related Absorption in Fibrous Diamonds. *EGS - AGU - EUG Joint Assembly, Abstracts from the meeting held in Nice, France, 6 - 11 April 03, abstract 4867*, (pp. 4867). 2

Zhang, H. F., Menzies, M. A., & Mattey, D. (2003). Mixed Mantle Provenance:

Diverse Garnet Compositions in Polymict Peridotites, Kaapvaal Craton, South Africa. *Earth Planet Sc Lett*, 216(3), 329–346. 7.4

Appendix A

Appdx A

A.1 EMPA Dataset

Table A.1 Individual major element compositions of inclusions in Mbuji Mayi and Panda diamond coats. Abbreviations: no. inc. - number of inclusions analysed nd - not detected, na - not analysed.

Table A.1:

inc.	weight % oxide + Cl (normalised to 100%)												molecular proportion (normalised to 100%)									
no.	SiO_2	TiO_2	Al_2O_3	FeO	MgO	CaO	BaO	Na_2O	K_2O	P_2O_5	Cl	total	Si	Ti	Al	Fe	Mg	Ca	Ba	Na	K	P	Cl
CTPs1																						
1	14.5	1.7	2.7	10.0	3.7	16.5	10.4	2.0	24.0	6.2	8.3	36.4	16.7	1.5	1.8	9.6	6.3	20.3	4.7	2.2	17.6	3.0	16.3
2	34.5	2.2	5.3	10.0	5.3	21.2	4.6	0.8	4.1	11.9	0.2	14.2	38.9	1.8	3.5	9.4	8.8	25.6	2.0	0.9	3.0	5.7	0.4
3	23.9	2.4	4.9	13.5	7.5	26.1	2.3	1.0	4.5	13.1	0.9	20.7	26.3	1.9	3.2	12.4	12.4	30.8	1.0	1.1	3.2	6.1	1.8
4	9.6	nd	1.7	13.8	3.3	37.6	7.5	1.3	1.6	22.4	1.0	16.3	11.5		1.2	13.7	5.9	48.0	3.5	1.5	1.2	11.3	2.1
5	43.6	3.7	9.0	11.9	5.5	9.1	1.8	0.7	8.0	6.3	0.3	22.4	48.8	3.1	6.0	11.2	9.2	11.0	0.8	0.7	5.7	3.0	0.5
6	38.2	1.8	6.2	7.0	2.8	6.9	2.1	1.8	20.8	6.6	5.8	25.4	42.9	1.6	4.1	6.6	4.6	8.3	0.9	1.9	14.9	3.1	11.0
7	46.0	4.4	10.0	9.2	6.1	8.4	nd	0.9	9.0	5.3	0.7	17.1	50.6	3.6	6.5	8.5	10.0	9.8	nd	0.9	6.3	2.5	1.3
8	39.8	2.8	6.0	8.0	2.5	19.8	nd	1.3	4.1	15.3	0.5	16.3	45.1	2.4	4.0	7.6	4.3	24.0	nd	1.4	2.9	7.3	1.0
9	50.3	1.7	4.5	7.1	3.9	14.7	5.6	1.0	3.3	7.8	nd	16.2	55.7	1.4	2.9	6.6	6.4	17.4	2.5	1.1	2.4	3.7	nd
10	42.7	3.2	8.0	14.1	8.4	15.9	nd	0.5	7.1	nd	0.2	15.2	44.3	2.5	4.9	12.2	13.0	17.7	nd	0.5	4.7	nd	0.3
11	30.5	3.7	5.3	11.3	5.6	23.3	1.7	0.8	3.6	13.9	0.4	22.5	34.2	3.1	3.5	10.5	9.4	28.0	0.7	0.8	2.5	6.6	0.7
12	46.9	4.0	9.1	9.5	5.4	9.0	nd	0.8	8.1	6.5	0.7	18.4	51.6	3.3	5.9	8.8	8.9	10.6	nd	0.9	5.7	3.0	1.2
13	18.4	2.7	3.3	15.8	7.9	30.4	6.5	1.5	2.1	11.1	0.4	19.7	20.3	2.2	2.1	14.6	13.1	35.9	2.8	1.6	1.5	5.2	0.7
14	39.4	1.7	2.7	4.8	2.1	28.0	nd	0.8	2.0	18.1	0.5	17.6	43.8	1.4	1.8	4.5	3.6	33.4	nd	0.8	1.4	8.5	0.9
15	50.5	2.7	7.7	10.9	5.4	15.3	nd	1.0	6.1	nd	0.4	11.0	52.5	2.1	4.7	9.5	8.4	17.0	nd	1.0	4.1	nd	0.8

inc.	weight% oxide + Cl (normalised to 100%)												molecular proportion (normalised to 100 %)									
no.	SiO_2	TiO_2	Al_2O_3	FeO	MgO	CaO	BaO	Na_2O	K_2O	P_2O_5	Cl	total	Si	Ti	Al	Fe	Mg	Ca	Ba	Na	K	P	Cl
16	44.3	3.8	8.1	10.4	5.9	11.0	1.7	0.7	7.0	6.6	0.5	22.1	48.8	3.1	5.2	9.6	9.8	13.0	0.8	0.7	4.9	3.1	0.9
17	32.3	3.0	6.8	16.2	5.9	16.2	2.8	1.0	5.5	9.8	0.5	18.3	36.4	2.6	4.5	15.2	9.8	19.5	1.2	1.1	4.0	4.7	0.9
18	41.1	1.7	6.0	8.4	4.8	17.6	nd	0.8	5.8	13.7	nd	18.7	46.0	1.5	4.0	7.9	8.0	21.2	nd	0.9	4.1	6.5	nd
19	36.0	2.2	6.0	10.5	6.1	21.6	nd	1.4	4.1	12.2	nd	13.7	39.4	1.8	3.9	9.6	10.0	25.4	nd	1.5	2.9	5.6	nd
20	49.3	4.4	10.2	13.6	5.4	3.3	nd	0.6	10.3	2.6	0.4	23.7	54.6	3.7	6.6	12.6	8.9	3.9	nd	0.6	7.3	1.2	0.7
21	36.6	1.8	5.9	9.7	3.3	4.2	5.8	1.6	20.4	1.8	9.0	31.3	39.9	1.5	3.8	8.8	5.3	4.9	2.5	1.7	14.2	0.8	16.6
CTPs2																							
1	28.7	1.9	4.6	16.7	5.2	20.2	5.3	1.3	4.2	11.9	nd	13.2	32.9	1.7	3.1	16.0	8.9	24.9	2.4	1.5	3.0	5.8	nd
2	45.3	4.1	7.1	19.3	8.1	5.0	nd	0.8	7.9	2.3	nd	23.8	48.7	3.3	4.5	17.4	13.0	5.8	nd	0.8	5.4	1.1	nd
3	45.8	3.4	6.8	10.7	5.3	11.8	nd	2.0	6.5	7.8	nd	35.9	50.3	2.8	4.4	9.8	8.6	13.8	nd	2.2	4.5	3.6	nd
4	42.3	5.0	7.4	21.2	11.6	3.7	nd	1.1	7.7	nd	nd	16.3	44.4	3.9	4.6	18.6	18.1	4.1	nd	1.1	5.1	nd	nd
5	18.1	nd	3.4	5.6	2.3	27.9	4.9	2.0	17.3	14.4	4.2	11.6	21.0	nd	2.3	5.4	3.9	34.7	2.2	2.3	12.8	7.1	8.2
6	42.0	2.5	6.0	15.4	6.1	13.2	nd	2.3	5.9	6.5	nd	10.1	45.5	2.0	3.8	13.9	9.9	15.4	nd	2.4	4.1	3.0	nd
7	46.0	nd	4.9	15.4	1.8	13.2	nd	2.8	4.3	11.6	nd	10.8	51.8	nd	3.3	14.5	3.0	15.9	nd	3.0	3.1	5.5	nd
8	43.4	1.1	6.0	9.1	3.4	19.5	4.0	1.4	5.1	7.3	nd	22.7	48.0	0.9	3.9	8.4	5.6	23.1	1.7	1.5	3.6	3.4	nd
9	25.1	nd	5.1	10.5	6.3	31.7	5.9	2.1	3.2	10.2	nd	10.8	27.6	nd	3.3	9.6	10.4	37.4	2.5	2.2	2.2	4.8	nd
10	31.9	2.9	5.3	19.0	9.1	16.4	nd	1.8	5.7	7.8	nd	14.4	34.3	2.4	3.3	17.1	14.6	18.9	nd	1.9	3.9	3.6	nd
11	41.3	3.3	6.8	15.6	9.4	9.6	3.2	1.5	7.3	1.9	nd	11.1	44.3	2.7	4.3	14.0	15.1	11.0	1.3	1.6	5.0	0.9	nd
12	35.1	3.0	5.6	11.8	6.7	18.6	1.7	1.6	5.3	10.6	nd	26.7	38.8	2.5	3.7	10.9	11.1	22.0	0.8	1.7	3.7	5.0	nd
13	26.7	1.4	4.8	12.9	5.8	26.9	5.6	1.0	4.7	10.2	nd	19.0	29.9	1.2	3.2	12.1	9.7	32.3	2.4	1.1	3.4	4.8	nd
14	56.6	1.2	9.7	8.9	0.3	6.1	nd	1.6	9.6	5.8	0.2	43.4	64.2	1.1	6.5	8.4	0.5	7.4	nd	1.7	7.0	2.8	0.4
15	11.1	nd	1.5	27.2	1.3	32.1	nd	2.1	1.1	22.9	0.8	9.0	13.1	nd	1.0	26.8	2.4	40.5	nd	2.4	0.8	11.4	1.6
16	19.8	nd	3.6	7.2	3.7	36.7	nd	1.4	3.1	24.6	nd	11.6	22.9	nd	2.4	7.0	6.4	45.4	nd	1.5	2.3	12.0	nd
17	31.1	2.8	5.2	11.3	6.1	20.9	2.0	1.7	5.0	14.0	nd	22.6	35.1	2.4	3.4	10.6	10.2	25.3	0.9	1.9	3.6	6.7	nd
18	38.3	nd	6.7	10.8	3.7	22.4	8.2	1.3	4.8	3.8	nd	24.5	42.5	nd	4.4	10.0	6.2	26.7	3.6	1.4	3.4	1.8	nd
19	44.1	2.3	6.0	14.8	5.7	11.8	1.7	1.4	6.8	5.5	nd	27.4	48.2	1.9	3.9	13.5	9.2	13.8	0.7	1.5	4.7	2.6	nd
20	40.6	3.2	9.4	4.2	1.5	15.8	0.9	0.9	10.9	12.5	0.3	49.3	47.7	2.8	6.6	4.1	2.6	19.9	0.4	1.0	8.1	6.2	0.6
21	28.3	2.9	4.7	17.3	7.4	20.5	2.1	1.9	4.3	10.3	0.4	19.7	31.0	2.4	3.0	15.9	12.1	24.1	0.9	2.0	3.0	4.8	0.7
CTPs5																							
1	58.5	nd	6.8	5.7	2.1	4.9	nd	2.1	12.1	3.9	4.0	11.0	62.4	nd	4.3	5.1	3.4	5.6	nd	2.1	8.2	1.8	7.2
2	42.4	2.5	9.5	10.2	4.3	12.0	3.9	0.9	8.1	6.3	nd	24.6	48.3	2.1	6.4	9.7	7.2	14.6	1.7	1.0	5.9	3.0	nd
3	47.2	2.3	7.2	11.9	3.9	11.4	nd	1.9	5.6	8.6	nd	15.1	52.3	1.9	4.7	11.1	6.4	13.5	nd	2.1	4.0	4.0	nd
4	47.7	nd	4.1	11.4	3.2	17.4	2.5	1.6	2.6	9.0	0.5	24.1	51.9	nd	2.6	10.3	5.1	20.3	1.1	1.7	1.8	4.1	0.9
5	54.2	4.2	11.1	12.2	4.9	2.4	nd	1.5	7.2	2.3	nd	25.7	59.6	3.5	7.2	11.2	8.0	2.8	nd	1.6	5.0	1.1	nd
6	44.3	nd	9.0	11.9	4.5	12.5	nd	1.6	7.4	8.0	0.7	30.0	48.9	nd	5.9	11.0	7.4	14.8	nd	1.7	5.2	3.7	1.3
7	53.3	nd	6.9	23.6	2.6	4.8	nd	4.9	4.0	nd	nd	5.0	57.1	nd	4.3	21.1	4.1	5.5	nd	5.1	2.7	nd	nd
8	42.0	2.2	7.1	12.9	4.2	14.5	nd	2.0	3.6	11.3	nd	16.1	46.9	1.9	4.7	12.1	7.0	17.3	nd	2.2	2.6	5.4	nd
9	41.9	2.7	6.9	13.7	4.8	13.5	nd	1.4	5.4	9.8	nd	19.0	46.6	2.3	4.5	12.8	7.9	16.1	nd	1.5	3.8	4.6	nd
10	50.7	3.2	9.8	16.2	6.8	2.1	nd	2.6	7.7	nd	0.9	21.3	54.1	2.6	6.2	14.4	10.8	2.4	nd	2.7	5.2	nd	1.6
11	45.7	1.6	6.6	13.7	5.2	11.5	nd	1.2	4.5	9.5	0.5	35.2	50.1	1.4	4.2	12.5	8.6	13.5	nd	1.3	3.1	4.4	0.9
12	40.7	2.7	7.7	7.3	4.3	9.5	nd	2.7	17.0	4.9	3.3	25.3	44.8	2.2	5.0	6.7	7.0	11.2	nd	2.9	11.9	2.3	6.1
13	60.0	3.2	8.3	7.9	3.5	5.0	nd	1.2	6.6	4.2	nd	29.5	65.4	2.6	5.4	7.2	5.7	5.8	nd	1.2	4.6	2.0	nd
14	53.2	2.1	6.0	9.6	3.4	10.6	nd	1.4	4.2	9.2	0.4	32.1	58.3	1.7	3.9	8.8	5.5	12.4	nd	1.5	2.9	4.3	0.7
15	50.1	2.3	6.3	8.5	5.7	6.9	nd	2.0	12.4	4.1	1.8	27.9	53.8	1.9	4.0	7.7	9.1	7.9	nd	2.1	8.5	1.9	3.2
16	41.1	4.6	8.8	21.0	7.3	4.8	nd	2.0	8.0	1.5	0.8	22.6	44.5	3.7	5.6	19.0	11.8	5.6	nd	2.1	5.5	0.7	1.5
17	43.7	2.6	6.9	11.4	4.0	14.3	nd	2.1	4.7	10.3	nd	14.9	48.6	2.2	4.5	10.6	6.6	17.0	nd	2.3	3.3	4.8	nd
18	45.3	3.1	7.0	14.9	5.3	11.0	0.5	1.2	4.9	7.0	nd	29.8	49.7	2.5	4.5	13.6	8.6	12.9	0.2	1.3	3.4	3.2	nd
19	48.1	2.1	10.6	12.5	4.1	6.5	nd	2.0	9.7	4.5	nd	30.4	53.8	1.7	7.0	11.7	6.8	7.8	nd	2.1	6.9	2.1	nd
20	53.7	2.5	9.1	10.3	3.8	5.9	nd	1.9	7.5	4.6	0.7	21.7	58.8	2.0	5.9	9.5	6.2	6.9	nd	2.0	5.2	2.1	1.4

inc.	weight% oxide + Cl (normalised to 100%)												molecular proportion (normalised to 100 %)									
no.	SiO_2	TiO_2	Al_2O_3	FeO	MgO	CaO	BaO	Na_2O	K_2O	P_2O_5	Cl	total	Si	Ti	Al	Fe	Mg	Ca	Ba	Na	K	P	Cl
21	44.1	2.8	9.8	15.7	4.7	8.3	nd	1.4	6.7	6.4	nd	24.8	49.4	2.4	6.5	14.7	7.8	10.0	nd	1.5	4.8	3.0	nd
CTPs6																							nd
1	37.5	8.3	4.7	12.5	6.1	12.1	nd	0.8	8.6	9.0	0.4	15.5	41.8	7.0	3.1	11.7	10.2	14.4	nd	0.8	6.1	4.2	0.8
2	54.0	4.4	9.2	9.6	4.8	3.8	1.5	0.5	9.7	2.4	nd	29.5	59.8	3.7	6.0	8.9	7.9	4.5	0.7	0.5	6.9	1.1	nd
3	56.0	2.7	6.6	5.1	3.1	11.5	2.4	0.8	7.8	3.9	nd	35.1	61.2	2.2	4.2	4.6	5.1	13.4	1.0	0.9	5.5	1.8	nd
4	23.9	nd	4.7	3.5	1.6	6.6	34.6	1.5	13.5	nd	10.1	13.8	30.0	nd	3.5	3.7	2.9	8.9	17.0	1.9	10.8	nd	21.4
5	43.0	3.2	7.8	7.5	4.6	14.1	5.6	1.0	6.1	6.4	0.5	32.1	48.3	2.7	5.2	7.1	7.8	17.0	2.5	1.1	4.3	3.1	1.0
6	44.0	3.9	9.0	10.0	6.1	11.4	3.8	2.0	7.1	1.9	0.8	20.0	47.8	3.2	5.8	9.1	9.9	13.3	1.6	2.1	4.9	0.9	1.4
7	21.1	nd	3.7	3.6	1.8	36.3	13.6	0.6	2.9	16.3	nd	47.3	25.5	nd	2.7	3.6	3.3	47.1	6.4	0.7	2.3	8.4	nd
8	35.3	2.3	5.6	6.9	3.7	26.3	3.9	1.1	4.3	10.7	nd	32.5	39.4	1.9	3.7	6.4	6.1	31.5	1.7	1.2	3.1	5.0	nd
9	53.3	4.9	8.1	12.1	7.1	1.0	nd	1.3	10.5	1.6	nd	24.9	57.9	4.0	5.2	11.0	11.4	1.2	nd	1.4	7.2	0.8	nd
10	50.5	2.4	6.9	4.5	2.9	12.5	2.2	1.2	6.3	10.7	nd	25.0	57.2	2.0	4.6	4.3	4.8	15.1	1.0	1.3	4.6	5.1	nd
11	43.6	6.4	8.7	10.5	7.2	8.9	4.2	1.0	9.4	nd	nd	46.9	47.8	5.3	5.6	9.6	11.8	10.5	1.8	1.0	6.6	nd	nd
12	46.3	3.7	6.6	7.7	4.6	14.0	nd	0.8	6.5	9.8	nd	35.4	51.2	3.1	4.3	7.2	7.6	16.6	nd	0.8	4.6	4.6	nd
13	32.9	1.6	4.3	5.8	3.6	19.3	4.6	2.4	15.4	7.5	2.7	35.4	36.9	1.3	2.8	5.5	5.9	23.1	2.0	2.6	11.0	3.6	5.2
14	45.6	3.4	7.6	5.7	2.6	7.3	3.3	1.7	16.4	4.1	2.3	29.4	51.7	2.9	5.1	5.4	4.5	8.8	1.5	1.8	11.9	2.0	4.5
15	40.8	2.7	4.1	5.2	2.6	20.3	4.0	1.1	4.1	15.2	nd	32.6	47.0	2.4	2.8	5.0	4.4	25.0	1.8	1.2	3.0	7.4	nd
16	34.4	nd	5.9	6.9	6.4	24.6	9.8	1.0	4.8	6.1	nd	27.1	38.2	nd	3.9	6.5	10.6	29.2	4.3	1.1	3.4	2.9	nd
17	46.5	3.4	7.8	3.9	2.4	5.7	2.8	1.5	20.0	3.5	2.5	26.4	53.0	2.9	5.2	3.8	4.0	7.0	1.3	1.7	14.6	1.7	4.9
18	27.4	nd	4.8	3.1	2.0	4.6	28.4	2.0	12.9	4.7	10.1	13.2	33.8	nd	3.5	3.2	3.6	6.1	13.7	2.4	10.2	2.4	21.1
19	41.5	3.7	7.2	4.4	3.3	7.9	17.5	1.3	5.5	6.8	0.8	17.3	50.9	3.4	5.2	4.5	6.0	10.4	8.4	1.6	4.3	3.5	1.7
20	43.6	3.0	7.6	6.1	4.1	17.4	6.6	0.7	7.4	3.5	nd	16.9	48.6	2.5	5.0	5.7	6.8	20.8	2.9	0.8	5.3	1.6	nd
21	24.1	nd	3.4	6.2	4.2	30.5	17.0	1.0	2.9	10.7	nd	18.9	28.6	nd	2.4	6.1	7.4	38.8	7.9	1.2	2.2	5.4	nd
CTPs7																							
1	49.0	3.6	8.2	8.4	4.0	11.5	nd	0.8	8.0	6.5	nd	33.5	54.2	3.0	5.4	7.8	6.6	13.6	nd	0.8	5.6	3.1	nd
2	49.7	3.6	7.6	7.2	3.4	9.9	2.4	0.6	7.5	8.1	nd	28.5	56.2	3.1	5.1	6.8	5.8	12.0	1.1	0.6	5.4	3.9	nd
3	48.9	7.3	10.8	12.5	6.7	1.0	nd	1.6	10.6	nd	0.5	26.1	53.4	6.0	7.0	11.4	11.0	1.2	nd	1.7	7.4	nd	0.8
4	49.1	7.3	9.1	9.0	6.1	11.4	nd	nd	8.1	nd	nd	6.0	52.3	5.8	5.7	8.0	9.6	13.0	nd	nd	5.5	nd	nd
5	42.5	3.3	5.6	7.2	3.7	17.9	4.4	0.9	6.5	7.8	nd	27.3	47.6	2.8	3.7	6.8	6.3	21.5	1.9	0.9	4.7	3.7	nd
6	44.4	8.9	9.1	17.4	8.2	1.8	nd	1.2	8.9	nd	nd	41.1	48.2	7.3	5.8	15.8	13.2	2.1	nd	1.3	6.2	nd	nd
7	49.5	4.3	7.9	8.4	4.3	8.5	3.7	0.4	8.7	4.4	nd	41.6	55.5	3.6	5.3	7.8	7.2	10.2	1.6	0.5	6.2	2.1	nd
8	56.8	5.3	13.4	5.1	5.2	2.5	nd	1.3	10.4	nd	nd	18.7	62.2	4.4	8.6	4.6	8.5	2.9	nd	1.4	7.3	nd	nd
9	44.6	nd	7.5	7.7	4.8	16.6	4.2	2.4	4.8	7.5	nd	14.3	49.3	nd	4.9	7.1	7.9	19.6	1.8	2.6	3.4	3.5	nd
10	55.7	5.4	9.9	9.6	5.3	3.5	nd	1.4	7.7	1.4	nd	31.8	60.4	4.4	6.3	8.7	8.6	4.1	nd	1.5	5.3	0.7	nd
11	50.7	4.6	8.7	8.4	5.3	6.9	nd	1.2	8.7	5.5	nd	19.0	55.9	3.8	5.6	7.7	8.8	8.2	nd	1.3	6.1	2.6	nd
12	52.9	3.9	7.5	8.3	4.8	7.8	2.7	1.3	7.7	2.7	0.4	31.0	57.6	3.2	4.8	7.6	7.8	9.1	1.2	1.4	5.4	1.2	0.8
13	55.0	4.0	6.7	8.4	3.7	7.7	3.2	1.2	6.1	4.0	nd	24.1	60.6	3.3	4.4	7.7	6.1	9.0	1.4	1.3	4.3	1.9	nd
14	53.9	nd	6.8	1.5	0.4	16.1	3.6	0.6	7.7	9.3	nd	16.0	61.3		4.6	1.5	0.7	19.6	1.6	0.7	5.6	4.5	nd
15	54.6	4.5	9.8	6.8	4.9	4.3	nd	1.0	9.6	4.4	nd	23.0	60.4	3.8	6.4	6.2	8.1	5.2	nd	1.0	6.8	2.1	nd
CTPs8																							nd
1	24.5	2.1	4.2	12.8	8.1	27.1	2.7	1.7	3.3	13.6	nd	24.3	26.9	1.7	2.7	11.8	13.3	31.9	1.2	1.8	2.3	6.3	nd
2	23.5	nd	5.4	11.4	8.2	22.1	8.7	1.7	4.1	13.5	1.4	10.0	26.7	nd	3.6	10.8	13.9	27.0	3.9	1.8	3.0	6.5	2.7
3	39.4	2.8	8.4	8.1	3.7	16.3	nd	1.1	6.8	12.9	0.6	26.4	44.8	2.4	5.6	7.7	6.3	19.8	nd	1.2	4.9	6.2	1.1
4	46.7	3.2	7.8	15.0	10.1	7.0	nd	1.5	8.0	nd	0.7	17.4	48.4	2.5	4.8	13.0	15.6	7.8	nd	1.5	5.3	nd	1.2
5	38.9	4.4	7.2	16.2	7.8	12.4	nd	0.8	5.7	6.4	nd	23.6	42.2	3.6	4.6	14.7	12.7	14.4	nd	0.8	4.0	2.9	nd
6	55.0	3.8	7.9	9.1	6.2	5.7	nd	1.2	6.9	4.2	nd	36.7	59.2	3.1	5.0	8.2	10.0	6.6	nd	1.3	4.7	1.9	nd
7	27.5	nd	4.9	6.0	4.6	16.6	2.6	4.2	17.7	10.4	5.5	21.5	30.5	nd	3.2	5.6	7.6	19.7	1.1	4.5	12.6	4.9	10.4
8	38.5	nd	6.4	12.9	7.2	16.0	5.0	1.3	5.3	7.5	nd	14.5	42.4	nd	4.2	11.9	11.8	18.9	2.2	1.3	3.7	3.5	nd
9	50.5	nd	6.5	10.3	6.6	12.3	nd	1.6	5.1	7.2	nd	18.3	53.8	nd	4.1	9.2	10.4	14.1	nd	1.7	3.5	3.2	nd

inc.	weight% oxide + Cl (normalised to 100%)												molecular proportion (normalised to 100 %)									
no.	SiO_2	TiO_2	Al_2O_3	FeO	MgO	CaO	BaO	Na_2O	K_2O	P_2O_5	Cl	total	Si	Ti	Al	Fe	Mg	Ca	Ba	Na	K	P	Cl
10	36.9	2.9	7.4	13.9	6.8	14.2	nd	1.0	7.4	9.0	0.5	26.6	40.7	2.4	4.8	12.8	11.1	16.7	nd	1.1	5.2	4.2	1.0
11	50.9	2.8	6.8	9.9	6.1	7.9	2.7	0.8	6.9	5.1	nd	21.1	55.7	2.3	4.4	9.1	10.0	9.3	1.2	0.9	4.8	2.3	nd
12	38.8	2.3	5.8	9.9	5.4	3.8	4.9	2.4	18.8	2.5	5.3	28.8	42.8	1.9	3.8	9.2	8.8	4.5	2.1	2.6	13.2	1.2	9.8
13	49.4	3.8	8.6	7.9	5.1	10.3	nd	1.4	6.1	7.5	nd	15.9	54.3	3.1	5.6	7.3	8.4	12.1	nd	1.5	4.2	3.5	nd
14	35.6	nd	4.7	16.0	9.0	16.5	4.5	1.4	4.1	7.7	0.6	19.3	38.3	nd	3.0	14.5	14.5	19.0	1.9	1.4	2.8	3.5	1.0
15	52.6	2.4	7.7	6.1	4.0	10.8	nd	1.3	6.9	8.2	nd	44.9	58.0	2.0	5.0	5.6	6.6	12.7	nd	1.4	4.8	3.8	nd
16	48.4	4.3	7.0	10.5	8.1	6.6	nd	1.6	7.7	5.0	0.8	15.5	51.7	3.5	4.4	9.3	12.9	7.5	nd	1.7	5.3	2.3	1.4
17	59.1	4.5	7.8	11.4	7.2	0.7	0.5	0.7	8.1	nd	nd	18.7	62.8	3.6	4.9	10.1	11.4	0.8	0.2	0.7	5.5	nd	nd
19	28.2	nd	6.4	9.5	5.8	21.9	7.3	1.8	4.7	13.6	0.9	18.7	32.5	nd	4.4	9.2	9.9	27.1	3.3	2.0	3.5	6.6	1.7
20	37.4	2.1	5.3	9.5	6.8	12.8	5.0	1.6	8.3	8.6	2.4	26.8	41.3	1.8	3.5	8.8	11.3	15.2	2.2	1.7	5.9	4.0	4.4
21	51.0	nd	7.3	2.2	0.9	18.8	nd	1.3	4.7	14.0	nd	28.1	57.5	nd	4.8	2.1	1.4	22.7	nd	1.4	3.3	6.7	nd
CTPs12																							
1	41.4	nd	8.9	8.5	4.7	6.6	nd	2.7	20.0	3.6	3.7	10.4	45.5		5.8	7.8	7.6	7.8	nd	2.9	14.0	1.7	6.9
2	53.5	3.7	5.4	7.4	3.8	11.1	nd	1.3	5.8	7.5	0.4	39.0	58.1	3.0	3.4	6.7	6.2	13.0	nd	1.4	4.0	3.5	0.8
3	48.6	3.2	5.2	10.0	4.6	13.3	nd	1.5	5.6	7.5	0.5	30.8	52.5	2.6	3.3	9.0	7.4	15.4	nd	1.6	3.9	3.4	1.0
4	35.8	3.5	4.9	13.4	8.1	19.7	nd	1.6	5.2	7.2	0.5	28.6	37.9	2.8	3.1	11.8	12.8	22.3	nd	1.7	3.5	3.2	0.9
5	48.1	4.1	7.4	10.3	5.3	9.6	nd	0.9	8.1	6.3	nd	40.7	52.9	3.4	4.8	9.4	8.7	11.3	nd	1.0	5.7	2.9	nd
6	55.6	4.4	12.1	9.9	4.8	nd	nd	0.9	11.2	1.0	nd	51.9	61.8	3.7	7.9	9.2	8.0	nd	nd	1.0	7.9	0.5	nd
7	20.6	nd	4.7	14.2	6.4	18.0	7.5	6.5	12.8	5.7	3.6	17.0	22.9	nd	3.1	13.2	10.6	21.5	3.3	7.0	9.1	2.7	6.7
8	51.4	3.8	7.2	11.9	7.9	5.3	nd	1.4	7.4	3.1	0.7	25.7	54.5	3.0	4.5	10.6	12.4	6.0	nd	1.4	5.0	1.4	1.2
9	58.1	3.8	7.3	9.9	3.9	3.6	nd	1.3	7.7	4.4	nd	36.8	63.6	3.1	4.7	9.1	6.4	4.2	nd	1.4	5.4	2.0	nd
CTPs13																							
1	53.6	5.0	10.2	10.1	2.2	3.0	nd	0.9	11.1	3.6	0.4	41.7	60.6	4.2	6.8	9.6	3.8	3.6	nd	1.0	8.0	1.7	0.7
2	55.3	2.9	11.3	9.2	2.4	1.6	3.1	1.6	10.6	2.0	nd	37.0	63.1	2.5	7.6	8.8	4.1	2.0	1.4	1.7	7.8	0.9	nd
3	50.1	6.0	11.0	14.6	3.4	1.3	nd	1.2	10.8	1.7	nd	52.6	56.6	5.1	7.3	13.8	5.7	1.6	nd	1.3	7.8	0.8	nd
4	65.1	2.4	6.2	4.4	1.8	6.3	5.4	2.1	6.4	nd	nd	20.5	70.9	1.9	4.0	4.0	3.0	7.3	2.3	2.2	4.4	nd	nd
5	58.0	4.5	8.6	10.0	2.5	2.4	nd	1.0	9.8	3.2	nd	43.8	64.7	3.8	5.7	9.3	4.1	2.9	nd	1.1	7.0	1.5	nd
6	59.0	2.5	14.5	6.1	1.2	1.7	nd	1.6	11.8	1.7	nd	27.3	67.2	2.1	9.7	5.8	2.1	2.1	nd	1.7	8.6	0.8	nd
7	42.7	8.2	7.4	24.3	5.6	nd	nd	1.1	9.2	1.5	nd	29.4	47.8	6.9	4.9	22.7	9.3	nd	nd	1.2	6.6	0.7	nd
8	57.6	2.8	5.5	6.5	1.5	5.1	2.7	2.1	10.8	4.9	0.6	42.0	64.8	2.4	3.6	6.1	2.4	6.1	1.2	2.3	7.8	2.3	1.1
9	58.2	nd	14.7	1.9	0.1	4.7	nd	1.2	14.8	4.4	nd	24.6	67.5	nd	10.1	1.9	0.2	5.9	nd	1.4	11.0	2.1	nd
10	51.0	3.1	8.6	8.3	2.2	8.2	nd	1.7	8.7	7.4	0.8	22.7	57.2	2.6	5.7	7.8	3.7	9.9	nd	1.8	6.2	3.5	1.5
CTPs14																							
1	42.2	nd	5.7	10.5	5.3	18.2	4.0	1.6	6.4	6.1	nd	11.1	46.1	nd	3.7	9.6	8.6	21.4	1.7	1.7	4.5	2.8	nd
2	12.8	0.3	4.2	6.0	3.5	44.6	nd	2.8	1.6	24.2	nd	11.8	14.6	0.2	2.9	5.8	6.0	54.6	nd	3.1	1.2	11.7	nd
3	41.6	5.9	9.3	12.7	8.2	11.8	nd	2.4	8.1	nd	nd	12.7	44.0	4.7	5.8	11.2	13.0	13.3	nd	2.5	5.5	nd	nd
4	36.7	nd	8.5	14.0	9.5	22.6	nd	3.6	5.1	nd	nd	11.1	37.2	nd	5.1	11.9	14.4	24.6	nd	3.5	3.3	nd	nd
5	45.7	4.4	7.2	11.7	7.2	10.6	2.1	1.7	6.3	2.6	0.6	30.1	48.9	3.5	4.5	10.5	11.4	12.2	0.9	1.7	4.3	1.2	1.0
6	45.7	3.2	7.9	9.2	5.3	8.8	4.1	1.0	9.8	4.4	0.6	16.0	51.1	2.7	5.2	8.6	8.8	10.6	1.8	1.1	7.0	2.1	1.1
7	40.3	2.9	6.3	11.1	7.8	15.6	5.3	1.4	5.3	4.0	nd	11.2	43.6	2.4	4.0	10.0	12.6	18.1	2.2	1.4	3.7	1.8	nd
8	36.0	nd	3.7	5.5	2.8	24.9	5.1	1.7	3.9	16.5	nd	19.7	41.5	nd	2.5	5.3	4.8	30.8	2.3	1.9	2.8	8.1	nd
9	27.5	2.9	5.3	5.3	2.9	5.2	24.6	1.9	8.5	10.3	5.7	15.7	35.3	2.8	4.0	5.7	5.5	7.1	12.4	2.4	7.0	5.6	12.4
10	33.5	2.6	6.0	7.8	2.8	2.7	20.7	1.8	11.1	5.4	5.5	22.8	41.3	2.4	4.4	8.0	5.2	3.6	10.0	2.1	8.7	2.8	11.5
11	31.8	2.9	5.6	6.9	3.6	5.3	19.5	2.4	9.7	7.7	4.6	22.8	39.2	2.7	4.0	7.0	6.7	7.0	9.4	2.9	7.6	4.0	9.5
12	33.6	4.1	7.2	12.8	8.0	13.2	4.3	1.6	14.1	nd	1.2	39.0	36.6	3.4	4.6	11.7	12.9	15.4	1.8	1.7	9.8	nd	2.2
13	46.4	nd	6.5	7.7	6.1	18.4	nd	1.7	3.8	9.4	nd	7.8	49.6		4.1	6.8	9.7	21.1	nd	1.8	2.6	4.3	nd
14	28.7	5.5	3.7	17.3	8.3	21.1	nd	1.3	4.7	8.5	0.8	9.5	30.6	4.4	2.3	15.4	13.2	24.2	nd	1.4	3.2	3.8	1.5
15	38.0	nd	5.3	5.9	2.8	10.0	25.9	1.4	4.7	6.0	nd	9.2	48.7		4.0	6.3	5.4	13.7	13.0	1.7	3.9	3.3	nd
16	44.8	4.4	6.9	12.4	6.6	12.3	nd	0.8	7.0	4.8	nd	24.9	48.2	3.6	4.4	11.2	10.6	14.2	nd	0.8	4.8	2.2	nd

inc.	weight% oxide + Cl (normalised to 100%)												molecular proportion (normalised to 100 %)										
no.	SiO_2	TiO_2	Al_2O_3	FeO	MgO	CaO	BaO	Na_2O	K_2O	P_2O_5	Cl	total	Si	Ti	Al	Fe	Mg	Ca	Ba	Na	K	P	Cl
17	10.7	nd	2.1	18.4	13.5	39.0	4.5	1.6	2.1	8.1	nd	12.2	11.0		1.3	15.8	20.6	43.0	1.8	1.6	1.4	3.5	nd
18	37.1	3.3	4.5	10.5	4.4	17.3	1.8	1.6	6.7	12.4	0.5	35.4	41.8	2.8	3.0	9.9	7.4	20.9	0.8	1.7	4.8	5.9	1.0
19	32.4	nd	1.8	11.2	7.0	28.0	3.7	4.5	1.1	7.1	3.2	9.5	33.0		1.1	9.5	10.6	30.6	1.5	4.5	0.7	3.1	5.5
20	39.2	4.0	6.1	18.2	9.2	13.0	2.6	2.2	5.6	nd	nd	22.8	41.1	3.1	3.8	15.9	14.3	14.7	1.1	2.3	3.7	nd	nd
21	47.8	nd	4.0	6.7	4.1	20.4	3.0	1.3	2.7	9.9	nd	33.7	51.9		2.5	6.1	6.7	23.7	1.3	1.4	1.9	4.6	nd
CTPs15																							
2	64.6	1.2	8.0	16.4	0.5	nd	0.6	0.8	6.8	1.2	nd	23.9	71.4	1.0	5.2	15.2	0.8	nd	0.3	0.8	4.8	0.5	nd
4	41.9	4.0	4.9	24.7	9.5	7.6	nd	2.1	5.4	nd	nd	25.8	43.6	3.1	3.0	21.5	14.7	8.4	nd	2.1	3.6	nd	nd
5	61.0	2.3	8.0	9.3	2.8	3.5	nd	1.5	9.5	2.2	nd	11.3	66.7	1.9	5.2	8.5	4.5	4.0	nd	1.6	6.6	1.0	nd
6	25.0	2.4	4.0	24.2	7.5	16.6	5.5	2.2	5.0	7.3	0.4	36.3	27.9	2.1	2.6	22.6	12.4	19.9	2.4	2.3	3.5	3.4	0.7
7	49.1	nd	4.8	2.3	0.6	20.2	nd	1.4	5.3	16.4	nd	9.8	55.8	nd	3.2	2.2	1.1	24.5	nd	1.6	3.8	7.9	nd
8	46.0	2.4	5.4	24.5	6.1	5.1	3.3	1.0	6.1	nd	nd	12.6	49.9	2.0	3.5	22.2	9.9	5.9	1.4	1.1	4.2	nd	nd
9	37.5	6.5	7.1	23.0	9.4	7.0	nd	1.0	8.6	nd	nd	11.7	40.0	5.2	4.5	20.5	15.0	8.0	nd	1.0	5.8	nd	nd
10	50.7	5.1	5.7	16.5	5.9	2.9	nd	1.3	8.3	3.6	nd	43.7	55.3	4.2	3.6	15.0	9.7	3.4	nd	1.4	5.8	1.7	nd
12	57.4	4.5	4.9	11.5	4.2	5.7	nd	0.9	6.4	4.7	nd	22.9	62.1	3.6	3.1	10.4	6.8	6.6	nd	0.9	4.4	2.1	nd
13	60.2	0.7	7.6	3.9	nd	7.7	nd	2.8	9.3	7.8	nd	12.9	67.9	0.6	5.0	3.7	nd	9.3	nd	3.0	6.7	3.7	nd
14	49.6	5.7	8.5	7.2	2.3	5.6	2.0	1.2	12.4	4.8	0.7	27.2	56.7	4.9	5.7	6.9	3.9	6.9	0.9	1.3	9.0	2.3	1.4
15	60.8	3.2	11.0	3.1	nd	nd	nd	2.5	15.8	nd	3.5	9.1	67.0	2.6	7.2	2.9	nd	nd	nd	2.6	11.1	nd	6.6
17	53.0	4.2	15.3	7.1	7.6	nd	nd	0.9	12.0	nd	nd	9.1	58.3	3.5	9.9	6.5	12.4	nd	nd	0.9	8.4	nd	nd
18	4.5	nd	nd	3.7	nd	31.3	23.2	2.0	1.5	32.7	1.1	8.1	6.5	nd	nd	4.5	nd	48.8	13.2	2.7	1.4	20.1	2.7
19	33.7	1.8	3.6	5.5	2.3	22.9	6.8	1.1	5.1	17.1	nd	26.9	40.1	1.6	2.5	5.5	4.1	29.2	3.2	1.2	3.9	8.6	nd
20	55.8	4.5	11.0	10.3	2.8	0.8	nd	0.9	12.5	1.0	0.3	26.7	62.5	3.8	7.2	9.7	4.7	0.9	nd	1.0	8.9	0.5	0.7
21	65.8	3.0	9.5	8.3	1.7	nd	nd	0.7	10.7	nd	0.3	30.0	72.2	2.4	6.1	7.6	2.7	nd	nd	0.8	7.5	nd	0.6
CTPb4																							
1	26.5	nd	3.7	5.5	nd	15.2	nd	nd	28.0	11.4	9.6	6.7	30.0	nd	2.5	5.2	nd	18.4	nd	nd	20.2	5.4	18.4
2	26.1	nd	3.5	12.9	6.1	14.7	nd	2.6	12.1	13.5	8.5	11.3	27.7	nd	2.2	11.4	9.6	16.7	nd	2.7	8.2	6.1	15.3
3	26.4	nd	4.2	9.2	6.0	17.1	nd	3.6	12.5	15.1	5.9	14.2	28.8	nd	2.7	8.4	9.8	20.0	nd	3.8	8.7	7.0	10.9
4	28.9	3.1	3.9	7.0	3.3	16.7	nd	2.6	14.5	13.7	6.2	12.2	32.0	2.6	2.5	6.5	5.5	19.8	nd	2.8	10.2	6.4	11.7
5	23.9	2.7	3.3	11.0	5.1	11.8	nd	4.0	22.4	8.6	7.1	13.8	26.2	2.2	2.1	10.1	8.4	13.8	nd	4.3	15.6	4.0	13.2
6	21.4	nd	4.0	8.9	5.8	10.4	9.2	6.8	24.5	nd	9.1	6.8	23.2	nd	2.5	8.0	9.4	12.1	3.9	7.1	16.9	nd	16.8
7	19.1	nd	3.8	8.6	3.9	11.6	7.8	4.5	24.4	6.7	9.6	11.8	21.5	nd	2.5	8.1	6.5	14.0	3.4	5.0	17.5	3.2	18.3
8	23.7	nd	3.7	7.2	4.6	11.5	7.6	3.2	22.9	7.5	8.1	13.4	26.7	nd	2.4	6.8	7.7	13.9	3.3	3.5	16.5	3.6	15.5
9	25.6	nd	3.5	8.5	4.2	12.1	6.2	2.9	22.0	9.5	5.5	25.4	29.6	nd	2.4	8.2	7.1	15.0	2.8	3.3	16.2	4.7	10.8
10	25.3	2.9	3.3	10.4	4.9	11.9	4.1	3.9	16.7	9.3	7.2	30.2	27.9	2.4	2.2	9.6	8.1	14.1	1.8	4.2	11.8	4.4	13.5
11	52.1	nd	6.3	4.7	3.6	7.2	nd	3.5	13.0	7.1	2.5	13.3	56.8	nd	4.1	4.3	5.8	8.4	nd	3.7	9.0	3.3	4.6
12	22.3	nd	3.7	9.9	4.9	9.5	7.5	4.1	24.4	5.0	8.7	17.5	24.9	nd	2.5	9.3	8.1	11.4	3.3	4.4	17.4	2.4	16.4
13	22.0	nd	3.8	11.4	4.4	12.0	5.4	4.1	23.0	6.6	7.4	17.9	24.6	nd	2.5	10.7	7.4	14.4	2.4	4.5	16.5	3.1	14.0
14	18.7	1.6	2.9	5.8	3.4	12.8	6.1	2.6	26.3	8.0	11.8	28.3	20.7	1.4	1.9	5.4	5.6	15.2	2.6	2.8	18.6	3.7	22.1
15	21.7	nd	3.8	8.3	3.8	12.0	7.0	3.0	23.9	7.7	8.8	11.0	24.5	nd	2.5	7.9	6.4	14.5	3.1	3.2	17.2	3.7	16.9
16	26.2	nd	4.6	8.7	4.6	9.2	5.4	4.7	23.3	6.4	6.8	18.3	29.5	nd	3.0	8.2	7.8	11.1	2.4	5.1	16.8	3.1	13.0
17	29.2	nd	4.1	9.3	5.0	15.4	nd	3.0	19.5	8.2	6.3	10.7	31.5	nd	2.6	8.4	8.0	17.7	nd	3.1	13.4	3.7	11.5
18	19.8	nd	3.0	12.2	7.4	16.7	4.5	6.7	13.6	8.0	8.1	21.4	20.9	nd	1.9	10.8	11.6	18.8	1.9	6.9	9.2	3.6	14.5
19	20.9	nd	4.2	8.9	5.0	10.7	4.2	4.3	25.7	7.2	8.8	14.7	23.2	nd	2.7	8.3	8.3	12.8	1.8	4.6	18.2	3.4	16.6
20	18.6	nd	3.4	8.0	3.6	13.1	8.6	3.8	23.8	7.9	9.2	17.3	21.2	nd	2.3	7.6	6.2	15.9	3.9	4.2	17.3	3.8	17.7
CTPb7																							
1	70.3	1.2	3.7	8.1	1.1	2.3	nd	1.3	6.7	3.8	1.5	36.8	74.9	0.9	2.3	7.2	1.8	2.7	nd	1.3	4.6	1.7	2.7
2	37.9	1.9	7.7	6.6	3.0	11.3	nd	2.5	18.0	7.3	3.8	39.4	42.4	1.6	5.0	6.2	5.1	13.6	nd	2.7	12.9	3.5	7.2
3	20.8	nd	5.2	9.7	5.3	31.5	nd	3.6	5.6	17.1	1.3	14.6	23.0	nd	3.4	9.0	8.8	37.5	nd	3.9	3.9	8.0	2.5
4	69.4	1.8	13.2	1.5	0.7	nd	nd	1.5	9.0	2.4	0.4	48.0	77.3	1.5	8.7	1.4	1.1	nd	nd	1.6	6.4	1.1	0.8

inc.	weight% oxide + Cl (normalised to 100%)												molecular proportion (normalised to 100 %)										
no.	SiO_2	TiO_2	Al_2O_3	FeO	MgO	CaO	BaO	Na_2O	K_2O	P_2O_5	Cl	total	Si	Ti	Al	Fe	Mg	Ca	Ba	Na	K	P	Cl
5	41.9	nd	7.1	7.2	4.2	7.7	nd	2.9	20.1	2.1	6.7	24.8	44.3	nd	4.4	6.4	6.6	8.7	nd	3.0	13.5	1.0	12.1
6	43.0	3.6	9.1	8.6	4.3	3.6	nd	2.1	18.0	3.2	4.5	38.6	47.3	3.0	5.9	7.9	7.0	4.3	nd	2.2	12.6	1.5	8.4
7	11.7	2.6	4.3	8.4	3.5	14.1	nd	3.5	31.6	nd	20.2	16.2	11.6	1.9	2.5	6.9	5.2	14.9	nd	3.3	19.9	nd	33.7
8	21.2	2.6	4.2	7.1	2.6	13.4	nd	4.6	26.2	4.1	14.1	17.3	22.0	2.0	2.6	6.2	4.1	14.8	nd	4.6	17.3	1.8	24.7
9	32.5	0.9	7.0	5.2	2.4	14.0	nd	2.7	19.7	8.5	7.0	51.7	35.7	0.7	4.5	4.7	4.0	16.5	nd	2.9	13.8	3.9	13.1
10	58.6	4.2	9.6	11.6	6.0	0.7	nd	0.7	8.6	nd	nd	15.8	63.1	3.4	6.1	10.4	9.6	0.9	nd	0.7	5.9	nd	nd
11	33.3	2.9	6.4	8.8	4.7	18.6	nd	2.3	11.6	9.0	2.4	28.8	36.5	2.4	4.1	8.1	7.7	21.9	nd	2.4	8.1	4.2	4.5
12	38.2	2.0	9.0	8.3	3.8	9.2	nd	2.6	16.3	4.6	5.9	28.6	41.4	1.6	5.8	7.5	6.1	10.7	nd	2.7	11.3	2.1	10.9
13	35.7	2.5	8.1	4.2	2.8	12.5	nd	3.4	18.5	5.9	6.5	19.3	38.9	2.0	5.2	3.8	4.5	14.6	nd	3.6	12.8	2.7	11.9
14	32.4	2.3	6.8	8.0	4.3	15.0	nd	2.3	15.3	8.0	5.4	46.9	35.3	1.9	4.4	7.3	6.9	17.5	nd	2.5	10.6	3.7	9.9
15	53.2	2.4	8.1	23.6	4.4	nd	nd	1.0	4.9	1.7	0.6	36.9	57.8	2.0	5.2	21.5	7.2	nd	nd	1.0	3.4	0.8	1.1
16	38.9	3.2	7.5	7.4	3.2	11.5	nd	2.6	16.3	5.6	3.9	22.4	42.8	2.6	4.9	6.8	5.2	13.6	nd	2.8	11.4	2.6	7.3
17	62.5	1.7	9.3	17.0	1.8	nd	nd	1.1	4.1	2.1	0.4	48.6	68.3	1.4	6.0	15.6	3.0	nd	nd	1.1	2.9	1.0	0.8
18	47.0	2.9	8.6	8.0	3.8	9.3	nd	2.9	12.0	2.5	3.0	17.3	50.4	2.4	5.4	7.2	6.1	10.7	nd	3.0	8.2	1.2	5.5
19	39.7	2.9	7.9	6.6	4.0	11.5	nd	2.8	14.3	6.9	3.4	27.2	43.7	2.4	5.1	6.1	6.6	13.6	nd	3.0	10.0	3.2	6.3
20	52.8	nd	9.7	8.3	3.4	6.0	nd	1.4	15.2	nd	3.2	7.5	56.5	nd	6.1	7.5	5.4	6.8	nd	1.4	10.4	nd	5.9
CTPb8																							
1	40.6	3.3	6.0	8.6	6.8	9.1	nd	1.6	15.8	4.7	3.5	8.8	43.6	2.6	3.8	7.7	10.8	10.5	nd	1.7	10.8	2.1	6.3
2	38.9	1.9	5.6	7.4	4.6	8.6	nd	2.0	19.7	5.8	5.4	23.0	42.2	1.6	3.6	6.7	7.4	10.0	nd	2.1	13.6	2.7	10.0
3	37.4	nd	7.8	5.8	2.8	9.0	nd	9.1	11.3	nd	16.9	7.8	35.6	nd	4.4	4.6	3.9	9.1	nd	8.4	6.8	nd	27.2
4	40.9	2.9	6.7	5.9	3.5	8.8	nd	1.6	18.4	5.1	6.2	20.9	44.1	2.3	4.3	5.3	5.7	10.2	nd	1.6	12.7	2.3	11.4
5	40.8	3.0	5.9	8.0	6.3	7.9	nd	1.5	17.0	4.0	5.5	24.8	43.2	2.4	3.7	7.1	9.9	9.0	nd	1.6	11.5	1.8	9.9
6	37.4	2.7	5.8	9.9	7.8	8.9	nd	2.4	16.8	4.1	4.1	25.7	39.7	2.2	3.7	8.8	12.4	10.2	nd	2.5	11.4	1.8	7.3
7	37.3	2.2	5.3	9.5	7.0	27.5	nd	3.7	5.0	2.0	0.5	30.0	37.9	1.7	3.2	8.1	10.6	30.0	nd	3.6	3.3	0.9	0.9
8	33.3	1.7	5.2	10.8	8.1	15.6	nd	2.9	13.2	6.3	2.9	19.0	35.3	1.4	3.3	9.6	12.8	17.8	nd	2.9	8.9	2.8	5.3
9	30.6	nd	4.9	9.7	7.9	18.3	nd	3.9	13.7	7.4	3.7	13.5	32.2	nd	3.0	8.5	12.5	20.7	nd	4.0	9.2	3.3	6.6
10	29.0	2.0	4.9	11.6	8.6	18.5	nd	2.7	11.7	7.4	3.4	21.7	30.5	1.6	3.1	10.3	13.6	20.9	nd	2.8	7.9	3.3	6.1
11	38.3	1.7	4.9	9.3	6.7	19.2	nd	0.6	4.9	11.0	3.3	34.2	40.4	1.4	3.1	8.2	10.5	21.7	nd	0.6	3.3	4.9	6.0
12	30.7	4.0	5.8	8.4	7.0	15.5	nd	3.2	13.5	7.3	4.5	11.1	32.7	3.2	3.7	7.5	11.2	17.7	nd	3.3	9.2	3.3	8.2
13	42.1	4.7	7.8	9.4	8.5	6.7	nd	1.4	13.4	2.7	3.4	29.8	44.4	3.7	4.8	8.3	13.4	7.5	nd	1.4	9.0	1.2	6.1
14	16.5	1.8	3.1	10.7	7.8	31.3	nd	2.0	9.4	14.4	3.0	28.1	17.8	1.5	2.0	9.7	12.6	36.1	nd	2.1	6.4	6.6	5.4
15	33.8	2.0	5.0	9.3	7.4	16.4	nd	2.4	13.6	6.8	3.3	35.1	35.9	1.6	3.1	8.2	11.8	18.6	nd	2.5	9.2	3.1	6.0
16	56.1	3.5	9.9	8.3	8.3	1.9	nd	2.2	5.3	nd	4.6	12.0	56.5	2.7	5.9	7.0	12.5	2.1	nd	2.1	3.4	nd	7.8
17	33.5	nd	4.8	9.3	7.9	14.0	nd	3.1	15.1	8.3	4.1	15.4	35.7	nd	3.0	8.3	12.5	15.9	nd	3.2	10.3	3.7	7.3
18	31.6	1.9	4.7	6.7	6.6	17.1	nd	2.5	14.3	10.7	3.9	22.0	34.2	1.6	3.0	6.1	10.7	19.8	nd	2.7	9.9	4.9	7.1
19	50.0	nd	7.1	6.4	8.1	10.9	nd	2.3	8.0	nd	7.2	10.5	48.6	nd	4.1	5.2	11.8	11.4	nd	2.2	5.0	nd	11.8
20	37.7	2.8	5.8	10.4	7.6	12.8	nd	2.8	12.5	4.9	2.6	19.4	40.0	2.2	3.7	9.3	12.1	14.5	nd	2.9	8.5	2.2	4.7
21	44.6	3.0	6.7	8.9	6.2	4.2	nd	2.0	18.5	2.1	3.7	28.1	48.0	2.5	4.3	8.0	10.0	4.8	nd	2.1	12.7	1.0	6.7
22	22.6	1.2	4.0	4.5	3.9	21.0	nd	2.1	22.1	11.1	7.6	33.2	24.6	1.0	2.6	4.1	6.4	24.6	nd	2.2	15.4	5.1	14.1
24	38.8	2.1	5.8	6.8	4.9	9.5	nd	1.6	20.1	5.7	4.7	32.1	42.3	1.7	3.7	6.2	7.9	11.1	nd	1.7	14.0	2.7	8.7
25	51.5	6.0	7.5	13.9	7.9	nd	nd	0.6	10.9	1.7	nd	37.6	55.9	4.9	4.8	12.6	12.8	nd	nd	0.7	7.6	0.8	nd
26	33.5	2.5	5.3	7.3	4.6	12.9	nd	2.0	19.0	8.3	4.6	27.3	37.0	2.0	3.5	6.8	7.5	15.3	nd	2.2	13.4	3.9	8.5
27	36.5	2.0	4.5	9.7	7.1	16.3	nd	1.5	11.4	8.3	2.6	48.6	39.0	1.6	2.9	8.7	11.3	18.7	nd	1.6	7.8	3.8	4.7
29	44.9	3.2	6.9	8.4	7.6	7.0	nd	2.0	12.4	5.0	2.8	17.6	47.9	2.6	4.3	7.5	12.0	7.9	nd	2.1	8.4	2.2	5.0
30	27.1	nd	5.2	10.2	7.8	22.0	nd	2.8	9.9	11.8	3.2	12.1	29.0	nd	3.3	9.2	12.5	25.3	nd	2.9	6.7	5.3	5.7
32	31.6	2.9	4.7	9.3	6.9	17.5	nd	1.9	11.8	9.7	3.6	24.7	34.0	2.3	3.0	8.3	11.1	20.2	nd	2.0	8.1	4.4	6.6
33	31.0	2.0	4.3	9.5	6.3	16.7	nd	2.3	14.2	10.2	3.3	29.5	33.8	1.7	2.7	8.7	10.2	19.6	nd	2.5	9.9	4.7	6.2
34	45.9	nd	14.0	nd	6.7	6.9	nd	8.5	nd	nd	18.2	5.5	41.5	nd	7.5	nd	9.0	6.7	nd	7.4	nd	nd	27.9
35	35.9	3.2	6.0	8.3	4.7	10.0	nd	2.3	19.2	5.1	5.4	22.8	38.9	2.6	3.8	7.5	7.6	11.6	nd	2.4	13.3	2.4	9.9

inc.	weight% oxide + Cl (normalised to 100%)												molecular proportion (normalised to 100 %)									
no.	SiO_2	TiO_2	Al_2O_3	FeO	MgO	CaO	BaO	Na_2O	K_2O	P_2O_5	Cl	total	Si	Ti	Al	Fe	Mg	Ca	Ba	Na	K	P	Cl
36	49.8	3.6	7.5	7.5	5.0	3.5	nd	0.7	13.6	3.4	5.3	43.0	52.9	2.9	4.7	6.7	7.9	4.0	nd	0.7	9.2	1.5	9.6
37	34.1	nd	5.0	6.6	3.9	12.4	nd	3.0	20.3	8.4	6.3	13.0	37.1	nd	3.2	6.0	6.4	14.4	nd	3.2	14.1	3.9	11.7
37	34.1	nd	5.0	6.6	3.9	12.4	nd	3.0	20.3	8.4	6.3	13.0	37.1		3.2	6.0	6.4	14.4	nd	3.2	14.1	3.9	11.7
38	35.9	1.9	6.2	8.2	5.1	10.0	nd	2.1	19.3	5.7	5.7	21.7	38.8	1.5	4.0	7.4	8.2	11.6	nd	2.2	13.3	2.6	10.4
39	34.4	2.6	5.3	10.3	5.9	12.9	nd	2.3	13.8	4.9	7.5	41.5	35.6	2.0	3.3	8.9	9.1	14.4	nd	2.3	9.1	2.2	13.2
40	56.6	nd	5.5	4.3	3.5	3.3	nd	1.7	17.2	2.8	5.0	15.0	59.8	nd	3.4	3.8	5.5	3.8	nd	1.8	11.6	1.3	9.0
MM8																							
1	53.3	6.5	11.7	5.3	1.6	3.4	2.6	2.2	11.2	1.8	0.5	8.3	61.0	5.6	7.9	5.0	2.7	4.1	1.2	2.5	8.2	0.9	0.9
2	35.6	2.1	5.6	8.9	4.9	18.0	2.4	0.8	6.9	14.6	0.3	28.3	40.9	1.8	3.8	8.5	8.5	22.1	1.1	0.9	5.0	7.1	0.5
3	49.6	2.3	7.2	8.7	4.0	8.2	0.9	1.8	8.4	7.0	1.9	21.7	54.4	1.9	4.6	7.9	6.5	9.6	0.4	2.0	5.9	3.3	3.5
4	44.6	2.7	7.1	14.4	5.7	9.3	nd	2.0	6.2	7.2	0.8	8.3	48.7	2.2	4.6	13.2	9.3	10.9	nd	2.1	4.3	3.3	1.4
5	34.9	1.5	7.0	12.6	5.2	15.4	nd	1.3	5.4	15.9	0.6	8.8	39.9	1.3	4.7	12.0	8.9	18.9	nd	1.4	4.0	7.7	1.2
6	52.3	4.8	8.1	13.3	7.1	4.0	0.2	2.0	5.9	2.4	0.0	14.4	56.0	3.8	5.1	11.9	11.4	4.6	0.1	2.0	4.1	1.1	0.0
7	39.1	1.6	6.3	11.8	5.8	15.5	3.0	0.9	5.8	9.4	0.8	15.9	43.3	1.4	4.1	11.0	9.6	18.4	1.3	1.0	4.1	4.4	1.4
8	38.4	3.1	6.9	14.5	6.4	11.2	3.5	0.8	6.8	7.4	0.8	15.5	42.9	2.6	4.5	13.6	10.6	13.4	1.5	0.9	4.9	3.5	1.6
9	33.7	1.9	7.1	6.5	4.8	9.2	4.6	2.9	20.1	3.6	5.5	10.5	37.4	1.6	4.7	6.1	7.9	11.0	2.0	3.1	14.3	1.7	10.3
10	32.4	1.7	7.0	12.5	3.8	12.1	4.1	3.1	10.6	7.8	4.8	7.4	36.1	1.4	4.6	11.6	6.3	14.4	1.8	3.3	7.6	3.7	9.1
11	38.6	1.5	6.9	10.8	6.1	11.8	5.5	2.1	9.0	6.3	1.4	8.7	43.1	1.3	4.5	10.0	10.1	14.2	2.4	2.3	6.4	3.0	2.6
12	31.7	2.4	6.3	9.5	4.8	16.8	3.9	1.4	11.0	9.8	2.4	27.8	35.8	2.0	4.2	9.0	8.1	20.4	1.7	1.5	8.0	4.7	4.5
13	34.7	2.5	6.9	10.1	5.0	16.0	3.1	1.5	8.5	10.0	1.8	14.1	39.1	2.1	4.5	9.5	8.3	19.2	1.4	1.7	6.1	4.8	3.4
14	60.2	3.0	9.4	7.2	4.2	2.2	nd	1.1	9.4	3.0	0.2	25.7	65.9	2.5	6.1	6.6	6.8	2.6	nd	1.1	6.6	1.4	0.4
15	53.1	2.8	8.4	11.5	5.9	3.6	2.4	1.2	8.0	2.6	0.5	19.0	58.0	2.3	5.4	10.5	9.6	4.3	1.0	1.3	5.6	1.2	0.9
16	48.5	3.4	8.4	10.2	4.0	9.1	2.3	1.0	6.9	6.1	0.1	22.2	54.4	2.9	5.5	9.5	6.7	10.9	1.0	1.1	4.9	2.9	0.1
17	36.0	1.7	6.8	10.1	3.6	17.8	4.4	1.1	5.6	12.3	0.6	14.3	41.5	1.4	4.6	9.7	6.2	22.0	2.0	1.2	4.1	6.0	1.1
18	41.6	1.7	5.6	9.7	3.2	9.4	2.6	2.9	10.9	8.4	3.8	35.6	46.3	1.4	3.7	9.0	5.3	11.2	1.1	3.1	7.8	4.0	7.2
19	16.3	4.0	3.3	24.9	9.1	22.0	6.4	3.1	2.7	7.5	0.6	8.8	17.9	3.3	2.2	23.0	15.0	26.0	2.8	3.3	1.9	3.5	1.1
20	62.8	3.5	13.9	2.9	0.6	0.1	nd	1.4	12.9	1.7	0.1	27.6	71.7	3.0	9.4	2.7	1.1	0.1	nd	1.6	9.4	0.8	0.3
21	42.4	2.5	7.4	11.1	5.3	11.9	4.4	1.5	6.2	6.9	0.6	23.0	47.4	2.1	4.8	10.3	8.8	14.2	1.9	1.6	4.4	3.2	1.2
22	36.1	1.9	5.3	8.5	3.3	15.9	2.0	0.2	6.1	15.9	4.6	19.3	40.4	1.6	3.5	8.0	5.6	19.1	0.9	0.2	4.4	7.6	8.8
23	41.6	1.9	6.1	8.6	4.9	9.0	1.2	3.0	12.2	6.9	4.5	12.4	45.0	1.6	3.9	7.8	7.8	10.4	0.5	3.2	8.4	3.2	8.2
24	46.9	0.4	7.9	15.7	5.0	10.6	0.5	1.3	5.5	5.6	0.6	9.4	50.9	0.3	5.1	14.2	8.1	12.3	0.2	1.4	3.8	2.6	1.2
25	40.9	3.3	7.5	11.3	5.2	12.5	2.5	0.5	8.0	7.7	0.7	37.6	45.8	2.8	4.9	10.6	8.7	14.9	1.1	0.5	5.7	3.6	1.3
26	54.4	4.1	8.7	13.6	5.9	1.2	nd	1.4	7.4	2.3	1.0	16.6	58.6	3.4	5.5	12.3	9.4	1.4	nd	1.4	5.1	1.0	1.8
27	34.5	2.1	7.3	14.5	5.1	16.0	2.5	0.8	5.5	11.1	0.7	18.5	39.1	1.8	4.9	13.7	8.7	19.4	1.1	0.9	4.0	5.3	1.3
28	32.7	2.0	5.0	13.4	3.7	16.5	4.5	2.7	6.4	11.6	1.3	8.5	37.4	1.7	3.4	12.8	6.4	20.3	2.0	3.0	4.7	5.6	2.6
29	32.1	2.3	6.0	7.2	4.5	12.7	3.9	2.4	17.6	6.2	5.0	11.6	35.7	1.9	3.9	6.7	7.5	15.1	1.7	2.6	12.5	2.9	9.4
30	34.4	3.2	6.7	6.4	4.6	10.9	2.8	2.3	17.8	5.3	5.5	12.8	37.8	2.7	4.3	5.9	7.5	12.9	1.2	2.5	12.5	2.5	10.3
MM23																							
1	21.6	3.1	3.8	6.7	3.0	17.4	5.6	1.6	20.3	8.5	8.4	7.8	24.2	2.6	2.5	6.2	4.9	20.9	2.4	1.8	14.5	4.0	15.9
2	25.8	2.2	5.2	11.8	5.5	14.6	5.0	1.2	16.3	8.8	3.7	7.3	29.4	1.9	3.5	11.2	9.4	17.8	2.2	1.3	11.9	4.3	7.1
3	49.9	4.6	8.2	14.4	6.6	4.9	1.6	0.9	7.1	1.9	nd	5.8	54.2	3.8	5.2	13.1	10.7	5.7	0.7	0.9	4.9	0.9	nd
4	60.2	1.0	8.7	10.5	1.4	4.7	0.9	nd	8.6	2.7	1.5	10.8	65.9	0.8	5.6	9.6	2.3	5.5	0.4	nd	6.0	1.2	2.7
5	21.4	nd	3.8	11.4	2.9	29.1	2.5	0.6	4.7	22.2	1.3	6.6	25.2	nd	2.6	11.2	5.2	36.7	1.2	0.7	3.5	11.1	2.7
6	22.2	1.4	3.4	11.6	6.7	31.3	3.0	1.6	2.9	15.4	0.5	17.6	24.6	1.1	2.2	10.8	11.0	37.1	1.3	1.8	2.0	7.2	0.9
7	16.7	2.5	3.7	15.0	8.9	28.2	6.2	1.1	3.4	14.3	0.1	11.8	18.8	2.2	2.5	14.2	15.0	34.1	2.7	1.2	2.4	6.8	0.2
8	29.7	2.4	5.7	10.9	6.5	19.2	2.2	1.3	8.5	11.2	2.4	9.7	32.8	2.0	3.7	10.1	10.7	22.7	0.9	1.3	6.0	5.2	4.5
9	33.0	1.6	5.9	11.7	6.7	19.0	2.7	0.9	5.2	12.6	0.7	10.3	36.9	1.4	3.9	10.9	11.1	22.7	1.2	1.0	3.7	5.9	1.3
10	28.4	1.5	4.5	11.9	7.2	25.4	9.4	1.0	3.7	6.7	0.4	13.8	31.4	1.3	2.9	11.0	11.8	30.1	4.1	1.0	2.6	3.1	0.7
11	16.8	1.9	3.5	10.9	4.7	27.1	2.8	1.2	6.6	16.5	8.1	8.9	18.1	1.5	2.3	9.9	7.5	31.4	1.2	1.2	4.5	7.5	14.8

inc.	weight% oxide + Cl (normalised to 100%)												molecular proportion (normalised to 100 %)									
no.	SiO_2	TiO_2	Al_2O_3	FeO	MgO	CaO	BaO	Na_2O	K_2O	P_2O_5	Cl	total	Si	Ti	Al	Fe	Mg	Ca	Ba	Na	K	P	Cl
12	26.8	1.5	5.3	10.3	4.5	23.9	4.5	1.3	5.7	15.6	0.5	8.7	31.1	1.3	3.6	10.0	7.8	29.8	2.1	1.5	4.2	7.7	1.0
13	36.7	nd	6.7	8.0	2.7	21.8	5.1	0.2	4.3	14.1	0.3	18.0	42.5	nd	4.6	7.7	4.8	27.1	2.3	0.3	3.2	6.9	0.7
14	40.9	5.4	6.9	17.2	9.3	6.6	1.6	1.0	7.8	3.0	0.2	9.7	44.1	4.4	4.4	15.5	15.0	7.7	0.7	1.1	5.4	1.4	0.4
15	43.4	4.7	7.0	18.6	9.5	3.4	1.9	1.0	7.9	2.7	nd	8.5	47.0	3.8	4.5	16.9	15.3	4.0	0.8	1.1	5.4	1.3	nd
16	28.7	2.4	4.2	10.6	5.2	20.2	6.4	1.2	6.2	13.9	1.1	6.3	33.2	2.1	2.9	10.3	8.9	25.0	2.9	1.3	4.5	6.8	2.1
17	30.5	4.0	4.6	16.4	7.5	12.5	3.9	3.5	8.5	7.1	1.6	9.7	33.7	3.3	3.0	15.1	12.3	14.8	1.7	3.7	6.0	3.3	3.0
18	43.7	2.3	6.0	13.3	4.5	9.7	2.4	0.8	7.6	8.2	1.6	5.3	48.6	2.0	3.9	12.4	7.4	11.5	1.0	0.9	5.4	3.9	3.0
19	5.4	nd	1.6	11.2	5.3	38.8	16.5	1.1	1.8	17.6	0.6	8.2	6.5	nd	1.1	11.4	9.5	50.5	7.9	1.3	1.4	9.0	1.3
20	41.9	3.1	7.4	15.4	6.0	9.2	4.6	0.2	7.0	4.7	0.6	11.7	46.8	2.6	4.8	14.4	9.9	11.0	2.0	0.2	5.0	2.2	1.1
MM21																							
1	48.8	3.0	6.9	7.4	3.4	4.9	0.7	2.3	15.8	2.6	4.2	5.5	52.8	2.4	4.4	6.7	5.5	5.7	0.3	2.4	10.9	1.2	7.7
2	29.3	0.3	4.2	5.8	3.2	18.0	4.6	3.1	16.3	10.0	5.2	9.0	32.8	0.3	2.8	5.4	5.3	21.7	2.0	3.3	11.6	4.8	9.9
3	48.7	3.1	11.4	8.1	4.3	9.0	1.9	0.5	7.6	5.0	0.3	14.5	54.5	2.6	7.5	7.6	7.3	10.8	0.8	0.6	5.5	2.4	0.6
4	38.4	2.1	7.1	9.1	4.3	16.6	5.4	1.7	8.2	6.1	0.8	9.5	43.1	1.8	4.7	8.5	7.3	20.0	2.4	1.9	5.9	2.9	1.5
5	35.1	0.8	6.2	9.6	3.1	11.3	9.5	1.6	12.3	4.9	5.6	9.0	39.5	0.7	4.1	9.0	5.3	13.6	4.2	1.8	8.8	2.3	10.7
6	52.3	2.0	6.7	7.8	3.2	10.2	3.2	0.9	7.1	6.1	0.4	13.9	58.1	1.7	4.4	7.3	5.4	12.2	1.4	0.9	5.0	2.9	0.8
7	73.0	0.8	12.3	2.1	0.6	0.0	nd	1.2	9.5	0.4	0.3	19.6	80.0	0.7	7.9	1.9	0.9	0.0	nd	1.3	6.6	0.2	0.5
8	59.6	0.3	10.0	3.1	0.5	6.6	1.2	1.3	9.8	5.6	1.8	24.7	66.4	0.2	6.6	2.9	0.8	7.9	0.5	1.5	7.0	2.6	3.5
9	41.0	2.3	6.5	6.1	4.2	11.7	2.0	3.1	12.0	8.7	2.4	13.4	45.7	2.0	4.3	5.7	6.9	14.0	0.9	3.3	8.5	4.1	4.6
10	44.5	2.4	7.2	5.6	2.9	9.4	1.8	2.8	14.9	5.3	3.3	21.6	49.2	2.0	4.7	5.2	4.8	11.2	0.8	3.0	10.5	2.5	6.2
11	46.5	4.0	12.6	9.4	5.4	4.5	5.0	1.0	9.9	1.4	0.2	16.1	52.9	3.5	8.5	8.9	9.2	5.5	2.2	1.1	7.2	0.7	0.4
12	55.2	2.2	6.2	8.9	4.4	10.5	1.7	0.4	5.6	4.7	0.0	14.7	59.7	1.8	4.0	8.1	7.0	12.2	0.7	0.4	3.9	2.2	0.1
13	60.7	1.3	7.3	9.1	2.8	5.0	1.1	1.4	5.7	5.2	0.3	14.1	66.5	1.1	4.7	8.3	4.5	5.9	0.5	1.5	4.0	2.4	0.5
14	32.2	2.0	3.9	6.3	2.4	11.4	5.3	1.9	19.6	7.6	7.3	16.2	36.1	1.7	2.6	5.9	4.0	13.7	2.3	2.1	14.0	3.6	13.9
15	50.1	2.4	9.7	10.6	4.9	6.8	1.0	0.9	8.7	4.7	0.3	11.1	55.6	2.0	6.3	9.8	8.0	8.0	0.4	0.9	6.2	2.2	0.5
16	48.4	2.9	7.9	11.3	4.8	7.6	1.8	1.0	9.0	4.0	1.2	18.6	53.1	2.4	5.1	10.4	7.8	8.9	0.8	1.0	6.3	1.9	2.2
17	46.5	1.1	5.3	7.6	2.7	11.9	8.5	1.5	5.3	8.7	0.9	8.4	53.5	0.9	3.6	7.3	4.6	14.7	3.8	1.6	3.9	4.2	1.8
18	35.5	0.3	5.9	5.1	2.6	19.1	2.6	1.8	11.5	12.4	3.2	15.6	40.1	0.3	3.9	4.8	4.4	23.1	1.1	2.0	8.2	5.9	6.1
19	44.6	3.0	6.3	8.8	5.3	13.3	0.5	1.5	8.4	7.9	0.5	13.0	48.9	2.5	4.1	8.1	8.7	15.6	0.2	1.6	5.9	3.7	0.9
20	37.8	0.6	3.5	10.9	4.2	16.2	3.2	2.0	10.1	9.6	1.9	14.5	42.0	0.5	2.3	10.1	7.0	19.3	1.4	2.2	7.2	4.5	3.6
MM6																							
1	29.9	0.4	4.6	7.4	4.3	22.6	6.5	1.5	5.2	15.8	1.7	4.1	34.5	0.3	3.1	7.2	7.5	27.9	3.0	1.7	3.8	7.7	3.3
2	31.1	0.7	6.2	2.4	0.3	23.3	2.4	1.0	9.3	20.1	3.2	7.5	36.9	0.6	4.3	2.4	0.5	29.5	1.1	1.2	7.0	10.0	6.5
3	48.9	4.2	7.9	11.7	7.1	5.5	2.9	1.0	7.7	2.1	0.8	9.4	52.9	3.4	5.0	10.6	11.5	6.4	1.2	1.0	5.3	1.0	1.5
4	57.8	nd	9.7	13.7	8.9	1.9	nd	1.1	7.0	nd	nd	11.8	60.4	nd	6.0	11.9	13.8	2.1	nd	1.1	4.7		
5	42.2	nd	6.5	11.0	5.9	7.6	nd	1.4	15.5	5.8	4.0	11.2	45.5	nd	4.2	10.0	9.4	8.7	nd	1.5	10.7	2.6	7.4
6	49.7	4.3	7.3	12.4	7.6	6.6	nd	nd	8.2	2.9	1.0	16.5	52.8	3.4	4.6	11.0	12.0	7.5	nd	nd	5.6	1.3	1.8
7	37.9	3.3	6.5	11.8	6.0	10.6	3.0	nd	9.3	6.3	5.2	10.8	40.7	2.7	4.1	10.6	9.6	12.3	1.3	nd	6.4	2.9	9.5
8	33.8	2.2	5.2	7.0	4.0	12.3	3.7	1.3	17.4	7.5	5.6	13.2	37.5	1.8	3.4	6.5	6.6	14.7	1.6	1.4	12.3	3.5	10.6
9	33.3	2.6	5.1	9.7	3.7	14.7	5.9	0.8	15.1	4.6	4.4	10.7	37.1	2.1	3.4	9.0	6.2	17.6	2.6	0.8	10.7	2.2	8.4
10	47.5	nd	7.6	13.3	6.6	9.0	nd	nd	7.9	5.6	2.6	8.0	50.4	nd	4.7	11.8	10.4	10.2	nd	nd	5.4	2.5	4.7
11	35.1	nd	4.5	7.0	4.2	22.3	nd	1.5	4.9	17.6	2.8	6.7	38.7	nd	2.9	6.5	6.9	26.4	nd	1.6	3.5	8.2	5.3
12	25.0	3.0	4.0	9.2	7.4	25.7	3.0	1.5	3.9	16.6	0.9	8.7	28.0	2.5	2.7	8.6	12.3	30.8	1.3	1.6	2.8	7.9	1.7
13	38.1	3.7	6.0	9.6	5.8	14.9	3.1	nd	8.2	8.3	2.3	17.5	41.9	3.0	3.9	8.8	9.5	17.5	1.3	nd	5.8	3.9	4.3
14	35.6	3.0	7.6	14.3	6.1	13.2	nd	1.4	9.6	8.0	1.3	6.6	39.4	2.5	5.0	13.2	10.0	15.6	nd	1.5	6.8	3.7	2.4
15	40.4	3.1	5.7	10.7	7.9	15.1	nd	0.9	5.8	10.4	nd	13.4	43.9	2.5	3.6	9.8	12.8	17.6	nd	0.9	4.0	4.8	
16	38.9	3.4	5.0	13.1	8.7	16.6	nd	0.5	5.5	7.0	1.2	13.3	40.8	2.7	3.1	11.5	13.7	18.7	nd	0.5	3.7	3.1	2.2
17	40.0	nd	4.3	3.5	1.1	16.6	4.7	1.3	14.4	9.1	5.1	16.4	44.6	nd	2.8	3.3	1.8	19.8	2.0	1.4	10.3	4.3	9.7
18	27.3	nd	3.8	12.0	3.7	27.4	nd	0.6	3.2	20.7	1.2	9.0	31.0	nd	2.6	11.5	6.4	33.3	nd	0.7	2.3	10.0	2.3

inc.	weight% oxide + Cl (normalised to 100%)												molecular proportion (normalised to 100 %)									
no.	SiO_2	TiO_2	Al_2O_3	FeO	MgO	CaO	BaO	Na_2O	K_2O	P_2O_5	Cl	total	Si	Ti	Al	Fe	Mg	Ca	Ba	Na	K	P	Cl
19	41.9	4.3	7.7	13.4	6.7	10.6	nd	0.5	6.5	6.4	2.0	8.4	45.1	3.5	4.9	12.1	10.7	12.2	nd	0.6	4.4	2.9	3.7
20	50.9	2.2	8.0	11.2	4.4	9.1	2.7	0.6	6.2	3.6	1.0	13.5	55.5	1.8	5.1	10.2	7.1	10.6	1.2	0.6	4.3	1.7	1.9
MM17																							
1	42.7	3.5	5.9	7.2	3.4	16.7	nd	2.9	8.1	7.7	1.9	7.0	46.2	2.9	3.7	6.5	5.6	19.4	nd	3.0	5.6	3.5	3.5
2	44.9	3.1	5.0	10.8	5.3	16.0	nd	2.6	4.9	7.4	nd	5.2	48.2	2.5	3.2	9.7	8.5	18.4	nd	2.7	3.4	3.4	
3	32.1	4.3	8.2	10.0	5.1	12.0	14.0	1.9	5.4	7.2	nd	5.3	38.8	3.9	5.8	10.1	9.2	15.5	6.6	2.2	4.1	3.7	
4	29.3	3.2	7.7	13.8	6.6	17.6	nd	3.4	6.7	10.6	1.0	5.5	32.4	2.7	5.0	12.8	11.0	20.8	nd	3.6	4.7	5.0	2.0
5	39.7	2.8	4.3	7.6	2.5	16.4	2.4	3.7	7.7	10.9	2.1	13.9	44.4	2.3	2.8	7.1	4.1	19.7	1.0	4.0	5.5	5.2	3.9
6	25.9	nd	4.9	19.2	9.1	18.0	7.7	3.1	6.5	5.5	nd	5.5	28.7	nd	3.2	17.8	15.1	21.3	3.3	3.3	4.6	2.6	
7	40.6	1.8	10.2	10.1	4.1	12.1	5.1	1.7	8.2	4.7	1.4	11.8	45.8	1.5	6.8	9.6	6.9	14.6	2.3	1.8	5.9	2.3	2.6
8	48.3	3.8	8.4	11.3	5.5	5.1	1.5	1.5	9.2	4.5	0.8	23.1	53.4	3.2	5.5	10.4	9.0	6.1	0.7	1.6	6.5	2.1	1.5
9	16.8	nd	3.2	15.2	5.7	20.9	16.5	0.7	5.4	13.8	1.8	8.4	20.5	nd	2.3	15.6	10.5	27.4	7.9	0.8	4.2	7.2	3.7
10	53.8	2.5	15.4	9.7	5.5	nd	nd	nd	12.3	nd	0.8	11.3	59.6	2.1	10.1	9.0	9.2	nd	nd	nd	8.7		1.4
11	41.4	2.3	7.8	10.1	5.5	13.1	2.6	1.3	7.7	7.8	0.4	13.7	46.2	1.9	5.1	9.5	9.1	15.7	1.2	1.4	5.5	3.7	0.7
12	35.0	3.7	10.0	14.9	8.2	14.7	nd	2.1	8.9	2.0	0.5	12.0	37.4	2.9	6.3	13.3	13.1	16.9		2.2	6.1	0.9	0.8
13	36.4	3.2	8.5	8.6	4.9	13.6	1.8	2.3	9.7	8.9	2.0	13.9	40.8	2.7	5.6	8.1	8.3	16.3	0.8	2.5	6.9	4.2	3.7
14	32.2	3.1	5.0	10.5	5.5	19.4	nd	2.0	7.4	13.8	1.3	10.8	35.8	2.6	3.3	9.7	9.1	23.1		2.1	5.2	6.5	2.5
15	55.2	nd	5.9	8.5	2.8	10.8	4.3	2.1	9.1	nd	1.3	8.5	59.2	nd	3.7	7.6	4.5	12.4	1.8	2.2	6.2		2.4
16	35.7	2.4	7.5	16.7	6.9	14.7	2.2	1.0	8.1	3.9	0.9	10.3	38.7	1.9	4.8	15.2	11.2	17.1	0.9	1.0	5.6	1.8	1.7
17	41.6	2.5	6.1	10.0	3.8	13.0	2.1	3.3	10.7	5.9	1.0	11.6	46.2	2.1	4.0	9.2	6.3	15.4	0.9	3.5	7.6	2.8	1.9
18	23.3	nd	4.5	14.5	6.8	27.8	3.9	2.5	4.6	12.2	nd	7.4	25.9	nd	3.0	13.5	11.2	33.1	1.7	2.7	3.3	5.7	
19	50.0	5.0	11.9	11.5	6.1	1.7	nd	nd	10.4	2.5	1.0	8.8	55.2	4.2	7.7	10.6	10.0	2.0	nd	nd	7.3	1.2	1.8
20	36.5	nd	5.2	nd	nd	22.5	nd	1.6	9.4	20.3	4.5	12.2	41.7	nd	3.5	nd	nd	27.6	nd	1.8	6.8	9.8	8.7
MM2																							
1	42.4	3.2	6.1	14.5	8.7	5.6	2.6	nd	8.6	7.4	0.9	2.3	46.7	2.7	4.0	13.3	14.4	6.6	1.1	nd	6.1	3.5	1.7
2	49.4	2.0	5.8	11.2	3.8	5.3	4.1	2.2	7.4	6.1	2.7	4.4	54.5	1.6	3.7	10.3	6.2	6.2	1.8	2.3	5.2	2.8	5.1
4	54.3	1.9	7.2	12.6	3.9	3.3	3.4	nd	7.6	5.0	0.8	5.2	60.7	1.6	4.7	11.8	6.6	3.9	1.5	nd	5.4	2.3	1.4
5	54.0	3.1	9.8	5.2	1.8	3.5	1.0	1.5	17.3	2.6	0.2	4.5	61.9	2.7	6.6	5.0	3.1	4.3	0.4	1.6	12.7	1.2	0.3
6	61.3	2.5	11.1	4.8	1.4	1.1	nd	1.7	13.5	2.6	nd	3.5	69.4	2.1	7.4	4.6	2.4	1.3	nd	1.9	9.7	1.3	
7	69.5	2.3	12.8	1.5	nd	nd	nd	nd	13.9	nd	nd	4.1	78.2	2.0	8.5	1.4	nd	nd	nd	nd	10.0		
8	47.4	2.5	6.5	12.9	4.6	2.9	3.1	nd	10.8	5.3	4.0	3.3	52.1	2.1	4.2	11.8	7.5	3.4	1.3	nd	7.6	2.5	7.4
9	41.2	nd	4.8	14.5	3.8	5.3	5.2	2.1	9.9	7.3	5.9	1.8	45.3	nd	3.1	13.3	6.2	6.3	2.3	2.2	7.0	3.4	11.0
10	63.3	3.6	12.2	4.6	1.3	nd	nd	nd	13.3	1.6	nd	5.1	71.8	3.1	8.2	4.4	2.2	nd	nd	nd	9.6	0.8	nd
11	62.3	2.0	14.1	3.0	0.9	nd	nd	nd	16.1	1.1	0.5	7.7	71.2	1.8	9.5	2.9	1.5	nd	nd	nd	11.8	0.6	0.9
12	63.8	2.5	12.7	3.2	0.8	nd	nd	nd	14.9	1.8	0.3	6.2	72.6	2.2	8.5	3.0	1.4	nd	nd	nd	10.8	0.8	0.6
13	43.4	nd	6.9	10.0	3.6	3.7	4.2	2.3	16.6	6.0	3.4	3.1	49.4	nd	4.6	9.5	6.1	4.5	1.9	2.6	12.1	2.9	6.5
14	36.4	4.2	6.3	5.8	4.2	10.0	nd	4.5	14.1	9.7	4.8	1.8	40.1	3.5	4.1	5.3	6.9	11.8	nd	4.8	9.9	4.5	9.0
15	39.3	nd	8.6	9.6	3.8	17.3	nd	nd	4.6	17.0	nd	1.3	45.4	nd	5.9	9.2	6.5	21.4	nd	nd	3.4	8.3	nd
MM1																							
1	13.8	nd	2.7	16.9	2.6	27.8	nd	4.6	5.2	25.0	1.4	2.5	16.4		1.9	16.8	4.7	35.5		5.3	4.0	12.6	2.9
2	38.4	2.5	5.8	16.8	5.0	9.9	nd	2.1	9.1	8.2	2.3	2.9	42.2	2.0	3.7	15.4	8.3	11.6		2.2	6.4	3.8	4.3
3	32.8	2.3	5.4	20.6	4.3	9.5	8.9	1.8	6.1	5.8	2.5	5.5	37.5	2.0	3.7	19.7	7.3	11.6	4.0	2.0	4.5	2.8	4.9
4	34.0	2.3	6.4	29.4	4.8	4.1	nd	3.5	8.2	5.0	2.3	2.9	37.7	1.9	4.2	27.2	7.9	4.9		3.7	5.8	2.4	4.3
5	36.6	nd	6.0	19.5	3.2	9.8	nd	2.5	8.2	13.0	1.2	2.3	42.1		4.0	18.8	5.6	12.1		2.8	6.0	6.3	2.3
6	42.9	3.0	5.8	20.3	4.9	3.0	0.4	3.2	8.3	7.0	1.2	3.2	47.8	2.5	3.8	18.9	8.2	3.6	0.2	3.5	5.9	3.3	2.3
8	42.9	3.2	14.4	12.7	4.5	7.4	nd	nd	7.8	7.1	nd	3.1	49.3	2.8	9.8	12.2	7.7	9.1			5.7	3.4	nd
9	27.0	1.9	3.9	17.8	4.0	14.3	12.0	2.6	4.8	11.0	0.7	4.3	32.6	1.7	2.8	17.9	7.1	18.4	5.7	3.0	3.7	5.6	1.5
10	40.5	3.0	6.9	15.8	5.9	4.4	nd	1.9	10.1	9.2	2.3	3.1	45.2	2.5	4.5	14.8	9.8	5.2		2.1	7.2	4.3	4.4
11	40.0	2.9	7.9	14.2	4.3	13.6	1.9	1.7	4.9	8.0	0.7	4.4	44.6	2.4	5.2	13.3	7.2	16.2	0.8	1.9	3.5	3.8	1.3

inc.	weight% oxide + Cl (normalised to 100%)												molecular proportion (normalised to 100 %)									
no.	SiO_2	TiO_2	Al_2O_3	FeO	MgO	CaO	BaO	Na_2O	K_2O	P_2O_5	Cl	total	Si	Ti	Al	Fe	Mg	Ca	Ba	Na	K	P	Cl
12	44.8	4.7	7.9	16.9	5.5	6.2	nd	1.9	7.6	3.5	0.9	5.2	48.9	3.8	5.1	15.4	8.9	7.3		2.0	5.3	1.6	1.7
13	59.1	1.4	10.5	11.8	2.6	0.8	nd	2.2	7.4	3.5	0.7	6.1	65.4	1.2	6.8	10.9	4.3	1.0		2.3	5.2	1.6	1.2
15	14.5	nd	4.0	17.5	1.3	24.1	5.5	4.1	5.3	22.9	0.9	4.1	18.1		3.0	18.3	2.4	32.3	2.7	5.0	4.2	12.2	1.8
16	55.5	2.4	8.8	14.7	4.4	0.9	nd	2.2	8.4	2.0	0.8	4.9	60.3	1.9	5.6	13.3	7.1	1.1		2.4	5.8	0.9	1.5
17	33.0	2.9	4.7	15.3	4.1	13.5	1.8	2.3	6.7	13.6	2.0	6.2	37.7	2.5	3.2	14.6	7.0	16.5	0.8	2.5	4.9	6.5	3.8
18	33.8	2.7	5.0	24.6	4.7	8.9	2.6	2.1	7.7	5.8	2.1	5.9	37.6	2.3	3.2	22.9	7.8	10.6	1.1	2.3	5.5	2.7	4.0
20	28.3	3.1	5.3	21.7	5.4	13.0	3.2	1.8	6.7	10.2	1.3	5.8	32.3	2.7	3.6	20.7	9.2	15.9	1.4	2.0	4.9	4.9	2.5
MM4																							
1	56.3	5.5	9.6	9.6	5.3	0.6	nd	0.5	10.7	1.8	nd	6.4	62.0	4.6	6.2	8.9	8.7	0.7	nd	0.5	7.5	0.8	nd
2	65.3	4.4	6.6	11.4	3.6	nd	nd	nd	6.7	2.0	nd	4.1	70.6	3.5	4.2	10.3	5.8	nd	nd	nd	4.6	0.9	nd
3	49.6	2.0	7.1	15.9	7.6	6.2	nd	2.1	6.1	3.3	nd	4.5	52.8	1.6	4.5	14.1	12.1	7.0	nd	2.2	4.2	1.5	nd
4	41.5	7.3	7.0	23.3	7.9	1.0	nd	1.7	8.2	2.2	nd	4.1	45.5	6.0	4.5	21.4	12.9	1.2	nd	1.8	5.7	1.0	nd
5	56.1	6.0	9.6	10.5	5.0	nd	nd	0.4	10.4	2.0	nd	10.6	62.1	5.0	6.2	9.7	8.3	nd	nd	0.5	7.4	0.9	nd
MM11																							
1	53.9	3.2	9.0	11.2	5.6	3.6	nd	nd	7.0	6.5	nd	4.2	59.6	2.7	5.9	10.4	9.3	4.2	nd	nd	4.9	3.0	nd
2	35.7	2.2	6.0	12.5	5.0	13.6	3.7	1.0	8.3	10.1	1.9	4.7	40.3	1.9	4.0	11.8	8.4	16.4	1.6	1.1	6.0	4.8	3.7
3	41.7	3.0	6.7	7.4	5.2	3.7	nd	5.2	21.1	nd	6.0	3.0	44.2	2.4	4.2	6.6	8.2	4.2	nd	5.3	14.2	nd	10.7
4	51.9	1.7	7.6	4.9	3.5	1.8	1.9	1.9	17.2	3.0	4.7	6.0	56.6	1.4	4.9	4.5	5.7	2.1	0.8	2.0	12.0	1.4	8.6
5	55.0	2.9	8.7	9.5	4.3	4.5	1.8	nd	8.0	4.5	0.7	7.7	60.9	2.4	5.7	8.8	7.1	5.4	0.8	nd	5.7	2.1	1.3
6	32.7	3.5	5.6	11.5	4.7	13.6	nd	3.9	11.7	9.1	3.7	2.9	35.8	2.9	3.6	10.5	7.7	16.0	nd	4.1	8.2	4.2	6.9
7	45.5	3.6	8.5	14.7	7.7	3.8	nd	1.1	7.7	7.1	0.4	6.2	50.2	3.0	5.5	13.5	12.6	4.5	nd	1.2	5.4	3.3	0.7
8	37.2	1.4	5.3	5.4	3.6	12.8	2.1	3.9	15.5	8.8	4.1	5.3	41.3	1.2	3.5	5.0	5.9	15.2	0.9	4.2	11.0	4.1	7.7
9	49.0	2.9	7.6	6.2	4.1	3.3	nd	3.0	16.3	3.8	3.8	4.6	53.3	2.4	4.9	5.6	6.7	3.8	nd	3.1	11.3	1.7	7.1
10	30.2	3.4	5.4	10.9	6.5	19.7	3.7	1.5	5.8	13.0	nd	7.7	34.3	2.9	3.6	10.4	11.0	24.0	1.7	1.6	4.2	6.2	nd
11	22.0	2.7	3.7	13.4	4.6	23.6	nd	1.0	2.1	27.0	nd	3.2	26.4	2.4	2.6	13.5	8.2	30.4	nd	1.1	1.6	13.7	nd
12	35.9	2.1	5.6	9.6	5.2	12.4	2.1	3.4	12.3	8.2	3.4	6.2	39.5	1.7	3.6	8.8	8.5	14.6	0.9	3.6	8.6	3.8	6.4
13	33.4	2.6	5.1	14.4	6.1	18.0	nd	nd	5.1	15.3	nd	4.7	37.8	2.2	3.4	13.6	10.2	21.8	nd	nd	3.7	7.3	nd
14	35.4	2.3	5.9	9.0	5.3	11.7	2.9	3.2	14.0	6.7	3.5	9.7	39.1	1.9	3.9	8.3	8.7	13.9	1.2	3.4	9.9	3.1	6.5
15	50.9	2.5	7.6	6.1	4.2	4.6	nd	3.0	13.6	5.1	2.2	8.5	55.9	2.1	4.9	5.6	6.9	5.4	nd	3.2	9.5	2.4	4.1
16	44.6	2.4	7.7	6.0	4.6	6.6	nd	3.5	16.5	4.6	3.5	5.1	48.6	2.0	5.0	5.4	7.5	7.7	nd	3.7	11.5	2.1	6.4
17	47.3	4.4	9.6	9.7	5.5	7.3	nd	0.6	9.2	5.9	0.6	5.5	52.4	3.6	6.3	9.0	9.1	8.7	nd	0.7	6.5	2.8	1.1
18	45.6	4.3	8.1	11.8	6.1	7.6	nd	0.5	8.1	7.9	nd	8.7	50.8	3.6	5.3	11.0	10.2	9.0	nd	0.5	5.7	3.7	nd
19	49.6	3.8	8.7	10.4	5.5	5.1	nd	nd	8.4	7.6	0.9	5.5	55.1	3.2	5.7	9.7	9.1	6.0	nd	nd	6.0	3.6	1.7
20	44.4	3.6	7.5	13.8	6.2	7.9	nd	nd	5.8	10.8	nd	5.4	49.8	3.0	5.0	13.0	10.4	9.5	nd	nd	4.1	5.1	nd
MM7																							
1	26.1	nd	4.6	10.9	5.3	9.5	5.3	2.7	22.8	7.4	5.4	5.7	29.8	nd	3.1	10.4	9.1	11.7	2.4	3.0	16.6	3.6	10.4
2	25.9	2.0	3.8	7.5	4.9	11.5	4.5	3.1	21.3	9.8	5.7	25.5	29.5	1.7	2.5	7.2	8.4	14.0	2.0	3.5	15.5	4.7	11.0
3	30.7	nd	5.2	9.0	4.7	10.0	nd	4.1	23.5	7.8	5.0	9.3	34.2	nd	3.4	8.4	7.9	12.0	nd	4.4	16.7	3.7	9.4
4	35.4	3.6	5.0	10.2	6.0	5.9	nd	3.2	20.6	4.4	5.7	13.5	38.2	2.9	3.2	9.2	9.6	6.8	nd	3.4	14.2	2.0	10.5
5	28.2	1.9	3.9	9.5	4.5	8.7	4.5	3.4	21.8	8.0	5.6	20.2	32.1	1.6	2.6	9.0	7.7	10.6	2.0	3.7	15.8	3.8	10.9
6	28.6	nd	4.6	9.2	4.3	8.8	3.9	4.6	23.0	6.9	6.1	13.3	32.2	nd	3.1	8.7	7.3	10.6	1.7	5.0	16.5	3.3	11.6
7	44.1	3.1	6.3	7.0	5.0	4.5	nd	2.2	17.8	6.4	3.6	27.9	48.7	2.6	4.1	6.4	8.2	5.3	nd	2.4	12.6	3.0	6.7
8	29.3	2.2	4.0	7.7	4.9	8.2	4.4	3.4	22.7	7.4	5.8	19.0	33.2	1.9	2.6	7.3	8.3	9.9	1.9	3.7	16.4	3.5	11.1
9	52.0	4.7	8.8	13.2	8.1	nd	nd	1.1	9.2	2.9	nd	22.6	56.5	3.9	5.7	12.0	13.1	nd	nd	1.1	6.4	1.4	nd
10	52.4	3.5	7.2	10.5	7.9	1.5	nd	2.5	9.1	4.5	0.8	20.1	56.4	2.9	4.6	9.4	12.7	1.7	nd	2.6	6.3	2.1	1.4
11	49.1	3.6	7.5	11.7	7.1	6.8	nd	0.8	8.7	3.9	0.7	31.9	52.8	2.9	4.8	10.5	11.3	7.8	nd	0.9	5.9	1.8	1.3
12	41.0	2.8	6.2	12.2	5.9	9.6	nd	nd	8.1	9.9	4.4	13.3	44.2	2.3	3.9	11.0	9.5	11.0	nd	nd	5.6	4.5	8.0
13	32.8	2.6	4.5	7.6	5.1	6.6	5.1	2.9	22.3	4.3	6.0	20.2	36.6	2.2	2.9	7.1	8.5	7.9	2.2	3.1	15.9	2.1	11.4
14	37.0	3.5	5.5	12.6	6.9	9.7	2.3	0.7	7.9	12.7	1.3	29.0	41.9	3.0	3.6	12.0	11.6	11.8	1.0	0.8	5.7	6.1	2.5

inc.	weight% oxide + Cl (normalised to 100%)												molecular proportion (normalised to 100 %)									
no.	SiO_2	TiO_2	Al_2O_3	FeO	MgO	CaO	BaO	Na_2O	K_2O	P_2O_5	Cl	total	Si	Ti	Al	Fe	Mg	Ca	Ba	Na	K	P	Cl
15	44.6	3.1	6.0	12.4	7.0	9.3	nd	nd	7.2	7.5	2.8	29.8	47.5	2.5	3.8	11.0	11.1	10.6	nd	nd	4.9	3.4	5.1
16	51.6	4.0	7.0	14.0	8.5	nd	nd	1.3	8.8	3.9	0.9	36.2	55.4	3.2	4.5	12.5	13.6	nd	nd	1.3	6.0	1.8	1.7
17	25.8	2.0	4.4	11.2	6.2	12.6	4.0	2.8	14.8	11.4	4.8	19.1	29.1	1.7	2.9	10.5	10.4	15.2	1.8	3.0	10.6	5.5	9.3
18	41.2	3.1	6.2	8.4	5.4	5.9	nd	2.6	17.8	4.3	5.2	17.1	44.3	2.5	3.9	7.5	8.6	6.8	nd	2.7	12.2	2.0	9.5
19	24.7	1.9	4.0	9.0	4.7	12.3	5.4	3.3	20.5	9.6	4.6	27.1	28.5	1.7	2.8	8.7	8.0	15.3	2.5	3.7	15.1	4.7	9.0
20	24.9	2.9	3.7	8.9	4.8	8.5	4.2	3.8	24.7	6.9	6.7	21.0	28.2	2.5	2.5	8.4	8.1	10.3	1.9	4.2	17.8	3.3	12.8
21	31.0	3.0	5.1	10.7	6.2	5.5	nd	2.5	23.0	6.4	6.7	15.3	34.0	2.4	3.3	9.8	10.1	6.4	nd	2.7	16.1	2.9	12.4
22	31.2	2.2	4.8	9.3	5.1	8.9	3.7	2.5	18.4	8.7	5.3	15.9	35.2	1.9	3.2	8.8	8.5	10.8	1.6	2.7	13.3	4.2	10.0
23	55.7	3.8	6.6	13.2	9.0	nd	nd	1.1	6.3	3.8	0.5	26.0	58.9	3.0	4.1	11.7	14.2	nd	nd	1.2	4.3	1.7	0.9
24	57.4	3.5	7.7	10.0	7.2	1.1	nd	0.8	9.2	2.3	0.9	30.2	61.2	2.8	4.8	8.9	11.4	1.2	nd	0.9	6.3	1.0	1.5
MM9																							
1	35.7	2.3	6.4	11.0	5.2	8.9	4.5	4.1	13.9	5.0	3.1	22.0	39.8	1.9	4.2	10.2	8.6	10.6	2.0	4.4	9.9	2.4	5.9
2	26.7	2.6	4.8	12.4	7.2	17.5	2.4	5.3	11.3	6.5	3.3	22.4	28.7	2.1	3.1	11.1	11.6	20.2	1.0	5.5	7.7	2.9	6.0
3	25.6	nd	4.8	12.0	6.8	18.8	4.5	5.7	11.6	6.7	3.6	13.4	27.7	nd	3.1	10.9	11.0	21.8	1.9	6.0	8.0	3.1	6.6
4	33.2	nd	5.5	14.3	4.8	15.6	nd	1.6	5.8	18.2	1.0	22.6	38.2	nd	3.7	13.7	8.2	19.2	nd	1.8	4.2	8.9	2.0
5	31.5	1.7	5.6	8.5	4.0	13.3	4.6	3.0	13.9	9.9	3.9	3.6	35.9	1.4	3.7	8.1	6.8	16.3	2.1	3.3	10.1	4.8	7.6
6	47.3	3.4	8.1	13.6	5.3	6.0	nd	nd	7.8	8.4	nd	9.1	53.2	2.9	5.4	12.8	8.9	7.3	nd		5.6	4.0	nd
7	44.4	2.2	7.4	13.6	5.5	6.9	nd	1.3	8.3	10.3	nd	23.6	50.3	1.9	5.0	12.9	9.2	8.4	nd	1.4	6.0	4.9	nd
8	44.1	2.2	7.2	7.8	3.3	6.5	nd	2.5	15.6	6.7	4.2	29.9	48.7	1.8	4.7	7.2	5.4	7.7	nd	2.7	11.0	3.1	7.8
9	36.2	2.1	6.8	7.9	4.5	8.6	nd	3.8	18.1	7.7	4.4	20.5	40.1	1.7	4.4	7.3	7.4	10.3	nd	4.1	12.8	3.6	8.3
10	39.2	2.7	6.1	7.2	2.8	7.9	2.9	2.7	17.9	7.1	3.5	26.4	44.8	2.4	4.1	6.8	4.8	9.7	1.3	3.0	13.0	3.4	6.7
11	46.2	2.4	7.0	5.6	3.3	7.5	nd	2.0	15.0	7.7	3.1	30.0	51.3	2.0	4.6	5.2	5.5	9.0	nd	2.2	10.6	3.6	5.9
12	50.9	2.2	7.7	15.4	4.2	1.0	nd	2.7	8.3	7.0	0.7	6.0	57.0	1.8	5.1	14.5	7.0	1.2	nd	2.9	5.9	3.3	1.3
13	39.2	3.8	5.6	4.6	2.8	13.6	nd	2.3	12.7	11.6	3.9	12.1	43.7	3.2	3.7	4.3	4.6	16.2	nd	2.5	9.0	5.5	7.4
14	34.5	3.0	6.5	7.7	4.0	9.5	nd	3.8	19.3	7.4	4.3	22.4	38.5	2.5	4.3	7.2	6.6	11.4	nd	4.1	13.7	3.5	8.1
15	46.7	3.0	7.5	15.9	4.3	7.8	nd	1.0	6.9	6.8	nd	20.1	52.0	2.5	4.9	14.8	7.2	9.3	nd	1.1	4.9	3.2	nd
16	48.7	3.0	6.3	5.5	2.8	7.3	nd	3.1	14.6	5.6	3.2	19.3	53.4	2.4	4.1	5.0	4.5	8.6	nd	3.3	10.2	2.6	5.9
18	38.4	3.9	7.4	7.5	4.6	6.6	nd	2.6	19.5	5.2	4.4	22.0	42.5	3.3	4.8	6.9	7.6	7.8	nd	2.8	13.7	2.4	8.3
19	35.7	2.3	7.1	12.0	5.6	14.3	nd	1.9	6.5	13.5	1.2	22.5	40.1	2.0	4.7	11.2	9.4	17.2	nd	2.0	4.7	6.4	2.2
20	50.3	2.8	7.5	10.2	4.5	5.8	nd	2.0	8.1	8.6	nd	21.4	56.4	2.4	5.0	9.6	7.5	7.0	nd	2.1	5.8	4.1	nd
MM12																							
1	50.1	3.3	7.1	12.3	5.9	5.4	nd	nd	6.5	9.3	nd	29.8	55.8	2.8	4.7	11.5	9.9	6.4	nd	nd	4.6	4.4	nd
2	40.8	2.0	7.3	9.3	5.4	8.5	nd	1.8	10.6	12.1	2.3	18.7	45.8	1.7	4.8	8.7	9.1	10.2	nd	2.0	7.6	5.7	4.4
3	46.8	nd	6.8	13.9	4.2	8.6	3.0	nd	8.3	6.2	2.2	28.7	51.6	nd	4.4	12.8	6.9	10.1	1.3	nd	5.8	2.9	4.2
4	41.6	3.0	6.7	11.9	7.3	11.0	nd	2.2	8.0	7.1	1.2	6.4	44.9	2.5	4.3	10.7	11.7	12.7	nd	2.3	5.5	3.2	2.2
5	47.6	3.7	7.9	12.3	7.0	3.8	nd	1.9	9.8	4.5	1.3	25.9	51.7	3.0	5.1	11.1	11.3	4.5	nd	2.0	6.8	2.1	2.4
6	46.1	2.9	7.9	15.0	7.8	1.2	nd	2.5	9.6	6.4	0.6	25.4	50.8	2.4	5.1	13.9	12.9	1.4	nd	2.7	6.8	3.0	1.1
7	49.3	nd	7.3	5.5	nd	12.4	nd	3.3	9.6	9.5	3.0	6.9	54.7	nd	4.8	5.2	nd	14.8	nd	3.5	6.8	4.5	5.7
8	41.6	6.1	6.5	17.2	10.5	0.8	nd	2.0	9.2	5.1	0.9	20.9	44.9	5.0	4.1	15.5	16.9	1.0	nd	2.1	6.3	2.3	1.7
9	54.7	nd	8.3	9.2	4.3	5.8	nd	1.7	7.9	7.4	0.7	19.6	60.1	nd	5.3	8.5	7.0	6.8	nd	1.8	5.6	3.5	1.4
10	38.3	3.4	5.6	6.3	2.6	9.2	nd	3.2	20.1	6.7	4.6	15.0	42.7	2.8	3.7	5.8	4.4	11.0	nd	3.5	14.3	3.2	8.7
11	33.9	nd	7.8	9.0	4.7	8.9	nd	4.7	17.4	9.4	4.3	9.7	37.9	nd	5.2	8.4	7.9	10.6	nd	5.1	12.4	4.4	8.1
12	43.7	3.3	7.5	8.4	6.0	7.6	nd	2.5	11.1	6.8	3.0	22.1	47.3	2.7	4.8	7.6	9.8	8.9	nd	2.6	7.7	3.1	5.5
13	52.9	2.0	7.8	10.0	5.6	2.5	nd	1.7	9.4	6.7	1.4	20.2	58.0	1.6	5.0	9.2	9.2	3.0	nd	1.8	6.6	3.1	2.6
14	38.2	nd	5.8	6.3	4.1	10.2	5.9	3.7	13.4	8.6	3.7	12.7	43.2	nd	3.9	6.0	6.9	12.4	2.6	4.0	9.7	4.1	7.2
15	56.8	2.2	8.3	8.7	4.5	1.8	nd	3.0	9.4	3.7	1.6	24.7	61.4	1.8	5.3	7.9	7.3	2.1	nd	3.2	6.5	1.7	2.9
16	40.0	2.5	6.7	6.4	4.7	8.5	nd	4.1	14.5	8.0	4.4	19.3	43.7	2.1	4.3	5.8	7.7	9.9	nd	4.4	10.1	3.7	8.2
17	40.8	2.8	8.0	9.9	5.9	6.5	2.2	2.4	12.4	5.6	3.5	27.2	44.8	2.3	5.2	9.1	9.7	7.6	1.0	2.6	8.7	2.6	6.5
18	40.4	2.4	6.6	7.9	5.3	5.4	nd	4.4	18.4	4.0	5.2	20.4	43.5	1.9	4.2	7.1	8.5	6.2	nd	4.6	12.7	1.8	9.5

inc.	weight% oxide + Cl (normalised to 100%)												molecular proportion (normalised to 100 %)										
no.	SiO_2	TiO_2	Al_2O_3	FeO	MgO	CaO	BaO	Na_2O	K_2O	P_2O_5	Cl	total	Si	Ti	Al	Fe	Mg	Ca	Ba	Na	K	P	Cl
19	40.9	nd	7.3	8.0	5.2	12.8	nd	2.9	11.4	7.7	3.9	11.1	43.9	nd	4.6	7.1	8.3	14.7	nd	3.0	7.8	3.5	7.0
20	54.7	4.3	7.5	13.7	5.7	nd	nd	1.4	8.1	4.1	0.5	24.6	59.8	3.5	4.8	12.5	9.4	nd	nd	1.5	5.6	1.9	1.0
21	36.4	nd	6.0	10.5	5.9	8.5	3.5	5.2	14.6	5.4	3.9	22.7	39.8	nd	3.9	9.7	9.7	10.0	1.5	5.5	10.2	2.5	7.3
MM15																							
1	31.3	nd	7.4	9.4	6.3	8.8	nd	5.2	18.6	7.2	5.7	9.1	34.0		4.8	8.6	10.2	10.2	nd	5.5	12.9	3.3	10.5
2	27.9	1.6	4.6	17.1	5.4	15.9	3.8	1.7	7.3	11.9	2.9	24.7	31.4	1.4	3.1	16.1	9.0	19.2	1.7	1.9	5.2	5.7	5.4
3	30.5	2.3	5.4	8.3	4.5	9.8	2.7	4.2	19.8	7.7	4.7	26.6	34.4	2.0	3.6	7.9	7.5	11.8	1.2	4.6	14.2	3.7	9.1
4	31.9	3.2	6.2	9.5	6.0	8.3	nd	4.4	21.1	4.4	5.0	17.3	34.7	2.6	4.0	8.7	9.7	9.7	nd	4.7	14.6	2.0	9.3
5	46.1	3.4	8.3	8.1	4.8	5.6	nd	2.3	15.3	3.6	2.5	21.5	50.6	2.8	5.4	7.4	7.9	6.5	nd	2.4	10.7	1.7	4.6
6	36.0	2.2	6.4	11.0	8.3	14.7	nd	3.7	12.2	3.0	2.5	25.9	37.6	1.7	4.0	9.6	12.9	16.5	nd	3.7	8.2	1.3	4.4
7	40.2	2.1	5.9	8.3	4.2	15.0	nd	2.4	11.0	8.8	2.1	19.7	44.1	1.7	3.8	7.6	6.8	17.6	nd	2.5	7.7	4.1	4.0
8	42.4	2.8	8.0	10.8	8.2	10.7	nd	2.4	11.1	2.7	1.0	23.7	45.1	2.3	5.0	9.6	12.9	12.2	nd	2.4	7.5	1.2	1.7
9	32.5	2.2	7.1	11.0	4.5	10.5	nd	3.0	16.8	8.5	4.0	17.0	36.4	1.9	4.7	10.3	7.4	12.5	nd	3.3	12.0	4.0	7.6
10	31.4	2.6	5.4	8.3	4.2	9.8	2.3	3.7	21.0	6.9	4.5	28.7	35.4	2.2	3.6	7.8	7.1	11.9	1.0	4.0	15.1	3.3	8.6
11	33.4	nd	5.8	7.1	3.7	9.6	6.1	4.1	20.2	4.5	5.4	22.4	37.6		3.8	6.7	6.2	11.6	2.7	4.5	14.5	2.1	10.4
12	42.0	3.8	8.1	16.2	7.9	0.8	nd	3.1	8.8	8.7	0.8	20.9	47.0	3.2	5.3	15.2	13.1	1.0	nd	3.3	6.3	4.1	1.5
13	44.5	3.1	7.6	13.1	5.1	8.4	nd	0.6	7.3	9.9	0.4	23.6	50.0	2.6	5.0	12.4	8.5	10.1	nd	0.7	5.2	4.7	0.8
14	44.7	3.4	7.1	10.2	4.4	9.6	nd	2.0	9.8	7.1	1.7	15.9	49.2	2.8	4.6	9.3	7.3	11.3	nd	2.1	6.9	3.3	3.1
15	20.7	2.3	4.2	12.1	4.9	14.9	3.0	3.6	19.4	9.7	5.2	21.7	23.5	2.0	2.8	11.5	8.2	18.1	1.3	4.0	14.1	4.6	9.9
16	23.6	nd	4.1	8.6	3.3	14.7	2.7	4.4	22.7	9.9	5.9	20.3	26.9		2.8	8.2	5.5	17.9	1.2	4.8	16.5	4.8	11.4
17	39.8	1.3	6.2	6.6	2.6	18.1	1.9	1.4	6.4	15.0	0.8	10.2	45.7	1.1	4.2	6.4	4.4	22.3	0.8	1.5	4.7	7.3	1.5
18	55.4	3.5	7.5	8.2	5.6	1.3	nd	4.1	6.7	6.9	0.8	16.0	60.6	2.9	4.8	7.5	9.1	1.5	nd	4.4	4.7	3.2	1.5
19	36.7	2.1	7.2	11.4	4.6	12.8	nd	2.5	10.2	9.6	3.0	18.8	40.5	1.7	4.7	10.5	7.5	15.2	nd	2.7	7.2	4.5	5.5
20	46.3	2.2	7.7	11.2	4.7	6.5	nd	2.0	9.3	8.9	1.1	21.4	51.8	1.9	5.1	10.5	7.8	7.8	nd	2.2	6.7	4.2	2.1
21	23.7	2.1	4.5	9.7	5.6	13.1	3.8	3.3	21.2	8.2	4.8	26.6	26.9	1.8	3.0	9.2	9.4	15.9	1.7	3.7	15.4	3.9	9.3
22	46.3	nd	8.0	6.4	3.8	10.7	nd	3.5	11.7	7.5	2.0	12.1	50.9		5.2	5.8	6.3	12.6	nd	3.8	8.2	3.5	3.8
MM20																							
1	44.7	3.6	6.8	9.3	7.6	10.0	2.5	0.9	7.2	7.3	nd	28.9	49.2	3.0	4.4	8.5	12.5	11.8	1.1	1.0	5.1	3.4	nd
2	43.2	2.3	6.0	10.1	5.9	10.9	3.6	0.5	8.4	7.9	1.1	20.4	48.1	1.9	3.9	9.4	9.8	13.0	1.6	0.5	6.0	3.7	2.1
3	41.6	4.5	7.3	7.9	6.6	5.4	nd	2.6	14.6	7.3	2.2	15.6	46.1	3.8	4.8	7.3	10.9	6.4	nd	2.8	10.4	3.4	4.2
4	43.2	3.3	7.4	10.2	7.4	8.2	nd	1.7	8.2	9.7	0.7	9.0	47.8	2.8	4.8	9.4	12.1	9.7	nd	1.8	5.8	4.5	1.2
5	50.4	2.7	7.9	11.6	7.8	7.3	nd	nd	6.1	6.2	nd	14.4	54.4	2.2	5.0	10.5	12.5	8.4	nd	nd	4.2	2.8	nd
6	38.0	nd	7.7	7.1	6.2	14.3	nd	nd	11.6	12.3	2.8	12.4	42.0	nd	5.0	6.6	10.3	17.0	nd	nd	8.2	5.8	5.2
7	45.6	2.2	6.6	8.4	5.0	9.8	3.0	0.8	7.0	10.6	1.0	32.2	51.4	1.8	4.4	7.9	8.5	11.8	1.3	0.9	5.0	5.1	1.9
8	51.0	3.0	8.2	6.9	5.6	7.3	0.7	0.9	8.2	7.4	0.8	19.4	56.1	2.5	5.3	6.3	9.2	8.6	0.3	1.0	5.7	3.4	1.5
9	39.1	nd	6.6	6.7	6.7	8.2	nd	4.3	18.9	7.3	2.2	11.8	43.3	nd	4.3	6.2	11.0	9.7	nd	4.6	13.4	3.4	4.1
10	46.4	nd	6.0	4.2	4.3	8.4	nd	4.9	13.8	9.2	2.7	15.8	51.0	nd	3.9	3.8	7.1	9.9	nd	5.2	9.7	4.3	5.0
11	36.3	2.1	7.1	5.7	7.2	8.2	6.9	4.3	16.0	3.8	2.2	20.3	40.8	1.8	4.7	5.4	12.0	9.9	3.1	4.7	11.5	1.8	4.2
MM22																							
1	38.0	nd	8.3	4.6	5.3	10.6	3.8	4.2	16.5	3.1	5.5	15.8	40.9	nd	5.3	4.2	8.5	12.2	1.6	4.4	11.4	1.4	10.1
2	49.8	2.5	7.6	6.8	2.4	8.9	nd	1.6	6.5	13.0	0.9	28.7	56.8	2.2	5.1	6.4	4.1	10.9	nd	1.8	4.7	6.3	1.7
3	45.6	3.0	8.0	8.8	2.6	9.3	nd	2.0	8.3	10.9	1.5	18.7	51.7	2.6	5.4	8.4	4.4	11.3	nd	2.2	6.0	5.2	2.8
4	34.1	nd	7.7	4.5	4.7	12.3	4.4	3.6	18.0	5.7	5.0	28.4	37.9	nd	5.0	4.2	7.8	14.6	1.9	3.9	12.8	2.7	9.3
5	37.3	nd	8.6	4.8	4.6	12.0	3.3	3.2	14.0	7.9	4.2	25.1	41.5	nd	5.6	4.5	7.6	14.3	1.4	3.4	9.9	3.7	8.0
6	42.3	nd	7.7	5.3	2.5	9.8	nd	2.0	17.2	7.9	5.3	11.5	46.6	nd	5.0	4.9	4.1	11.6	nd	2.1	12.1	3.7	9.9
7	42.6	2.6	9.7	15.6	4.5	6.0	nd	2.5	7.5	9.1	nd	18.8	48.8	2.2	6.5	14.9	7.6	7.3	nd	2.8	5.5	4.4	nd
8	39.7	2.9	7.9	7.5	5.4	9.4	nd	4.0	14.2	5.9	3.1	17.7	43.3	2.4	5.0	6.9	8.9	11.0	nd	4.2	9.9	2.7	5.8
9	40.9	3.5	7.4	6.4	4.6	9.7	nd	3.5	14.5	6.9	2.6	18.7	45.2	2.9	4.8	5.9	7.6	11.5	nd	3.7	10.2	3.2	4.9
10	50.1	3.9	8.2	17.5	6.1	nd	nd	3.3	7.4	3.6	nd	15.9	55.1	3.2	5.3	16.1	9.9	nd	nd	3.5	5.2	1.7	nd

inc.	weight% oxide + Cl (normalised to 100%)												molecular proportion (normalised to 100 %)									
no.	SiO_2	TiO_2	Al_2O_3	FeO	MgO	CaO	BaO	Na_2O	K_2O	P_2O_5	Cl	total	Si	Ti	Al	Fe	Mg	Ca	Ba	Na	K	P	Cl
11	40.5	nd	7.7	4.0	4.2	7.0	3.6	5.0	17.4	5.5	5.2	16.3	44.7	nd	5.0	3.7	6.9	8.2	1.5	5.3	12.2	2.6	9.8
12	41.6	nd	7.8	5.4	3.8	9.1	nd	3.6	16.2	7.7	4.8	17.5	45.6	nd	5.1	4.9	6.2	10.7	nd	3.8	11.3	3.5	8.9
13	32.5	nd	6.3	11.0	5.7	23.1	6.0	2.8	2.9	8.7	0.9	15.7	35.8	nd	4.1	10.1	9.4	27.2	2.6	3.0	2.0	4.0	1.7
14	41.7	nd	7.6	3.9	3.6	9.8	4.0	4.5	16.1	4.5	4.4	13.0	45.9	nd	5.0	3.6	5.9	11.5	1.7	4.8	11.3	2.1	8.2
15	34.9	nd	6.6	6.4	5.1	21.0	nd	1.9	12.6	2.7	8.9	16.2	34.8	nd	3.9	5.3	7.5	22.4	nd	1.8	8.0	1.1	15.1
16	43.3	3.0	7.9	4.1	3.7	8.7	nd	3.6	15.7	6.0	4.0	21.5	47.4	2.5	5.1	3.8	6.0	10.2	nd	3.8	10.9	2.8	7.5
17	34.1	1.6	6.9	4.4	3.8	13.9	3.8	3.6	16.0	7.0	4.7	27.7	38.0	1.3	4.5	4.1	6.3	16.6	1.7	3.9	11.4	3.3	8.9
18	46.3	3.1	8.4	7.1	3.1	10.0	nd	2.0	7.1	12.1	0.9	16.3	52.6	2.7	5.6	6.8	5.3	12.2	nd	2.2	5.2	5.8	1.7
19	50.5	1.9	10.0	7.6	2.5	10.4	nd	2.2	6.4	7.9	0.5	25.3	56.5	1.6	6.6	7.1	4.1	12.4	nd	2.4	4.6	3.8	0.9
20	41.3	1.8	6.0	12.3	5.4	13.3	nd	2.5	5.8	10.4	1.2	21.7	45.2	1.5	3.9	11.2	8.8	15.7	nd	2.7	4.0	4.8	2.3
CDR3																							
1	51.0	1.9	6.1	4.8	5.5	3.8	nd	3.4	15.0	8.4	nd	3.2	57.4	1.6	4.0	4.5	9.2	4.6	nd	3.7	10.7	4.0	nd
2	47.3	1.3	5.1	4.4	5.4	5.5	3.7	3.0	13.7	10.5	nd	4.6	54.6	1.2	3.4	4.3	9.3	6.8	1.7	3.4	10.1	5.1	nd
3	47.2	nd	7.0	5.4	5.5	3.7	4.1	3.0	14.0	10.1	nd	2.5	55.0	nd	4.8	5.3	9.6	4.6	1.9	3.3	10.4	5.0	nd
4	51.8	2.5	6.6	5.8	5.2	3.7	nd	2.9	13.1	8.5	nd	3.1	58.3	2.1	4.4	5.4	8.7	4.5	nd	3.1	9.4	4.1	nd
5	47.8	1.8	7.0	4.8	6.0	3.6	3.7	2.9	14.4	8.1	nd	4.2	54.9	1.6	4.7	4.6	10.3	4.4	1.6	3.3	10.5	3.9	nd
6	44.8	nd	5.8	5.3	6.0	4.6	3.8	4.3	15.7	9.7	nd	4.0	51.8	nd	4.0	5.1	10.4	5.7	1.7	4.8	11.6	4.8	nd
7	43.5	2.4	5.9	4.5	7.4	5.0	nd	4.3	15.6	11.4	nd	3.2	49.5	2.1	4.0	4.3	12.5	6.1	nd	4.7	11.3	5.5	nd
8	46.2	3.3	5.9	4.7	5.5	3.6	2.3	3.4	16.0	9.0	nd	5.8	53.4	2.9	4.0	4.6	9.5	4.5	1.0	3.9	11.8	4.4	nd
9	48.3	2.1	6.0	4.5	5.6	3.7	2.7	3.3	15.2	8.7	nd	5.4	55.5	1.8	4.1	4.3	9.5	4.5	1.2	3.6	11.1	4.2	nd
10	45.9	1.7	5.3	4.1	4.8	6.1	3.5	2.4	13.8	12.4	nd	5.9	53.8	1.5	3.7	4.0	8.5	7.7	1.6	2.7	10.3	6.1	nd
11	47.9	2.5	5.8	5.1	6.3	4.2	nd	3.8	14.7	9.6	nd	4.9	54.0	2.1	3.8	4.8	10.6	5.1	nd	4.1	10.6	4.6	nd
12	43.6	nd	6.0	6.0	6.9	5.1	4.5	3.7	14.2	9.9	nd	2.7	50.3	nd	4.1	5.8	11.9	6.3	2.0	4.2	10.4	4.8	nd
13	53.4	3.0	8.0	4.3	5.4	2.5	nd	2.4	14.4	6.7	nd	4.1	59.9	2.5	5.3	4.1	9.0	3.0	nd	2.6	10.3	3.2	nd
14	56.3	2.4	6.8	2.9	4.2	3.7	nd	1.8	13.9	8.0	nd	8.6	63.3	2.0	4.5	2.7	7.1	4.5	nd	1.9	10.0	3.8	nd
15	43.7	2.8	5.4	5.4	6.7	5.3	nd	4.3	15.1	11.4	nd	5.2	49.8	2.4	3.6	5.1	11.3	6.5	nd	4.7	11.0	5.5	nd
16	45.4	2.3	5.6	5.8	6.3	4.5	2.2	3.5	14.5	10.0	nd	6.1	52.0	2.0	3.8	5.5	10.7	5.5	1.0	3.9	10.6	4.8	nd
17	44.7	2.4	5.9	5.4	6.3	4.4	2.4	3.6	15.3	9.6	nd	7.2	51.4	2.0	4.0	5.2	10.8	5.5	1.1	4.0	11.2	4.7	nd
18	49.4	2.5	6.3	4.6	5.9	3.9	nd	3.4	15.5	8.3	nd	3.5	55.7	2.2	4.2	4.3	9.9	4.7	nd	3.8	11.2	4.0	nd
19	52.4	2.8	6.7	4.3	5.5	3.0	1.3	2.4	13.8	7.8	nd	9.4	59.2	2.4	4.5	4.0	9.3	3.6	0.6	2.6	9.9	3.7	nd
20	52.2	2.7	6.0	3.9	5.2	3.6	1.7	2.6	13.9	8.2	nd	9.0	59.1	2.3	4.0	3.7	8.8	4.4	0.8	2.8	10.1	3.9	nd
PAN2																							
1	8.6	nd	6.9	29.1	9.2	12.6	17.2	3.9	7.6	nd	5.0	8.5	9.8	nd	4.6	27.6	15.6	15.3	7.6	4.2	5.5	nd	9.7
2	4.4	nd	1.4	7.7	2.6	4.2	15.5	3.1	31.1	nd	30.0	7.2	4.4	nd	0.8	6.5	3.9	4.5	6.1	3.1	19.9	nd	50.9
3	5.2	nd	nd	17.4	8.9	4.7	20.2	3.0	24.2	nd	16.4	10.2	5.6	nd	nd	15.8	14.4	5.4	8.6	3.2	16.8	nd	30.2
4	7.9	nd	3.3	9.2	8.3	8.6	20.9	9.2	16.8	nd	15.8	6.6	8.4	nd	2.1	8.2	13.2	9.8	8.8	9.6	11.5	nd	28.5
5	5.4	nd	2.3	21.1	11.5	10.0	19.2	5.8	11.2	nd	13.5	9.1	5.7	nd	1.4	18.5	18.0	11.2	7.9	5.9	7.5	nd	23.9
6	12.9	nd	2.8	31.4	7.4	9.0	10.7	6.4	9.4	3.0	7.2	12.7	14.1	nd	1.8	28.8	12.0	10.6	4.6	6.8	6.5	1.4	13.4
8	4.0	nd	0.7	11.4	4.2	7.8	30.1	2.4	12.6	2.0	24.7	14.8	4.3	nd	0.5	10.2	6.7	9.0	12.6	2.5	8.6	0.9	44.8
9	3.0	nd	1.0	6.4	1.7	3.2	9.8	3.9	38.8	nd	32.2	11.9	2.9	nd	0.6	5.3	2.5	3.3	3.8	3.7	24.3	nd	53.6
11	8.1	nd	2.5	20.8	14.2	16.7	22.3	3.6	6.4	nd	5.3	7.6	8.9	nd	1.6	19.1	23.1	19.6	9.6	3.8	4.5	nd	9.9
12	4.2	nd	0.1	10.5	5.0	6.5	20.3	3.7	26.2	nd	23.5	13.9	4.4	nd	0.1	9.2	7.9	7.3	8.3	3.8	17.5	nd	41.6
13	2.7	nd	0.9	9.3	3.9	5.1	13.9	5.9	28.6	nd	29.7	15.6	2.7	nd	0.5	7.6	5.7	5.4	5.3	5.6	17.9	nd	49.3
14	4.9	nd	1.0	5.2	1.6	3.5	20.6	8.2	24.4	nd	30.7	7.2	4.9	nd	0.6	4.4	2.4	3.8	8.1	8.0	15.6	nd	52.3
15	8.7	nd	0.9	12.2	4.1	5.2	18.6	1.7	29.0	nd	19.5	24.4	9.5	nd	0.6	11.1	6.7	6.1	7.9	1.8	20.2	nd	36.1
16	10.0	nd	1.2	18.0	9.7	8.7	10.9	3.3	22.4	nd	15.8	8.6	10.2	nd	0.7	15.4	14.7	9.5	4.4	3.2	14.6	nd	27.3
17	5.7	nd	6.5	9.7	6.1	6.1	28.9	3.4	18.9	nd	14.6	8.6	6.7	nd	4.5	9.5	10.8	7.8	13.4	3.9	14.2	nd	29.1
18	4.0	nd	1.4	30.7	15.6	20.8	6.6	2.3	10.6	nd	7.9	21.2	4.0	nd	0.8	25.4	22.9	22.1	2.6	2.2	6.7	nd	13.2
19	3.3	nd	0.4	3.3	1.4	2.3	7.5	4.3	44.5	nd	32.9	11.9	3.3	nd	0.2	2.7	2.0	2.5	2.9	4.1	27.8	nd	54.6

inc.	weight% oxide + Cl (normalised to 100%)												molecular proportion (normalised to 100 %)										
no.	SiO_2	TiO_2	Al_2O_3	FeO	MgO	CaO	BaO	Na_2O	K_2O	P_2O_5	Cl	total	Si	Ti	Al	Fe	Mg	Ca	Ba	Na	K	P	Cl
21	2.8	nd	1.2	5.9	2.6	4.2	12.7	4.6	33.9	nd	31.9	12.5	2.8	nd	0.7	4.9	3.9	4.4	4.9	4.4	21.2	nd	52.9
22	4.2	nd	0.9	13.9	4.9	6.5	20.3	4.2	23.7	nd	21.3	14.2	4.5	nd	0.6	12.3	7.8	7.4	8.5	4.3	16.1	nd	38.5
23	3.5	nd	1.1	21.7	15.6	22.1	27.3	4.1	1.2	nd	3.5	14.5	3.8	nd	0.7	20.0	25.7	26.2	11.8	4.4	0.8	nd	6.5
24	7.0	nd	1.2	19.7	8.3	15.6	16.0	3.5	13.7	nd	15.0	14.8	7.3	nd	0.7	17.0	12.7	17.2	6.5	3.5	9.0	nd	26.2
26	4.1	nd	0.2	8.3	3.6	6.6	36.8	1.6	12.2	1.4	25.2	14.3	4.6	nd	0.1	7.6	6.0	7.8	15.9	1.7	8.6	0.7	47.2
27	5.0	nd	1.9	9.6	5.3	5.3	15.7	5.5	24.6	nd	27.3	7.5	4.9	nd	1.1	8.0	7.8	5.6	6.1	5.3	15.5	nd	45.8
28	3.6	nd	0.6	8.0	2.8	4.5	17.5	4.3	28.5	nd	30.3	13.0	3.6	nd	0.3	6.7	4.1	4.8	6.9	4.2	18.1	nd	51.3
31	3.5	nd	1.5	2.5	1.5	4.3	17.0	8.2	30.0	nd	31.5	9.6	3.5	nd	0.9	2.1	2.3	4.6	6.6	7.9	19.0	nd	53.1
32	3.1	nd	1.1	4.4	1.6	2.2	18.4	3.5	33.4	nd	32.3	13.4	3.1	nd	0.6	3.7	2.5	2.4	7.3	3.4	21.5	nd	55.4
33	1.8	nd	nd	7.2	1.2	1.8	20.1	4.3	32.4	nd	31.2	19.0	1.8	nd	nd	6.2	1.9	2.0	8.1	4.3	21.3	nd	54.4
34	2.9	nd	nd	9.4	6.6	9.7	27.0	2.6	20.4	nd	21.4	18.3	3.1	nd	nd	8.4	10.6	11.1	11.4	2.7	13.9	nd	38.8
35	4.1	nd	nd	6.8	2.6	4.1	21.3	7.4	21.9	nd	31.9	9.5	4.0	nd	nd	5.6	3.8	4.4	8.2	7.1	13.8	nd	53.2
37	2.8	nd	0.8	8.4	3.8	4.9	14.9	5.2	28.8	nd	30.5	15.2	2.8	nd	0.5	6.9	5.5	5.1	5.7	4.9	18.0	nd	50.6
38	6.7	nd	1.7	30.5	15.5	18.3	16.1	3.7	3.6	nd	4.0	20.1	7.1	nd	1.1	26.9	24.3	20.7	6.7	3.8	2.4	nd	7.1
39	3.9	nd	1.0	12.4	5.2	5.5	18.1	1.6	31.0	nd	21.4	13.3	4.2	nd	0.6	11.2	8.3	6.3	7.6	1.7	21.2	nd	38.9
40	2.7	nd	0.9	4.9	3.0	4.3	19.2	4.7	30.5	nd	29.9	14.4	2.8	nd	0.5	4.1	4.6	4.7	7.6	4.6	19.8	nd	51.4
41	3.9	nd	1.0	5.6	2.2	2.6	11.6	4.5	35.1	nd	33.6	12.8	3.7	nd	0.6	4.5	3.1	2.7	4.4	4.2	21.7	nd	55.1
42	7.7	nd	2.2	15.3	11.8	13.8	29.4	3.4	7.4	nd	8.9	9.8	8.7	nd	1.5	14.4	19.9	16.6	13.0	3.7	5.3	nd	17.0
43	3.0	nd	0.6	20.7	9.6	10.8	15.8	2.8	20.6	nd	15.9	28.3	3.2	nd	0.4	18.1	15.0	12.1	6.5	2.8	13.7	nd	28.2
44	3.9	nd	1.0	6.4	5.3	4.4	13.9	4.4	32.2	nd	28.6	10.7	3.8	nd	0.6	5.3	7.8	4.6	5.4	4.2	20.3	nd	47.9
45	3.4	nd	0.6	9.2	5.4	5.9	22.1	5.8	22.2	nd	25.4	13.9	3.5	nd	0.4	7.9	8.3	6.5	8.9	5.7	14.5	nd	44.2
46	4.2	nd	0.9	8.2	4.1	4.6	12.9	2.6	36.1	nd	26.4	11.2	4.3	nd	0.5	7.0	6.3	5.0	5.1	2.6	23.5	nd	45.6
47	5.5	nd	1.7	17.5	8.8	11.4	25.7	1.6	13.1	nd	14.8	21.8	6.0	nd	1.1	16.0	14.3	13.4	11.0	1.7	9.1	nd	27.4
48	2.0	nd	0.5	3.0	1.3	1.6	7.2	1.6	47.9	nd	34.9	16.7	2.0	nd	0.3	2.5	1.9	1.7	2.8	1.6	29.8	nd	57.6
49	5.1	nd	nd	28.7	4.9	7.6	1.6	2.6	30.2	1.3	17.8	21.5	5.2	nd	nd	24.6	7.5	8.3	0.7	2.6	19.7	0.6	30.9
50	2.8	nd	1.1	6.6	2.6	1.8	27.5	3.9	23.7	nd	30.0	11.8	3.0	nd	0.7	5.8	4.1	2.0	11.3	3.9	15.9	nd	53.4
PAN3																							
1	4.4	nd	1.9	12.2	2.9	6.8	18.4	6.5	20.9	nd	25.8	5.5	4.5	nd	1.2	10.4	4.5	7.4	7.4	6.4	13.6	nd	44.6
2	4.6	nd	nd	12.6	6.0	7.7	17.5	4.9	23.1	nd	23.6	6.5	4.7	nd	nd	10.6	9.1	8.4	7.0	4.8	14.9	nd	40.5
3	2.3	nd	nd	3.8	2.4	3.5	15.7	6.1	33.2	nd	33.0	6.2	2.2	nd	nd	3.2	3.5	3.7	6.0	5.8	20.8	nd	54.9
5	3.5	nd	nd	4.8	2.4	4.1	15.9	3.6	34.9	nd	30.7	4.0	3.5	nd	nd	4.1	3.6	4.5	6.2	3.5	22.3	nd	52.3
6	3.6	nd	nd	7.4	3.8	4.3	13.0	nd	36.4	nd	31.5	3.3	3.5	nd	nd	6.1	5.6	4.5	5.0	nd	22.8	nd	52.4
7	4.0	nd	nd	8.7	2.9	3.6	20.5	nd	27.7	nd	32.6	3.0	4.0	nd	nd	7.3	4.3	3.8	8.0	nd	17.6	nd	55.0
8	4.1	nd	nd	9.6	4.2	6.1	11.3	3.5	30.2	nd	31.0	4.8	3.9	nd	nd	7.7	6.1	6.3	4.2	3.2	18.4	nd	50.2
10	2.7	nd	0.3	8.9	3.3	7.1	23.5	4.4	22.3	nd	27.3	6.8	2.8	nd	0.2	7.7	5.1	7.9	9.5	4.3	14.7	nd	47.8
11	2.4	nd	nd	5.9	2.2	3.7	22.1	4.0	26.1	nd	33.7	5.5	2.4	nd	nd	4.9	3.2	3.9	8.6	3.8	16.5	nd	56.7
12	2.8	nd	0.7	6.3	2.9	3.7	16.7	5.0	31.7	nd	30.2	6.3	2.8	nd	0.4	5.3	4.3	4.0	6.6	4.8	20.3	nd	51.5
13	2.9	nd	nd	4.0	1.5	2.9	18.9	5.6	30.1	nd	34.2	5.1	2.8	nd	nd	3.3	2.2	3.0	7.3	5.3	18.9	nd	57.1
14	3.2	nd	0.4	7.7	2.4	5.0	19.9	4.2	28.6	nd	28.7	5.7	3.3	nd	0.2	6.6	3.7	5.5	8.0	4.1	18.7	nd	49.9
15	4.0	nd	nd	5.6	8.1	12.5	30.2	6.0	14.8	1.1	17.8	13.7	4.3	nd	nd	5.1	13.2	14.6	12.9	6.3	10.3	0.5	32.8
16	2.4	nd	nd	4.4	2.1	3.9	13.7	3.7	35.6	nd	34.2	6.2	2.4	nd	nd	3.6	3.0	4.0	5.2	3.4	22.1	nd	56.3
17	3.0	nd	0.7	5.7	4.0	3.6	13.2	4.2	34.6	nd	31.0	6.1	2.9	nd	0.4	4.7	5.9	3.7	5.1	4.0	21.7	nd	51.5
18	2.7	nd	nd	5.7	2.5	3.6	18.7	4.7	27.9	nd	34.3	8.0	2.6	nd	nd	4.6	3.6	3.7	7.1	4.5	17.3	nd	56.5
20	2.7	nd	nd	8.2	3.4	4.2	12.2	5.5	32.0	nd	32.0	6.6	2.6	nd	nd	6.6	4.8	4.4	4.6	5.1	19.7	nd	52.2
PAN5																							
1	3.9	3.4	nd	34.0	22.4	30.5	nd	2.2	1.3	nd	2.4	4.7	3.6	2.4	nd	26.3	30.9	30.3	nd	1.9	0.8	nd	3.7
2	10.5	nd	1.3	36.3	11.5	15.2	17.9	3.1	2.3	nd	1.8	10.9	11.7	nd	0.9	33.9	19.1	18.1	7.8	3.4	1.6	nd	3.4
3	6.6	nd	nd	26.6	5.5	7.5	8.7	5.1	21.2	nd	18.7	7.7	6.7	nd	nd	22.6	8.3	8.2	3.5	5.0	13.7	nd	32.1
4	6.3	nd	1.4	61.4	5.9	6.2	7.2	3.9	3.3	nd	4.5	8.9	7.0	nd	0.9	57.0	9.7	7.4	3.1	4.2	2.3	nd	8.4

inc.	weight% oxide + Cl (normalised to 100%)												molecular proportion (normalised to 100 %)									
no.	SiO_2	TiO_2	Al_2O_3	FeO	MgO	CaO	BaO	Na_2O	K_2O	P_2O_5	Cl	total	Si	Ti	Al	Fe	Mg	Ca	Ba	Na	K	P	Cl
5	3.4	nd	nd	11.9	nd	nd	3.8	13.1	32.9	nd	34.8	7.8	3.2	nd	nd	9.3	nd	nd	1.4	11.8	19.5	nd	54.9
6	5.2	nd	1.4	29.0	2.5	4.0	9.1	9.3	17.9	nd	21.6	7.3	5.3	nd	0.9	24.5	3.8	4.3	3.6	9.1	11.6	nd	37.0
7	9.0	nd	nd	11.7	7.4	11.0	20.7	3.6	19.4	nd	17.2	5.1	9.5	nd	nd	10.3	11.6	12.4	8.6	3.7	13.0	nd	30.8
8	8.4	nd	6.7	31.6	12.7	17.0	16.9	3.1	2.1	nd	1.5	7.2	9.4	nd	4.4	29.5	21.2	20.4	7.4	3.3	1.5	nd	2.9
9	6.9	nd	nd	32.3	15.5	20.5	17.4	4.1	1.4	nd	1.8	7.3	7.3	nd	nd	28.8	24.6	23.5	7.3	4.2	1.0	nd	3.3
11	4.6	nd	nd	47.7	3.0	4.0	6.3	6.3	15.0	nd	13.2	8.2	4.9	nd	nd	42.6	4.7	4.6	2.6	6.5	10.2	nd	23.8
12	4.3	nd	nd	13.1	7.3	9.0	13.8	15.3	15.7	nd	21.6	7.0	4.2	nd	nd	10.7	10.6	9.4	5.3	14.5	9.7	nd	35.7
14	8.3	nd	1.3	53.5	6.5	7.8	11.2	1.6	4.2	nd	5.7	10.3	9.3	nd	0.8	49.7	10.7	9.2	4.9	1.7	3.0	nd	10.7
20	2.3	nd	0.7	6.5	5.4	28.8	3.5	5.6	24.2	nd	23.1	10.8	2.1	nd	0.4	5.0	7.4	28.5	1.3	5.0	14.2	nd	36.1
21	5.5	nd	1.1	17.9	18.4	37.4	14.7	1.6	1.1	nd	2.2	9.7	5.4	nd	0.7	14.9	27.3	40.0	5.8	1.6	0.7	nd	3.7
23	5.0	nd	nd	8.0	3.0	5.7	7.1	13.5	29.0	nd	28.6	7.3	4.7	nd	nd	6.4	4.3	5.8	2.7	12.4	17.6	nd	46.1
25	8.0	nd	nd	24.2	6.6	8.6	7.5	3.0	21.8	nd	20.3	6.6	7.9	nd	nd	19.9	9.7	9.1	2.9	2.9	13.7	nd	33.9
26	3.5	nd	nd	21.4	15.6	22.9	29.8	2.0	2.2	nd	2.5	6.0	4.0	nd	nd	20.3	26.2	27.8	13.2	2.2	1.6	nd	4.8
28	8.3	nd	1.2	30.5	11.0	14.5	21.0	3.2	5.6	nd	4.9	8.3	9.3	nd	0.8	28.5	18.4	17.3	9.2	3.5	4.0	nd	9.2
29	11.4	nd	2.0	36.9	8.4	11.7	21.8	3.1	3.0	nd	1.6	7.2	13.5	nd	1.4	36.5	14.8	14.8	10.1	3.6	2.3	nd	3.1
30	1.5	nd	nd	4.6	3.1	5.7	4.4	14.5	32.9	nd	33.3	8.6	1.4	nd	nd	3.5	4.3	5.6	1.6	12.9	19.2	nd	51.6
31	4.9	nd	nd	34.5	3.9	4.6	11.4	9.2	12.9	0.7	17.9	5.1	5.1	nd	nd	29.9	6.0	5.1	4.6	9.2	8.5	0.3	31.3
35	3.4	nd	4.9	43.0	2.7	2.9	4.2	5.4	17.1	nd	16.4	11.6	3.6	nd	3.1	37.8	4.2	3.3	1.7	5.5	11.5	nd	29.3
PAN7																							
1	1.6	nd	nd	5.6	0.8	1.8	4.7	24.6	19.4	nd	41.4	18.5	1.4	nd	nd	3.9	1.1	1.7	1.6	20.3	10.5	nd	59.6
2	7.9	nd	nd	33.0	11.5	16.3	18.3	4.2	4.5	nd	4.3	7.8	8.6	nd	nd	30.2	18.7	19.1	7.9	4.5	3.1	nd	8.0
3	3.8	nd	0.8	16.0	5.8	6.6	20.4	3.8	24.8	nd	17.9	12.1	4.1	nd	0.5	14.7	9.5	7.7	8.8	4.0	17.3	nd	33.3
4	2.6	nd	nd	13.8	4.8	8.0	7.0	8.7	29.1	nd	25.9	11.4	2.6	nd	nd	11.1	6.9	8.3	2.6	8.2	17.9	nd	42.4
5	7.5	nd	nd	25.7	8.7	12.7	22.6	2.1	11.3	nd	9.5	9.5	8.3	nd	nd	23.9	14.5	15.1	9.9	2.3	8.1	nd	17.9
6	2.4	nd	nd	22.6	9.1	14.0	22.4	5.5	11.4	2.4	10.2	10.2	2.7	nd	nd	21.1	15.1	16.7	9.8	5.9	8.1	1.1	19.3
7	3.7	nd	1.1	10.7	4.7	7.6	18.0	2.4	30.1	nd	21.6	12.4	4.0	nd	0.7	9.6	7.4	8.7	7.5	2.5	20.5	nd	39.1
8	2.2	nd	nd	45.3	12.0	30.4	2.5	3.2	1.3	1.8	1.3	11.8	2.3	nd	nd	38.5	18.2	33.1	1.0	3.1	0.8	0.8	2.2
9	5.0	nd	nd	34.8	6.4	6.7	22.6	5.5	10.5	nd	8.5	8.7	5.8	nd	nd	33.8	11.1	8.3	10.3	6.1	7.8	nd	16.8
10	1.7	nd	nd	10.6	2.4	5.3	9.1	19.3	17.1	nd	34.4	22.4	1.5	nd	nd	8.0	3.2	5.1	3.2	16.8	9.8	nd	52.3
11	2.4	nd	nd	14.8	3.4	6.5	20.3	6.7	21.5	nd	24.5	18.5	2.5	nd	nd	12.8	5.2	7.2	8.2	6.7	14.2	nd	43.1
12	3.4	nd	0.6	10.1	4.0	5.2	13.0	11.5	23.8	nd	28.5	20.5	3.3	nd	0.3	8.2	5.7	5.4	4.9	10.8	14.7	nd	46.7
14	4.5	nd	nd	8.7	4.6	8.0	6.2	9.2	30.4	nd	28.4	23.0	4.3	nd	nd	6.8	6.5	8.1	2.3	8.4	18.3	nd	45.4
15	3.7	nd	0.9	10.8	3.6	8.2	2.7	4.4	38.4	nd	27.2	26.8	3.6	nd	0.5	8.8	5.2	8.5	1.0	4.1	23.7	nd	44.6
16	2.9	nd	0.7	15.0	2.1	3.2	4.7	17.9	22.2	nd	31.4	43.7	2.6	nd	0.4	11.5	2.9	3.2	1.7	15.9	13.0	nd	48.9
17	3.3	nd	nd	19.6	12.0	19.3	20.7	5.9	8.5	nd	10.7	27.4	3.4	nd	nd	17.2	18.8	21.6	8.5	6.0	5.7	nd	18.9
18	4.0	nd	nd	9.6	4.4	6.4	10.3	6.8	32.1	nd	26.3	23.9	4.0	nd	nd	7.9	6.5	6.8	4.0	6.5	20.2	nd	44.0
19	5.0	nd	nd	80.8	nd	nd	nd	3.6	6.6	nd	4.0	29.6	5.7	nd	nd	77.6	nd	nd	nd	4.0	4.9	nd	7.9
20	2.8	nd	0.7	7.2	3.1	4.7	11.7	10.9	29.3	nd	29.5	32.5	2.7	nd	0.4	5.8	4.5	4.9	4.5	10.3	18.2	nd	48.6
21	3.3	nd	nd	13.4	4.2	6.1	12.6	14.2	18.6	nd	27.6	29.5	3.1	nd	nd	10.7	6.0	6.3	4.7	13.2	11.3	nd	44.7
23	3.8	nd	0.9	11.9	4.5	9.8	7.3	12.7	21.5	nd	27.5	32.7	3.5	nd	0.5	9.3	6.3	9.8	2.7	11.5	12.8	nd	43.6
24	2.8	nd	nd	10.4	5.7	10.0	15.6	16.0	13.9	nd	25.5	23.9	2.7	nd	nd	8.3	8.1	10.2	5.9	14.9	8.5	nd	41.4
25	2.7	nd	0.8	29.5	nd	nd	nd	18.2	19.1	nd	29.7	31.3	2.5	nd	0.4	22.8	nd	nd	nd	16.3	11.3	nd	46.7
26	2.4	nd	nd	19.4	4.7	8.8	13.4	8.7	20.9	nd	21.7	32.3	2.4	nd	nd	16.4	7.1	9.5	5.3	8.5	13.5	nd	37.2
27	3.8	nd	nd	10.4	4.0	7.9	20.7	7.5	21.4	nd	24.3	29.2	3.9	nd	nd	9.0	6.1	8.7	8.4	7.5	14.0	nd	42.4
28	2.5	nd	nd	5.9	2.2	5.7	7.1	19.0	24.8	nd	32.8	24.0	2.3	nd	nd	4.5	3.0	5.6	2.5	16.8	14.4	nd	50.8
29	2.6	nd	nd	18.2	2.6	4.4	9.4	11.2	24.7	nd	26.9	43.2	2.5	nd	nd	14.9	3.8	4.6	3.6	10.6	15.4	nd	44.6
30	2.7	nd	0.9	19.9	3.0	5.9	10.1	6.8	26.6	nd	24.0	29.3	2.8	nd	0.5	16.8	4.5	6.4	4.0	6.7	17.1	nd	41.1
PAN6																							
1	5.7	nd	nd	37.5	11.6	16.9	22.4	2.5	1.5	nd	2.0	9.7	6.5	nd	nd	35.7	19.6	20.6	10.0	2.8	1.1	nd	3.8

inc.	weight% oxide + Cl (normalised to 100%)												molecular proportion (normalised to 100 %)									
no.	SiO_2	TiO_2	Al_2O_3	FeO	MgO	CaO	BaO	Na_2O	K_2O	P_2O_5	Cl	total	Si	Ti	Al	Fe	Mg	Ca	Ba	Na	K	P	Cl
2	3.8	nd	nd	9.3	3.9	10.3	18.3	10.4	17.8	nd	26.2	9.3	3.7	nd	nd	7.7	5.8	10.9	7.1	10.0	11.2	nd	43.7
3	2.1	nd	nd	7.2	2.0	3.9	10.3	6.6	34.8	nd	33.0	13.7	2.0	nd	nd	5.8	2.9	4.0	3.9	6.1	21.4	nd	53.9
4	2.8	nd	nd	5.4	1.1	3.0	11.7	6.9	33.8	1.6	33.7	7.0	2.7	nd	nd	4.4	1.7	3.2	4.4	6.5	21.0	0.7	55.5
5	2.7	nd	1.6	12.0	2.9	6.6	12.5	7.8	27.5	nd	26.5	6.2	2.7	nd	0.9	10.0	4.4	7.1	4.9	7.6	17.5	nd	44.9
7	2.6	nd	nd	7.2	2.7	5.0	14.1	6.8	31.1	nd	30.4	9.9	2.6	nd	nd	6.0	4.0	5.3	5.4	6.5	19.5	nd	50.7
8	3.0	nd	nd	17.2	4.7	9.6	16.1	6.7	20.1	nd	22.5	9.3	3.1	nd	nd	14.6	7.1	10.4	6.4	6.6	13.0	nd	38.8
9	2.5	nd	nd	17.7	1.9	4.6	11.7	12.1	20.5	nd	29.1	16.0	2.4	nd	nd	14.3	2.8	4.7	4.4	11.3	12.6	nd	47.6
10	3.3	nd	nd	16.0	2.9	8.7	11.6	4.1	28.9	nd	24.6	10.0	3.4	nd	nd	13.5	4.4	9.4	4.6	4.0	18.6	nd	42.1
11	3.3	nd	nd	34.1	5.3	6.9	15.4	3.6	15.6	nd	15.9	12.8	3.5	nd	nd	30.6	8.5	7.9	6.5	3.7	10.6	nd	28.8
12	3.4	nd	1.0	9.1	2.4	3.2	12.8	9.4	28.7	nd	30.0	9.0	3.3	nd	0.6	7.4	3.6	3.4	4.9	8.9	18.0	nd	49.9
13	5.0	nd	nd	38.0	6.1	9.6	17.0	3.5	8.1	nd	12.6	8.0	5.4	nd	nd	34.3	9.8	11.1	7.2	3.7	5.5	nd	23.0
14	10.8	nd	nd	31.3	3.4	4.0	15.0	nd	19.6	nd	15.8	4.4	11.8	nd	nd	28.5	5.5	4.7	6.4	nd	13.7	nd	29.3
15	2.2	nd	nd	27.7	7.3	12.9	25.3	10.0	2.2	nd	12.5	12.8	2.4	nd	nd	25.1	11.8	14.9	10.7	10.5	1.6	nd	23.0
16	2.1	nd	nd	27.7	7.3	12.9	25.2	10.0	2.3	nd	12.5	14.6	2.3	nd	nd	25.1	11.8	14.9	10.7	10.5	1.6	nd	23.0
17	2.6	7.8	1.2	6.5	3.9	6.7	na	8.9	27.9	nd	34.6	8.8	2.3	5.2	0.6	4.8	5.2	6.4	nd	7.6	15.8	nd	52.1
18	4.4	7.0	2.0	7.5	4.0	5.8	na	10.2	27.7	nd	31.4	5.2	4.0	4.8	1.1	5.7	5.4	5.7	nd	9.0	16.0	nd	48.3
19	7.2	5.0	1.7	45.4	3.0	2.6	na	7.3	13.3	nd	14.4	7.0	7.5	3.9	1.0	39.1	4.6	2.9	nd	7.3	8.8	nd	25.1
20	4.6	6.4	1.2	10.5	3.1	4.6	na	5.3	36.1	nd	28.1	7.2	4.4	4.6	0.6	8.4	4.4	4.7	nd	5.0	22.1	nd	45.7
21	3.4	9.4	0.9	16.0	8.4	15.7	na	3.6	22.7	nd	19.7	13.1	3.2	6.7	0.5	12.7	11.9	16.0	nd	3.3	13.8	nd	31.8
22	3.8	4.8	1.2	6.9	2.1	3.0	na	15.7	28.2	nd	34.3	5.2	3.4	3.2	0.6	5.2	2.8	2.9	nd	13.7	16.1	nd	52.1
24	4.4	3.6	1.0	9.3	2.7	3.0	na	6.7	39.4	nd	29.9	8.9	4.2	2.6	0.6	7.4	3.9	3.1	nd	6.2	23.9	nd	48.2
25	3.6	13.6	1.2	19.1	5.8	9.8	na	6.2	16.8	nd	23.8	8.5	3.3	9.6	0.7	15.0	8.1	9.9	nd	5.7	10.0	nd	37.7
29	10.4	18.1	2.3	23.4	17.6	22.6	na	1.7	1.5	1.0	1.5	4.9	10.3	13.5	1.3	19.5	26.0	24.0	nd	1.6	0.9	0.4	2.5
31	3.4	8.2	1.2	10.3	3.8	7.5	na	10.6	25.7	nd	29.2	4.9	3.1	5.7	0.7	7.9	5.3	7.4	nd	9.5	15.1	nd	45.4
33	4.7	6.4	1.3	6.8	3.7	5.9	na	13.0	27.5	nd	30.8	3.4	4.3	4.3	0.7	5.1	5.0	5.7	nd	11.5	15.9	nd	47.5
35	3.0	5.6	1.0	5.3	2.3	3.4	na	9.8	36.2	nd	33.3	8.2	2.8	3.9	0.6	4.1	3.2	3.3	nd	8.7	21.3	nd	52.1
PAN8																							
3	6.6	10.4	1.6	36.1	11.8	15.6	na	5.0	5.5	nd	7.5	5.5	6.6	7.7	1.0	29.9	17.4	16.6	nd	4.8	3.5	nd	12.6
4	3.1	5.3	1.3	6.0	2.2	1.9	na	24.2	17.5	nd	38.5	6.9	2.7	3.4	0.7	4.2	2.7	1.7	nd	19.9	9.5	nd	55.3
5	4.4	5.9	1.7	9.0	5.3	6.6	na	13.7	24.7	nd	28.8	5.0	4.0	4.0	0.9	6.8	7.2	6.4	nd	12.0	14.3	nd	44.3
6	4.7	4.7	1.4	13.1	4.2	5.5	na	11.4	26.0	nd	28.9	6.8	4.4	3.2	0.8	10.1	5.8	5.4	nd	10.2	15.3	nd	45.0
7	4.7	7.0	1.2	12.3	4.3	5.4	na	14.5	22.5	nd	28.1	5.7	4.3	4.9	0.6	9.4	5.9	5.3	nd	12.9	13.2	nd	43.6
9	4.0	9.2	1.5	14.5	3.7	5.5	na	11.9	23.4	nd	26.2	4.8	3.8	6.5	0.8	11.4	5.2	5.5	nd	10.8	14.0	nd	41.8
10	2.8	5.6	1.0	5.5	2.9	3.7	na	13.5	30.2	nd	34.8	7.8	2.5	3.8	0.5	4.2	3.8	3.5	nd	11.7	17.2	nd	52.8
11	4.5	6.1	1.2	6.8	3.9	5.5	na	12.6	27.8	nd	31.6	5.8	4.0	4.2	0.7	5.1	5.2	5.3	nd	11.1	16.0	nd	48.4
12	3.5	6.7	1.1	8.9	4.7	7.5	na	14.1	22.1	nd	31.3	6.4	3.1	4.5	0.6	6.6	6.3	7.1	nd	12.1	12.5	nd	47.2
13	4.6	9.9	1.3	19.6	6.7	8.9	na	4.6	23.0	nd	21.4	8.5	4.4	7.2	0.7	15.7	9.6	9.2	nd	4.3	14.1	nd	34.8
14	6.6	2.7	2.3	31.8	19.1	28.1	na	4.2	2.4	nd	2.9	5.5	6.2	1.9	1.3	25.2	26.9	28.5	nd	3.8	1.4	nd	4.6
15	3.0	4.7	1.0	7.5	4.4	5.4	na	13.5	27.2	nd	33.2	6.1	2.7	3.2	0.5	5.6	5.8	5.1	nd	11.6	15.4	nd	50.0
16	3.3	5.3	1.0	6.6	3.8	5.7	na	8.3	34.6	nd	31.5	5.8	3.0	3.6	0.6	5.1	5.2	5.6	nd	7.4	20.3	nd	49.2
17	11.1	7.4	1.7	40.1	7.2	8.3	na	6.2	8.7	0.9	8.4	7.2	11.5	5.7	1.1	34.6	11.1	9.2	nd	6.2	5.7	0.4	14.6
18	5.1	8.5	1.3	7.7	5.7	8.7	na	7.8	26.3	nd	29.1	10.1	4.6	5.8	0.7	5.9	7.7	8.5	nd	6.8	15.2	nd	44.8
19	4.0	4.7	1.2	8.3	4.7	4.8	na	15.1	30.9	nd	26.4	7.8	3.7	3.3	0.7	6.5	6.6	4.8	nd	13.8	18.5	nd	42.0
20	1.1	0.4	0.7	nd	nd	nd	na	20.7	30.6	nd	46.4	15.7	0.9	0.2	0.4	nd	nd	nd	nd	16.7	16.3	nd	65.5
PAN4																							
2	18.9	nd	nd	13.2	nd	8.2	17.6	5.5	17.1	4.5	15.1	3.4	21.1	nd	nd	12.3	nd	9.8	7.7	5.9	12.2	2.1	28.7
4	22.7	nd	3.2	9.1	3.6	8.1	6.5	4.5	21.2	4.0	17.3	5.7	23.3	nd	1.9	7.8	5.5	8.9	2.6	4.4	13.8	1.7	30.0
5	15.3	nd	1.7	11.5	nd	2.9	12.5	3.7	28.0	nd	24.4	7.9	15.9	nd	1.0	10.0	nd	3.2	5.1	3.7	18.5	nd	42.7
7	18.9	1.8	1.9	8.6	1.8	5.1	11.8	2.9	25.6	3.0	18.6	15.2	20.2	1.4	1.2	7.7	2.8	5.8	5.0	3.1	17.5	1.4	33.9

inc.	weight% oxide + Cl (normalised to 100%)												molecular proportion (normalised to 100 %)									
no.	SiO_2	TiO_2	Al_2O_3	FeO	MgO	CaO	BaO	Na_2O	K_2O	P_2O_5	Cl	total	Si	Ti	Al	Fe	Mg	Ca	Ba	Na	K	P	Cl
8	13.2	nd	1.0	8.8	1.2	5.1	17.0	4.2	23.7	3.3	22.5	14.8	14.1	nd	0.6	7.9	1.9	5.9	7.1	4.3	16.1	1.5	40.6
9	22.8	nd	1.8	10.9	1.8	5.7	12.3	3.2	22.1	3.1	16.4	6.2	24.5	nd	1.1	9.8	2.8	6.5	5.2	3.4	15.2	1.4	30.0
13	6.0	nd	1.6	11.7	0.9	3.3	16.7	3.5	25.0	1.3	29.9	12.5	6.0	nd	1.0	9.9	1.4	3.6	6.6	3.5	16.2	0.6	51.3
14	25.8	nd	2.8	11.0	1.8	5.8	11.2	3.0	22.2	2.4	14.0	4.3	28.1	nd	1.8	10.0	2.9	6.8	4.8	3.2	15.4	1.1	25.9
17	11.0	nd	1.9	11.6	1.1	3.5	11.6	3.8	27.1	1.9	26.4	8.6	11.2	nd	1.1	9.9	1.7	3.9	4.6	3.8	17.6	0.8	45.5
20	12.3	nd	1.1	8.2	0.9	3.5	11.9	4.6	30.3	2.2	25.2	6.9	12.7	nd	0.7	7.0	1.3	3.9	4.8	4.6	19.9	1.0	44.2
21	5.9	nd	0.6	nd	nd	nd	4.0	4.1	46.6	0.9	38.0	6.3	5.5	nd	0.3	nd	nd	nd	1.5	3.7	28.0	0.4	60.6
23	10.3	1.7	1.4	10.7	1.1	4.2	17.7	5.6	24.6	3.5	19.3	5.8	11.5	1.4	0.9	10.0	1.8	5.0	7.7	6.0	17.5	1.6	36.5
24	13.0	nd	1.5	11.9	1.8	4.2	12.1	5.1	25.2	3.3	22.0	6.2	13.7	nd	0.9	10.4	2.8	4.7	5.0	5.1	16.8	1.5	39.1

A.2 LA-ICP-MS dataset

Table A.2 Trace element data of individual sample spots along DRC coated diamond traverses analysed by LA-ICP-MS and normalised to an Al concentration of 8600 ppm (Carbonaceous chondrites, McDonough & Sun (1995). Data for individual sample spots is given along with the sample medium taken to be the bulk composition of the micro-inclusions (highlighted grey). Abbreviations: na - not analysed, nd - not detected.

Table A.2:

sample	spot	Na	K	Sc	Ti	Mn	Fe	Co	Ni	Ga	Sr	Zr	Nb	Ba	La	Ta	U
CTPb8																	
core	1d	nd	nd	nd	nd	nd	5402	nd	nd	nd	nd	90	nd	46	68	nd	nd
core	2d	nd	nd	nd	15738	nd	11083	128	2967	nd	222	nd	8	175	2	nd	nd
coat	3d	nd	19453	43	3540	nd	14923	nd	nd	324	1849	216	45	6802	390	nd	29
coat	4d	nd	5861	26	1805	nd	9567	nd	nd	104	1146	96	25	2651	213	nd	10
coat	1a	1411	7418	818	2816	na	nd	33	39	45	479	na	44	1646	100	na	na
coat	2a	4524	16233	841	5792	na	nd	9	231	76	2089	na	121	5689	434	na	na
coat	3a	3039	12589	1259	3923	na	nd	nd	nd	89	1877	na	134	3778	367	na	na
coat	4a	5349	19517	524	4400	na	nd	nd	222	78	2591	na	110	5424	449	na	na
coat	5a	4722	22330	769	3970	na	nd	8	71	84	2328	na	43	5228	392	na	na
coat	6a	2751	23230	191	2425	na	nd	19	111	87	1915	na	12	5038	400	na	na
coat	7a	2616	23232	333	3268	na	nd	7	30	119	1787	na	14	6383	363	na	na
core	8a	nd	16197	3325	3103	na	nd	nd	7	69	1016	na	nd	2840	143	na	na
core	9a	nd	9959	4305	nd	na	13567	147	3439	99	424	na	nd	1765	55	na	na
core	10a	7090	13131	3369	4093	na	6708	76	1169	126	385	na	56	312	62	na	na
core	11a	35400	1305	5216	6337	na	3461	61	1129	55	83	na	43	241	43	na	na
coat	12a	4543	25493	181	2877	na	nd	nd	198	143	1993	na	35	7229	401	na	na
coat	13a	7019	28231	222	3002	na	nd	3	202	87	1850	na	25	4952	373	na	na
coat	14a	5416	23514	357	2705	na	nd	24	419	87	2172	na	51	4851	382	na	na
coat	15a	5551	22478	354	5016	na	nd	25	111	142	2779	na	73	5805	432	na	na
coat	16a	5357	29139	755	4061	na	nd	nd	291	88	1658	na	63	3078	271	na	na
coat	17a	2027	6521	466	831	na	nd	5	168	34	584	na	45	1093	70	na	na
CTPs13																	
coat	1d	3434	5396	2	68990	214	1742	3	54	5	136	38	41	135	8	1	1
coat	2d	1113	16921	8	3529	79	8808	6	78	125	281	198	7	2553	131	nd	8
core	3d	16106	31337	nd	23122	nd	20074	327	8570	nd	341	nd	nd	1507	77	27	46
core	4d	8742	14552	nd	15372	nd	127092	198	nd	14	nd	218	27	137	33	nd	16
coat	1a	2492	617	283	16264	na	nd	10	10	24	212	na	12	1735	88	na	na
core	2a	2330	nd	396	39503	na	601	30	nd	8	67	na	19	451	38	na	na
core	3a	nd	nd	984	23572	na	5731	nd	13	nd	68	na	25	152	29	na	na

sample	spot	Na	K	Sc	Ti	Mn	Fe	Co	Ni	Ga	Sr	Zr	Nb	Ba	La	Ta	U
core	4a	nd	nd	807	40889	na	3376	28	nd	nd	70	na	8	78	nd	na	na
core	5a	nd	nd	966	63937	na	4682	36	nd	nd	46	na	nd	42	26	na	na
core	6a	nd	nd	1117	29621	na	3524	nd	nd	nd	41	na	nd	15	8	na	na
core	8a	7010	8418	nd	71142	na		38	188	4	176	na	12	26	14	na	na
core	9a	3000	4713	120	15987	na	447	12	194	14	7	na	16	138	9	na	na
core	10a	4993	14635	596	9558	na	1600	24	913	nd	19	na	46	118	nd	na	na
core	11a	1985	25008	359	5499	na	nd	21	681	37	342	na	13	2324	95	na	na
coat	12a	1121	17601	30	4605	na	nd	5	76	34	153	na	5	1840	101	na	na
coat	1c	836	17911	37	3006	na	nd	3	62	32	155	na	4	1846	99	na	na
coat	2c	15342	38645	378	18896	na	nd	nd	8	31	149	na	20	1462	71	na	na
core	3c	12172	21809	374	64566	na	nd	nd	nd	nd	72	na	22	282	nd	na	na
core	4c	5990	14842	2553	53306	na	nd	nd	46	nd	35	na	nd	224	nd	na	na
core	5c	615	5591	561	34642	na	nd	nd	nd	nd	14	na	46	103	nd	na	na
core	6c	1901	9157	665	74276	na	nd	nd	370	nd	43	na	27	119	nd	na	na
coat	7c	835	20322	150	8100	na	nd	6	126	36	219	na	7	1827	105	na	na
CTPs2																	
core	1d	774	545	nd	324	nd	nd	5	nd	nd	9	nd	1	4	1	1	0
core	2d	74097	26636	nd	23525	nd	nd	126	nd	nd	519	nd	nd	17	nd	57	16
core	3d	120590	10182	nd	3489	nd	nd	182	nd	nd	160	251	52	62	32	13	nd
coat	4d	7647	6659	nd	19297	nd	9621	96	nd	159	1812	209	144	3932	251	5	49
coat	5d	4431	13873	nd	5955	nd	13549	30	nd	237	2820	184	99	6184	441	4	51
coat	1a	nd	11533	171	19111	na	nd	nd	937	nd	911	na	40	1646	75	na	na
coat	2a	1778	14450	nd	2758	na	nd	nd	329	76	1578	na	28	4148	335	na	na
coat	3a	1876	15546	5	13565	na	nd	1	92	71	1363	na	16	4243	324	na	na
coat	4a	174	11678	302	42005	na	nd	nd	323	18	815	na	48	2099	118	na	na
core	5a	nd	10731	1362	32707	na	nd	nd	433	nd	592	na	37	809	96	na	na
core	6a	4394	11597	2606	7991	na	nd	89	707	33	223	na	19	420	21	na	na
core	7a	1425	10977	2064	30203	na	6274	70	3081	103	41	na	nd	45	nd	na	na
core	8a	1038	14753	4998	1424	na	9273	117	3265	20	20	na	37	117	nd	na	na
core	9a	nd	7168	6918	7874	na	8650	154	2442	86	nd	na	49	nd	110	na	na
core	10a	nd	6443	3826	3518	na	15427	nd	3534	90	nd	na	nd	37	47	na	na
coat	11a	2273	22380	321	6111	na	nd	nd	251	100	2086	na	7	6625	424	na	na
coat	12a	2292	22109	349	3705	na	nd	10	252	81	1929	na	23	5393	339	na	na

sample	spot	Na	K	Sc	Ti	Mn	Fe	Co	Ni	Ga	Sr	Zr	Nb	Ba	La	Ta	U
coat	13a	1948	14931	520	3050	na	nd	9	228	58	1818	na	73	3754	277	na	na
coat	14a	1336	19261	654	3466	na	nd	15	642	78	1731	na	78	3544	213	na	na
coat	2c	nd	52076	795	6789	na	nd	nd	nd	266	4502	na	nd	12513	873	na	na
coat	9c	nd	69658	3979	18042	na	nd	nd	nd	461	8758	na	nd	21585	1892	na	na
B9																	
coat	1d	6611	20956	5	5910	640	15293	10	217	439	2444	45	198	8230	645	2	34
coat	2d	8380	21216	184	8766	695	53061	84	327	858	3262	44	23	15585	1104	nd	19
core	3d	4607	5217	254	23911	366	828	84	nd	57	28	78	nd	44	nd	nd	34
core	4d	6544	11635	287	171964	nd	nd	163	nd	27	240	nd	nd	130	nd	nd	4
coat	1a	5153	5530	196	32067	na	nd	17	225	330	2816	na	243	10440	798	na	na
coat	2a	8316	12578	1044	4282	na	nd	41	493	1829	9638	na	335	48406	3506	na	na
coat/core?	3a	12226	1918	3385	4028	na	294	nd	9	243	1863	na	93	8269	455	na	na
coat/core?	4a	30928	4808	3545	1307	na	nd	nd	970	431	1819	na	555	12115	659	na	na
core	5a	45702	nd	8013	1568	na	9191	29	5438	79	383	na	93	2224	66	na	na
core	6a	14773	nd	2144	24658	na	nd	105	3170	nd	137	na	282	156	19	na	na
core	7a	34504	nd	4012	21599	na	nd	90	4283	20	178	na	170	46	25	na	na
core	8a	8381	nd	716	4496	na	989	263	750	1	9	na	nd	117	nd	na	na
core	9a	31907	nd	2653	57055	na	2722	22	1465	nd	37	na	82	28	15	na	na
core	10a	26098	nd	2360	122731	na	3742	8	743	nd	22	na	32	6	6	na	na
core	11a	34097	4707	nd	33575	na	nd	52	2364	41	28	na	25	nd	23	na	na
core	12a	40488	2280	1087	86032	na	nd	111	3721	nd	45	na	39	28	37	na	na
coat	13a	23915	23457	nd	172	na	nd	52	1160	2486	15256	na	621	65005	5098	na	na
CTPs14																	
coat	1a	2187	14813	21	2768	na	8412	19	180	317	1066	459	4	6738	222	1	22
coat	2a	2824	17625	35	3794	na	11284	4	218	195	1638	391	12	4405	319	1	18
coat	3a	3475	17403	53	5062	na	13529	nd	188	230	1797	364	14	4584	375	1	26
coat	4a	3414	16993	19	4474	na	11856	nd	95	195	1613	392	18	4421	339	2	12
coat	5a	3028	16326	2	4121	na	10088	nd	176	202	1430	399	22	4264	279	nd	9
coat	6a	3618	17905	20	4106	na	10633	nd	98	204	1581	280	15	4077	248	2	3
CDR3																	
coat	1a	1863	2198	38	2213	na	nd	nd	111	21	2286	na	86	5679	397	na	na

sample	spot	Na	K	Sc	Ti	Mn	Fe	Co	Ni	Ga	Sr	Zr	Nb	Ba	La	Ta	U
coat	2a	2621	2702	nd	3397	na	nd	23	105	28	3194	na	145	8001	535	na	na
coat	3a	2486	2231	nd	2935	na	nd	15	164	14	2605	na	78	6070	458	na	na
coat	4a	3299	3063	nd	3431	na	nd	20	489	20	3526	na	85	8046	590	na	na

Appendix B

Publications

B.1 Papers:

Tomlinson, E.L., Jones, A.P., and Milledge, H.J. (2004) High-pressure experimental growth of diamond using C-K_2CO_3-KCl as an analogue for Cl-bearing carbonate fluid. *Lithos 77 (1-4) 287-294.*

Emma Tomlinson, Isabel De Schrijver, Katrien De Corte, Adrian P. Jones, Luc Moens, Frank Vanhaecke. Trace element compositions of sub-microscopic inclusions in coated diamond: a tool for understanding diamond petrogenesis. *In press, GCA.*

Emma Tomlinson, Jeff W. Harris, Adrian P. Jones. Fluid and silicate inclusions in coated diamonds from the Panda kimberlite, Canada. *In prep.*

Emma Tomlinson, Paul F. McMillan, Ming Zhang, Adrian P. Jones, Simon A.T. Redfern. IR spectroscopy of C-O-H inclusions in fibrous diamonds: Calibrated P-T relations and the nature of mantle fluid during fibrous diamond growth. *In prep.*

B.2 Conference Abstracts:

Tomlinson, E.L., Jones, A.P. and Milledge, H.J. (2003). Multiple fluids in micro inclusions in diamond coat and their role in diamond growth. 8^{th} International Kimberlite Conference, Vancouver, Canada. June 2003. 3.P29.

Emma Tomlinson, Adrian Jones and Judith Millegde (2002). The role of mantle fluid in diamond growth. 54^{th} DeBeers Diamond Conference, Cambridge, UK. July 2003.

Emma Tomlinson and Adrian Jones (2004). Experimental diamond growth in carbonate-KCl: an analogue for the growth of natural diamond coat in the mantle. Goldschmidt Conference, Copenhagen, Denmark. June 2004. 3.5PO7.

Emma Tomlinson, Isabel De Schrijver, Katrien De Corte and Adrian Jones (2004). A LA-ICP-MS study of trace elements in coated diamonds. 55^{th} DeBeers Diamond Conference, Warwick, UK. July 2004.

Emma Tomlinson (2004) Variable Temperature Infrared Spectroscopy of Mantle Fluids in Natural Fibrous Diamond. 55^{th} DeBeers Diamond Conference, Warwick, UK. July 2004.

Emma Tomlinson, Jeff Harris (2005) Fluid and silicate inclusions in fibrous diamonds from Panda, Canada. 56^{th} DeBeers Diamond Conference, Oxford, UK. July 2005.

Emma Tomlinson, Isabel De Schrijver, Katrien De Corte, Daniel Howell, Judith Milledge, Adrian P. Jones. A synthesis of diamond and inclusion trace element studies. 56^{th} DeBeers Diamond Conference, Oxford, UK. July 2005.